Applying organoid technology to pediatric cancer research

towards organoid-directed treatment of pediatric kidney cancer patients

Camilla Calandrini

Applying organoid technology to pediatric cancer research

towards organoid-directed treatment of pediatric kidney cancer patients

Toepassen van organoïde technologie in onderzoek naar kinderkanker – richting organoïde gebaseerde behandeling van nierkanker bij kinderen

(met een samenvatting in het Nederlands)

Proefschrift

ter verkrijging van de graad van doctor aan de
Universiteit Utrecht
op gezag van de
rector magnificus, prof.dr. H.R.B.M. Kummeling,
ingevolge het besluit van het college voor promoties
in het openbaar te verdedigen op

vrijdag 25 november 2022 des ochtends te 10.15 uur

door

Camilla Calandrini

geboren op 9 januari 1993
te Ravenna (RA), Italië

"All models are wrong, but some are useful"

George Box

Table of contents

Chapter 1

General introduction

Camilla Calandrini[1]

[1] Princess Máxima Center for Pediatric Oncology, Oncode Institute, Heidelberglaan 25, 3584 CS Utrecht, the Netherlands

Pediatric cancer

Cancer represents one of the leading causes of death in children and adolescents in the Western world[1]. This translates in the passing of approximately 100 children per year in the Netherlands alone[2]. In the past decades, the introduction of better treatment strategies significantly improved life expectancy, increasing overall survival rates from 40% of the 1970s to approximately 80% of recent years (**Figure 1A**)[3-6]. However, cancer survivors still suffer from severe side effects caused by the harsh treatments, with serious negative impact on their quality of life[7]. Furthermore, no effective therapies are yet available for ~25% of the patients, which are destined to succumb to the disease[8]. Thus, there is an urgent need to develop effective and less-toxic therapies to achieve the aim of curing every child from cancer.

Pediatric and adult tumors diverge in many aspects. Firstly, unlike adult tumors, childhood cancer is a relatively rare disease[9]. Secondly, while adult cancers are characterized by genomic instability and by an high mutational burden, pediatric malignancies generally harbor few somatic mutations, where driver mutations often occur in genes encoding for epigenetic machinery or transcription factors, in a cancer-type specific manner[10-12]. Alongside, pediatric patients show more frequent germline predisposition to cancer development than adult patients[10, 11, 13]. Thirdly, adult tumors are most often carcinomas, originating from epithelial tissues, such as breast, lung and colon. On the contrary, pediatric tumors comprise a wide spectrum of cancer types, spacing from hematological malignancies and central nervous system tumors, to lymphomas and sarcomas[10, 14]. Lastly, some childhood malignancies have been described to originate during embryogenesis, as a result of aberrant development[15, 16], while adult cancers have been mostly associated with aging and lifestyle[17, 18]. All together, pediatric malignancies greatly differ from adult tumors and, as such, should be studies as separate entities.

Improvement on overall survival rates registered in the past decades has been achieved through the adaptations of protocols used for adult cancer patient treatment. To further increase overall survivals, more pediatric-specific oriented treatment approaches, targeting unique mechanisms of childhood cancer, should be investigated. To achieve this, a deeper understanding of pediatric cancer biology and development is crucial.
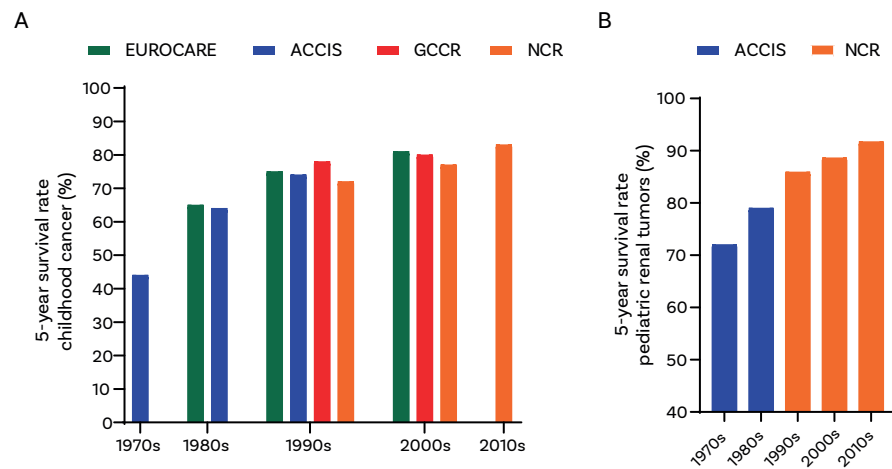
Figure 1. **Overall survival of children with cancer is improving. A**. Five-year survival rates of pediatric cancer patients (0-14 years) from 1970s to 2010s. Data collected from several European registries: EUROCARE[8], ACCIS (European Automated Childhood Cancer Information System)[19], GCCR (German Childhood Cancer Registry)[6] and NCR (Netherlands Cancer Registry)[5]. **B**. Five-year overall survival of patients with pediatric renal tumors from 1970s to 2010s. Data collected from NCR and ACCIS registries[5, 20].

Pediatric renal and rhabdoid tumors

Pediatric renal tumors account for ~6% of all childhood malignancies, comprising several distinct subtypes that greatly differ in etiology, histology and prognosis[21]. The vast majority of the patients (~90%) are diagnosed with a Wilms tumor[22], while the most common non-Wilms tumors include malignant rhabdoid tumor of the kidney (MRTK), renal cell carcinoma (RCC) and clear cell sarcoma of the kidney (CCSK)[21] (**Figure 2**). Treatment of these malignancies is multimodal, consisting of surgery, chemotherapy, and/or radiotherapy[23]. Although considerable improvement in the overall survival has been achieved in the past decades for children with a Wilms tumor (**Figure 1B**), few treatment options are available for specific high-risk subgroups and for non-Wilms tumor patients[23, 24]. Furthermore, the current treatment regimens cause severe side effects, including kidney failure, cardiotoxicity, infertility and secondary malignancies, which results in decreased quality of life and in a reduced life expectancy[25-27]. A deeper understanding of the biology of pediatric renal tumors is crucial for the development of more effective and less toxic therapies to achieve improved overall survival and an optimal quality of life for all patients.
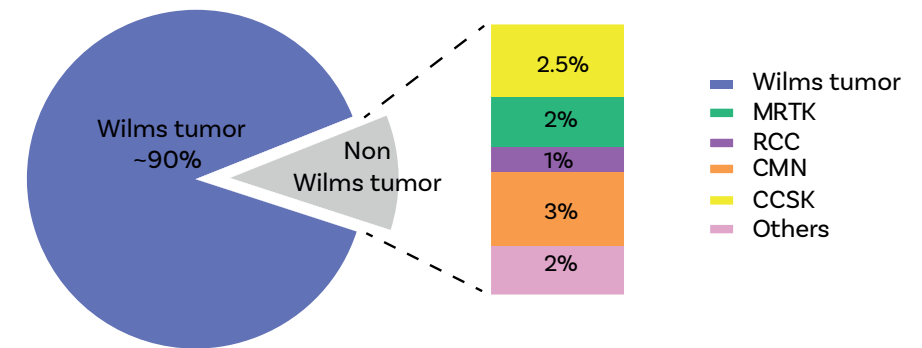

Figure 2. **Pediatric kidney tumors comprise a wide spectrum of cancer types.** Distribution of diagnosis of pediatric kidney tumors according to SIOP-RSTG 2001 registration. MRTK, malignant rhabdoid tumor of the kidney; RCC, renal cell carcinoma; CMN, congenital mesoblastic nephroma; CCSK, clear cell sarcoma of the kidney.

Wilms tumor

Wilms tumor (or nephroblastoma) affects 1 in every 14000 children worldwide. In the Netherlands, this translates to 25-30 cases each year[22, 28, 29]. Children are commonly diagnosed between the age of 2 and 4 years with a sporadic Wilms tumor[30]. In 5% of the patients, Wilms tumor can show a bilateral presentation with both kidneys affected simultaneously[31]. In these cases, patients often show a familial history of Wilms tumor or congenital abnormalities, suggesting the presence of an underlying genetic predisposition[32, 33]. Overall, about 10% of children diagnosed with Wilms tumor are affected by syndromes predisposing to Wilms tumor occurrence[32]. WAGR syndrome (characterized by genito-urinary malformations, aniridia and intellectual disability caused by deletion of *WT1* gene) and Beckwith-Wiedemann syndrome (overgrowth syndrome caused by aberrant imprinting of chromosomal region 11p15) are among the most common[32].

Wilms tumor is an embryonal cancer thought to arise as a consequence of a differentiation block during early nephrogenesis[16, 34]. Its embryonal origin is reflected in the peculiar triphasic histology containing blastemal, stromal and epithelial components (**Figure 3**). While blastemal cells are typically undifferentiated small blue round cells (**Figure 3 c-f**), stromal cells show a mesenchymal-like phenotype (**Figure 3 g,h**) and epithelial cells recall the typical epithelial structures found in the kidney, such as primitive tubules and glomeruli (**Figure 3 a,b**)[35, 36]. The distribution of these cellular components can greatly differ among patients, making Wilms tumor an highly morphologically heterogenous tumor[36].
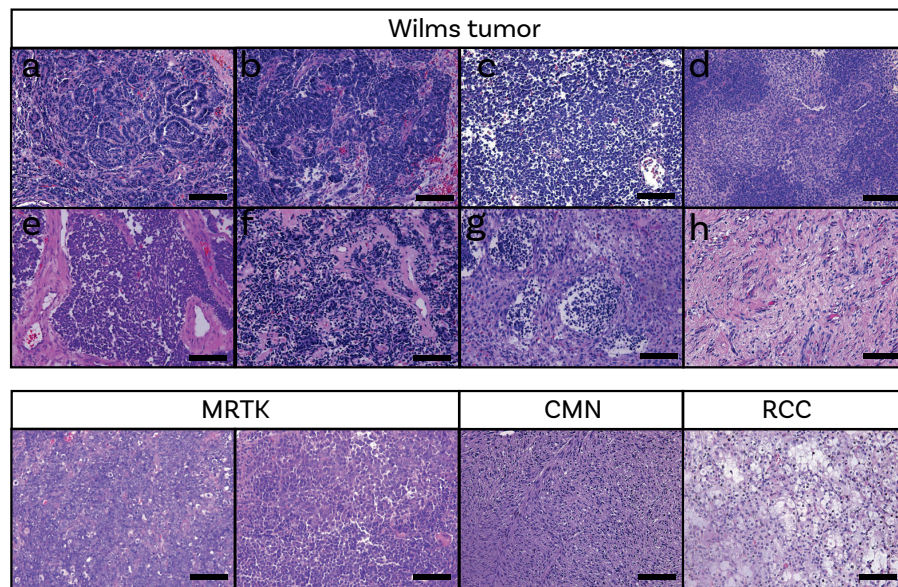
Figure 3. **Histological characterization of several pediatric kidney tumor entities.** Representative Hematoxylin and Eosin staining of various pediatric kidney tumor tissues. MRTK, malignant rhabdoid tumor of the kidney; CMN, congenital mesoblastic nephroma RCC, renal cell carcinoma. Wilms tumor tissues (**a-h**) display an highly heterogenous histology. Scale bar: 100μm

The heterogeneous nature of Wilms tumor also manifests at the genetic level[37]. Wilms tumors can show both complex patterns of chromosomal gains and losses, as well as normal diploid karyotypes[38]. Recurrent mutations found in genes involved in nephrogenesis such as *WT1, WTX (or AMER1)* and *CTNNB1*, are detected in ~40% of cases[39, 40]. Another group of recurrent mutations is found in genes involved in miRNA processing (e.g. *DROSHA, DICER1, DGCR8* etc., ~15%)[38, 41, 42]. The remaining cases are characterized by mutations in a variety of other genes, all manifesting at lower frequencies[29]. Alterations in *TP53* are detected in 7-8% of all Wilms tumor patients[37, 43]. The presence of *TP53* mutations has been correlated with the occurrence of anaplasia, defined as presence of tumor cells with hyperchromatic, large nuclei and atypical mitosis, and have been associated with a worse outcome[43-45]. Next to the genetic alterations, ~70% of all Wilms tumor patients show somatic loss of imprinting or loss of heterozygosity of chromosomal region 11p15, resulting in overexpression of *IGF2* gene, the same event associated with Beckwith-Wiedemann syndrome[38, 41, 46]. Although representing the

most recurrent alteration found in Wilms tumor patients, this event alone is likely not sufficient to initiate tumorigenesis[47, 48].

Children diagnosed with renal tumors can be treated following two different strategies: upfront surgical removal of the affected kidney, applied by the Children's Oncology Group – Renal Tumor Group (COG-RTG), or pre-operative chemotherapy treatment (for children ≥ 6 months old), implemented by the International Society of Pediatric Oncology Renal Tumor Study Group (SIOP-RTSG)[23, 49]. While the COG protocol is applied for the treatment of children in North America, the SIOP-RTSG strategy is followed mostly in Europe. Albeit the fundamental differences in treatment strategies, patient's overall survivals achieved by the two groups are both excellent and comparable[24, 49].

The current therapy for Wilms tumor patients treated according to the SIOP-RTSG consists of pre-operative chemotherapy, followed by the surgical removal (total or partial) of the affected kidney, and by post-operative chemotherapy, adjusted to the assigned histological risk category[23, 24, 49, 50]. Patients displaying a completely necrotic tumor at completion of pre-operative chemotherapy are classified as low-risk; tumors with a high percentage of blastema component (> 66%) and/or presence of diffuse anaplasia are categorized as high-risk. Overall, the majority of the patients is categorized as intermediate-risk, characterized either by a regressive type, a prevalent epithelial, stromal or a mixed histology, or by the presence of focal regions with anaplasia.

Approximately 15% of all Wilms tumor patients eventually develops one or more relapses[51]. In the Netherlands, this translates in a total of 4/5 patients per year[52]. For these patients, overall survival significantly drops from 90% to 50%, with very high-risk stratified patients alone showing a dismal 10% survival chance[50, 52, 53]. Of notice, most patients experiencing disease relapse - in absolute numbers- belong to the intermediate risk group[54, 55]. This stresses how the current patient stratification methods are not able to identify all patients with an increased risk of relapse, that would benefit from a harsher treatment of the primary presentation. Many studies are currently ongoing to identify biological markers to aid the recognition of such patients[56-59]. Among others, 1q gain and 1p/16q loss are currently under investigation as biological markers associated with poor outcome.

Wilms tumor relapses generally occur at distant locations, most often in lung and abdominal cavity, and mostly within 2 years from the treatment of the primary tumor[60]. Based on the chemotherapy regimen given as treatment of the primary presentation, as well as staging and histological classification, patients are further stratified into relapse groups AA, BB and CC, corresponding to a standard,

high and very high-risk categories[23, 55]. While patients belonging to the AA group have a general good prognosis (OS: 80%), CC patients are likely not to respond to standardized chemotherapy regimens and consequentially succumb to the disease (OS: 10%)[53-55, 61]. For these patients, testing of novel targeted agents in a pre-clinical setting, or inclusion in ongoing clinical trials, are options that should be stimulated.

Malignant rhabdoid tumor

Malignant rhabdoid tumor (MRT) is a rare but extremely aggressive malignancy that primarily affects infants and young children[62]. Children are mostly diagnosed before the age of 3 years, and they often present with metastatic disease[63-65]. MRTs can arise in different locations of the body, spacing from the central nervous system (where they are referred to as Atypical Teratoid/Rhabdoid Tumors (ATRT)), soft tissues and several organs such as liver and kidney (collectively named Extra Cranial Rhabdoid Tumors (ECRT)). When arising in the kidneys specifically, they are referred to as Malignant Rhabdoid Tumors of the Kidney (MRTKs). Albeit topologically diverse, MRTs are characterized by a single recurrent genetic driver mutation, the bi-allelic loss of the SWItch/Sucrose Non-Fermentable (SWI/SNF) chromatin remodeling complex subunit *SMARCB1* (95% of the cases) or, in rare cases, *SMARCA4* (5%)[66, 67]. Germline *SMARCB1* mutations are detected in about 30% of the patients, which often manifest an early onset of synchronous or metachronous tumors affecting different organs[68].

The SWI/SNF chromatin remodeling complex plays a crucial role in controlling transcription factors access to chromatin via nucleosome repositioning, consequentially regulating gene expression[69]. Mutations in its subunits are thought to trigger cell reprogramming and to activate oncogenic transformation. Interestingly, perturbations in subunits of the SWI/SNF complex are not only described in MRTs, but in more than 20% of all human cancers[70, 71]. In the context of MRT development, it is suggested that loss of *SMARCB1* drives tumorigenesis by inhibiting binding of the SWI/SNF complex to typical enhancers, required for cell differentiation, while promoting binding to non-canonical super-enhancers[72].

Like many other pediatric cancers, MRTs are thought to originate during embryonic development[73-75]. This hypothesis has been supported by recent studies using genetically engineered mouse models, where the appearance of rhabdoid tumors was observed only when *smarcb1* depletion was induced during early embryogenesis, and not during adult life[74]. Furthermore, different studies have identified neural crest as putative cell-of-origin for MRT tumors[75, 76]. Histologically, MRTs are typically composed of cells characterized by large nuclei, surrounded by abundant eosinophilic cytoplasm[62] (**Figure 3**). However, rhabdoid-like features can occasionally be found in other tumor types, including central nervous system tumors, neuroblastoma and kidney tumors (e.g. Wilms tumor), which can complicate the correct identification of the tumor entity[77, 78]. Negative immunostaining for INI1 (protein encoded by *SMARCB1*) or BRG1 (protein encoded by *SMARCA4*) is used to confirm an MRT diagnosis[79].

MRTs are overall characterized by a low mutational burden and a stable karyotype[76, 80]. Although genetically rather homogeneous, MRTs can be classified into different subgroups based on their epigenetic landscape. ATRTs can be separated into MYC, sonic hedgehog (SHH) and tyrosinase (TYR) subtypes based on their DNA methylation and gene expression profiles[81-83]. ECRTs on the other hand, mostly resemble the ATRT-MYC subgroup[76]. These classifications mirror the group-specific overactivation of transcriptional programs and oncogenic pathways, and they are suggested to reflect different cells-of-origin, which could also explain the differences in age and location of onset registered in the different subgroups[82]. Although the identification of such transcriptional programs could suggest the use of therapeutic approaches targeting the group-specific overactivated oncogenic pathways, nowadays MRT patients are treated regardless of their epigenetic profile. Interestingly, ATRT-TYR patient have been shown to display a better outcome compared to ATRT-MYC and ATRT-SHH patients, suggesting that methylation profiling should be introduced as standard diagnostic procedure to improve patient risk-stratefication[84]. Patients' age, presence of a *SMARCB1* germline mutation and tumor stage are still the most commonly used prognostic factors[65].

Remarkably, about 70% of MRT patients, albeit treated with a combination of harsh chemotherapy, radiotherapy and surgery, eventually succumb to the disease[85]. For this reason, MRT still represents one of the biggest challenges of modern pediatric oncology.

Preclinical models of pediatric tumors

Therapeutic innovation for pediatric cancer patients has been impaired by different factors affecting both clinical and pre-clinical research.

First, pediatric cancer is a relatively rare disease and the paucity of patients limits the possibility of initiating tumor entity-specific clinical trials[86]. Centralization of patients to specialized care centers and, in case of even rarer malignancies, international collaborations are therefore crucial[87]. Alongside, many ethical

issues arise when considering testing of novel therapeutic approaches directly on children. Therefore, much relevance is given to the results of pre-clinical testing of novel therapeutic approaches, as well as to the gather of knowledge about the biology underpinning tumor development. Pre-clinical models are indispensable to achieve such results. However, such models are scarce or, for some entities, even lacking.

Historically, pediatric cancer research has mostly relied on cancer cell lines, patient-derived tumor xenograft (PDTXs) and genetically engineered mouse models (GEMMs) (**Figure 4**). Even though each of these models have their limitations, they have all significantly contributed to the current understanding of the biology of pediatric tumors.

Cancer cell lines represent the most commonly used *in vitro* model to study cancer[88]. This is especially due to their ease of propagation and genetic manipulation, possible at a low cost. Although many cell lines are available for pediatric cancer research, these are often not representative of the original tumor, both genetically and phenotypically[89-92]. To achieve long term propagation, cancer cell lines often have to undergo immortalization procedures, which transforms the genetic background of the original cell lines. Furthermore, cancer cell lines often fail to represent the cellular heterogeneity of the tissue they were derived from[90]. Lastly, efficiency of establishment for 2D-growing cell lines is generally poor, and the successfully established lines are often derived from metastatic tumors, resulting in an underrepresentation of early stage cancers[88, 93].

PDTXs offer an *in vivo* set up for the testing of compounds on patient-derived tumors implanted subcutaneously or orthotopically[94]. The main advantage of this model is the possibility of testing the effects of drug treatment in a full organism, where blood vessels, tumor-associated stromal cells and a tumor in its close to native environment are co-existing in one model. PDTXs also allow for the systemic assessment of off-target toxic effects of drug treatment. Recent efforts from the scientific community have substantially increased the availability of PDTX models for pediatric solid tumors, with great benefits for the community[95]. Albeit representing a rather complete model, mice used to generated PDTX are lacking an active immune system, making it impossible to study tumor-immune cells interaction and to test immunotherapy approaches[90, 96]. Furthermore, a recent study demonstrated the occurrence in PDTXs of mouse-specific tumor evolution, which results in tumor tissues loosing the original genetic landscape[97].

GEMMs allow for a more physiological modelling of tumorigenesis, where precisely timed induction of tumor driver mutations triggers the formation of tumors in an immunocompetent host[74, 98]. Therefore, GEMMs represent important tools that can be used to pinpoint the cell of origin of pediatric tumors, as well as to study the tumors in a native and immunocompetent environment. Albeit of undeniable value, GEMMs are time and resource-consuming models and they can be established only for those tumors from which the tumor-driver mutations and cells-of-origin have been established. Moreover, oncogenic processes taking place in human cancer are not always amenable to be reproduced in mice, given the biological differences between the species. Like observed in PDTX models, GEMMs can develop tumors that fail to recapitulate the genetics of the original human cancers[99]. At last, another caveat of *in vivo* mouse models, both PDTXs and GEMMs, comprise the impracticality of conducting high-throughput studies[100].

Even though many pre-clinical models of different nature are available to study pediatric tumors, the vast majority of the drugs entering clinical trials still results in a disappointing outcome, either due to insufficient efficacy or to heavy burden of side effects[96, 101]. All this emphasizes the poor translational power of the currently available pre-clinical models and the need for improved models that can bridge the gap between bench and bedside.

	Establishment efficiency	Genetic manipulation	Relative cost	Resemblance phenotypic features	Resemblance genotypic features	Vascularization & Immune cells	Representation tumor heterogeneity	High-throughput screening	Prediction clinical response
2D cells	±	+++	+++	-	±	-	±	+++	±
Organoids	++	++	++	++	+++	-/±*	++	++	+++
PDTXs	±	-	±	+++	++	++/-	±	-	+++
GEMMs	±	±	±	+++	±	+++	±	-	±

Figure 4. Feature comparison between the described preclinical tumor models. Features were evaluated as: best (+++), good (++), partly suitable (±), not suitable (-). * possible with the development of co-culture systems. Figure adapted from Broutier et al. 2021[92] and Kim et al. 2020[102].

Organoid technology for pediatric cancer research

One of the new frontiers of *in vitro* culture allows for the expansion of multicellular structures, derived from stem cells, in a three-dimensional (3D) fashion. Thanks to the use of protein-based matrix scaffolds and media composed of well-defined growth factor cocktails, together mimicking the *in vivo* stem cell niche, these 3D structures self-organize while resembling characteristics of the tissues of origin. These *in vitro* models are known as organoids[103]. Organoids can be generated

from both embryonic (pluripotent stem cells, PSC) and organ-restricted adult stem cells (ASC), allowing, at least partially, for the modeling of organ-specific functions[103, 104].

The first ASC-derived organoid model was developed for the mouse small intestine, as described by Sato et al[105]. The authors showed that mouse intestinal stem cells can be cultured *in vitro* when plated in conditions mimicking the native stem cell niche, and generate highly organized structures resembling the typical crypt-villi formation found *in vivo*[105]. This finding paved the way for the development of many more organoid models, derived from both mouse and human epithelial tissues, including colon[106], stomach[107], lung[108], liver[109, 110], kidney[111], pancreas[112], breast[113], fallopian tube[114] and prostate[115, 116]. Organoids have been shown to maintain a stable karyotype during long-term culturing, representing therefore the first normal-tissue derived *in vitro* models recapitulative of the genetics and phenotype of the tissue of origin[106, 110, 111, 117]. Organoid cultures can be established with high efficiency from tissue samples received from surgery or explorative biopsies, but also, in case of the urinary system, from more easily accessible sources such as urine[111]. Lastly, organoids can be genetically modified, making them appealing models to study tumorigenesis[118, 119].

Following the successful establishment of organoid cultures from mouse and human intestinal tissues, alike protocols were developed to grow organoid cultures from diseased tissues, such as cancer[104] (**Figure 4**). The relatively high establishment efficiency of patient-derived tumor organoid cultures resulted in the generation of numerous novel tumor models. Among others, tumor organoid cultures have been established from colorectal[120], breast[113, 121], liver[122], stomach[107] and prostate cancer[123], from both primary and metastatic disease. In these studies, tumor organoids were described to retain the cellular heterogeneity, the transcriptomic profiles and the genetics of the parental tissues. The high efficiency of establishment of patient-derived tumor and normal organoids has already allowed for the generation of large "living" collections of organoids, also known as biobanks, representing a valuable resource for pre-clinical studies and for future investigation of personalized medicine approaches[104].

Given the high resemblance to the tissues they were derived from, patient-derived organoids provide a representative model for drug testing. While tumor organoids can be used to investigate the sensitivity to drugs of specific tumor entities, normal tissue-derived organoids can be used to assess toxicity and treatment specificity. Previous studies have already shown the feasibility of investigating genotype/drug response correlations in organoid models[118, 119]. Moreover, several independent studies have shown that tumor organoids hold a predictive value for patient response to therapy[124-128]. In Vlachogiannis et al.[128], patient-derived gastrointestinal organoids were tested for the response to specific chemotherapy and targeted therapy. The results were compared to those obtained *in vivo*, from matching patients which had received the same treatment. Overall, a remarkable 88% of positive predictive value (response in patient/response in organoids) and 100% negative predictive value (no response in patient/no response in organoids) was registered. This and many other studies[124-127], opened the doors for the use of organoids as clinically relevant models. Future studies will be needed to further investigate their validity to predict patient response to standard of care therapy and for the discovery of novel therapeutic strategies.

The application of the organoid technology to pediatric tumors could translate in significant advances for this research field. From the generation of novel and improved models, providing with new opportunities for the understanding of the etiology and biology of pediatric tumors, to the use of these models for the discovery of novel therapeutic vulnerabilities, organoids have the potential to shortened the gap between bench and bedside.

Scope and thesis outline

Children diagnosed with cancer are faced with great challenges. From the burden of side effects induced by the current therapy regimens, to the inadequate treatment options available for some subgroups. Among them, patients with refractory relapsed Wilms tumor and patients affected by MRT still carry a dismal prognosis. Thus, there is an urgent need for improved, less toxic therapeutic approaches. Advances in the treatment of pediatric renal and rhabdoid tumors have been hampered by the lack of representative pre-clinical models able to capture the genetics, transcriptomic profile and cellular heterogeneity of these high-risk tumors. Therefore, the development of novel, reliable pre-clinical models is imperative.

In this thesis, we aimed to generate and characterize patient-derived pediatric renal and rhabdoid tumor organoids and exploit them to identify novel therapeutic options for high-risk patients. After a general introduction on the topic (**Chapter 1**), we describe the 3D *in vitro* organoid cultures currently available to model and study pediatric renal tumors, and the advantages and disadvantages of their use (**Chapter 2**[129]). In **Chapter 3**[130], we present the first pediatric tumor organoid biobank, comprising a wide spectrum of different pediatric kidney tumors, such as Wilms tumors, malignant rhabdoid tumors of the kidney and renal cell

carcinomas. We performed a comprehensive characterization of the tumor organoid cultures and demonstrate their close resemblance to the parental tissues, via genomic, transcriptomic and histological characterization. Finally, we demonstrate the use of such tumor organoids for disease modeling and for proof of principle drug screening. Next to patient-derived kidney tumor organoids, we generated a collection of patient-matching normal kidney organoid cultures, also referred to as tubuloids[111]. In **Chapter 4**[131], we illustrate the protocol to generate and expand such tubuloid cultures, using both tissue as well as urine as starting material. Given the urgent need for more effective and less toxic therapies for patients with MRT, we then focused on the use of MRT organoids for explorative drug screening (**Chapter 5**[132]). By comparing the sensitivity of MRT to 150 targeted compounds to the sensitivity of a panel of healthy tissue-derived organoids, we identified neddylation inhibition as specific therapeutic vulnerability of MRTs. Neddylation inhibitor MLN4924 showed MRT-specific cytotoxic effects, which were also recapitulated in an *in vivo* MRT PDTX model. In **Chapter 6**[133], we describe a detailed protocol for the use of organoids as platform for low- to medium-throughput drug screening. To take a step forward towards meeting the therapeutic needs of relapsed Wilms tumor patients, in **Chapter 7** we describe the generation of novel *in vitro* models from relapsed Wilms tumor samples. In this study, we evaluated the feasibility of generating organoid models from relapsed Wilms tumors and performing drug screening on these models in a clinically-relevant time window. Finally, in **Chapter 8** we elaborate on the results described in this thesis and evaluate how these contribute to the advancement of pediatric renal and rhabdoid tumor research.

References

1. Siegel RL, Miller KD, Jemal A. Cancer statistics, 2020. CA: a cancer journal for clinicians. 2020;70(1):7-30.
2. www.cbs.nl. Epidemiological data on cancer-related death in the Netherlands 2007-2016 [Available from: https://opendata.cbs.nl/#/CBS/nl/dataset/7233/table?dl=60187.
3. Pui C-H, Gajjar AJ, Kane JR, Qaddoumi IA, Pappo AS. Challenging issues in pediatric oncology. Nature reviews Clinical oncology. 2011;8(9):540-9.
4. Saletta F, Seng MS, Lau LM. Advances in paediatric cancer treatment. Translational pediatrics. 2014;3(2):156.
5. Schulpen M, Visser O, Reedijk AM, Kremer LC, Zwaan CM, Eggermont AM, et al. Significant improvement in survival of advanced stage childhood and young adolescent cancer in the Netherlands since the 1990s. European Journal of Cancer. 2021;157:81-93.
6. Kaatsch P. Epidemiology of childhood cancer. Cancer treatment reviews. 2010;36(4):277-85.
7. Erdmann F, Frederiksen LE, Bonaventure A, Mader L, Hasle H, Robison LL, et al. Childhood cancer: survival, treatment modalities, late effects and improvements over time. Cancer epidemiology. 2021;71:101733.
8. Gatta G, Botta L, Rossi S, Aareleid T, Bielska-Lasota M, Clavel J, et al. Childhood cancer survival in Europe 1999–2007: results of EUROCARE-5—a population-based study. The lancet oncology. 2014;15(1):35-47.
9. Steliarova-Foucher E, Colombet M, Ries LA, Moreno F, Dolya A, Bray F, et al. International incidence of childhood cancer, 2001–10: a population-based registry study. The Lancet Oncology. 2017; 18(6):719-31.
10. Gröbner SN, Worst BC, Weischenfeldt J, Buchhalter I, Kleinheinz K, Rudneva VA, et al. The landscape of genomic alterations across childhood cancers. Nature. 2018;555(7696):321-7.
11. Ma X, Liu Y, Liu Y, Alexandrov LB, Edmonson MN, Gawad C, et al. Pan-cancer genome and transcriptome analyses of 1,699 paediatric leukaemias and solid tumours. Nature. 2018;555(7696):371-6.
12. Sweet-Cordero EA, Biegel JA. The genomic landscape of pediatric cancers: implications for diagnosis and treatment. Science. 2019;363(6432):1170-5.
13. Sylvester DE, Chen Y, Jamieson RV, Dalla-Pozza L, Byrne JA. Investigation of clinically relevant germline variants detected by next-generation sequencing in patients with childhood cancer: a review of the literature. Journal of medical genetics. 2018;55(12):785-93.
14. Steliarova-Foucher E, Stiller C, Lacour B, Kaatsch P. International classification of childhood cancer. Cancer. 2005;103(7):1457-67.
15. Filbin M, Monje M. Developmental origins and emerging therapeutic opportunities for childhood cancer. Nature medicine. 2019;25(3):367-76.
16. Behjati S, Gilbertson RJ, Pfister SM. Maturation block in childhood cancer. Cancer Discovery. 2021; 11(3):542-4.
17. DePinho RA. The age of cancer. Nature. 2000;408(6809):248-54.
18. Khan N, Afaq F, Mukhtar H. Lifestyle as risk factor for cancer: Evidence from human studies. Cancer letters. 2010;293(2):133-43.
19. Steliarova-Foucher E, Stiller C, Kaatsch P, Berrino F, Coebergh J-W, Lacour B, et al. Geographical patterns and time trends of cancer incidence and survival among children and adolescents in Europe since the 1970s (the ACCIS project): an epidemiological study. The Lancet. 2004;364(9451):2097-105.

20. Pastore G, Znaor A, Spreafico F, Graf N, Pritchard-Jones K, Steliarova-Foucher E. Malignant renal tumours incidence and survival in European children (1978–1997): report from the Automated Childhood Cancer Information System project. European journal of cancer. 2006;42(13):2103-14.

21. Nakata K, Colombet M, Stiller CA, Pritchard-Jones K, Steliarova-Foucher E, contributors I. Incidence of childhood renal tumours: An international population-based study. International journal of cancer. 2020;147(12):3313-27.

22. Breslow N, Olshan A, Beckwith JB, Green DM. Epidemiology of Wilms tumor. Medical and pediatric oncology. 1993;21(3):172-81.

23. Van Den Heuvel-eibrink MM, Hol JA, Pritchard-Jones K, Van Tinteren H, Furtwängler R, Verschuur AC, et al. Rationale for the treatment of Wilms tumour in the UMBRELLA SIOP–RTSG 2016 protocol. Nature Reviews Urology. 2017;14(12):743-52.

24. Brok J, Treger TD, Gooskens SL, van den Heuvel-Eibrink MM, Pritchard-Jones K. Biology and treatment of renal tumours in childhood. European Journal of Cancer. 2016;68:179-95.

25. Pritchard-Jones K, Moroz V, Vujanić G, Powis M, Walker J, Messahel B, et al. Treatment and outcome of Wilms' tumour patients: an analysis of all cases registered in the UKW3 trial. Annals of oncology. 2012;23(9):2457-63.

26. Green DM, Breslow NE, Beckwith JB, Finklestein JZ, Grundy P, Thomas PR, et al. Effect of duration of treatment on treatment outcome and cost of treatment for Wilms' tumor: a report from the National Wilms' Tumor Study Group. Journal of clinical oncology. 1998;16(12):3744-51.

27. Termuhlen AM, Tersak JM, Liu Q, Yasui Y, Stovall M, Weathers R, et al. Twenty-five year follow-up of childhood Wilms tumor: a report from the Childhood Cancer Survivor Study. Pediatric blood & cancer. 2011;57(7):1210-6.

28. Ferlay J, Ervik M, Lam F, Colombet M, Mery L, Piñeros M, et al. Global cancer observatory: cancer today. Lyon, France: international agency for research on cancer. 2018:1-6.

29. Spreafico F, Fernandez CV, Brok J, Nakata K, Vujanic G, Geller JI, et al. Wilms tumour. Nature Reviews Disease Primers. 2021;7(1):1-21.

30. Breslow NE, Beckwith JB, Perlman EJ, Reeve AE. Age distributions, birth weights, nephrogenic rests, and heterogeneity in the pathogenesis of Wilms tumor. Pediatric blood & cancer. 2006;47(3):260-7.

31. Charlton J, Irtan S, Bergeron C, Pritchard-Jones K. Bilateral Wilms tumour: a review of clinical and molecular features. Expert reviews in molecular medicine. 2017;19.

32. Scott RH, Stiller CA, Walker L, Rahman N. Syndromes and constitutional chromosomal abnormalities associated with Wilms tumour. Journal of medical genetics. 2006;43(9):705-15.

33. Merks JHM, Caron HN, Hennekam RC. High incidence of malformation syndromes in a series of 1,073 children with cancer. American Journal of Medical Genetics Part A. 2005;134(2):132-43.

34. Young MD, Mitchell TJ, Vieira Braga FA, Tran MG, Stewart BJ, Ferdinand JR, et al. Single-cell transcriptomes from human kidneys reveal the cellular identity of renal tumors. science. 2018; 361(6402):594-9.

35. Rivera MN, Haber DA. Wilms' tumour: connecting tumorigenesis and organ development in the kidney. Nature Reviews Cancer. 2005;5(9):699-712.

36. Popov SD, Sebire NJ, Vujanic GM. Wilms' Tumour–Histology and Differential Diagnosis. 2016.

37. Gadd S, Huff V, Walz AL, Ooms AH, Armstrong AE, Gerhard DS, et al. A Children's Oncology Group and TARGET initiative exploring the genetic landscape of Wilms tumor. Nature genetics. 2017; 49(10):1487-94.

38. Walz AL, Ooms A, Gadd S, Gerhard DS, Smith MA, Auvil JMG, et al. Recurrent DGCR8, DROSHA, and SIX homeodomain mutations in favorable histology Wilms tumors. Cancer cell. 2015;27(2):286-97.

39. Ruteshouser EC, Robinson SM, Huff V. Wilms tumor genetics: mutations in WT1, WTX, and CTNNB1 account for only about one-third of tumors. Genes, Chromosomes and Cancer. 2008; 47(6):461-70.

40. Huff V. Wilms' tumours: about tumour suppressor genes, an oncogene and a chameleon gene. Nature Reviews Cancer. 2011;11(2):111-21.

41. Wegert J, Ishaque N, Vardapour R, Geörg C, Gu Z, Bieg M, et al. Mutations in the SIX1/2 pathway and the DROSHA/DGCR8 miRNA microprocessor complex underlie high-risk blastemal type Wilms tumors. Cancer cell. 2015;27(2):298-311.

42. Rakheja D, Chen KS, Liu Y, Shukla AA, Schmid V, Chang T-C, et al. Somatic mutations in DROSHA and DICER1 impair microRNA biogenesis through distinct mechanisms in Wilms tumours. Nature communications. 2014;5(1):1-11.

43. Bardeesy N, Falkoff D, Petruzzi M-J, Nowak N, Zabel B, Adam M, et al. Anaplastic Wilms' tumour, a subtype displaying poor prognosis, harbours p53 gene mutations. Nature genetics. 1994;7(1):91-7.

44. Ooms AH, Gadd S, Gerhard DS, Smith MA, Auvil JMG, Meerzaman D, et al. Significance of TP53 mutation in Wilms tumors with diffuse anaplasia: A report from the children's oncology group. Clinical Cancer Research. 2016;22(22):5582-91.

45. Wegert J, Vokuhl C, Ziegler B, Ernestus K, Leuschner I, Furtwängler R, et al. TP53 alterations in Wilms tumour represent progression events with strong intratumour heterogeneity that are closely linked but not limited to anaplasia. The Journal of Pathology: Clinical Research. 2017; 3(4):234-48.

46. Scott J, Cowell J, Robertson M, Priestley L, Wadey R, Hopkins B, et al. Insulin-like growth factor-II gene expression in Wilms' tumour and embryonic tissues. Nature. 1985;317(6034):260-2.

47. Hu Q, Gao F, Tian W, Ruteshouser EC, Wang Y, Lazar A, et al. Wt1 ablation and Igf2 upregulation in mice result in Wilms tumors with elevated ERK1/2 phosphorylation. The Journal of clinical investigation. 2011;121(1):174-83.

48. Brioude F, Toutain A, Giabicani E, Cottereau E, Cormier-Daire V, Netchine I. Overgrowth syndromes—clinical and molecular aspects and tumour risk. Nature Reviews Endocrinology. 2019; 15(5):299-311.

49. Dome JS, Perlman EJ, Graf N. Risk stratification for wilms tumor: current approach and future directions. American Society of Clinical Oncology Educational Book. 2014;34(1):215-23.

50. Dome JS, Graf N, Geller JI, Fernandez CV, Mullen EA, Spreafico F, et al. Advances in Wilms tumor treatment and biology: progress through international collaboration. Journal of Clinical Oncology. 2015;33(27):2999.

51. Groenendijk A, Spreafico F, de Krijger RR, Drost J, Brok J, Perotti D, et al. Prognostic factors for Wilms tumor recurrence: a review of the literature. Cancers. 2021;13(13):3142.

52. Brok J, Lopez-Yurda M, Tinteren HV, Treger TD, Furtwängler R, Graf N, et al. Relapse of Wilms' tumour and detection methods: a retrospective analysis of the 2001 Renal Tumour Study Group–International Society of Paediatric Oncology Wilms' tumour protocol database. The Lancet Oncology. 2018;19(8):1072-81.

53. Dome JS, Cotton CA, Perlman EJ, Breslow NE, Kalapurakal JA, Ritchey ML, et al. Treatment of anaplastic histology Wilms' tumor: results from the fifth National Wilms' Tumor Study. J Clin Oncol. 2006;24(15):2352-8.

54. Reinhard H, Schmidt A, Furtwängler R, Leuschner I, Rübe C, Von Schweinitz D, et al. Outcome of relapses of nephroblastoma in patients registered in the SIOP/GPOH trials and studies. Oncology reports. 2008;20(2):463-7.

55. Brok J, Mavinkurve-Groothuis AMC, Drost J, Perotti D, Geller JI, Walz AL, et al. Unmet needs for relapsed or refractory Wilms tumour: Mapping the molecular features, exploring organoids and designing early phase trials - A collaborative SIOP-RTSG, COG and ITCC session at the first SIOPE meeting. Eur J Cancer. 2021;144:113-22.

56. Lu Y-J, Hing S, Williams R, Pinkerton R, Shipley J, Pritchard-Jones K, et al. Chromosome 1q expression profiling and relapse in Wilms' tumour. The Lancet. 2002;360(9330):385-6.

57. Gratias EJ, Jennings LJ, Anderson JR, Dome JS, Grundy P, Perlman EJ. Gain of 1q is associated with inferior event-free and overall survival in patients with favorable histology Wilms tumor: A report from the Children's Oncology Group. Cancer. 2013;119(21):3887-94.

58. Hing S, Lu Y-J, Summersgill B, King-Underwood L, Nicholson J, Grundy P, et al. Gain of 1q is associated with adverse outcome in favorable histology Wilms' tumors. The American journal of pathology. 2001;158(2):393-8.

59. Grundy PE, Breslow NE, Li S, Penman E, Beckwith JB, Ritchey ML, et al. Loss of heterozygosity for chromosomes 1p and 16q is an adverse prognostic factor in favorable-histology Wilms tumor: a report from the National Wilms Tumor Study Group. Journal of clinical oncology. 2005;23(29):7312-21.

60. Malogolowkin M, Cotton CA, Green DM, Breslow NE, Perlman E, Miser J, et al. Treatment of Wilms tumor relapsing after initial treatment with vincristine, actinomycin D, and doxorubicin. A report from the National Wilms Tumor Study Group. Pediatric blood & cancer. 2008;50(2):236-41.

61. Spreafico F, Pritchard Jones K, Malogolowkin MH, Bergeron C, Hale J, De Kraker J, et al. Treatment of relapsed Wilms tumors: lessons learned. Expert review of anticancer therapy. 2009;9(12):1807-15.

62. Weeks DA, Beckwith JB, Mierau GW, Luckey DW. Rhabdoid tumor of kidney. A report of 111 cases from the National Wilms' Tumor Study Pathology Center. The American journal of surgical pathology. 1989;13(6):439-58.

63. Cheng H, Yang S, Cai S, Ma X, Qin H, Zhang W, et al. Clinical and Prognostic Characteristics of 53 Cases of Extracranial Malignant Rhabdoid Tumor in Children. A Single-Institute Experience from 2007 to 2017. The oncologist. 2019;24(7):e551.

64. Tomlinson GE, Breslow NE, Dome J, Guthrie KA, Norkool P, Li S, et al. Rhabdoid tumor of the kidney in the National Wilms' Tumor Study: age at diagnosis as a prognostic factor. Journal of clinical oncology. 2005;23(30):7641-5.

65. van den Heuvel-Eibrink MM, van Tinteren H, Rehorst H, Coulombe A, Patte C, de Camargo B, et al. Malignant rhabdoid tumours of the kidney (MRTKs), registered on recent SIOP protocols from 1993 to 2005: a report of the SIOP renal tumour study group. Pediatric blood & cancer. 2011;56(5):733-7.

66. Biegel JA, Zhou J-Y, Rorke LB, Stenstrom C, Wainwright LM, Fogelgren B. Germ-line and acquired mutations of INI1 in atypical teratoid and rhabdoid tumors. Cancer research. 1999;59(1):74-9.

67. Versteege I, Sévenet N, Lange J, Rousseau-Merck M-F, Ambros P, Handgretinger R, et al. Truncating mutations of hSNF5/INI1 in aggressive paediatric cancer. Nature. 1998;394(6689):203-6.

68. Sredni ST, Tomita T. Rhabdoid tumor predisposition syndrome. Pediatric and Developmental Pathology. 2015;18(1):49-58.

69. Mashtalir N, D'Avino AR, Michel BC, Luo J, Pan J, Otto JE, et al. Modular organization and assembly of SWI/SNF family chromatin remodeling complexes. Cell. 2018;175(5):1272-88. e20.

70. Sima X, He J, Peng J, Xu Y, Zhang F, Deng L. The genetic alteration spectrum of the SWI/SNF complex: the oncogenic roles of BRD9 and ACTL6A. PLoS One. 2019;14(9):e0222305.

71. Kadoch C, Hargreaves DC, Hodges C, Elias L, Ho L, Ranish J, et al. Proteomic and bioinformatic analysis of mammalian SWI/SNF complexes identifies extensive roles in human malignancy. Nature genetics. 2013;45(6):592-601.

72. Wang X, Lee RS, Alver BH, Haswell JR, Wang S, Mieczkowski J, et al. SMARCB1-mediated SWI/SNF complex function is essential for enhancer regulation. Nature genetics. 2017;49(2):289-95.

73. Terada Y, Jo N, Arakawa Y, Sakakura M, Yamada Y, Ukai T, et al. Human pluripotent stem cell-derived tumor model uncovers the embryonic stem cell signature as a key driver in atypical teratoid/rhabdoid tumor. Cell Reports. 2019;26(10):2608-21. e6.

74. Han Z-Y, Richer W, Fréneaux P, Chauvin C, Lucchesi C, Guillemot D, et al. The occurrence of intracranial rhabdoid tumours in mice depends on temporal control of Smarcb1 inactivation. Nature communications. 2016;7(1):1-11.

75. Custers L, Khabirova E, Coorens TH, Oliver TR, Calandrini C, Young MD, et al. Somatic mutations and single-cell transcriptomes reveal the root of malignant rhabdoid tumours. Nature communications. 2021;12(1):1-11.

76. Chun H-JE, Lim EL, Heravi-Moussavi A, Saberi S, Mungall KL, Bilenky M, et al. Genome-wide profiles of extra-cranial malignant rhabdoid tumors reveal heterogeneity and dysregulated developmental pathways. Cancer cell. 2016;29(3):394-406.

77. Bourdeaut F, Freneaux P, Thuille B, Lellouch-Tubiana A, Nicolas A, Couturier J, et al. hSNF5/INI1-deficient tumours and rhabdoid tumours are convergent but not fully overlapping entities. The Journal of Pathology: A Journal of the Pathological Society of Great Britain and Ireland. 2007;211(3):323-30.

78. Beckwith J, Palmer N. Histopathology and prognosis of Wilms tumor Results from the first national wilms' tumor study. Cancer. 1978;41(5):1937-48.

79. Judkins AR, Mauger J, Ht A, Rorke LB, Biegel JA. Immunohistochemical analysis of hSNF5/INI1 in pediatric CNS neoplasms. The American journal of surgical pathology. 2004;28(5):644-50.

80. Lee RS, Stewart C, Carter SL, Ambrogio L, Cibulskis K, Sougnez C, et al. A remarkably simple genome underlies highly malignant pediatric rhabdoid cancers. The Journal of clinical investigation. 2012;122(8):2983-8.

81. Johann PD, Erkek S, Zapatka M, Kerl K, Buchhalter I, Hovestadt V, et al. Atypical teratoid/rhabdoid tumors are comprised of three epigenetic subgroups with distinct enhancer landscapes. Cancer cell. 2016;29(3):379-93.

82. Ho B, Johann PD, Grabovska Y, De Dieu Andrianteranagna MJ, Yao F, Frühwald M, et al. Molecular subgrouping of atypical teratoid/rhabdoid tumors—a reinvestigation and current consensus. Neuro-oncology. 2020;22(5):613-24.

83. Torchia J, Picard D, Lafay-Cousin L, Hawkins CE, Kim S-K, Letourneau L, et al. Molecular subgroups of atypical teratoid rhabdoid tumours in children: an integrated genomic and clinicopathological analysis. The lancet oncology. 2015;16(5):569-82.

84. Frühwald MC, Hasselblatt M, Nemes K, Bens S, Steinbügl M, Johann PD, et al. Age and DNA methylation subgroup as potential independent risk factors for treatment stratification in children with atypical teratoid/rhabdoid tumors. Neuro-oncology. 2020;22(7):1006-17.

85. Reinhard H, Reinert J, Beier R, Furtwängler R, Alkasser M, Rutkowski S, et al. Rhabdoid tumors in children: prognostic factors in 70 patients diagnosed in Germany. Oncology reports. 2008;19(3):819-23.

86. Adamson PC, Houghton PJ, Perilongo G, Pritchard-Jones K. Drug discovery in paediatric oncology: roadblocks to progress. Nature Reviews Clinical Oncology. 2014;11(12):732-9.

87. Houghton PJ, Kurmasheva RT. Challenges and Opportunities for Childhood Cancer Drug Development. Pharmacological Reviews. 2019;71(4):671-97.

88. Barretina J, Caponigro G, Stransky N, Venkatesan K, Margolin AA, Kim S, et al. The Cancer Cell Line Encyclopedia enables predictive modelling of anticancer drug sensitivity. Nature. 2012;483(7391):603-7.

89. Masters JR. Human cancer cell lines: fact and fantasy. Nature reviews Molecular cell biology. 2000;1(3):233-6.

90. Sachs N, Clevers H. Organoid cultures for the analysis of cancer phenotypes. Current opinion in genetics & development. 2014;24:68-73.

91. Lee J, Kotliarova S, Kotliarov Y, Li A, Su Q, Donin NM, et al. Tumor stem cells derived from glioblastomas cultured in bFGF and EGF more closely mirror the phenotype and genotype of primary tumors than do serum-cultured cell lines. Cancer cell. 2006;9(5):391-403.

92. Broutier L, Barbet V. Future Match Making: When Pediatric Oncology Meets Organoid Technology. Frontiers in Cell and Developmental Biology. 2021;9:1415.

93. Van Staveren W, Solís DW, Hebrant A, Detours V, Dumont JE, Maenhaut C. Human cancer cell lines: Experimental models for cancer cells in situ? For cancer stem cells? Biochimica et Biophysica Acta (BBA)-Reviews on Cancer. 2009;1795(2):92-103.

94. Tentler JJ, Tan AC, Weekes CD, Jimeno A, Leong S, Pitts TM, et al. Patient-derived tumour xenografts as models for oncology drug development. Nature reviews Clinical oncology. 2012;9(6):338-50.

95. Zarzosa P, Navarro N, Giralt I, Molist C, Almazán-Moga A, Vidal I, et al. Patient-derived xenografts for childhood solid tumors: a valuable tool to test new drugs and personalize treatments. Clinical and Translational Oncology. 2017;19(1):44-50.

96. Caponigro G, Sellers WR. Advances in the preclinical testing of cancer therapeutic hypotheses. Nature reviews Drug discovery. 2011;10(3):179-87.

97. Ben-David U, Ha G, Tseng Y-Y, Greenwald NF, Oh C, Shih J, et al. Patient-derived xenografts undergo mouse-specific tumor evolution. Nature genetics. 2017;49(11):1567-75.

98. Hanahan D, Wagner EF, Palmiter RD. The origins of oncomice: a history of the first transgenic mice genetically engineered to develop cancer. Genes & development. 2007;21(18):2258-70.

99. Cheon D-J, Orsulic S. Mouse models of cancer. Annual Review of Pathology: Mechanisms of Disease. 2011;6:95-119.

100. Bleijs M, van de Wetering M, Clevers H, Drost J. Xenograft and organoid model systems in cancer research. The EMBO journal. 2019;38(15):e101654.

101. Wong CH, Siah KW, Lo AW. Estimation of clinical trial success rates and related parameters. Biostatistics. 2019;20(2):273-86.

102. Kim J, Koo B-K, Knoblich JA. Human organoids: model systems for human biology and medicine. Nature Reviews Molecular Cell Biology. 2020;21(10):571-84.

103. Clevers H. Modeling development and disease with organoids. Cell. 2016;165(7):1586-97.

104. Drost J, Clevers H. Organoids in cancer research. Nature Reviews Cancer. 2018;18(7):407-18.

105. Sato T, Vries RG, Snippert HJ, Van De Wetering M, Barker N, Stange DE, et al. Single Lgr5 stem cells build crypt-villus structures in vitro without a mesenchymal niche. Nature. 2009;459(7244):262-5.

106. Sato T, Stange DE, Ferrante M, Vries RG, Van Es JH, Van Den Brink S, et al. Long-term expansion of epithelial organoids from human colon, adenoma, adenocarcinoma, and Barrett's epithelium. Gastroenterology. 2011;141(5):1762-72.

107. Bartfeld S, Bayram T, van de Wetering M, Huch M, Begthel H, Kujala P, et al. In vitro expansion of human gastric epithelial stem cells and their responses to bacterial infection. Gastroenterology. 2015;148(1):126-36. e6.

108. Rock JR, Onaitis MW, Rawlins EL, Lu Y, Clark CP, Xue Y, et al. Basal cells as stem cells of the mouse trachea and human airway epithelium. Proceedings of the National Academy of Sciences. 2009; 106(31):12771-5.

109. Huch M, Gehart H, Van Boxtel R, Hamer K, Blokzijl F, Verstegen MM, et al. Long-term culture of genome-stable bipotent stem cells from adult human liver. Cell. 2015;160(1-2):299-312.

110. Hu H, Gehart H, Artegiani B, LÖpez-Iglesias C, Dekkers F, Basak O, et al. Long-term expansion of functional mouse and human hepatocytes as 3D organoids. Cell. 2018;175(6):1591-606. e19.

111. Schutgens F, Rookmaaker MB, Margaritis T, Rios A, Ammerlaan C, Jansen J, et al. Tubuloids derived from human adult kidney and urine for personalized disease modeling. Nature biotechnology. 2019;37(3):303-13.

112. Boj SF, Hwang C-I, Baker LA, Chio IIC, Engle DD, Corbo V, et al. Organoid models of human and mouse ductal pancreatic cancer. Cell. 2015;160(1-2):324-38.

113. Rosenbluth JM, Schackmann RC, Gray GK, Selfors LM, Li CM-C, Boedicker M, et al. Organoid cultures from normal and cancer-prone human breast tissues preserve complex epithelial lineages. Nature communications. 2020;11(1):1-14.

114. Kessler M, Hoffmann K, Brinkmann V, Thieck O, Jackisch S, Toelle B, et al. The Notch and Wnt pathways regulate stemness and differentiation in human fallopian tube organoids. Nature communications. 2015;6(1):1-11.

115. Chua CW, Shibata M, Lei M, Toivanen R, Barlow LJ, Bergren SK, et al. Single luminal epithelial progenitors can generate prostate organoids in culture. Nature cell biology. 2014;16(10):951-61.

116. Karthaus WR, Iaquinta PJ, Drost J, Gracanin A, Van Boxtel R, Wongvipat J, et al. Identification of multipotent luminal progenitor cells in human prostate organoid cultures. Cell. 2014;159(1):163-75.

117. Sachs N, Papaspyropoulos A, Zomer-van Ommen DD, Heo I, Böttinger L, Klay D, et al. Long-term expanding human airway organoids for disease modeling. The EMBO journal. 2019;38(4):e100300.

118. Drost J, Van Jaarsveld RH, Ponsioen B, Zimberlin C, Van Boxtel R, Buijs A, et al. Sequential cancer mutations in cultured human intestinal stem cells. Nature. 2015;521(7550):43-7.

119. Matano M, Date S, Shimokawa M, Takano A, Fujii M, Ohta Y, et al. Modeling colorectal cancer using CRISPR-Cas9–mediated engineering of human intestinal organoids. Nature medicine. 2015; 21(3):256-62.

120. van de Wetering M, Francies HE, Francis JM, Bounova G, Iorio F, Pronk A, et al. Prospective derivation of a living organoid biobank of colorectal cancer patients. Cell. 2015;161(4):933-45.

121. Sachs N, de Ligt J, Kopper O, Gogola E, Bounova G, Weeber F, et al. A living biobank of breast cancer organoids captures disease heterogeneity. Cell. 2018;172(1-2):373-86. e10.

122. Broutier L, Mastrogiovanni G, Verstegen MM, Francies HE, Gavarró LM, Bradshaw CR, et al. Human primary liver cancer–derived organoid cultures for disease modeling and drug screening. Nature medicine. 2017;23(12):1424-35.

123. Gao D, Vela I, Sboner A, Iaquinta PJ, Karthaus WR, Gopalan A, et al. Organoid cultures derived from patients with advanced prostate cancer. Cell. 2014;159(1):176-87.

124. Ooft SN, Weeber F, Dijkstra KK, McLean CM, Kaing S, van Werkhoven E, et al. Patient-derived organoids can predict response to chemotherapy in metastatic colorectal cancer patients. Science translational medicine. 2019;11(513).

125. Ganesh K, Wu C, O'Rourke KP, Szeglin BC, Zheng Y, Sauvé C-EG, et al. A rectal cancer organoid platform to study individual responses to chemoradiation. Nature medicine. 2019;25(10):1607-14.

126. Tiriac H, Belleau P, Engle DD, Plenker D, Deschênes A, Somerville TD, et al. Organoid profiling identifies common responders to chemotherapy in pancreatic cancer. Cancer discovery. 2018; 8(9):1112-29.

127. Yao Y, Xu X, Yang L, Zhu J, Wan J, Shen L, et al. Patient-derived organoids predict chemoradiation responses of locally advanced rectal cancer. Cell stem cell. 2020;26(1):17-26. e6.

128. Vlachogiannis G, Hedayat S, Vatsiou A, Jamin Y, Fernández-Mateos J, Khan K, et al. Patient-derived organoids model treatment response of metastatic gastrointestinal cancers. Science. 2018; 359(6378):920-6.

129. Ooms AH, Calandrini C, de Krijger RR, Drost J. Organoid models of childhood kidney tumours. Nature Reviews Urology. 2020;17(6):311-3.

130. Calandrini C, Schutgens F, Oka R, Margaritis T, Candelli T, Mathijsen L, et al. An organoid biobank for childhood kidney cancers that captures disease and tissue heterogeneity. Nature communications. 2020;11(1):1-14.

131. Calandrini C, Drost J. Generation of Human Kidney Tubuloids from Tissue and Urine. JOVE-JOURNAL OF VISUALIZED EXPERIMENTS. 2021(170).

132. Calandrini C, van Hooff SR, Paassen I, Ayyildiz D, Derakhshan S, Dolman MEM, et al. Organoid-based drug screening reveals neddylation as therapeutic target for malignant rhabdoid tumors. Cell reports. 2021;36(8):109568.

133. Calandrini C, Drost J. Normal and tumor-derived organoids as a drug screening platform for tumor-specific drug vulnerabilities. STAR Protocols. 2022;3(1):101079.

Chapter 2

Organoid models of childhood kidney tumors

Ariadne H.A.G. Ooms[1,2,#], Camilla Calandrini[1,2,#], Ronald R. de Krijger[1,3] and Jarno Drost[1,2]

[1] Princess Máxima Center for Pediatric Oncology, Utrecht, the Netherlands
[2] Oncode Institute, Utrecht, the Netherlands
[3] Department of Pathology, University Medical Center, Utrecht, the Netherlands
[#]These authors contributed equally to this work

Summary

Pediatric kidney tumors comprise many different subtypes, each being heterogeneous in their cellular as well as genetic composition. Advances in the past decade in 3D culture models create new opportunities for the generation of preclinical models capturing this phenotypic and genetic heterogeneity, potentially enabling the generation of patient- tailored therapies.

Introduction

Pediatric kidney tumors comprise ~7% of all childhood cancers and consist of distinct subtypes that differ in histology and prognosis (National Cancer Institute information on Wilms tumor and other childhood kidney tumors). The most common subtype is Wilms tumor, followed by clear cell sarcoma of the kidney (CCSK), malignant rhabdoid tumor of the kidney (MRTK), renal cell carcinoma (RCC) and congenital mesoblastic nephroma (CMN). These tumors are treated with surgery combined with chemotherapy and/or radiotherapy. These regimens have considerable early and late adverse effects, emphasizing the need for targeted therapies. The development of such therapies strongly depends on the availability of preclinical research models that recapitulate key aspects of the different kidney tumor subtypes. Classical preclinical cancer models include cell lines, genetically engineered mouse models and patient- derived xenografts. However, these models are scarce in pediatric kidney cancer (and for some subtypes even lacking) and typically do not capture the cellular and genetic heterogeneity of native tumor tissues. Thus, many therapies that demonstrate efficacy in models fail in patients. Advances in 3D culture technologies, such as organoids, hold promise for the development of representative models of pediatric kidney tumors and further progress in pediatric kidney cancer research. Organoids can be derived from pluripotent stem cells (PSCs) or organ- restricted adult stem cells (ASCs).

PSC-derived kidney organoids

Wilms tumors, CMN, CCSK and MRTK usually occur in infants and very young children (<5 years of age) and are, therefore, considered embryonal tumors that result from a differentiation block during embryonic development. A detailed understanding of which developmental pathways are impaired in kidney tumorigenesis could provide new therapeutic targets. PSC- derived organoid models potentially enable identifying such pathways, as they recapitulate organ development *in vitro*. PSCs can be derived from embryonic stem cells (ESCs) or from forced dedifferentiation of committed cells (induced PSCs (iPSCs)) through the expression of specific pluripotency factors in somatic cells. PSCs can then be differentiated into essentially all cell types of the body through their strictly timed exposure to specific growth factor cocktails. Takasato et al.[1] published a detailed protocol for the generation of kidney organoids from iPSCs, which results in the

progenitors required for the development of nephrons, the functional units of the kidney. These organoids contained nephrons segmented into glomeruli as well as all tubule compartments, from proximal tubule to collecting duct, an endothelial network and renal interstitium. In a subsequent study, Low et al.[2] described a protocol for differentiation of iPSCs into segmentally patterned kidney organoids including an intrinsic vascular network that developed from a specific subpopulation of the nephron progenitor cells. These organoids were functional when orthotopically xenografted into mice. Kidney organoids derived from iPSCs provide the means to study kidney development and renal physiology. Thus, they might also enable studying the initiating steps of pediatric kidney tumorigenesis by, for example, introducing recurrent tumor- driving mutations in early nephron progenitor cells. Indeed, human iPSCs were used to study tumorigenesis of extrarenal rhabdoid tumors. Through neural induction of *SMARCB1* -deficient human iPSCs, Terada et al.[3] demonstrated that *SMARCB1* loss induces an ESC- like signature. When these cells were transplanted into the mouse brain, highly aggressive brain tumors with rhabdoid histology developed.

ASC-derived kidney organoids

ASCs can be expanded as organoids by providing a cocktail of stem cell niche factors mimicking the native environment of the respective ASC pool. After being embedded in an extracellular matrix, they typically grow as polarized structures resembling the organ they were derived from[4]. ASC- derived organoids can be expanded long term while remaining genetically and phenotypically stable. We and others have established ASC- derived organoids from adult human kidney tissue[5,6]. These cultures, termed tubuloids, primarily contain tubular epithelial cells from proximal and distal nephron segments. These studies show that the tubular cells express functional transporter proteins, such as P- glycoprotein, and that tubuloids can be used to study nephrotoxicity and model infectious diseases (for example, BK- virus- mediated infection). As ASC- derived organoids mainly comprise epithelial cells and recapitulate tissue repair rather than kidney development (early (mesenchymal) nephrogenic progenitors are absent), they seem not very suitable for genetic modelling of embryonal kidney tumor development. One major advantage of ASC- derived organoids compared with iPSC- derived organoids is that they can be grown from primary tumor tissue with high efficiency. Organoid models of many different adult cancers have been shown to reiterate the phenotypic and genetic heterogeneity of the tumor tissue they were derived

from[7]. We have established the first collection of organoid models from a large spectrum of different pediatric kidney cancer subtypes, including Wilms tumors, RCC, CMN and MRTK[6,8]. These models are generated by enzymatic digestion of tumor tissue pieces and subsequent plating in ASC- based culture conditions[6], which enables long- term propagation of primary tumor tissue. Importantly, the established models generally retain the phenotypic, genetic, epigenetic and transcriptomic characteristics of their respective tumor type. For instance, Wilms tumors usually present with a tri- phasic histology of blastemal, epithelial and stromal cells. The cellular composition of the tumor correlates with prognosis: tumors with a high percentage of blastemal cells after pre- operative chemotherapy represent a high- risk group. Thus, a representative preclinical cell culture model for Wilms tumors should consist of the different tumor elements. Wilms tumor organoid cultures largely capture the cellular heterogeneity of primary tumor tissue, with epithelial, stromal and blastemal- like tumor cells[8]. Wegert et al.[9] describe the generation of 3D spheroids composed of blastemal Wilms tumor cells, supporting another method to grow ASC- derived cultures from high-risk cases. The high establishment efficiency of tumor organoid cultures from primary patient material, their compatibility with (high- throughput) drug screening[8] and their demonstrated predictive value of patient drug responses[7] create opportunities for the development of more targeted, and perhaps even patient- tailored, therapies. Notably, expansion of healthy tissue, including kidney tissue, as organoids enables toxicity testing in drug screening by selecting drugs that specifically kill tumor organoids while leaving healthy cells unharmed. This approach could also be used in a patient- matched fashion.

Outlook

PSC- derived and ASC- derived organoid models have revolutionized adult cancer research. The recent developments of organoid technology in pediatric kidney cancer hold great promise and will aid in efficient translation of research findings from bench- to- bedside. However, some important aspects need consideration (**Figure 1**). For instance, Wilms tumors in particular are highly heterogeneous in their cellular composition and, although patient tumor- derived ASC organoids largely retain this heterogeneity, capturing the complexity of a Wilms tumor can possibly only be achieved by growing organoids from multiple different regions of the tumor. Moreover, the efficiency of establishing iPSC tumor models from primary material remains low and is influenced by differences in the genetic

background of tumors[2]. Some tumors are, therefore, resistant to the reprogramming protocol, which introduces a bias towards, as well as over- representation or underrepresentation of, specific tumor subtypes[10].
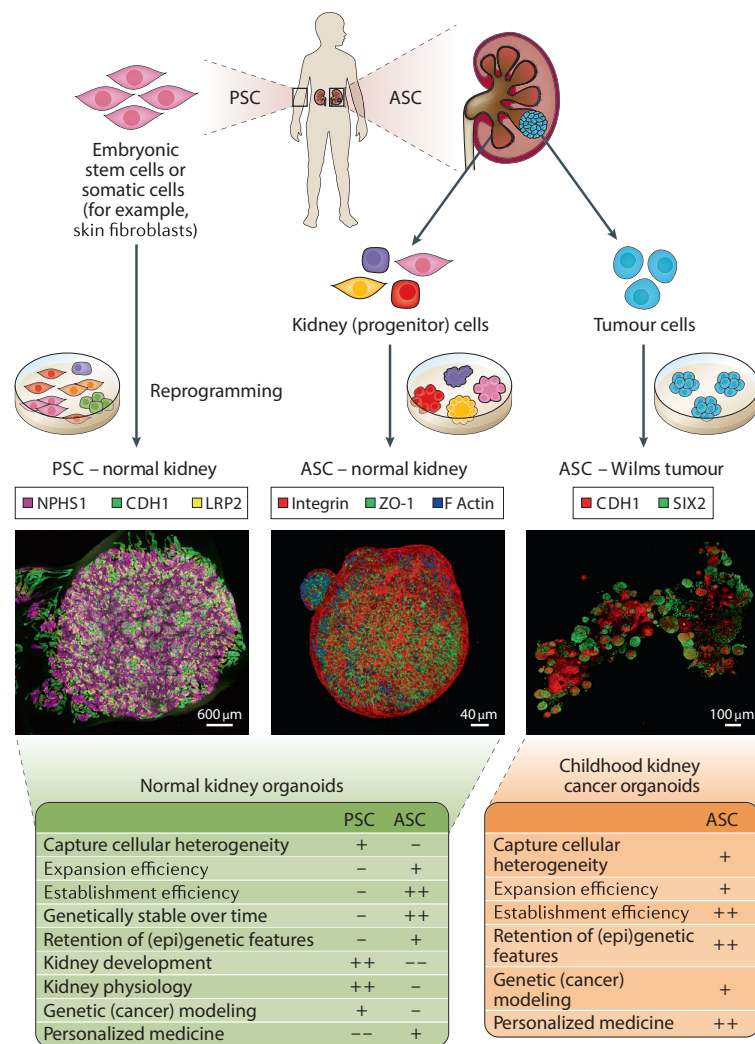

Figure 1. Kidney organoids derived from pluripotent and adult stem cells. Organoids from pluripotent stem cells (PSCs) can be derived from embryonic stem cells as well as by forced dedifferentiation of somatic cells. Organoids from adult stem cells (ASCs) are grown from tissue- resident stem cell populations, found both in healthy and tumor tissue. Organoids established with each approach have advantages and disadvantages as research models. Left: 3D immunofluorescence image of an induced- PSC- derived organoid showing distal tubules

(green), proximal tubules (yellow) and podocytes (magenta). Middle: 3D immunofluorescence image of an ASC- derived kidney organoid showing basolateral integrin (red), subapical tight junction protein (green) and filamentous actin (blue). Right: 3D immunofluorescence image of a Wilms tumor organoid showing epithelial cells (red) and blastemal cells (green). Respective features were judged as very suitable (+ +), suitable (+), not very suitable (–) or unsuitable (– –). Left image courtesy of M. Takasato, RIKEN Center for Biosystems Dynamics Research, Japan. Middle image courtesy of H. Clevers, Princess Máxima Center for Pediatric Oncology, Netherlands.

Furthermore, iPSCs usually retain the epigenetic status of the parental cells (for example, skin fibroblasts) and the reprogramming protocol can induce genetic instability[10], which can compromise the resemblance of the generated model to the epigenetic and genetic characteristics of the patient tumor. Lastly, organoid cultures consist of pure tumor cell populations without their native microenvironment, which encompasses infiltrated stromal cells, immune cells and vascularization. This tumor microenvironment is known to have an important role in drug sensitivity and efficacy. Organoid co- cultures with stromal cells, immune cells and even vascularization have been reported for adult normal and tumor kidney tissues and efforts are currently ongoing to generate more representative preclinical tumor models. This approach would make organoid models more accurate avatars of patient tumors.

Acknowledgments

References

1. Takasato, M. et al. Kidney organoids from human iPS cells contain multiple lineages and model human nephrogenesis. *Nature* **526**,564–568 (2015).

2. Low, J. H. et al. Generation of human PSC- derived kidney organoids with patterned nephron segments and a de novo vascular network. *Cell Stem Cell* **25**, 373–387 (2019).

3. Terada, Y. J. N. et al. Human pluripotent stem cell- derived tumor model uncovers the embryonic stem cell signature as a key driver in atypical teratoid/rhabdoid tumor. *Cell Rep.* **26**, 2608–2621 (2019).

4. Clevers, H. Modeling development and disease with organoids. *Cell* **165**, 1586–1597 (2016).

5. Jun, D. Y. et al. Tubular organotypic culture model of human kidney. *PLoS One* **13**, e0206447 (2018).

6. Schutgens, F. et al. Tubuloids derived from human adult kidney and urine for personalized disease modeling. *Nat. Biotechnol.* **37**, 303–313 (2019).

7. Drost, J. & Clevers, H. Organoids in cancer research. *Nat. Rev. Cancer* **18**, 407–418 (2018).

8. Calandrini, C. et al. An organoid biobank for childhood kidney cancers that captures disease and tissue heterogeneity. *Nat. Commun.* **11**, 1310 (2020).

9. Wegert, J. et al. High- risk blastemal Wilms tumor can be modeled by 3D spheroid cultures in vitro. *Oncogene* **39**, 849–861 (2020).

10. Papapetrou, E. P. Patient- derived induced pluripotent stem cells in cancer research and precision oncology. *Nat. Med.* **22**, 1392–1401 (2016).

Chapter 3
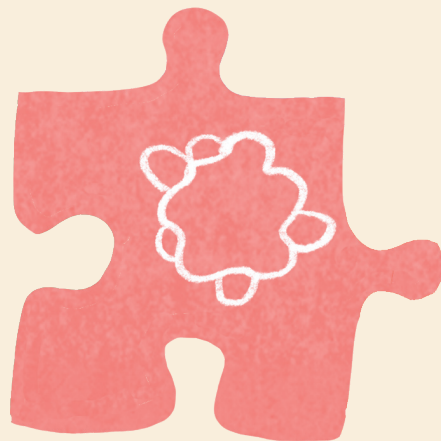
An organoid biobank for childhood kidney cancers that captures disease and tissue heterogeneity

Camilla Calandrini[1,#], Frans Schutgens[2,3,#], Rurika Oka[1], Thanasis Margaritis[4], Tito Candelli[4], Luka Mathijsen[1], Carola Ammerlaan[2,3], Ravian L. van Ineveld[1], Sepide Derakhshan[1], Sanne de Haan[1], Emmy Dolman[4], Philip Lijnzaad[4], Lars Custers[1], Harry Begthel[2], Hindrik H.D. Kerstens[4], Lindy L. Visser[4], Maarten Rookmaaker[3], Marianne Verhaar[3], Godelieve A.M. Tytgat[4], Patrick Kemmeren[4], Ronald R. de Krijger[4,5], Reem Al-Saadi[6], Kathy Pritchard-Jones[6], Marcel Kool[4,7,8], Anne C. Rios[1], Marry M. van den Heuvel-Eibrink[4], Jan J. Molenaar[4], Ruben van Boxtel[1], Frank C. P. Holstege[4], Hans Clevers[1,2], Jarno Drost[1]

[1] Oncode Institute, Princess Máxima Center for Pediatric Oncology, Heidelberglaan 25, 3584 CS Utrecht, the Netherlands

[2] Oncode Institute, Hubrecht Institute, Royal Netherlands Academy of Arts and Sciences and University Medical Center, Uppsalalaan 8, 3584 CT Utrecht, the Netherlands

[3] University Medical Center, Department of Nephrology and Hypertension, Heidelberglaan 100, 3584 CX Utrecht, the Netherlands

[4] Princess Máxima Center for Pediatric Oncology, Heidelberglaan 25, 3584 CS Utrecht, the Netherlands

[5] University Medical Center, Department of Pathology, Heidelberglaan 100, 3584 CX Utrecht, the Netherlands

[6] University College London, UCL Great Ormond Street Institute of Child Health, 30 Guilford Street, London WC1N 1EH, UK

[7] Hopp Children's Cancer Center (KiTZ), Im Neuenheimer Feld 280, 69120 Heidelberg, Germany

[8] Division of Pediatric Neurooncology, German Cancer Research Center (DKFZ) and German Cancer Research Consortium (DKTK), Im Neuenheimer Feld 280, 69120 Heidelberg, Germany

[#] These authors contributed equally

Abstract

Kidney tumors are among the most common solid tumors in children, comprising distinct subtypes differing in many aspects, including cell-of-origin, genetics, and pathology. Preclinical cell models capturing the disease heterogeneity are currently lacking. Here, we describe the first pediatric cancer organoid biobank. It contains tumor and matching normal kidney organoids from over 50 children with different subtypes of kidney cancer, including Wilms tumors, malignant rhabdoid tumors, renal cell carcinomas, and congenital mesoblastic nephromas. Pediatric kidney tumor organoids retain key properties of native tumors, useful for revealing patient-specific drug sensitivities. Using single cell RNA sequencing and high resolution 3D imaging, we further demonstrate that organoid cultures derived from Wilms tumors consist of multiple different cell types, including epithelial, stromal and blastemal-like cells. Our organoid biobank captures the heterogeneity of pediatric kidney tumors, providing a representative collection of well-characterized models for basic cancer research, drug-screening and personalized medicine.

Introduction

Although cure rates for children with cancer have significantly increased in recent decades, cancer is still the leading cause of death by disease in the Western world among children over 1 year of age[1,2]. Renal malignancies account for ~7% of all childhood cancers and comprise multiple distinct subtypes that greatly differ in appearance and prognosis. The majority are Wilms tumors, representing ~90% of cases[3]. The most common malignant non-Wilms tumor subtypes include malignant rhabdoid tumors of the kidney (MRTK), renal cell carcinomas (RCC), clear cell sarcomas of the kidney (CCSK) and congenital mesoblastic nephromas (CMN), a rare renal neoplasm of which, in the case of stage III disease, ~25% relapse[4]. Overall survival of children with Wilms tumor has greatly improved. Yet, few effective treatment options exist for high-risk Wilms and most non-Wilms tumors[5–7]. Moreover, survivors have significant risks of late effects of the harsh treatment regimen[8]. Wilms tumor is histologically characterized by a tri-phasic pattern, with blastemal, epithelial and stromal cell components[9]. Wilms tumor risk stratification is based on histological classification, where tumors with a high percentage of blastemal cells after pre-operative chemotherapy, or diffuse anaplastic features (hyperchromasia, atypical mitotic figures and marked nuclear enlargement) represent the high-risk group. Wilms tumors are genetically heterogeneous as well. Many different driver mutations have been described, including *WT1*, *CTNNB1*, *WTX*, *SIX1*, *SIX2* and microRNA-processing genes, but all with relatively low recurrence[10–13]. In addition, over 50% of Wilms tumors contain copy number alterations (CNAs)[14–17]. The non-Wilms tumor subtypes are histologically as well as genetically distinct. At least 95% of MRTKs harbor inactivating mutations in the SWI/SNF protein complex member *SMARCB1* (SNF5/INI1)[18], whereas RCCs commonly harbor Xp11.2 or t(6;11) translocations, affecting transcription factor E3 (*TFE3*) and EB (*TFEB*), respectively[19,20]. Pre-clinical cell culture models sustaining efficient and long-term *in vitro* propagation of patient-derived pediatric kidney tumor tissue have not been developed so far. Overall, *in vitro* cell culture models for these tumors are scarce. Cancer cell lines represent the most commonly used pre-clinical model system. Although the few available models have contributed significantly to our understanding of tumorigenesis, it has been challenging to develop cell lines capturing the phenotypic and genetic heterogeneity of pediatric kidney tumors[7]. This lack of physiologically relevant pre-clinical models for functional analyses hampers therapeutic innovation. Three-dimensional (3D) organoid culture models open opportunities for both fundamental and translational cancer research[21]. Originally established for mouse small intestine[22], organoids

can currently be grown from primary patient material of a wide range of healthy and tumor tissues, such as colon[23], prostate[24], pancreas[25,26], liver[27], gastric[28,29] and breast cancer[30]. Tumor-derived organoids recapitulate and maintain the genetic heterogeneity of native tumor tissue over time[25,27,30-34], and have predictive value for individual patient drug responses[35]. Organoid technology is of particular interest for less frequently occurring cancers, such as pediatric tumors, as it allows for the generation of large collections of living material for research purposes, despite their relative rarity and small tumor sample sizes. Here, we describe the establishment, characterization and several applications of the first organoid biobank for pediatric cancers. It contains tumor and matching normal organoid cultures from over 50 children with renal tumors and covers a large spectrum of different subtypes, including Wilms tumors, malignant rhabdoid tumors, renal cell carcinomas and congenital mesoblastic nephromas. The malignant rhabdoid tumor organoids represent the first organoid model allowing long-term expansion of tumors of non-epithelial origin.

Results

A living pediatric kidney tumor organoid biobank

We obtained tumor and matching normal kidney tissue from children that underwent nephrectomy or biopsy following informed consent (**Figure 1A**; **Supplementary Table 1**). Tissue was minced, and cells were isolated through a combination of enzymatic digestion and mechanical disruption. A key modification of the recently published human normal kidney organoid (tuboloid) protocol[36] was the addition of the Rho-associated coiled–coil containing protein kinase (ROCK) inhibitor Y-27632 during tissue processing. The ROCK inhibitor increases the survival of single cells in suspension by inhibition of anoikis[22,37]. Using this improved protocol, we established 54 organoid lines from different pediatric kidney tumor subtypes. These included a broad spectrum of pediatric kidney tumors, comprising Wilms tumor, MRTK, RCC, nephrogenic rest and metanephric adenoma. Of these, four known syndromal tumors (Beckwith–Wiedemann) and tumors with or without pre-surgery chemotherapy were included (**Supplementary Table 1**). In the majority of cases (47 out of 54), organoids were also generated from matched normal kidney tissue (**Figure 1A,B**; **Supplementary Table 1**). Efficiency of establishment (defined as organoid growth for at least five passages) was 100% for normal tissue and 75% for Wilms tumors (40/53), 100% for MRTK (7/7) and 75% for RCC (3/4).
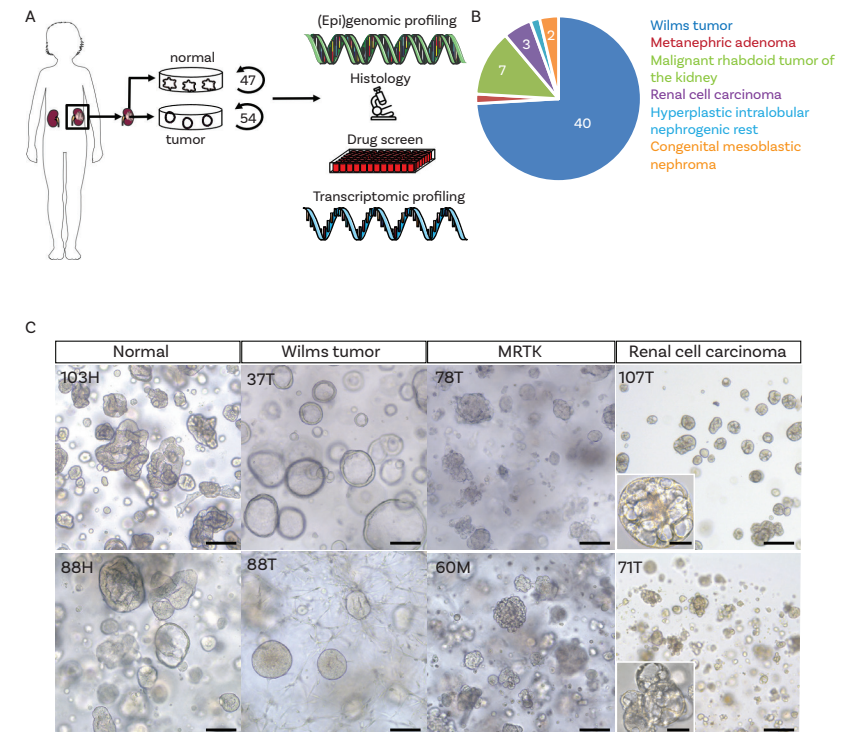

Figure 1. **Establishment of a biobank of pediatric kidney cancer organoids. A.** Overview of the procedure to generate and characterize pediatric kidney cancer organoids. Organoids were established from tumor and, if available, matching normal kidney tissue. Organoids were subsequently characterized using histology, whole-genome sequencing (WGS), RNA sequencing (RNA-seq) and DNA methylation profiling. Lastly, drug screens were performed on a subset of Wilms tumor organoids. Modified from Servier Medical Art, licensed under a Creative Common Attribution 3.0 Generic License. **B.** Pie chart representing the composition of the pediatric kidney cancer organoid biobank, consisting of organoids derived from Wilms tumors, MRTKs, RCCs, nephrogenic rests, metanephric adenoma and congenital mesoblastic nephromas. Clinical characteristics can be found in Supplementary Table 1. **C.** Representative brightfield microscopy images of normal kidney tissue-derived organoids, Wilms tumor organoids, MRTK organoids and RCC organoids (n = 3). H healthy, T primary tumor, M metastasis. Scale bar: 100 μm, zoom in 20 μm.

Organoids could not always be established from chemo-treated Wilms tumor and RCC tissue due to vast amounts of necrotic tissue, whereas an efficiency of ~100% was reached from chemo-naive tissue. In addition, organoids could be established from very rare kidney tumor subtypes, including CMNs (2/2), metanephric adenoma (1/1), and from a nephrogenic rest (1/1) (**Figure 1B**). Typically, kidney

tumor organoids appeared within 7 days after seeding, and can be first passaged after approximately 10–14 days. Expansion rates vary within and among different tumor types. Wilms tumor organoids can typically be passaged 1:2–1:3 every 10–14 days (>20 passages), and MRTKs weekly with 1:3 split ratios (>20 passages). Two chemo-treated RCCs were successfully maintained for ~10 passages with 1:2–1:3 splits every 14 days, whereas chemo-naive RCC could be expanded for >20 passages. As previously described[36], cultures derived from normal kidney tissue consistently contained a mixture of folded and cystic organoid structures (**Figure 1C**).

Organoids established from tumor tissue typically displayed a different phenotype than organoids derived from the matching normal kidney tissue (**Figure 1C**; **Supplementary Figure 1**), giving a first indication of a tumor origin. Wilms tumor organoid lines of independent patients differed greatly in their appearance. For instance, some displayed a mix of different cell types (epithelial- and stromal- like), while others displayed a completely cystic appearance from the start. MRTK-derived organoids typically appeared in grape-like clumps of cells, while RCC organoids presented as small, cell-dense, non-cystic structures (**Figure 1C**). We next set out to analyze the organoids in-depth by means of histology, whole-genome DNA sequencing (WGS), (single cell) transcriptome analyses (RNA-seq) and DNA methylation analyses (**Figure 1A**).

Phenotypic characterization of the kidney tumor organoids

Current classification of the different pediatric kidney cancer subtypes is based on histological examination. To determine whether phenotypic features are retained *in vitro*, we histologically characterized the pediatric kidney cancer organoids. This revealed that the tumor organoids generally resembled the parental tumor tissue (**Figure 2A**; **Supplementary Figures 1–3**). Moreover, the tri-phasic nature (epithelium, stroma and blastema) of Wilms tumors appeared to be retained in the organoid cultures (**Figure 2A**; **Supplementary Figure 2**).
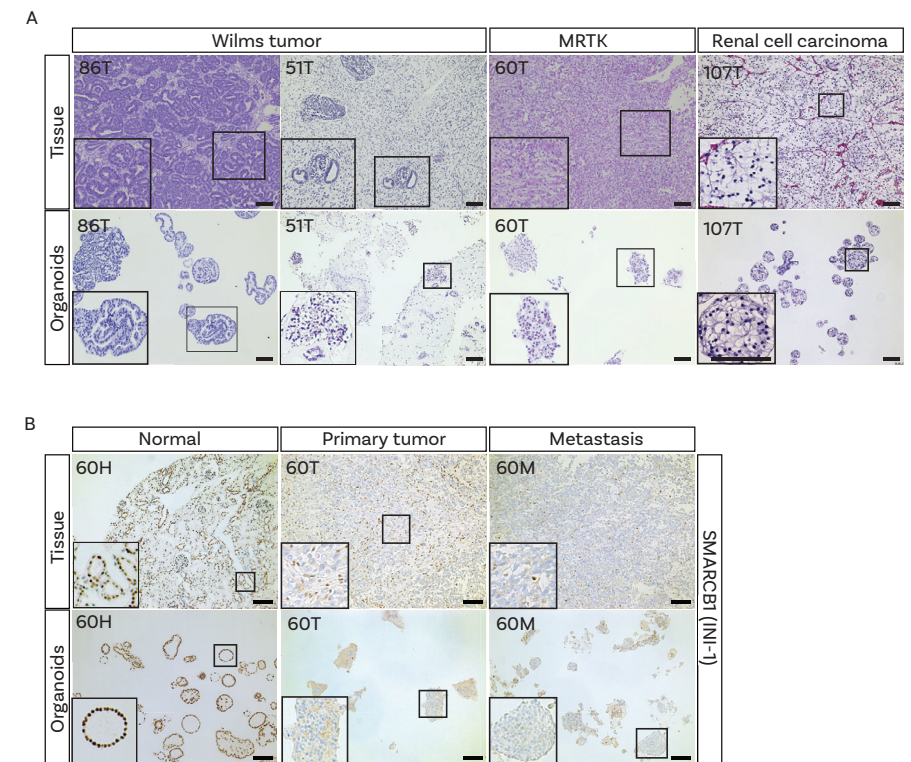

Figure 2. Histologic characterization of pediatric kidney cancer organoids. A. H&E staining on tissue (top) and matching organoids (bottom) derived from the indicated tumor types (n = 3). Additional cases can be found in Supplementary Figure 2. Scale bars: 100 μm, zoom in 50 μm. **B.** Representative SMARCB1 staining on normal (left), primary tumor (middle) and metastasis (right) tissue (top) and matching organoids (bottom) of a patient with a MRTK (n = 3). Of note, immune cells stain positive for SMARCB1 in MRTK tissue. Additional cases can be found in Supplementary Figure 3. Scale bars: 100 μm.

To verify that organoid cultures contain different Wilms tumor cell types, we performed single-cell RNA-sequencing (scRNA-seq) analyses on four different Wilms tumor organoid lines; two organoid cultures with a primarily epithelial appearance (80T, 101T) and two with a mixed appearance (88T, 51T; **Supplementary Figure 4A**). As expected, tumor organoid cultures primarily clustered in t-distributed stochastic neighbor embedding (t-SNE) plots based on the individual patient (**Figure 3A**; **Supplementary Figure 4B**). For instance, enrichment for *IGF2* and *H19* expression was detected in 51T, 80T and 88T, but was lacking in 101T (**Supplementary Figure 5A**). This suggests loss of imprinting of this locus in these three lines, which is a common event in Wilms tumors[12,13,17,38].
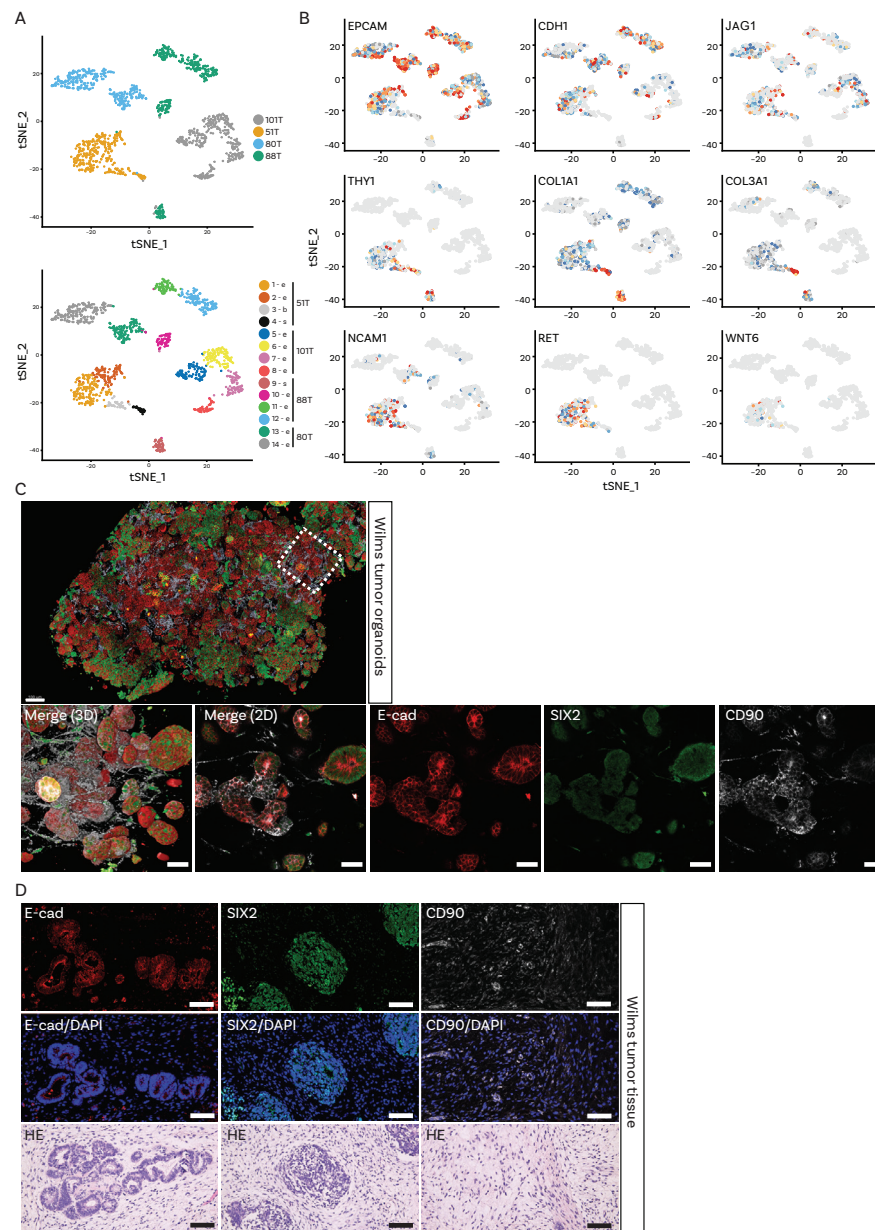
Figure 3. Cellular heterogeneity within Wilms tumor organoid cultures. A. t-SNE representation of single cells from four Wilms tumor organoid lines (51T, 80T, 88T and 101T). Cells are colored by organoid of origin (top panel) or clustering (bottom panel). Indicated are the cell types the populations are representing based on marker gene expression (see panel b). e: epithelial, s: stromal, b: blastemal-like. **B.** t-SNE maps showing the color-coded logged expression levels of several markers for each population demonstrating that different cell types

are present in 51T and 88T, whereas 80T and 101T organoids primarily consist of different epithelial subpopulations, which is in line with their histological appearance. **C.** High-resolution 3D imaging of 51T Wilms tumor organoids immunolabeled for E-cadherin (E-cad; red), SIX2 (green) and CD90 (white). Bottom panels depict enlargement from top panel in 3D (left panel) and a representative optical section (others panels). Scale bars, 100 μm (top) and 50 μm (bottom). Images are representative of n= 2 independent experiments. **D.** Immunofluorescence imaging on 51T Wilms tumor tissue sections immunolabeled for E-cadherin (E-cad; red), SIX2 (green) and CD90 (white). Scale bars 100 μm. Images are representative of n = 2 independent experiments.

Within organoid lines, different clusters could be distinguished as well. Whereas, 101T and 80T demonstrated a rather heterogeneous composition of different epithelial subpopulations (all marked by *EPCAM* and *CDH1* (E-cadherin) expression), distinct cell populations could be distinguished in 51T and 88T (**Figure 3A,B**; **Supplementary Figures 4C-E** and **5**). Organoid culture 88T demonstrated distinct clustering of three populations. Two of these demonstrated high levels of *EPCAM* and *CDH1*, therefore likely reflecting epithelial subpopulations. The third population showed strong enrichment for stromal markers such as multiple collagens, thus representing stromal cells (**Figure 3A,B**; **Supplementary Figures 4C-E** and **5**). In 51T, one population was enriched for epithelial markers (e.g., *EPCAM*, *CDH1*), therefore representing epithelial cells. A second population showed strong enrichment for stromal markers (e.g., collagens), whereas a third population appeared more undefined, co-expressing markers of both epithelial and stromal cells, but also more progenitor-like markers involved in neuro- and nephrogenesis (**Figure 3A,B**; **Supplementary Figures 4 C-E** and **5**). Although no exclusive markers of the blastemal compartment of Wilms tumors have been described, the latter population likely represents blastemal cells. In line with this, this population was enriched for *NCAM1* and *SIX1* expression, both proposed blastemal markers[39]. The different cell types could still be detected upon serial passaging, as determined by marker gene expression analysis using FACS and scRNA-seq on early- and late-passage cultures, although a slight enrichment was observed for epithelial progenitors (*EPCAM*, *CDH1*, *JAG1*-positive cells) and blastemal-like cells (**Supplementary Figures 5B,C** and **6A**).

To exclude that the cultured stromal cells represent non-tumorigenic tumor-infiltrating fibroblasts, we obtained pure epithelial and stromal cells from a stromal-type Wilms tumor organoid culture (88T) based on *EPCAM* (epithelial) or *THY1* (*CD90*, stromal) expression. Next, we performed targeted sequencing of bi-allelic WT1 mutations that were identified by WGS on the bulk tumor culture

(see below). Indeed WT1 mutations could be detected in both the epithelial as well as the stromal cells, thereby confirming that the stromal cells are indeed tumor cells. Of note, matching normal kidney organoids harbored wild-type WT1 (**Supplementary Figure 6D**). Altogether, these data indicate that the cellular heterogeneity of Wilms tumors can, at least partially, be maintained in organoid cultures. To visualize the spatial organization of the different cell types *in vitro*, we performed high-resolution 3D imaging[40] on two multi-phasic Wilms tumor organoid cultures (51T and 88T). We selected cell-type markers based on our scRNA-seq data with E-cadherin for epithelial cells, CD90 for stromal cells and SIX2 as putative blastemal marker. We observed a highly heterogeneous culture in which stromal cells formed an intricate network with epithelial organoids, as well as more blastemal-like (SIX2-positive) organoids (**Figure 3C**; **Supplementary Figure 6B**). Similar cell types could be observed in matching Wilms tumor tissue (**Figure 3D**; **Supplementary Figure 6C**). Mutations in the SWI/SNF complex member *SMARCB1* are found in >95% of rhabdoid tumors. SMARCB1 (INI-1) immunostainings are therefore routinely used to confirm MRTK diagnosis[41]. Indeed, loss of SMARCB1 expression was observed in MRTK tissue as well as in all organoids established from it, whereas strong nuclear expression was observed in normal kidney tissue from the same patient and organoids derived thereof (**Figure 2B**). In some cases, a mix of grape-like clumps of cells and more cystic organoid structures was observed, pointing towards contamination of the tumor organoid culture with organoids derived from normal kidney epithelium, which was confirmed by staining for SMARCB1 (**Supplementary Figure 3B**). In contrast to normal kidney tissue, MRTKs do not show epithelial differentiation[42]. Therefore, we separated MRTK cells from normal kidney cells based on expression of the epithelial marker EPCAM. As expected, no EPCAM-positive cells could be detected in MRTK organoids derived from a lymph node metastasis (**Supplementary Figure 3C**). In contrast, an EPCAM-positive cell population was observed in primary tumor-derived MRTK organoids. Indeed, a pure MRTK organoid culture, devoid of epithelial normal kidney organoid structures, could be established (**Supplementary Figure 3D**). Lastly, RCC organoids consist of cells with typical clear cytoplasms (**Figure 2A**; **Supplementary Figure 2**), whereas tumor origin of a *TP53*-mutated RCC-derived organoid was confirmed by immunostaining for P53 (**Supplementary Figure 3E**).

Genetic characterization of kidney cancer organoids

Several recent studies have revealed the heterogeneous genetic landscape of Wilms tumors[12,13,17]. In addition to a significant percentage of chromosomal alter-

ations, numerous mutated genes have been described, although all with relatively low frequency. To characterize the mutations and CNAs in kidney tumor organoids, we performed whole-genome sequencing (WGS) on 28 tumor organoids and compared these, when available, to their matching normal organoid counterparts. Nine out of 20 Wilms tumor organoids showed CNAs such as gain of 1q, 6, 12 and 17p, and loss of 1p, 4q, 16q, 17p, 14, 11 and 22 (**Figure 4A**; **Supplementary Figure 7A**), which is consistent with previous reports[12,13,17,43]. Moreover, mutations in typical Wilms tumor genes were identified, such as *WT1*, *DIS3L2*, *WTX*, *CTNNB1* and the miRNA processing genes *DROSHA*, *DGCR8* and *DICER1* (**Figure 4A**). In a few cases, no common tumor mutations could be detected. We detected a fusion of the *TFE3* gene with the *SFPQ* gene in an RCC-derived organoid culture (107T, **Figure 4A**), a frequently occurring event in pediatric RCCs[44]. In MRTK organoids, *SMARCB1* was the only recurrent mutated gene, varying from nonsense mutations to losses of chromosome 22q, on which locus *SMARCB1* is encoded. As previously described[45], no apparent differences in the total number of somatic mutations were found between Wilms tumors and MRTKs (**Supplementary Figure 7B,D**). Moreover, we detected a heterozygous KRASG12R mutation in metanephric adenoma tissue as well as in the organoids derived thereof, whereas this mutation was absent in matching normal kidney tissue and organoids (**Supplementary Figure 7C**).
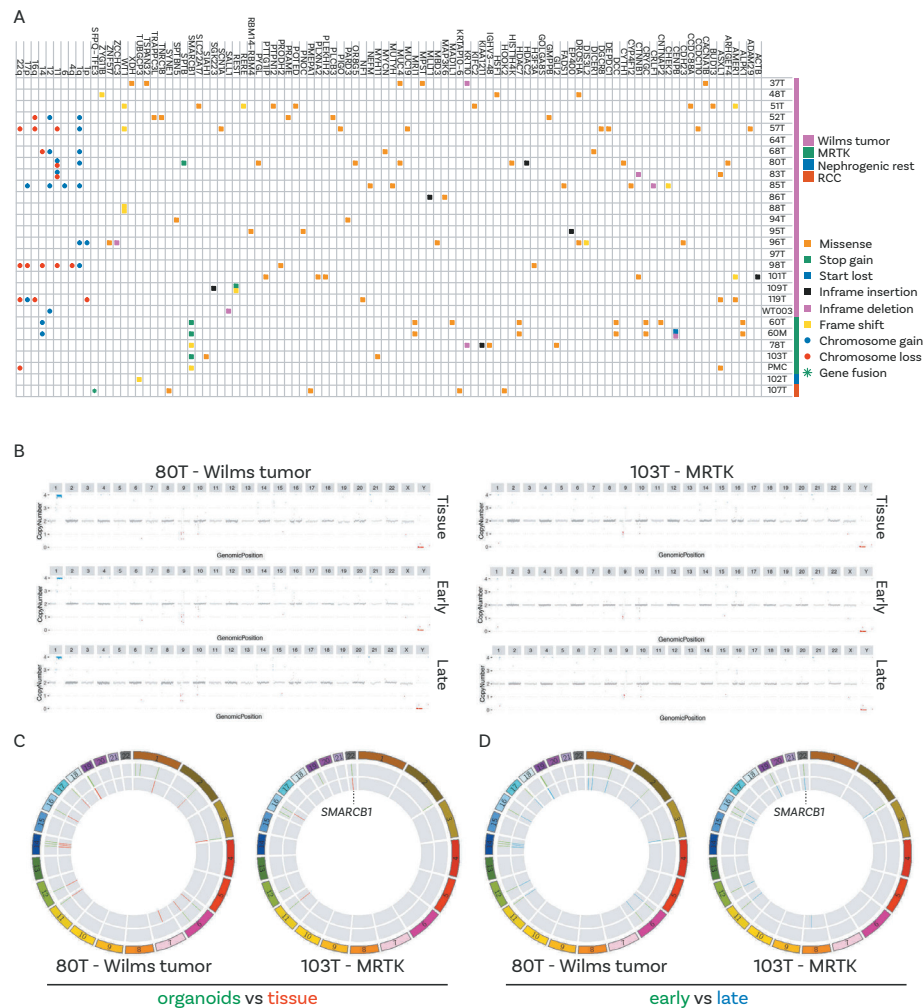
Figure 4. Genetic characterization of pediatric kidney cancer organoids reveals common driver mutations and copy number alterations. A. Overview of somatic mutations identified in pediatric kidney cancer organoids compared with their matching normal kidney organoids. When matching normal kidney organoids were not available, somatic mutations in known driver genes are indicated. **B.** Genome-wide CNAs (karyograms) and coding gene mutations (circos plots) (**C., D.**) in matching tumor tissue vs organoid and early vs serially passaged (P4, P5 vs P10, P11) reflecting ~3 months of culturing) organoid pairs reveal that organoids recapitulate the genetic landscape of the tissue they were derived from and that this genetic landscape is retained over time.

To determine whether pediatric kidney cancer organoids genetically recapitulate the tumors from which they were derived, we performed WGS on five tumor organoids and matching tumor tissues (three Wilms tumors, two MRTKs). Indeed, this demonstrated that organoids are genetically highly similar to their tumor tissue counterparts (**Figure 4B,C**; **Supplementary Figure 8**). Lastly, genetic characterization of early and serially passaged tumor organoids confirmed their genetic stability over time (**Figure 4B,D**). To further confirm that organoids preserve the genetic landscape of native tumors, we extracted mutational signatures[46,47] from the WGS data of our organoids, as well as from recently published WGS data sets of Wilms tumor and brain rhabdoid tumor (ATRT) tissue[45,48]. We subsequently compared these to recently described mutational signatures in the Catalogue of Somatic Mutations in Cancer (COSMIC) database[49] and signatures reported as pediatric cancer-specific[48]. This analysis revealed the presence of a large number of different signatures in Wilms and rhabdoid tumors, with most common occurrence of signatures 1, 5 and T10 (**Supplementary Figure 7D**). No apparent therapy-related signatures were observed in the organoids derived from pre-treated tumors. Importantly, the broad spectrum of mutational signatures identified in these tumor tissues were represented in our pediatric kidney cancer organoids (**Supplementary Figure 7D**). In summary, we show that pediatric kidney cancer organoids recapitulate the diverse genomic landscape of pediatric renal tumors, such as CNAs, cancer gene mutations, as well as mutational signatures.

Gene expression and DNA methylation profiling

To determine whether organoids represent gene expression profiles of the different pediatric kidney tumor subtypes, we performed paired end RNA-seq on organoids derived from 29 pediatric renal tumors. In 18 cases, matching tumor tissue was available and included in the analyses. The most variable genes were used to project the RNA samples in a linear dimensional reduction space using principal components (PCs). As expected, the first PC separates the growth microenvironment of the tumor cells (organism versus *in vitro*), the second PC the MRTKs, while the third separates the RCCs (**Supplementary Figure 9A,B**). After regressing out the growth microenvironment, the samples were clustered in sample populations (**Figure 5A**).
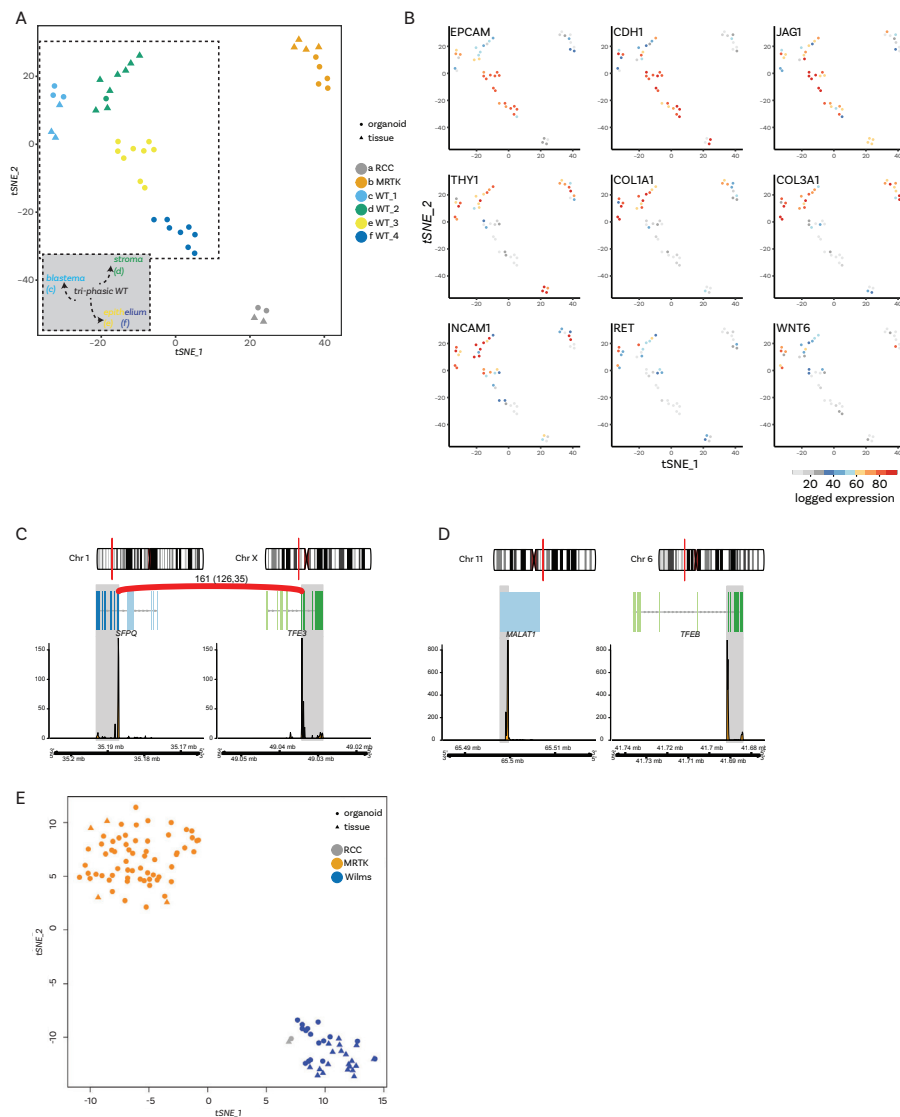
Figure 5. Transcriptome and DNA methylation profiling of pediatric kidney cancer organoids.
A. t-SNE representation of unsupervised graph-based clustering of pediatric kidney cancer organoids and tissues gene expression profiles, demonstrating a disease-based separation for the three main tumor types (RCC, MRTK and Wilms tumor) and a composition-based separation for the most prevalent one, Wilms tumor. **B.** t-SNE maps, as in a, showing the color-coded logged expression levels of several markers used in the clinic or separating the different populations. **C., D.** Depicted are fusion transcripts detected in tRCC-derived organoids 107T (C) and 71T (D) with their chromosomal location and exon structure and a schematic representation of the fusion breakpoint. Coverage track of the fusion genes is included at

the bottom, indicating RNA expression levels. The number above the red arc represents the sequencing reads that support the fusion event. **E**. t-SNE analysis was performed using the top 2000 most variably methylated CpG sites in pediatric kidney cancer organoids and tissues, and revealed that organoids cluster with the tumor entity they were derived from.

The resulting clusters separate the samples based on their tumor diagnosis. The first two sample clusters comprise the RCC and MRTK tissue and organoid samples (**a** and **b**, respectively; **Figure 5A**), demonstrating that RCC and MRTK organoids retain the identity of the native tumor tissue. Wilms tumor tissue and organoid samples were more heterogeneous separating into the remaining four clusters (**Figure 5A**). Cluster c has high levels of progenitor-like blastema markers. The clustering of 51T sample in cluster c thus supersedes the expression of epithelial markers *EPCAM* and E-cadherin (*CDH1*) coming from the epithelial population of the 51T organoid cells (**Figure 3A**). Cluster d has higher stromal expression, shown with the elevated levels of various collagen genes, while clusters e and f have progressively higher epithelial characteristics, evident by the increased levels of *CDH1* and *EPCAM* (**Figure 5B**). Bulk gene expression profiling can also point to the presence of mechanisms of carcinogenesis, not detected by DNA sequencing. For instance, elevated expression of insulin-like growth factor 2 (*IGF2*) is reported in the majority of Wilms tumors[12,13,38,50]. In line with this, the majority of Wilms tumor organoids demonstrated high IGF2 gene expression compared with normal kidney, MRTK and RCC organoids (**Supplementary Figure 10A**). Wilms tumor organoids largely retained the high *IGF2* expression detected in the parental tumor tissue (**Supplementary Figure 10B**). Compared with the other Wilms tumor organoid lines and normal kidney-derived organoids, WT003T showed markedly reduced *DICER1* gene expression (**Supplementary Figure 10C**). WT003T was derived from a cystic partially differentiated Wilms tumor, a rare Wilms tumor subtype composed of large cysts separated by septa. Remarkably, cystic nephroma, another childhood renal tumor composed of large cysts, has been previously linked to DICER1 mutations[51-54]. In contrast to MRTKs, no significant *hTERT* expression could be detected in Wilms tumor tissue and organoids derived thereof (**Supplementary Figure 10D**), which is in contrast to a study by Dome et al.[55] demonstrating *hTERT* expression in Wilms tumors using quantitative RT-PCR. Still, the vast majority of Wilms tumor organoid cultures could be long-term propagated, suggesting that alternative mechanisms are involved to maintain replicative potential, as previously suggested[56]. The RNA-seq analyses demonstrated expression of the *SFPQ-TFE3* fusion transcript in 107T RCC organoids (**Figure 5C**; **Supplementary Figure 10E**), thus confirming the WGS analyses (**Figure 4A**). In a second RCC-derived organoid line (71T), we detected

a *MALAT1-TFEB* fusion transcript (**Figure 5D**; **Supplementary Figure 10F**). Both these fusions have been described as drivers in pediatric RCCs[44]. Strikingly, we detected strongly decreased *TP53* transcript levels in 71T and 107T organoids as well as tissue (**Supplementary Figure 9C**), which confirms previous reports[57]. Thus, tumor organoids display representative gene expression profiles, which allow unsupervised separation of the majority of pediatric kidney cancer subtypes. Finally, we set out to determine whether pediatric kidney cancer organoids retain the epigenetic profile of their corresponding tumor entity. We therefore performed DNA methylation analyses on a subset of tumor organoids and compared these to the DNA methylation profiles of matching tumor tissues as well as recent DNA methylation data of malignant rhabdoid tumors[58]. In line with the transcriptome analyses, clustering analysis demonstrated that organoids clustered with their respective tumor types and thus maintained the epigenetic profile of the tumor (**Figure 5E**), as found previously for colorectal cancer organoids[59].

Gene editing and high-throughput drug screens.

TP53 mutations positively correlate with anaplasia[60–62]. To determine whether pediatric kidney tumor organoids can be genetically manipulated, we set out to model anaplastic Wilms tumors by generating TP53-knockout mutations in TP53-wild-type Wilms tumor organoids using CRISPR/Cas9 gene editing. We transiently transfected the 80T Wilms tumor organoid culture with either a control or *TP53* targeting sgRNA. Three days after transfection, we added nutlin-3 to the medium to select for *TP53*-mutant organoids (**Supplementary Figure 11A**)[63]. As expected, control sgRNA-transfected Wilms tumor organoids died upon nutlin-3 treatment (**Supplementary Figure 11B**). Surviving organoids in the *TP53* sgRNA-transfected culture were clonally expanded, and homozygous TP53 knockout was verified by genotyping and western blot (**Supplementary Figure 11C,D**). Subsequent histological characterization did not reveal any distinct anaplastic features in *TP53*-knockout Wilms tumor organoids (**Supplementary Figure 11E**). This suggests that loss of *TP53* is required but not sufficient for inducing anaplasia in Wilms tumors, which is in line with the findings of Wegert et al.[62] describing TP53 mutations in regions lacking signs of anaplasia. Possibly, persistent chromosome instability caused by the loss of *TP53* is required for the acquisition of an anaplastic phenotype.

In order to determine whether our patient-derived Wilms tumor organoids can be used as a drug-screening platform, we first tested their sensitivity towards standard-of-care chemotherapeutics. The current chemotherapy regimen encompasses actinomycin D (ACT-D) and vincristine (VCR) prior to radical nephrectomy, possibly followed by doxorubicin (DOX) and/or etoposide (ETO)[5].
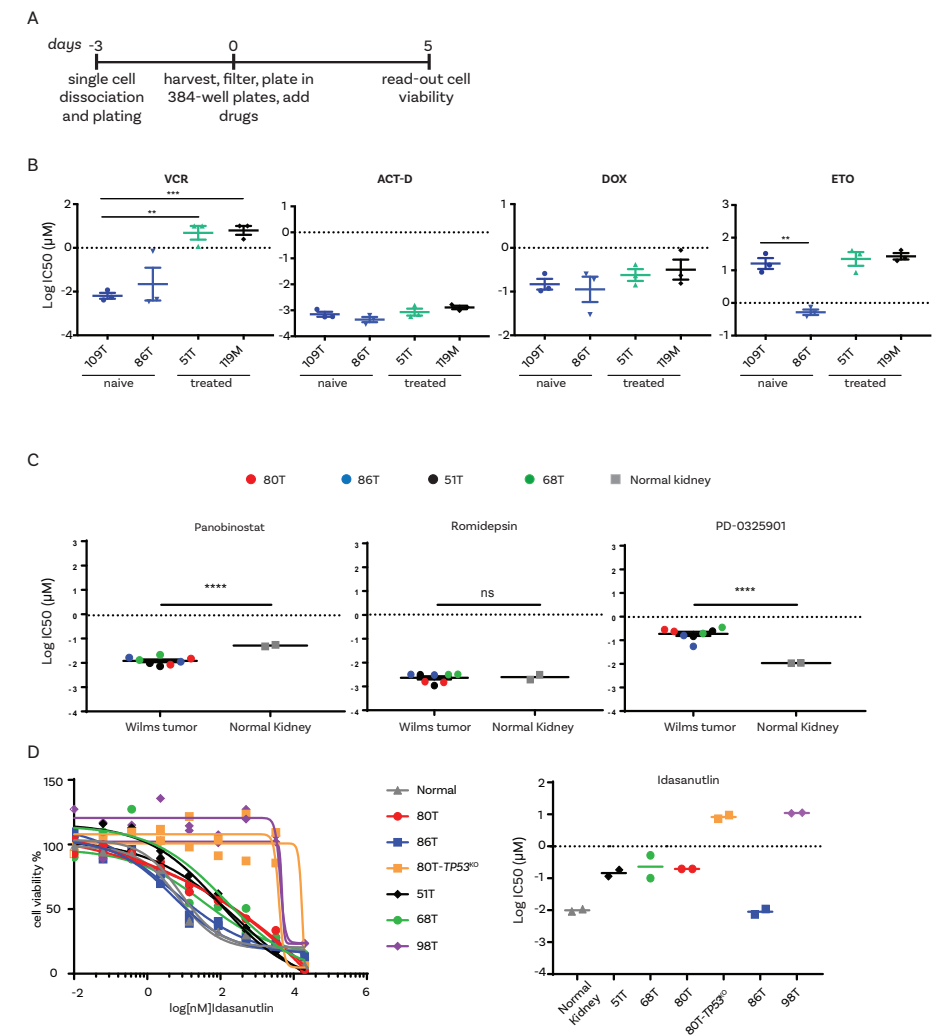
Figure 6. Organoid drug screens reveal patient-specific drug sensitivities. A. Schematic overview of the organoid drug treatment experiment. **B.** Graphs show the average IC50 values of vincristine (VCR), actinomycin D (ACT-D), doxorubicin (DOX) and etoposide (ETO) in the indicated Wilms tumor organoid lines. In case the IC50 value was not reached (see Supplementary Figure 12A), the highest tested concentration was used for the calculations. Error bars represent SEM of three independent experiments (each individual experiment includes technical quadruplicates). P-values were calculated using a two-tailed Student's t test, two-sided: **<0.01, ***<0.001. P-value VCR: 119M vs 109T= 0.0005; 109T vs 51T = 0.0049. P-value ETO: 109T vs 86T = 0.0044. **C.** Average IC50 values of romidepsin, panobinostat and PD0325901 in the indicated Wilms tumor and normal kidney organoid cultures. Each dot/square (two per organoid culture) represents the average of technical quadruplicates of an individual organoid culture. P-values were calculated using a two-tailed Student's t test,

two-sided: ****<0.0001. P-value romidepsin: Wilms tumor vs normal kidney=0.8339. **D.** Dose–response curves (left) and average IC50 (right) of idasanutlin on the indicated Wilms tumor and normal kidney organoid cultures. As control for P53 function, 80T-TP53KO organoids were included, thereby demonstrating that anaplastic Wilms tumor-derived organoids (98T) are less sensitive to idasanutlin treatment. Curves with the same color represent independent experiments. Each individual point represents the average of quadruplicate measurements.

We used two chemo-naive (109T, 86T) Wilms tumor organoid lines and two that were derived of chemo-treated Wilms tumors (51T, 119M) and subjected those to a previously established drug-screening platform and cell viability read-out[33] (**Figure 6A**). Testing six different concentrations per drug allowed us to generate reproducible dose–response curves (**Supplementary Figure 12A**) and calculate half-maximal inhibitory concentrations (IC$_{50}$) (**Figure 6B**).

While organoids derived from both pre-treated Wilms tumors were significantly less sensitive to VCR than the untreated Wilms tumor organoids, similar sensitivity was observed towards ACT-D. This suggests that remaining viable Wilms tumor cells after pre-operative chemotherapy are more resistant to VCR and demonstrates the added value of the combination treatment. Interestingly, organoid line 86T demonstrated markedly higher sensitivity to etoposide compared with all other lines. Yet, no apparent genetic biomarker could be identified in our WGS data. Next, we screened four Wilms tumor organoid lines using a ~150 compound library with six different concentrations. Ranking compounds based on the calculated area under the estimated dose–response curve (AUC) revealed multiple different MEK and HDAC inhibitors in the top 25 of most effective compounds (**Supplementary Figure 12B**). We then validated the most potent MEK and HDAC inhibitors (romidepsin, panobinostat and PD0325901) and additionally included normal kidney organoids to determine tumor-specific targeting. This showed that normal kidney organoids are equally sensitive to romidepsin (HDAC 1/2 inhibitor) and even more sensitive to MEK inhibition (**Figure 6C**; **Supplementary Figure 12C**). Interestingly, Wilms tumor organoids demonstrated significantly increased sensitivity to panobinostat (pan-HDAC inhibitor) compared with normal kidney organoids (**Figure 6C**; **Supplementary Figure 12C**), thereby possibly pointing towards a less toxic therapeutic strategy. Lastly, we established organoids from an anaplastic Wilms tumor (98T), which are characterized by mutations in *TP53*[60-62]. Indeed, 98T organoids expressed reduced *TP53* transcript levels (**Supplementary Figure 9C**) and showed several anaplastic characteristics (enlarged nuclei and hyperchromasia, **Supplementary Figure 12D**). To test for P53 functionality, we next tested 98T organoids together with the other (non-anaplastic) Wilms tumor-derived organoid lines for sensitiv-

ity to idasanutlin, a therapeutic P53 stabilizing agent. In addition, we included our genetically engineered 80T-TP53KO organoids as a control. A dramatically reduced sensitivity for idasanutlin was observed in 98T organoids compared with all other Wilms tumor organoids (**Figure 6D**). The observed sensitivity was comparable with the sensitivity of 80T-TP53KO organoids, indicating that P53 function is severely hampered in these organoids. Of note, as for etoposide, 86T organoids demonstrated a high sensitivity for idasanutlin (**Figure 6B,D**), indicating that this tumor is particularly sensitive to P53-activating agents. Altogether, our pediatric kidney cancer-derived organoid models are amenable to gene editing and allow for high-throughput drug testing to reveal patient-specific drug sensitivities and to make drug/mutation correlations.

Discussion

The development of 3D cell culture systems allows for the highly efficient establishment of pre-clinical cancer models from patient-derived tissue. Availability of such models is of particular interest for less common cancers, such as pediatric tumors, as it allows for the generation of large collections of living material for research purposes, despite their relative rarity. As for adult cancers, cell lines have been the gold standard for pediatric cancer research. Yet, it has been challenging to develop cell lines capturing the phenotypic and genetic heterogeneity of pediatric kidney tumors[7]. The establishment efficiency of cancer cell lines is very low, which makes them unsuitable for the generation of patient-specific models and individualized drug screening. In the rare cases a cell line can be established from primary tumor tissue, this usually involves extensive adaptation and selection to *in vitro* 2D culture conditions. As only rare clones can be expanded, the derived cell lines typically undergo substantial genetic changes, and no longer recapitulate the genetic background and genetic (as well as cellular) heterogeneity of the original tumors. Wilms tumor is the most common and extensively studied pediatric renal tumor. Although Wilms tumor cell lines have contributed tremendously to our understanding of Wilms tumor biology, they almost invariably derive from advanced cancers. Moreover, the current cell line panel does not reflect the heterogeneous nature of Wilms tumors[7,64,65]. Wegert et al.[56] recently developed a protocol for the establishment of cultures from primary Wilms tumor tissue. This protocol allowed them to generate cell cultures from 22% (12 out of 55) of Wilms tumor patients (versus 75% using our protocol). No confirmed matching healthy reference cultures were established. Moreover,

these 2D monolayer cultures phenotypically did not resemble parental tumor tissue very well, with mainly fibroblast-like features and no blastemal marker expression[56]. Finally, pre-clinical *in vitro* cell models are scarce for the other pediatric kidney cancer subtypes. Here, we describe the establishment of the first pediatric cancer organoid biobank, containing the majority of childhood kidney cancer subtypes: Wilms tumors, MRTKs, RCCs and several rarer renal tumor entities, such as CMNs and metanephric adenomas. To our knowledge, the malignant rhabdoid tumor organoids represent the first organoid model sustaining long-term growth of tumors of non-epithelial origin. So far, we have not established organoids from CCSK tissue, due to their low occurrence. We demonstrate that epithelial, stromal and blastemal-like populations can be maintained in Wilms tumor organoids, which are organized in an intricate 3D network. Moreover, we show that pediatric kidney cancer organoids retain phenotypic, genetic, epigenetic and gene expression characteristics of native tumors to a large extent. Besides tumor cells, clinical tumor samples typically contain areas of necrotic tissue as well as non-tumor cells (e.g., blood vessels, immune and stromal cells). This low tumor content of clinical samples can severely hamper molecular characterization and drug-sensitivity readouts. Tumor organoids are pure tumor cultures, therefore allowing for in-depth characterization of tumor cell-specific features and drug sensitivities. Moreover, the possibility to propagate and expand primary tumor tissue as organoids provides nearly limitless availability of material for research purposes. Importantly, we and others have demonstrated that tumor organoids largely retain the heterogeneity of the tissue they were derived from over serial passaging[27,34,66,67]. Since clonal dynamics within tumor organoid cultures may occur[34], early passage organoid cultures should preferentially be used for therapy development purposes. Similarly, variability induced by organoid production procedures might influence experimental readouts. Comprehensive genetic and phenotypic analyses of the cultures should therefore be considered before their utilization in downstream experimental procedures. The lack of blood vessels and immune cells are an intrinsic limitation of organoid technology as well. Recent efforts led to the development of co-cultures of tumor organoids with cancer-associated fibroblasts[68,69] and immune cells[70], demonstrating the potential of implementing these factors in pediatric kidney organoid cultures. Here, we report that organoids can be derived with high efficiency from the majority of pediatric kidney tumors and can be rapidly expanded, which allows for identifying patient-specific drug sensitivities, and potentially the development of improved therapeutic strategies.

Methods

Human tissue. All experiments with human tissue were approved by the medical ethical committee of the Erasmus Medical Center (Rotterdam, the Netherlands). The parents of all patients participating in the biobank study signed informed consent forms approved by the responsible authority.

Tissue processing. Following nephrectomy or biopsy, a random piece was selected from viable tumor tissue and, when available, normal kidney tissue. One or two random pieces were fixed in formalin for histopathological analysis. The remainder was minced into ~1-mm^3 pieces. Several pieces were snap frozen and stored at –80 °C for DNA and RNA isolation. The remainder was digested in AdDF+++ (Advanced DMEM/F12 containing 1× Glutamax, 10mM HEPES and antibiotics) containing 1mgml^{-1} collagenase (Sigma, C9407) and 10 µM Y-27632 on an orbital shaker for 45 min at 37 °C. Next, the suspension was washed with AdDF+++ followed by centrifugation at 250×g. In case of a visible red pellet, erythrocytes were lysed in 1–2mL red blood cell lysis buffer (Roche, 11814389001) for 5 min at room temperature before the addition of 10ml AdDF+++ and centrifugation at 250×g. Organoid culture. The cell pellets were seeded in growth factor-reduced BME (Trevigen, 3533-010-02) and cultured in kidney organoid medium (AdDF+++ supplemented with 1.5% B27 supplement (Gibco), 10% R-spondin-conditioned medium, EGF (50 ng ml–1, Peprotech), FGF-10 (100 ng ml–1, Peprotech), N-acetylcysteine (1.25 mM, Sigma), Rho-kinase inhibitor Y-27632 (10 µM, Abmole) and A83-01 (5 µM, Tocris Bioscience)[36]. Medium was changed every 3–4 days, and organoids were passaged every 1–3 weeks. Depending on organoid morphology, organoids were either passaged using mechanical dissociation (Wilms tumor organoids, MRTK organoids), or TrypLE Express (Invitrogen, 12605036) containing 10 µM Y-27632 (Wilms tumor organoids, RCCs). Following the addition of 5–10 ml AdDF+++ and centrifugation at 250×g, cells were reseeded in BME and topped with kidney organoid medium. All organoid cultures are stored in the biobank of the Princess Máxima Center and made available to the scientific community according to the rules and regulations under which the patients and parents gave informed consent for donating the tissue.

Organoid transfection and genotyping. Organoids were transfected using lipofection as previously described[63]. In brief: organoids were digested to single-cell suspensions using TrypLE Express with 10 µM Y-27632. Cells were subsequently resuspended in 450 µl kidney organoid medium and plated in 48-well plates at

high density (80–90% confluent). Nucleic acid–Lipofectamine 2000 complexes were prepared according to the standard Lipofectamine 2000 protocol (Invitrogen). Four microlitres of Lipofectamine 2000 reagent in 50 μl Opti-MEM medium (Gibco) and 1.5 μg of DNA (pSpCas9(BB)-2A-GFP control or sgRNA TP53 plasmid in 50 μl Opti-MEM medium) were mixed together, incubated for 5 min and added to the cells. The plate was centrifuged at 600 g at 32 °C for 1 h, and incubated for 4 h at 37 °C before single cells were plated in BME. Three days after transfection, 10 μM nutlin-3 (Cayman Chemical) was added to the growth medium. After approximately 2–3 weeks, surviving clones were picked and clonally expanded. For genotyping, genomic DNA was isolated using Viagen Direct PCR (Viagen). Primers for the PCR amplification using GoTaq Flexi DNA polymerase (Promega) were as follows: TP53_for 5′-CAGGAAGCCAAAGGGTGAAGA-3′;TP53_rev5′-CCCATCTA-CAGTCCCCCTTG -3′. For WT1 genotyping, DNA was isolated from FACS purified EPCAM+/CD90– and EPCAM–/CD90+ cells using Viagen Direct PCR (Viagen). Primers for the PCR amplification using GoTaq Flexi DNA polymerase (Promega) were as follows: WT1_exon10_for 5′-TTTCCAGAAGCACCGGTATC-3′; WT1_exon10_rev 5′-TGCCAAGTTGTCAGAAAAA-3′; WT1_exon7_for 5′-TTATTGCAGCCTGGGTAAGC-3′; WT1_exon7_rev 5′-GGAGTGTGAATGGGAGTGGT8 -3′. Products were cloned into pGEM-T Easy vector system I (Promega) and subsequently sequenced using T7 sequencing primer.

Histology, immunohistochemistry and immunofluorescence. Tissues and organoids were fixed in 4% paraformaldehyde, dehydrated and embedded in paraffin. Immunohistochemistry was performed according to standard protocols on 3–4 μm sections. Sections were subjected to H&E, immunohistochemical as well as immunofluorescence staining. The following primary antibodies were used for immunohistochemical staining: desmin (Leica Novacastra, NCL-L-Des-Der11, 1:100), INI-1 (BD Transduction Laboratories, 612111, 1:400), P53 (Dako, M7001, 1:6000). For immunofluorescence on tissues: SIX2 (Proteintech, 11562-1-AP, 1:200), E-cadherin clone ECCD-2 (ThermoFisher, 13-1900, 1:200), CD90 clone EPR3133 (Abcam, 133350, 1:100) were used. Imaging was performed using Leica DM6 microscope. High-resolution 3D organoid imaging. High-resolution 3D imaging on organoids was performed as described[40] using the following antibodies: SIX2 (Proteintech, 11562-1-AP, 1:200), E-cadherin clone ECCD-2 (ThermoFisher, 13-1900, 1:500), CD90-APC clone 5E10 (BioLegend, 328113, 1:200). Imaging was performed using Zeiss LSM880 microscope. Three-dimensional reconstruction was performed using the software Imaris v.9.2.1.

FACS. Organoids were dissociated into single-cell suspensions using TrypLE Express (ThermoFisher) supplemented with Rho-kinase inhibitor Y-27632 (10 μM, Abmole). Single-cell suspensions were stained using mouse Alexa-fluor 488 anti-human CD326 EPCAM clone 9C4 (BioLegend, 324210, 1:20), CD90-APC clone 5E10 (BioLegend, 328113, 1:50) as described[71]. Populations were sorted using BD-FACSAria—Fusion sorter (BD Biosciences) or MoFlow® Astrios (Beckman Coulter) and used for their respective applications (Supplementary Figure 13). Data were analyzed with software Kaluza analysis v2.1.

Whole-genome sequencing and DNA methylation profiling. Genomic DNA from tissue and organoids was extracted using the ReliaPrepTM gDNA Tissue Miniprep System (Promega) according to the manufacturer's instructions and sent for WGS. Samples were sequenced on BGI-SEQ500 platform (BGI Hong Kong) or with Illumina NovaSeq6000 sequencers (Hartwig Medical Foundation) to 30× base coverage. Sequence reads were mapped against human reference genome GRCh37 by using Burrows-Wheeler Aligner v0.7.5a mapping tool[72] with settings "bwa mem -c 100 -M". Sequence reads were marked for duplicates by using Sambamba v0.6.8 and realigned per donor by using Genome Analysis Toolkit (GATK) IndelRealigner v3.4-46. Full pipeline description and settings also available at https://github.com/ UMCUGenetics/IAP. Mutations were called and filtered as described[73]. Briefly, raw variants were multisample-called by using the GATK HaplotypeCaller v3.4-46[74]. To obtain high-quality somatic mutation catalogs, we filtered out variants with evidence in their corresponding normal samples, overlaps with the Single Nucleotide Polymorphism Database v137.b37, and the variants that did not reach our quality measurements (base coverage of 10×, variant allele frequency (VAF) of 0.1, GATK phred-scaled quality score of 100 for base substitutions, 250 for indels and mapping quality (MQ) of 60 for indels). Indels that were present within 100 bp of a called variant in the control were excluded. For signature analysis, additional filter on GATK genotype quality (GQ) of 10 in normals, 99 in samples was applied to obtain high-quality base substitutions. For samples without matching normals, base coverage of 20× was used instead of 10×, and these were not included in signature analysis. Only autosomal variants were considered. The scripts used for the filterings are available at https://github.com/UMCUGenetics/SNVFI and https://github.com/ToolsVanBox/INDELFI. Nonsynonymous mutations (missense mutation, start loss, stop gain, inframe insertion/ deletion and frame shift) in all genes identified in samples with matching normals, and in known driver genes from samples without matching normals were reported as driver mutations. Every coding mutation including drivers has

been manually inspected to exclude false calls. Average chromosome gain or loss were calculated based on the estimated copy number by freec[75] using copy number package in R[76]; low copy number changes indicate partial gain or loss. Signature analysis was performed together with published Wilms tumor[48] and atypical teratoid rhabdoid tumors[45] using an in-house developed R package (MutationalPatterns)[77]. All single base substitution signatures that are reported as plausible in the COSMIC SigProfiler signatures (https://www.synapse.org /#!Synapse:syn11967914]), except for signature 40, which is similar to signature 5 and therefore challenging to distinguish from signature 5 with a small sample set, and pediatric data specific signatures (T10 and T11[48]) were used in this analysis. Since signature 1 and 5 are associated with age, these signatures were assumed to be present in all samples. Thus, the mutational profile of every sample was re-fitted to signature 1 and 5, calculated its cosine similarity and then a signature that increases the cosine similarity the most was selected by adding and re-calculating the cosine similarity for the rest of signatures one by one. Until the overall cosine similarity reaches to 0.9 or the increase of cosine similarity by adding another signature dropped to <0.01, we repeated to add a signature with the highest increase in the cosine similarity. The total number of base substitutions and the absolute contributions of the selected signatures for each sample are reported. The script is available at https://github.com/ ToolsVanBox/MutSigPipe. DNA methylation profiles were assessed using Illumina Human MethylationEPIC BeadChip arrays at the German Cancer Research Center (DKFZ) Genomics and Proteomics Core Facility according to the manufacturer's instructions. Analysis was performed as described[78].

Single-cell RNA sequencing. Samples were prepared according to the Sort-seq method[79]. In brief, organoids were dissociated into single-cell suspensions using TrypLE Express (ThermoFisher) supplemented with Rho-kinase inhibitor Y-27632 (10 μM, Abmole). Viable single cells were sorted based on forward/side scatter properties and DAPI staining using FACS (FACSJazz, BD Biosciences) into 384-well plates (Biorad) containing 10 μL mineral oil (Sigma) and 50 nL of RT primers. Samples were subsequently processed into Illumina sequencing libraries as described[79]. Libraries were sequenced paired-end at 75 bp read length using the Illumina NextSeq sequencer. Sequencing data were processed using the Sharq pipeline as described[80]. We performed the mapping using STAR version 2.6.1 on the hg38 Patch 10 human genome and read assignment with featureCounts version 1.5.2 using a gene annotation based on GENCODE version 26. Transcripts mapping to the mitochondrial genome were removed and the percentage of

mitochondrial transcripts calculated. Cells with a percentage exceeding 40% of the total were excluded. In addition, cells with <1000 unique transcripts were also excluded. Genes with low expression (defined as either having less than five cells expressing the gene or less than two cells with less than two transcripts) were removed. All subsequent analyses were performed using the R package Seurat (version 3.0.2)[81]. Data were processed into a Seurat object and log normalized to 10,000 transcripts. In order to avoid the influence of specific cell processes on the clustering and visualization, the most variable genes were filtered to remove mitochondrial pseudogenes and cell cycle effects. Genes involved in cell cycle were derived as follows: a set of well-known cell cycle markers[82,83] were directly removed from variable genes. In addition, genes that correlate with the cell cycle process were identified. To do this, we used a set of well-known cell cycle markers[82] to calculate S and G2M scores using Seurat's "CellCycleScoring" function. We then correlated all genes with these two scores across all cells, obtaining per-gene correlations with S and G2M score. Using the distribution of correlations of well-known S and G2M genes with either S or G2M score, we calculated cut-offs. The S cut-off is calculated as follows:

$$Max(Med(S_S) - Med(S_{G2M}), Quantile_{25}(S_s)).$$

Where SS represents the correlation of known S phase genes with S phase score and SG2M represents the correlation of known S phase genes with G2M score. In the same manner, the G2M cut-off is:

$$Max(Med(G2M_{G2M}) - Med(G2M_S), Quantile_{25}(G2M_{G2M})).$$

Genes with a correlation to either S or G2M scores above the respective threshold were considered as cell cycle genes and therefore excluded from the variable genes removed. Additional filtering was carried out when processing the data set in Figure 3A. We removed ribosomal protein genes and unnamed transcripts by filtering genes symbols starting with "RP" from variable genes. The first eight principal components were used to calculate dimensionality reduction, and a resolution of 1.35 was used to define clusters. When processing early/late data sets shown in Supplementary Figure 5B, C, we removed heat shock protein genes, as defined by GO:0006986 (response to unfolded protein) as well as ribosomal protein genes, based on the term GO:0022626 (cytosolic ribosome). Lastly, we removed genes residing on chromosome Y, as well as female-exclusive XIST and TSIX. For the early/late comparison of organoid 51 and 80, the first six and ten

principal components, respectively, were used to calculate dimensionality reduction, and a resolution of 0.6 and 0.5, respectively, was used to define clusters. Differential expression analysis was performed comparing each population to all other populations originating from the same organoid using the Wilcoxon test with 1.8-fold expression cut-off, and 5% Bonferroni multiple testing corrected statistical significance cut-off. For enrichment analysis, the R package cluster-Profiler version 3.12 was used[84].Cell-type identification was performed using SingleR version 1.0.1[85]. The expression profile of each single cell was correlated to Human Primary Cell Atlas derived microarray expression data, containing 713 samples representing 38 main cell types. Four major cell types were present in the data set, neuroepithelial cells, epithelial cells, and stromal cells consisting of MSC, fibroblasts, chondrocytes and smooth muscle cells. Cells of each cluster were assigned to cell types by majority vote. All the scripts used are available at https://bitbucket.org /princessmaximacenter /kidney_organoid_biobank/src/ master/Bulk RNA sequencing. The total RNA was extracted from organoids and tissue using Trizol reagent (Invitrogen), and quality was checked with Bioanalyzer2100 RNA Nano 6000 chips (Agilent, Cat. 5067-1511). Sequencing libraries were prepared using the NEBNext® Ultra™ RNA Library Prep Kit (New England Biolabs) according to the manufacturer's protocol. Paired-end sequencing was performed on the Illumina HiSeq (PE150) by Novogene (Hong Kong). 3′-adaptors were trimmed with cutadapt version 1.16 and resulting sequences shorter than 20 bp were discarded. The remaining reads were mapped to hg38 Patch 10 using STAR version 2.6.1. Read assignment was performed with featureCounts version 1.5.2 as described for scRNA-seq. The resulting raw count table was converted to TPM before downstream analysis. The analysis of the bulk RNA-seq was done as described for the single-cell analysis, with the following modifications: no cell filtering was imposed; transcript counts were normalized to 1 million; regression of the growth environment was applied; the first four PCs were used for the graph-based clustering; a twofold change was used for differential expression using the bimodal test with the same significance cut-off as above. The STAR-fusion (version 1.4.0) pipeline was used to identify chimeric reads and call fusion transcripts using default parameters. Nonref splice hits were filtered out, and a FFPM cut-off was set at 1. Plots were generated using the Chimeraviz R package (version 3.8).

Western blot. Western blot on organoids was performed as described[63]. P53 clone DO-1 (sc-126, Santa Cruz Biotechnology, 1:1000) and GAPDH (ab-9485, Abcam, 1:1000) were used as primary antibodies.

Drug screening. Organoids were harvested and washed in ice-cold AdDF+++. Next, organoids were filtered using a 70-μm nylon cell strainer (Falcon) and resuspended in 5% BME in kidney organoid medium. Subsequently, ~500 organoids were plated using the Multi-dropTM Combi Reagent Dispenser on repellent black 384-well plates (Corning) to which medium with compounds were added (six different concentrations) using either the Caliper Sciclone—Robotic Liquid Handling robot or the Tecan D300e Digital Dispenser. Drugs and positive(staurosporin (Sigma-Aldrich)) and negative (DMSO) controls were dispensed such that final DMSO concentration was 1% in all wells. Four technical replicates were included in each experiment. Five days after adding the drugs, ATP levels were measured using CellTiter-Glo® 2.0 (Promega) according to the manufacturer's instructions on a Spark microplate reader (Tecan). The results were normalized to DMSO vehicle (100%). For the validation assays, nine concentrations and four technical replicates were included per compound per experiment. Data were analyzed with software GraphPad Prism v7.04.

Data availability. The sequencing data have been deposited to the European Genome-Phenome Archive (www.ebi.ac.uk/ega/) under accession numbers EGAD00001005319 and EGAD00001005318. DNA methylation data have been deposited to GEO (www.ncbi.nlm.nih.gov/geo/) under accession number GSE137544. COSMIC SigProfiler database [https://www.synapse.org/#!Synapse:syn11967914] has been used for mutational signatures analysis. Filtering scripts used mutational signatures analysis are available at https://github.com/UMCUGenetics/SNVFI and https://github.com/ToolsVanBox/INDELFI.

Acknowledgements

Competing interests

J.D. and H.C. are named as inventors on several patents related to leucine-rich repeat containing G protein-coupled receptor 5 (LGR5)+ stem cell-based organoid technology. The remaining authors declare no competing interests.

References

1. Pui, C. H., Gajjar, A. J., Kane, J. R., Qaddoumi, I. A. & Pappo, A. S. Challenging issues in pediatric oncology. Nat. Rev. Clin. Oncol. 8, 540–549 (2011).

2. Siegel, R. L., Miller, K. D. & Jemal, A. Cancer statistics, 2016. CA Cancer J. Clin. 66, 7–30 (2016).

3. Breslow, N., Olshan, A., Beckwith, J. B. & Green, D. M. Epidemiology of Wilms tumor. Med Pediatr. Oncol. 21, 172–181 (1993).

4. Gooskens, S. L. et al. Congenital mesoblastic nephroma 50 years after its recognition: a narrative review. Pediatr. Blood Cancer 64, e26437 (2017).

5. van den Heuvel-Eibrink, M. M. et al. Position paper: rationale for the treatment of Wilms tumor in the UMBRELLA SIOP-RTSG 2016 protocol. Nat. Rev. Urol. 14, 743–752 (2017).

6. Gooskens, S. L. et al. Position paper: Rationale for the treatment of children with CCSK in the UMBRELLA SIOP-RTSG 2016 protocol. Nat. Rev. Urol. 15, 309–319 (2018).

7. Brok, J., Treger, T. D., Gooskens, S. L., van den Heuvel-Eibrink, M. M. & Pritchard-Jones, K. Biology and treatment of renal tumors in childhood. Eur. J. Cancer 68, 179–195 (2016).

8. Pritchard-Jones, K. et al. Treatment and outcome of Wilms' tumor patients: an analysis of all cases registered in the UKW3 trial. Ann. Oncol. 23, 2457–2463 (2012).

9. Rivera, M. N. & Haber, D. A. Wilms' tumor: connecting tumorigenesis and organ development in the kidney. Nat. Rev. Cancer 5, 699–712 (2005).

10. Maiti, S., Alam, R., Amos, C. I. & Huff, V. Frequent association of β-cateninR and WT1 mutations in Wilms tumors. Cancer Res. 60, 6288–6292 (2000).

11. Ruteshouser, E. C., Robinson, S. M. & Huff, V. Wilms tumor genetics: mutations in WT1, WTX, and CTNNB1 account for only about one-third of tumors. Genes, Chromosomes Cancer 47, 461–470 (2008).

12. Walz, A. L. et al. Recurrent DGCR8, DROSHA, and SIX homeodomain mutations in favorable histology Wilms tumors. Cancer Cell 27, 286–297 (2015).

13. Wegert, J. et al. Mutations in the SIX1/2 pathway and the DROSHA/DGCR8 miRNA microprocessor complex underlie high-risk blastemal type Wilms tumors. Cancer Cell 27, 298–311 (2015).

14. Hawthorn, L. & Cowell, J. K. Analysis of wilms tumors using SNP mapping array-based comparative genomic hybridization. PLoS One 6, e18941 (2011).

15. Mengelbier, L. H. et al. Deletions of 16q in Wilms tumors localize to blastemal-anaplastic cells and are associated with reduced expression of the IRXB renal tubulogenesis gene cluster. Am. J. Pathol. 177, 2609–2621 (2010).

16. Hing, S. et al. Gain of 1q is associated with adverse outcome in favorable histology Wilms' tumors. Am. J. Pathol. 158, 393–398 (2001).

17. Gadd, S. et al. A Children's Oncology Group and TARGET initiative exploring the genetic landscape of Wilms tumor. Nat. Genet. 49, 1487–1494 (2017).

18. Jackson, E. M. et al. Genomic analysis using high-density single nucleotide polymorphism-based oligonucleotide arrays and multiplex ligation-dependent probe amplification provides a comprehensive analysis of INI1/SMARCB1 in malignant rhabdoid tumors. Clin. Cancer Res. 15, 1923–1930 (2009).

19. Song, H. C. et al. Biological characteristics of pediatric renal cell carcinoma associated with Xp11.2 translocations/TFE3 gene fusions. J. Pediatr. Surg. 49, 539–542 (2014).

20. Royer-Pokora, B. Genetics of pediatric renal tumors. Pediatr. Nephrol. 28, 13–23 (2013).

21. Drost, J. & Clevers, H. Organoids in cancer research. Nat. Rev. Cancer https: // doi.org/10.1038/s41568-018-0007-6 (2018).

22. Sato, T. et al. Single Lgr5 stem cells build crypt-villus structures in vitro without a mesenchymal niche. Nature 459, 262–265 (2009).

23. Sato, T. et al. Long-term expansion of epithelial organoids from human colon, adenoma, adeno-carcinoma, and Barrett's epithelium. Gastroenterology 141,1762–1772 (2011).

24. Gao, D. et al. Organoid cultures derived from patients with advanced prostate cancer. Cell 159, 176–187 (2014).

25. Boj, S. F. et al. Organoid models of human and mouse ductal pancreatic cancer. Cell 160, 324–338 (2015).

26. Huang, L. et al. Ductal pancreatic cancer modeling and drug screening using human pluripotent stem cell- and patient-derived tumor organoids. Nat. Med. 21, 1364–1371 (2015).

27. Broutier, L. et al. Human primary liver cancer-derived organoid cultures for disease modeling and drug screening. Nat. Med. https://doi.org/10.1038/nm.4438 (2017).

28. Nanki, K. et al. Divergent routes toward Wnt and R-spondin niche independency during human gastric carcinogenesis. Cell 174, 856–869 e817 (2018).

29. Yan, H. H. N. et al. A comprehensive human gastric cancer organoid biobank captures tumor sub-type heterogeneity and enables therapeutic screening. Cell Stem Cell https://doi.org/10.1016/j.stem.2018.09.016 (2018).

30. Sachs, N. et al. A living biobank of breast cancer organoids captures disease heterogeneity. Cell https://doi.org/10.1016/j.cell.2017.11.010 (2017).

31. Schutte, M. et al. Molecular dissection of colorectal cancer in pre-clinical models identifies bio-markers predicting sensitivity to EGFR inhibitors. Nat.Commun. 8, 14262, https://doi.org/10.1038/ncomms14262 (2017).

32. Pauli, C. et al. Personalized in vitro and in vivo cancer models to guide precision medicine. Cancer Discov. 7, 462–477 (2017).

33. van de Wetering, M. et al. Prospective derivation of a living organoid biobank of colorectal cancer patients. Cell 161, 933–945 (2015).

34. Fujii, M. et al. A colorectal tumor organoid library demonstrates progressive loss of niche factor requirements during tumorigenesis. Cell Stem Cell 18, 827–838 (2016).

35. Vlachogiannis, G. et al. Patient-derived organoids model treatment response of metastatic gas-trointestinal cancers. Science 359, 920–926 (2018).

36. Schutgens, F. et al. Tubuloids derived from human adult kidney and urine for personalized disease modeling. Nat. Biotechnol. 37, 303 (2019).

37. Watanabe, K. et al. A ROCK inhibitor permits survival of dissociated human embryonic stem cells. Nat. Biotechnol. 25, 681 (2007).

38. Scott, J. et al. Insulin-like growth factor-II gene expression in Wilms' tumor and embryonic tissues. Nature 317, 260–262 (1985).

39. Sehic, D., Ciornei, C. D. & Gisselsson, D. Evaluation of CITED1, SIX1, and CD56 protein expression for identification of blastemal elements in Wilms tumor. Am. J. Clin. Pathol. 141, 828–833 (2014).

40. Dekkers, J. F. et al. High-resolution 3D imaging of fixed and cleared organoids. Nat. Protoc. 14, 1756–1771 (2019).

41. Sigauke, E. et al. Absence of expression of SMARCB1/INI1 in malignant rhabdoid tumors of the central nervous system, kidneys and soft tissue: an immunohistochemical study with implica-tions for diagnosis. Mod. Pathol. 19,717–725 (2006).

42. Judkins, A. R., Mauger, J., Ht, A., Rorke, L. B. & Biegel, J. A. Immunohistochemical analysis of hSNF5/INI1 in pediatric CNS neoplasms. Am. J. Surg. Pathol. 28, 644–650 (2004).

43. Natrajan, R. et al. Array CGH profiling of favourable histology Wilms tumors reveals novel gains and losses associated with relapse. J. Pathol. 210, 49–58 (2006).

44. Young, E. E., Brown, C. T., Merguerian, P. A. & Akhavan, A. Pediatric and adolescent renal cell carci-noma. Urol. Oncol. 34, 42–49 (2016).

45. Grobner, S. N. et al. The landscape of genomic alterations across childhood cancers. Nature 555, 321–327 (2018).

46. Alexandrov, L. B. et al. Signatures of mutational processes in human cancer. Nature 500, 415–421 (2013).

47. Alexandrov, L. B., Nik-Zainal, S., Wedge, D. C., Campbell, P. J. & Stratton, M. R. Deciphering signatures of mutational processes operative in human cancer. Cell Rep. 3, 246–259 (2013).

48. Ma, X. et al. Pan-cancer genome and transcriptome analyses of 1,699 pediatric leukaemias and solid tumors. Nature 555, 371–376 (2018).

49. Alexandrov, L. B. et al. The repertoire of mutational signatures in human cancer. Nature 578, 94–101 (2020).

50. Gadd, S. et al. Clinically relevant subsets identified by gene expression patterns support a re-vised ontogenic model of Wilms tumor: a Children's Oncology Group Study. Neoplasia 14, 742–756 (2012).

51. Joshi, V. V., Banerjee, A. K., Yadav, K. & Pathak, I. C. Cystic partially differentiated nephroblastoma: a clinicopathologic entity in the spectrum of infantile renal neoplasia. Cancer 40, 789–795 (1977).

52. Slade, I. et al. DICER1 syndrome: clarifying the diagnosis, clinical features and management im-plications of a pleiotropic tumor predisposition syndrome. J. Med. Genet. 48, 273–278 (2011).

53. Wu, M. K. et al. Biallelic DICER1 mutations occur in Wilms tumors. J.Pathol. 230, 154–164 (2013).

54. Doros, L. A. et al. DICER1 mutations in childhood cystic nephroma and its relationship to DI-CER1-renal sarcoma. Mod. Pathol. 27, 1267–1280 (2014).

55. Dome, J. S. et al. High telomerase RNA expression level is an adverse prognostic factor for favor-able-histology Wilms' tumor. J. Clin. Oncol. 23, 9138–9145 (2005).

56. Wegert, J. et al. Characterization of primary Wilms tumor cultures as an in vitro model. Genes, Chromosomes Cancer 51, 92–104 (2012).

57. Malouf, G. G. et al. Genomic heterogeneity of translocation renal cell carcinoma. Clin. Cancer Res. 19, 4673–4684 (2013).

58. Chun, H. E. et al. Identification and analyses of extra-cranial and cranial rhabdoid tumor molecular subgroups reveal tumors with cytotoxic T cell infiltration. Cell Rep. 29, 2338–2354 e2337 (2019).

59. Roerink, S. F. et al. Intra-tumor diversification in colorectal cancer at the single-cell level. Nature 556, 457–462 (2018).

60. Bardeesy, N. et al. Anaplastic Wilms' tumor, a subtype displaying poor prognosis, harbours p53 gene mutations. Nat. Genet. 7, 91–97 (1994).

61. Ooms, A. H. et al. Significance of TP53 mutation in Wilms tumors with diffuse anaplasia: a report from the Children's Oncology Group. Clin. Cancer Res. 22, 5582–5591 (2016).

62. Wegert, J. et al. TP53 alterations in Wilms tumor represent progression events with strong in-tratumor heterogeneity that are closely linked but not limited to anaplasia. J. Pathol. Clin. Res. 3, 234–248 (2017).

63. Drost, J. et al. Sequential cancer mutations in cultured human intestinal stem cells. Nature 521, 43–47 (2015).

64. Cresswell, G. D. et al. Intra-tumor genetic heterogeneity in Wilms tumor: clonal evolution and clinical implications. eBioMedicine 9, 120–129 (2016).

65. Karlsson, J. et al. Four evolutionary trajectories underlie genetic intratumoral variation in childhood cancer. Nat. Genet. 50, 944–950 (2018).

66. Weeber, F. et al. Preserved genetic diversity in organoids cultured from biopsies of human colorectal cancer metastases. Proc. Natl Acad. Sci. USA 112,13308–13311 (2015).

67. Kopper, O. et al. An organoid platform for ovarian cancer captures intra- and interpatient heterogeneity. Nat. Med. 25, 838–849 (2019).

68. Ohlund, D. et al. Distinct populations of inflammatory fibroblasts and myofibroblasts in pancreatic cancer. J. Exp. Med. 214, 579–596 (2017).

69. Seino, T. et al. Human Pancreatic tumor organoids reveal loss of stem cell niche factor dependence during disease progression. Cell Stem Cell https://doi.org/10.1016/j.stem.2017.12.009 (2018).

70. Dijkstra, K. K. et al. Generation of tumor-reactive T cells by co-culture of peripheral blood lymphocytes and tumor organoids. Cell 174, 1586–1598 e1512 (2018).

71. Drost, J. et al. Organoid culture systems for prostate epithelial and cancer tissue. Nat. Protoc. 11, 347–358 (2016).

72. Li, H. & Durbin, R. Fast and accurate long-read alignment with Burrows-Wheeler transform. Bioinformatics 26, 589–595 (2010).

73. Blokzijl, F. et al. Tissue-specific mutation accumulation in human adult stem cells during life. Nature 538, 260–264 (2016).

74. DePristo, M. A. et al. A framework for variation discovery and genotyping using next-generation DNA sequencing data. Nat. Genet. 43, 491–498 (2011).

75. Boeva, V. et al. Control-FREEC: a tool for assessing copy number and allelic content using next-generation sequencing data. Bioinformatics 28, 423–425 (2012).

76. Nilsen, G. et al. Copynumber: efficient algorithms for single- and multi-track copy number segmentation. BMC Genomics 13, 591 (2012).

77. Blokzijl, F., Janssen, R., van Boxtel, R. & Cuppen, E. MutationalPatterns: comprehensive genome-wide analysis of mutational processes. Genome Med.10, 33 (2018).

78. Johann, P. D. et al. Atypical teratoid/rhabdoid tumors are comprised of three epigenetic subgroups with distinct enhancer landscapes. Cancer Cell 29, 379–393 (2016).

79. Muraro, M. J. et al. A single-cell transcriptome atlas of the human pancreas. Cell Syst. 3, 385–394 e383 (2016).

80. Candelli, T. et al. Sharq, A versatile preprocessing and QC pipeline for Single Cell RNA-seq. BioRxiv, 2018.

81. Butler, A., Hoffman, P., Smibert, P., Papalexi, E. & Satija, R. Integrating single cell transcriptomic data across different conditions, technologies, and species. Nat. Biotechnol. 36, 411–420 (2018).

82. Kowalczyk, M. S. et al. Single-cell RNA-seq reveals changes in cell cycle and differentiation programs upon aging of hematopoietic stem cells. Genome Res. 25, 1860–1872 (2015).

83. Lun, A. T., McCarthy, D. J. & Marioni, J. C. A step-by-step workflow for low level analysis of single-cell RNA-seq data with Bioconductor. F1000Res 5, 2122 (2016).

84. Yu, G., Wang, L. G., Han, Y. & He, Q. Y. clusterProfiler: an R package for comparing biological themes among gene clusters. OMICS 16, 284–287 (2012).

85. Aran, D. et al. Reference-based analysis of lung single-cell sequencing reveals a transitional profibrotic macrophage. Nat. Immunol. 20, 163–172 (2019).

Supplementary Information
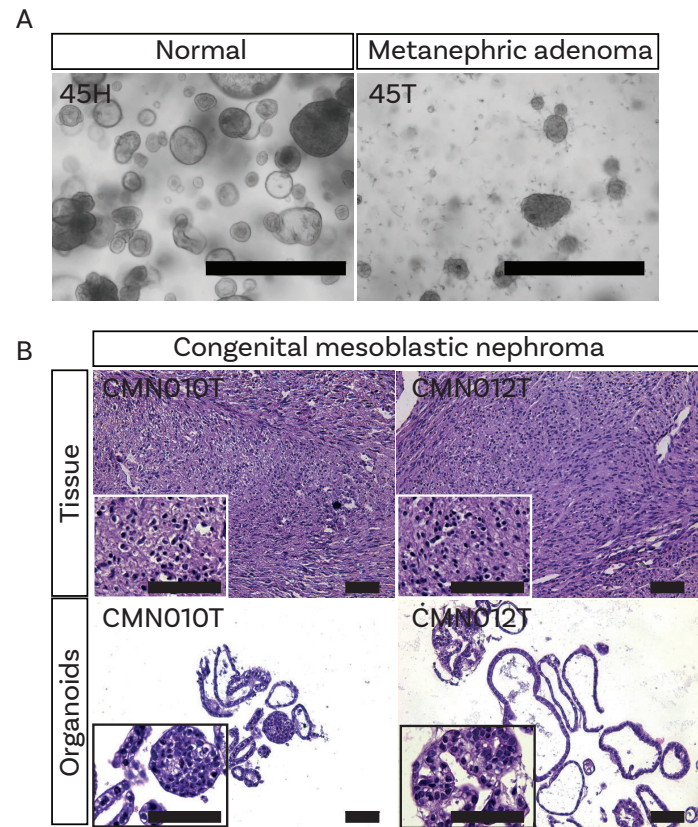
Supplementary Figure 1. Phenotypic characterization of pediatric kidney cancer organoids. A. Representative brightfield microscopy images of normal kidney tissue-derived organoids and matching metanephric adenoma organoids (n=3). Scale bar: 1mm. **B.** H&E staining on tissue (top) and matching organoids (bottom) derived of two congenital mesoblastic nephromas (n=3). Scale bars: 100 μm.
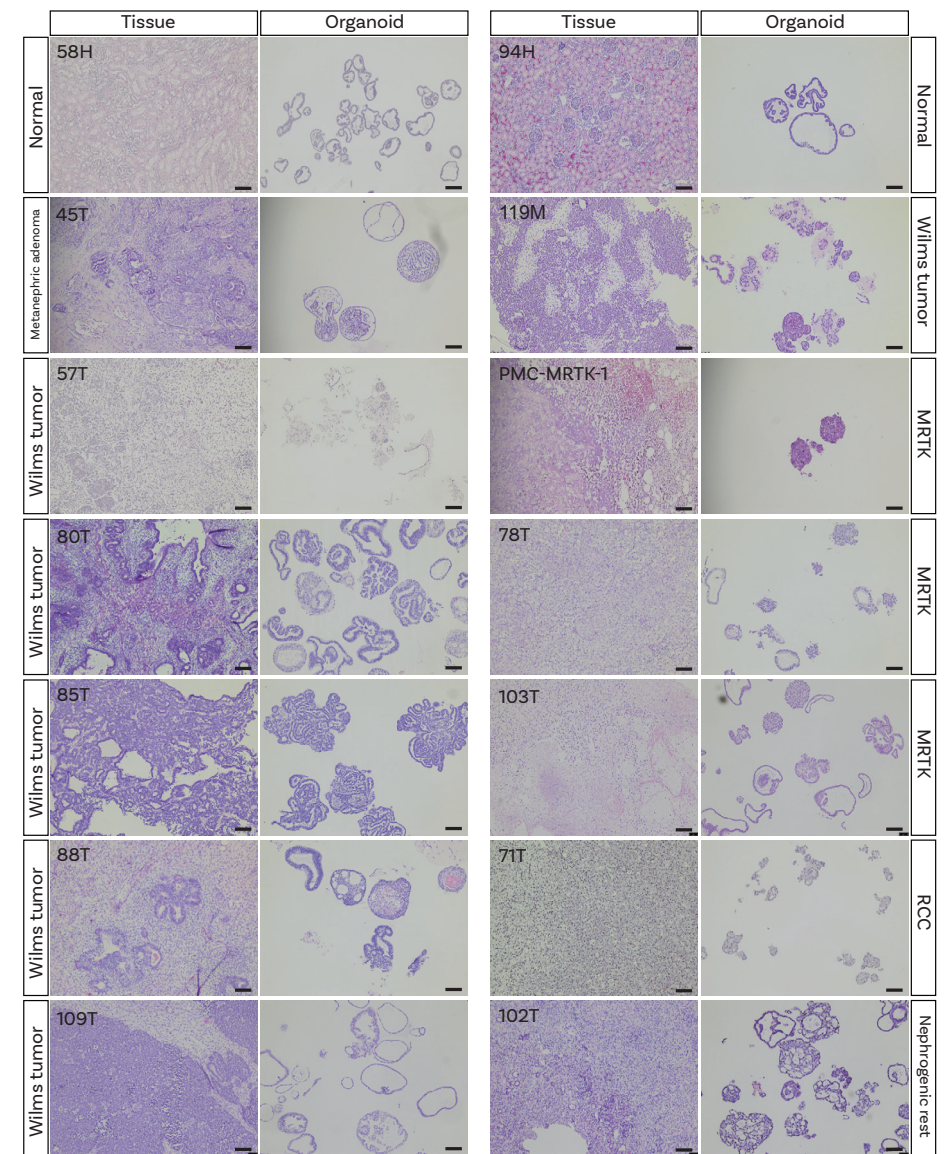
Supplementary Figure 2. Histology of pediatric kidney cancer organoid lines resembles primary tumor tissue. H&E staining on tissue (left panels) and matching organoids (right panels) derived of the indicated tumor types (n=3). Additional cases can be found in Figure 2A and Supplementary Figure 1B. H, healthy; T, primary tumor; M, metastasis. Scale bars: 100 μm.
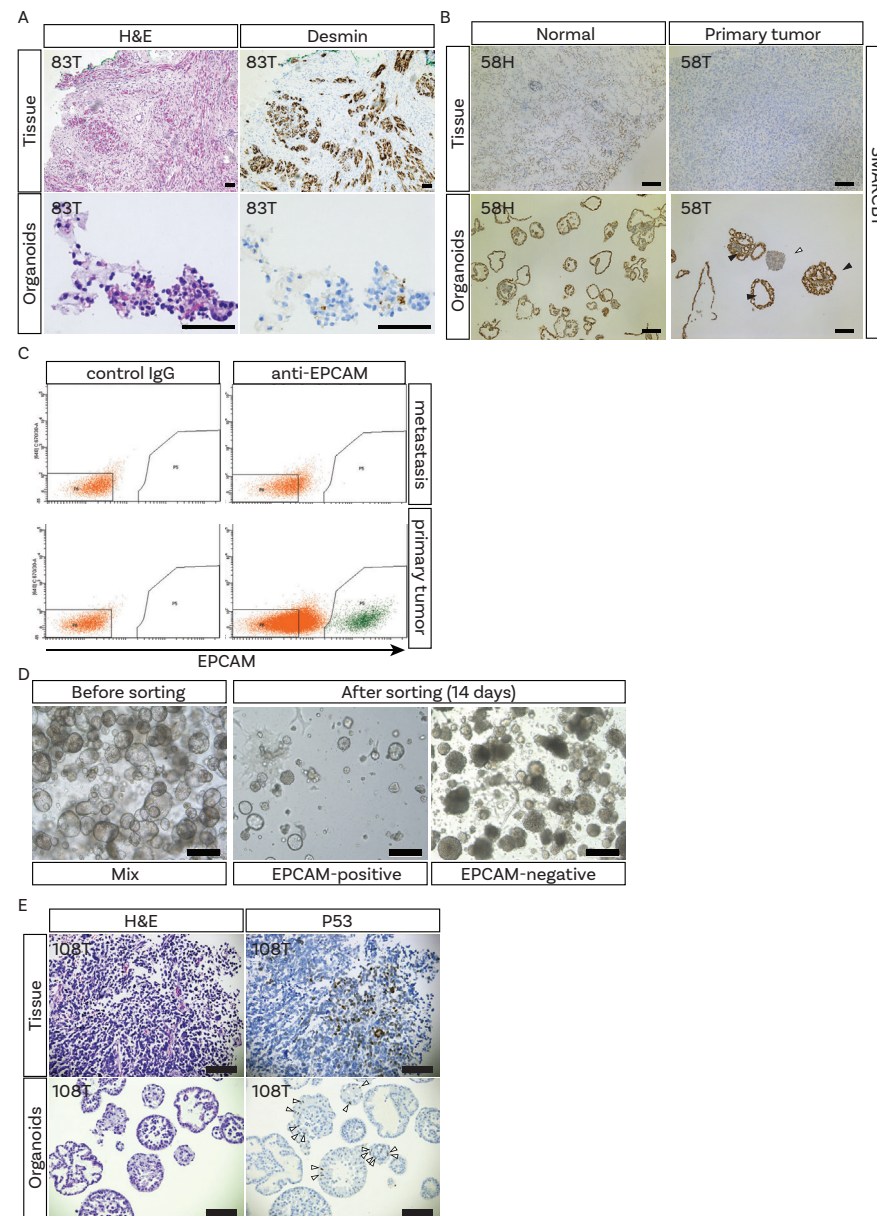
Supplementary Figure 3. Confirmation of tumor origin of organoids. A. Representative H&E (left) and desmin (right) stainings on a Wilms tumor (tissue (top) and organoids (bottom)) with rhabdomyomatous differentiation (n=3). Scale bars: 50 µm. **B.** SMARCB1 stainings on normal kidney (left) and MRTK tumor (right) tissue (top) and organoids derived thereof (bottom), demonstrating the presence of SMARCB1-positive normal kidney tissue-derived organoids in the tumor organoid culture (n=3). Of note, immune cells stain positive for SMARCB1 in MRTK tissue. Open arrowhead indicates SMARCB1-negative MRTK organoids; closed arrowheads indicate SMARCB1-positive normal kidney organoids. Scale bars: 100 µm. **C.** EPCAM-negative MRTK cells are purified from a mixed culture (Supplementary Figure 3B) using FACS. Gating strategy are exemplified in Supplementary Figure 13A. **D.** Representative brightfield microscopy images of MRTK organoid cultures before (left) and after FACS-purification of EPCAM-positive (middle) and -negative (right) cells (n=2). Scale bar: 200 µm. **E.** H&E (left) and P53 (right) on an RCC expressing mutant P53 (n=3). Arrowheads indicate several P53-positive nuclei. Scale bars: 100 µm.
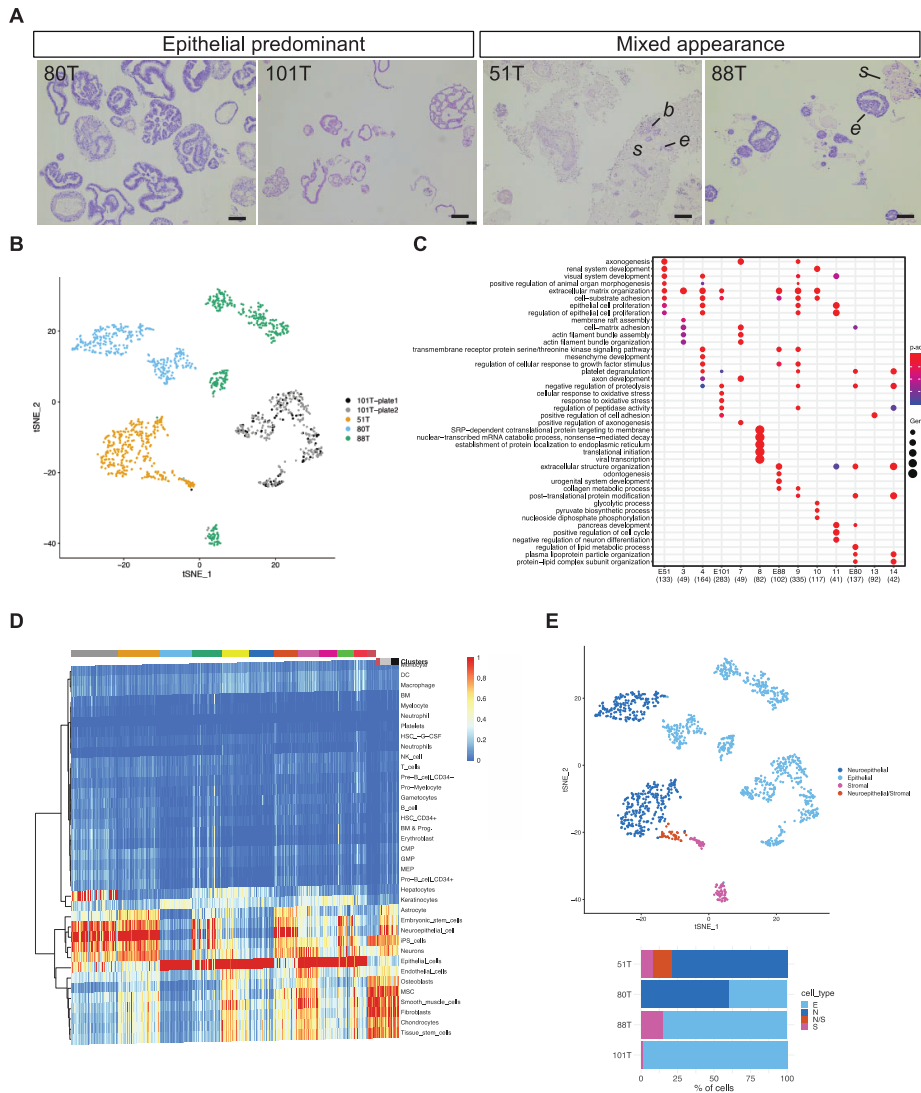
Supplementary Figure 4. Cellular heterogeneity within Wilms tumor organoid cultures. A. H&E staining on the four Wilms tumor organoid cultures that were used for the scRNAseq experiment. Two predominantly epithelial cultures (80T, 101T) and two with apparent different cell types (51T, 88T) b, blastemal; e, epithelial; s, stromal (n=3). Scale bars: 100 μm. **B.** t-SNE representation of single cells from four Wilms tumor organoid lines (51T, 80T, 88T, 101T). Cells are colored by plate of origin. For one organoid (101T), cells were sorted in two plates, which were processed separately. Cells from these two plates cluster together, thereby excluding technical batch effects. **C.** Gene Ontology- Biological Process (GO BP) enrichment analysis of higher expressed genes between organoid source or cell population, as shown in Figure 3A. The Benjamini-Hochberg adjusted p-value levels are color-coded, while the size of the dots represents the ratio of differentially expressed genes belonging to the specific GO BP term. **D.** Unbiased cell type identification with SingleR classification using the Human Primary Cell Atlas Reference. Heatmap showing the Spearman correlation scores of the expression profile of every single cell with that of each reference sample. The four major cell types present in the dataset are: Neuroepithelial cells, epithelial cells, and a stromal component consisting of MSC, fibroblasts, chondrocytes, and smooth muscle cells. **E.** t-SNE map showing the four major cell types and a bar plot depicting the fraction cell types for each organoid.
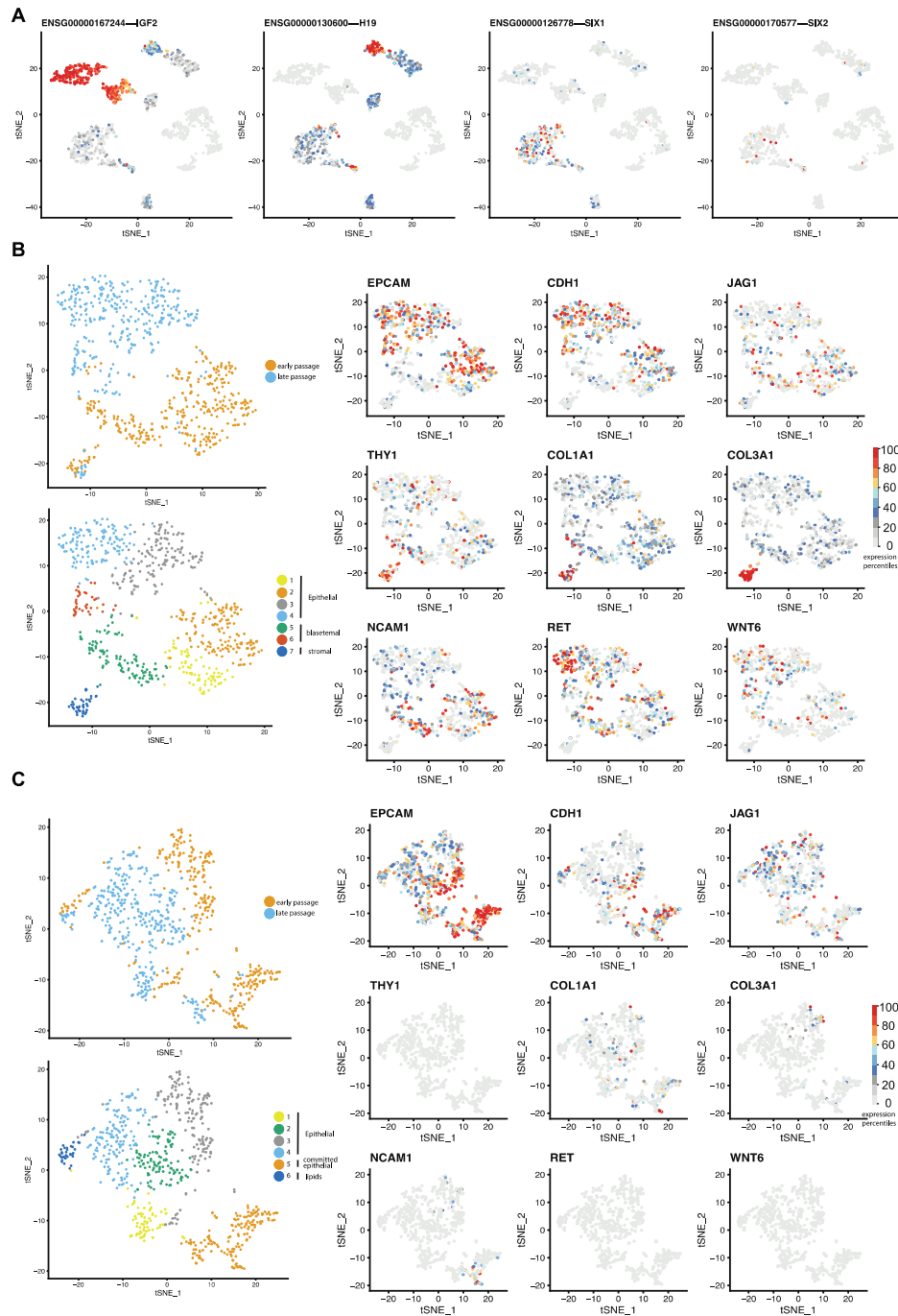
Supplementary Figure 5. Different cell types in Wilms tumor organoids can be retained over time. A. Additional t-SNE maps showing the color-coded logged expression levels of several markers demonstrating that different cell types are present in 51T and 88T, whereas 80T and 101T organoids primarily consist of different epithelial sub-populations, which is in line with their histological appearance (additionally see Figure 3B and Supplementary Figure 4). **B.** and **C.** t-SNE representation of single cells from two different passages (early and late (5 – 6 passages in between, representing approximately 3 months of culturing)) of two Wilms tumor organoid lines (51T (B), 80T (C)). Cells are color-coded by early/late passage (top left) or clustering results (bottom left). t-SNE maps showing the color-coded logged expression levels of several markers (right panels) for each population demonstrating that different cell types are retained over time. For instance, population number 7 in 51T consists of early as well as late passage cells. These results are in line with the FACS experiments for different cell types (Supplementary Figure 6A).
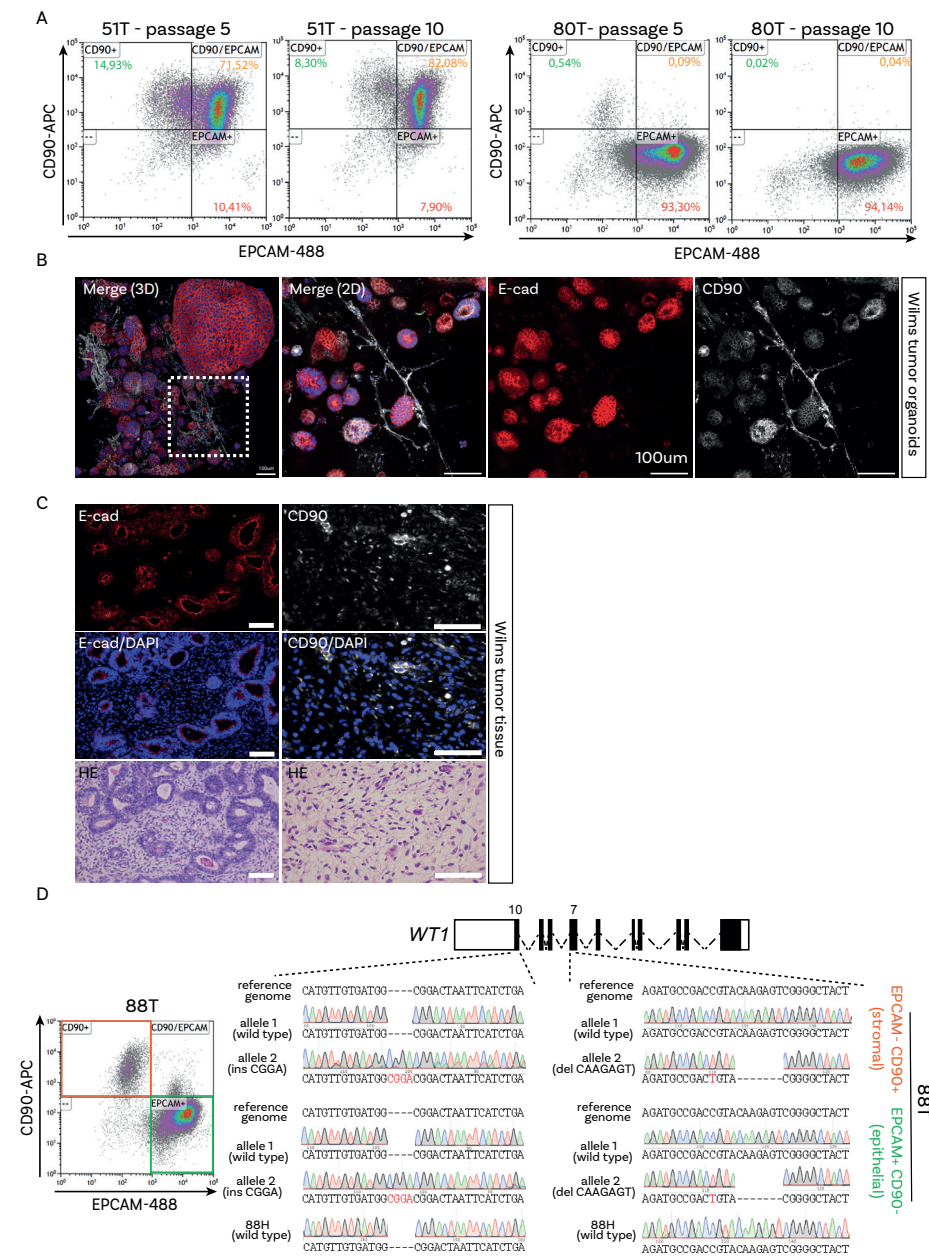
Supplementary Figure 6. Cellular heterogeneity within Wilms tumor organoid cultures visualized with high resolution 3D imaging. A. FACS analyses of two different passages (early and late (5 passages in between, representing approximately 3 months of culturing)) of two Wilms tumor organoid lines (51T (tri-phasic), 80T (epithelial predominant). EPCAM (epithelial marker) and CD90 (THY1, stromal marker) were used to quantify epithelial (EPCAM single positive), stromal (CD90 single positive, and "blastemal"-like cells (expressing both markers (i.e. EPCAM/CD90 double positive)). Gating strategy are exemplified in Supplementary Figure 13B. **B.** High resolution 3D imaging of 88T Wilms tumor organoids (containing stromal cells based on scRNA-seq (Figure 3A,B) immunolabeled for E-cadherin (E-cad; red) and CD90 (white) (n=2). Scale bars, 100 µm (left panel) and 50 µm (other panels). **C.** Immunofluorescence imaging on 88T Wilms tumor tissue sections immunolabeled for E-cadherin (E-cad; red), CD90 (white), and DAPI (blue) (n=2). Scale bars 100 µm. **D.** Based on marker expression, epithelial (EPCAM-positive) and stromal (CD90-positive) cells were purified using FACS from 88T (left panel). Purified populations were subsequently genotyped for the presence of *WT1* mutations (as revealed by WGS on bulk organoid culture and matching tumor tissue (Figure 4A)). *WT1* (exon 7, exon 10) mutations are present in epithelial as well as stromal cells, thereby demonstrating that both are tumor cells. *WT1* mutations are absent in matching normal kidney-derived organoids (88H, bottom).
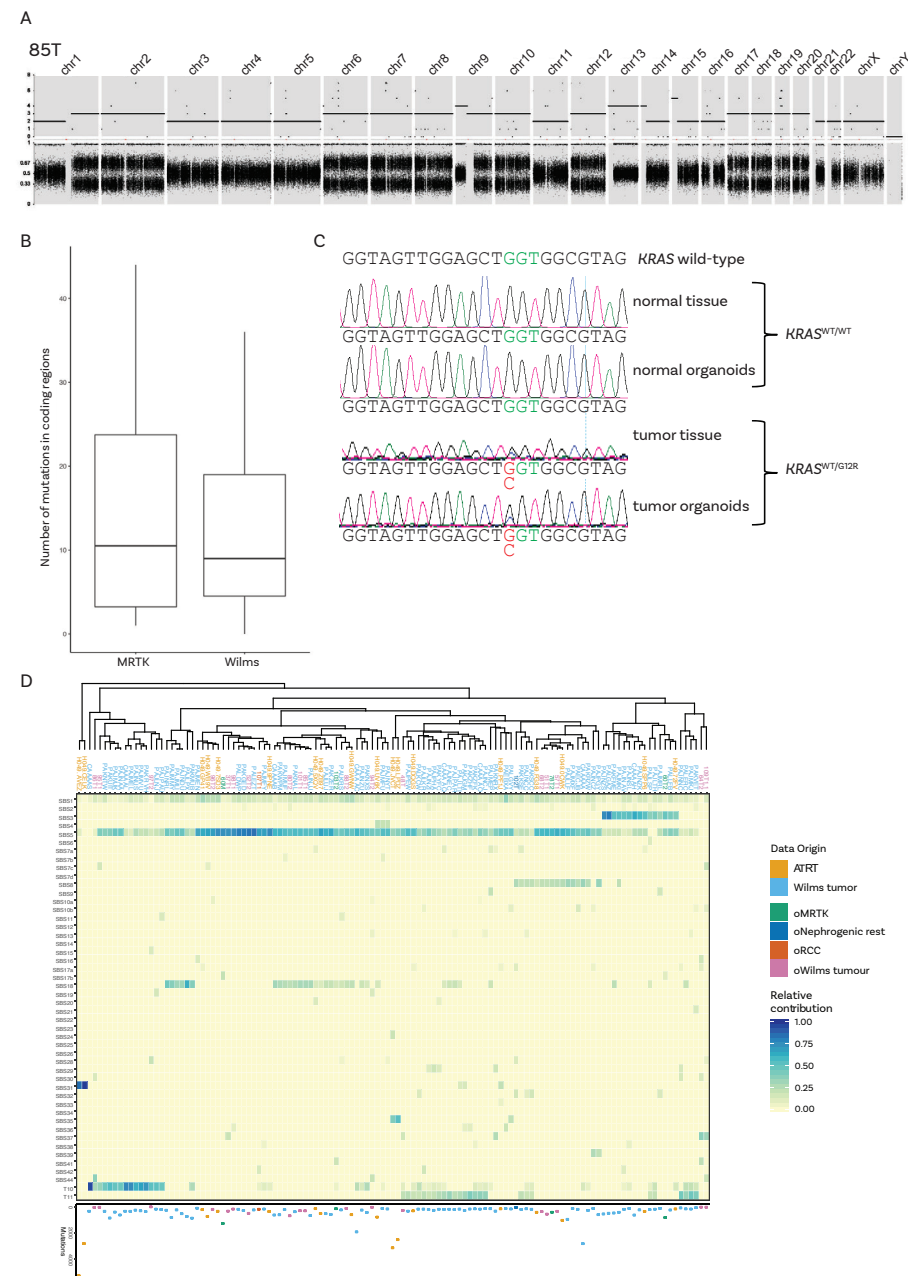
Supplementary Figure 7. Genetic characterization of pediatric kidney cancer organoids. A. Example of copy number alteration (top) and B Allele Frequency (BAF) plots (bottom) for one of the Wilms tumor organoid lines (85T). **B.** Boxplot depicting the average number of mutations in coding regions in all primary tumor-derived MRTK (left) and Wilms tumor (right) organoids. MRTK: minima=1, maxima=44, mean=16.5, 1st Qu=3.25, 3rd Qu=23.75, highest whisker =44, lower whisker =1. Wilms: minima=0, maxima=36, mean=12.28, 1st Qu=4.5, 3rd Qu=19, highest whisker =36, lower whisker =0. **C.** Targeted amplification and subsequent Sanger sequencing of part of the *KRAS* gene reveals a heterozygous *KRASG12R* mutation in metanephric adenoma tissue and organoids derived thereof. This mutation is absent in matching normal tissue and organoids. **D.** Hierarchical clustering of samples based on the relative contributions of signatures (top, dendrogram), the relative contributions of the COSMIC signatures (middle, heatmap) and the mutation load in each sample (bottom, dot plot). The colors of the sample names and dot plot indicate the cancer types (ATRT: atypical teratoid rhabdoid tumor, MRTK: malignant rhabdoid tumor of the kidney, RCC: renal cell carcinoma) with the preceding "o" indicating they are from organoids.
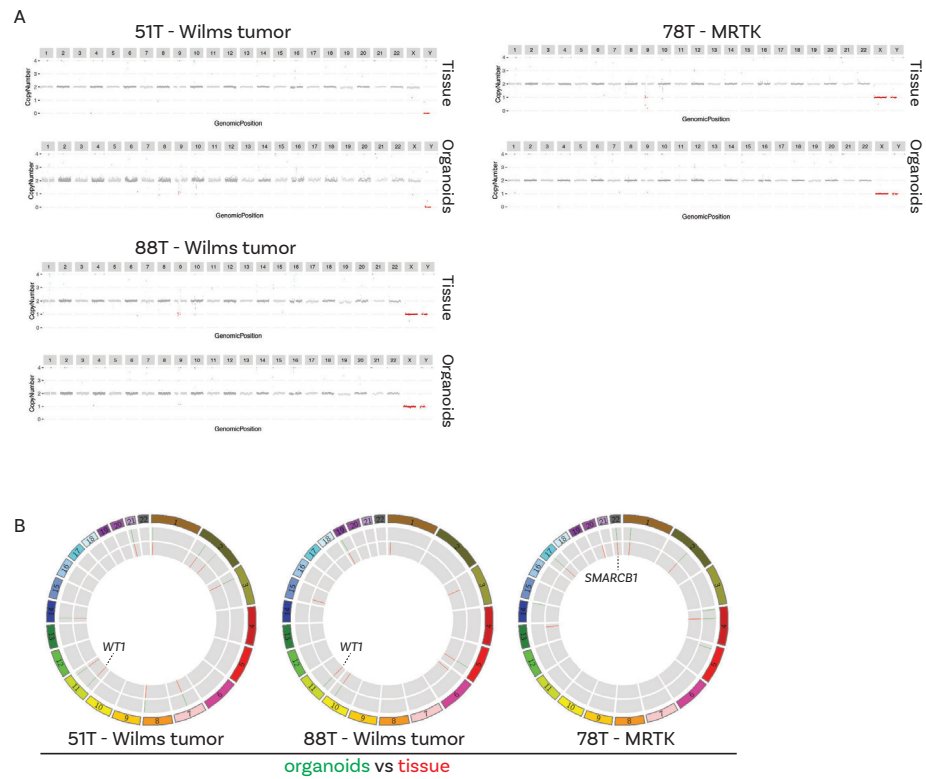
Supplementary Figure 8. Pediatric kidney cancer organoids reflect the genetic landscape of parental tumor tissues. A. Genome-wide CNAs (karyograms) and **B.** coding gene mutations (circos plots) in matching tumor tissue vs organoid pairs reveal that organoids recapitulate the genetic landscape of the tissue they were derived from.
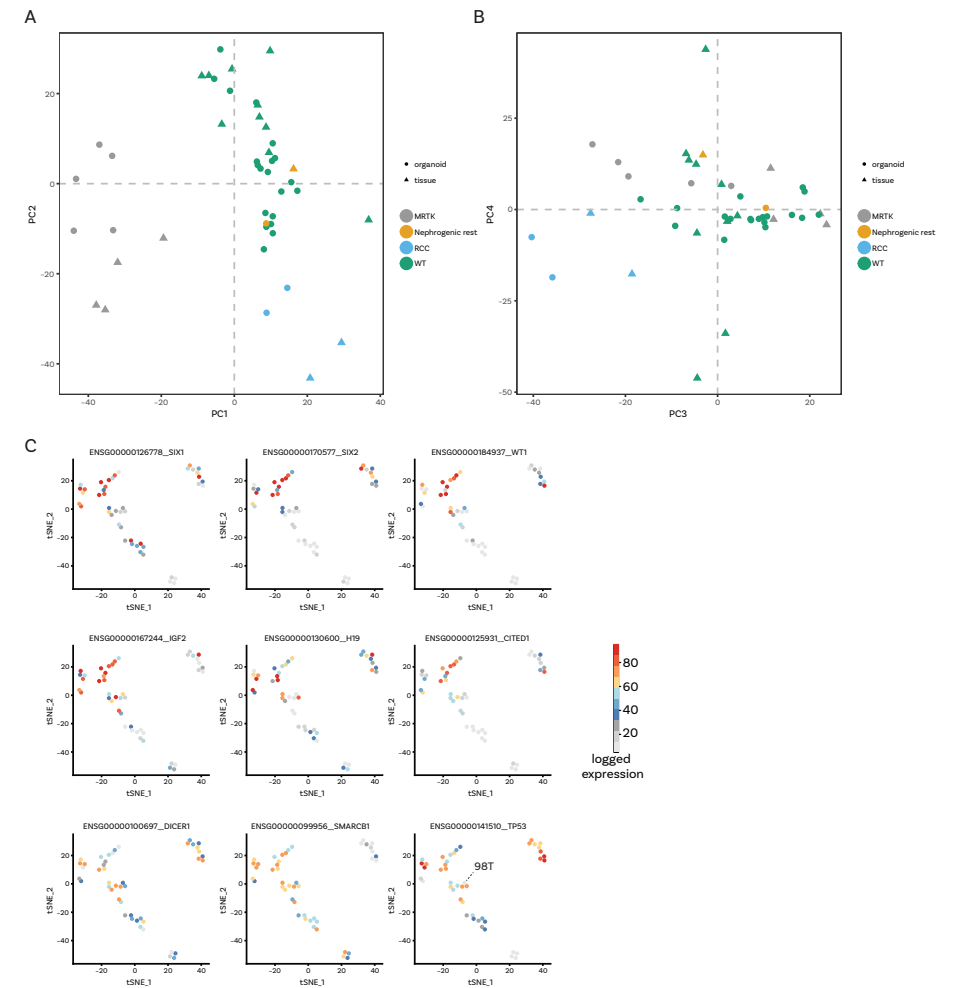
Supplementary Figure 9. Transcriptome profiling of pediatric kidney cancer organoids using RNA-seq. A., B. Principal component analysis of the tumor organoid and tissue samples without regressing batch effects separate growth conditions and tumor type. **C.** t-SNE maps, as in Figure 5A, showing expression levels of additional marker genes to the ones shown in Figure 5B.
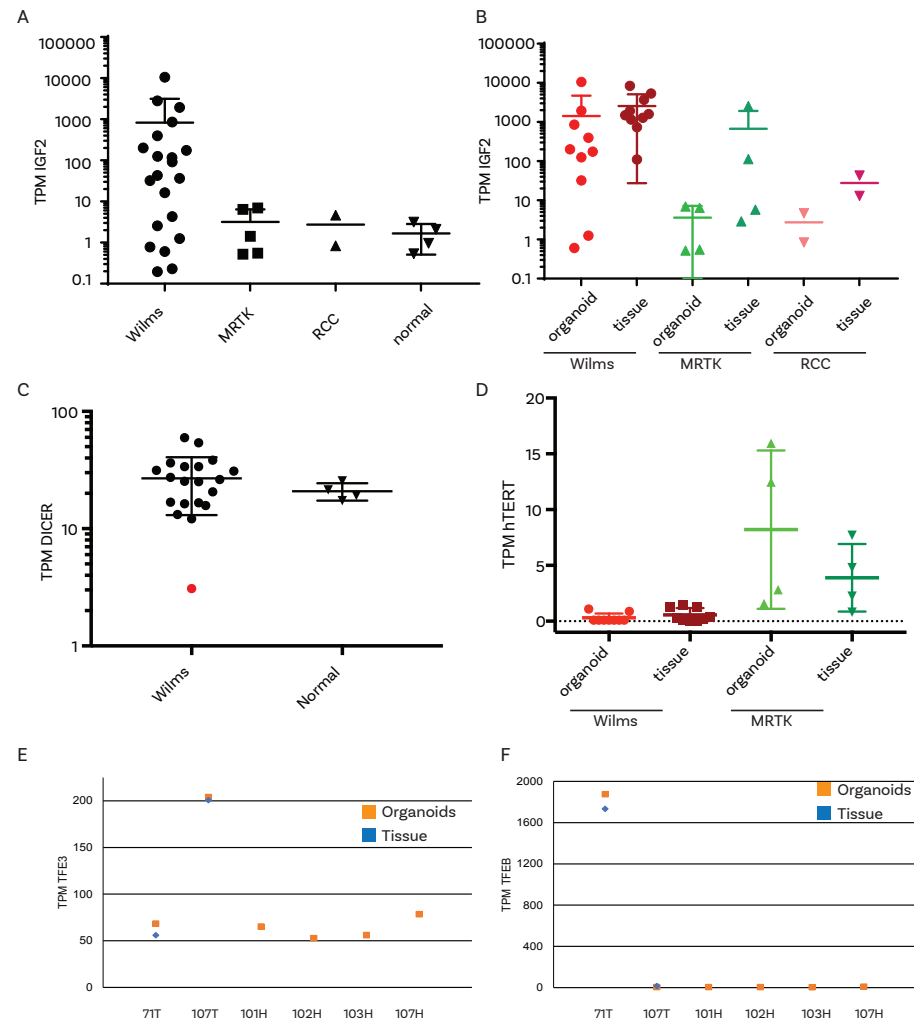
Supplementary Figure 10. RNA-seq reveals common gene expression profiles of pediatric kidney tumors. A. Normalized *IGF2* transcripts per million (TPM) values in the indicated pediatric kidney tumor organoids. Data are represented as mean values ± SD; for RCC group, data is represented as mean values (Wilms: n=21, MRTK: n=5, RCC: n=2, normal: n=4). **B.** Normalized *IGF2* TPM values in the indicated pediatric kidney tumor organoids and parental tumor tissues. Data are represented as mean values ± SD; for RCC organoid and tissue data are represented as mean values (Wilms organoid: n=10, MRTK organoid: n=4, RCC organoid: n=2, Wilms tissue: n=10, MRTK tissue: n=4, RCC tissue: n=2). **C.** Normalized *DICER1* TPM values in Wilms tumor and normal tissue-derived organoids. Red dot represents cystic Wilms tumor-derived organoid line (WT003T). Data are represented as mean values ± SD (Wilms: n=20, normal: n=4) **D.** As in B, but for *hTERT*. Data are represented as mean values ± SD (Wilms organoid: n=9, MRTK organoid: n=4, Wilms tissue: n=9, MRTK tissue: n=4). **E.** Normalized *TFE3* TPM values in the indicated pediatric tRCC-derived (71T, 107T) and normal tissue-derived organoids. **F.** Normalized *TFEB* TPM values in the indicated pediatric tRCC-derived (71T, 107T) and normal tissue-derived organoids.
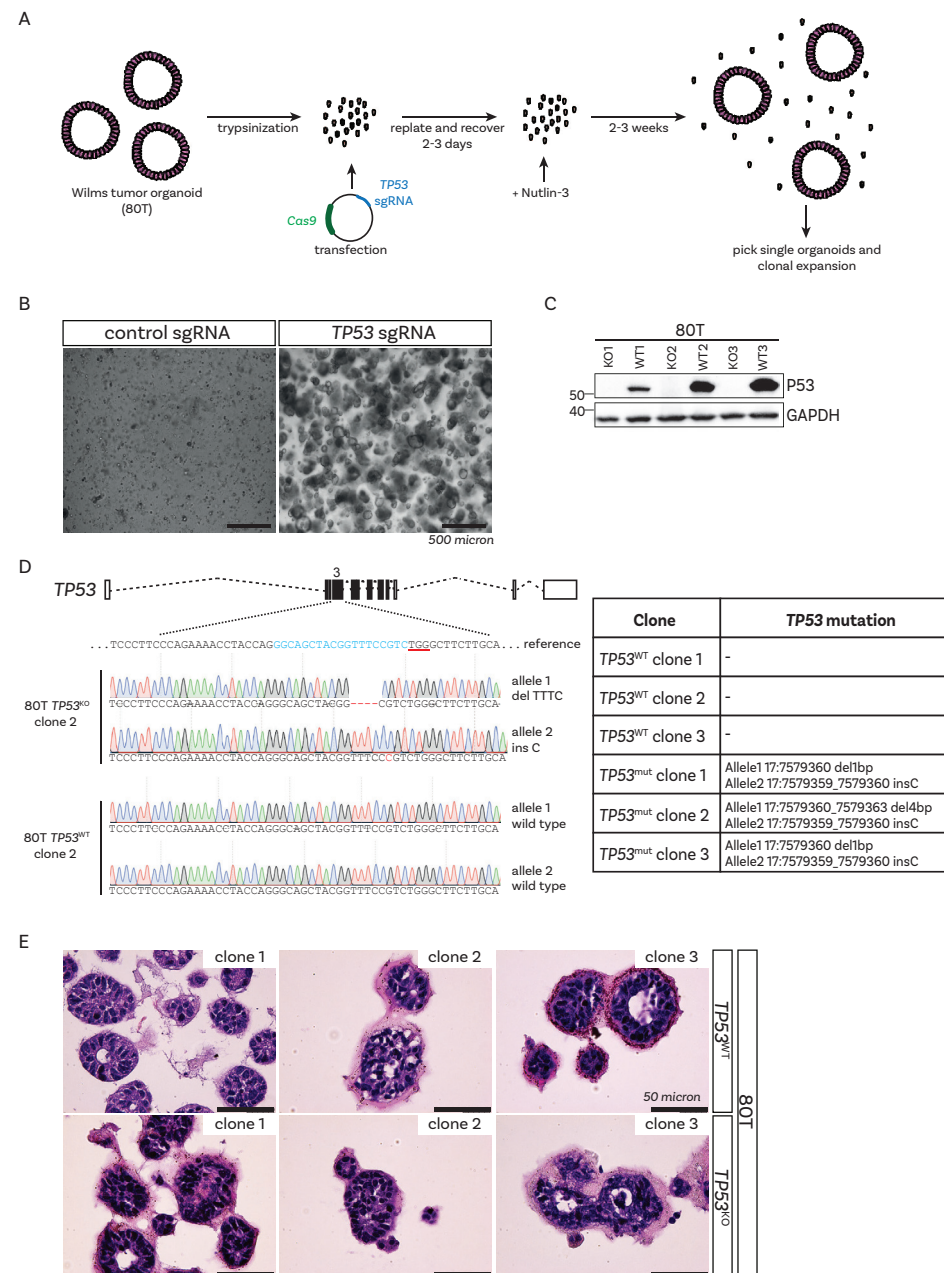
Supplementary Figure 11. Gene editing of Wilms tumor organoids. A. Scheme depicting the process of generating *TP53* mutant Wilms tumor organoids. **B.** Representative brightfield images of 80T Wilms tumor organoids transfected with either control sgRNA (left) or *TP53* sgRNA (right) and grown in medium containing nutlin-3 to select for *TP53* mutant cells. Scale bars 500 μm. **C.** Western blot analysis of P53 expression in clonally expanded 80T (TP53 wild-type (WT)) and 80T-TP53KO organoids. The experiment has been performed for three independent clones of each genotype (WT 1-3; KO 1-3). **D.** Sequence analysis of the targeted *TP53* exon. PCR amplification products of the mutated alleles were obtained using primers flanking the targeted exon. Subsequent sequencing revealed indels at the expected locations. PAM sequence is underlined in red in wild-type sequence. **E.** H&E staining on three independent 80T TP53 wild-type and three independent 80T-TP53KO clones. No apparent differences can be observed. Images are representative of n=2 independent experiments. Scale bars 50 μm.
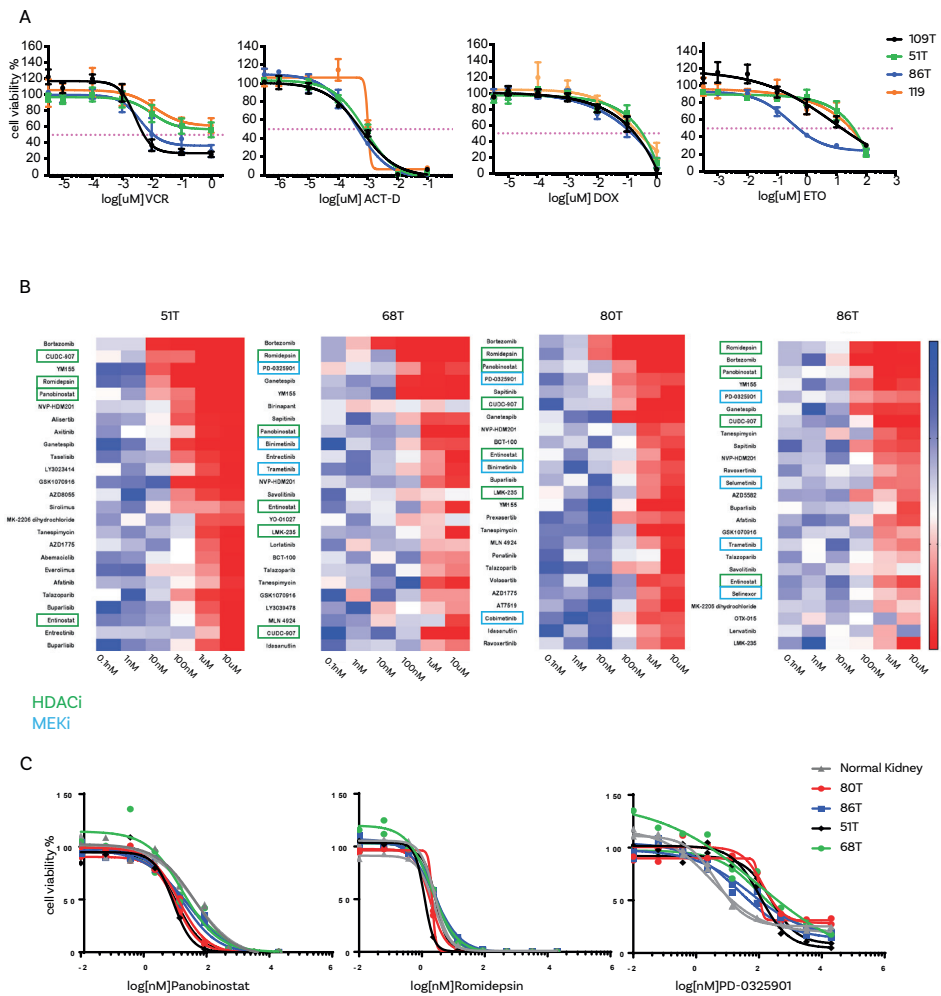
Supplementary Figure 12. Organoid drug screens reveal patient-specific drug sensitivities.
A. Dose-response curves of vincristine (VCR), actinomycin D (ACT-D), doxorubicin (DOX,), and etoposide (ETO) of the indicated Wilms tumor organoid lines. Error bars represent SEM of three independent experiments (each individual experiment includes technical quadruplicates). **B.** Compound screens (approximately 150 compounds) were performed on the indicated Wilms tumor organoid cultures. Depicted are the top 25 calculated area under the estimated dose-response curve (AUC) per organoid culture. Multiple MEK (blue) and HDAC (green) inhibitors are shared between the four cultures. Color scale blue to red indicates decreasing ATP levels relative to DMSO control. **C.** Dose-response curves of panobinostat, romidepsin, and PD-0325901 of the indicated Wilms tumor organoid lines. Curves with the same color represent independent experiments. Each individual point represents the average of quadruplicate measurements. **D.** H&E staining on an anaplastic Wilms tumor-derived organoid culture (98T) showing two anaplastic features: hyperchromatic nuclei (arrow) and enlarged nuclei (arrowhead). In addition, a mitotic figure is present (*). No atypical mitoses were detected (n=3). Scale bar: 50 μm.

A

B
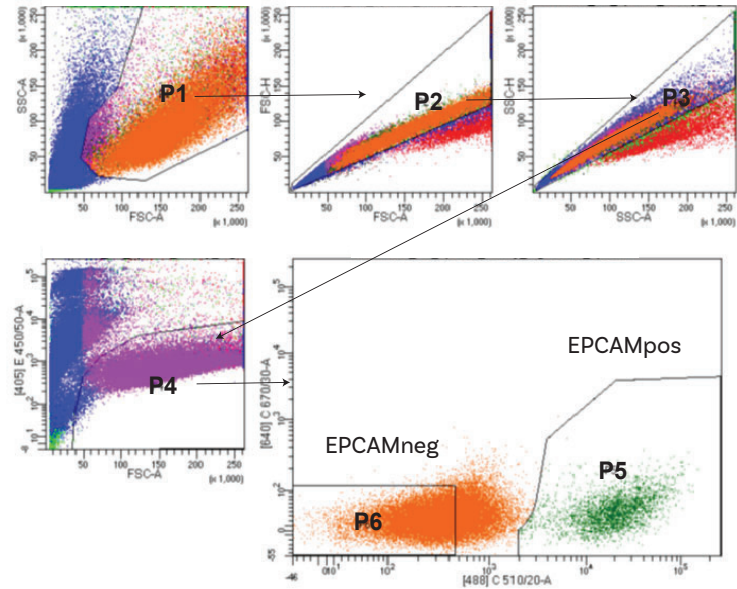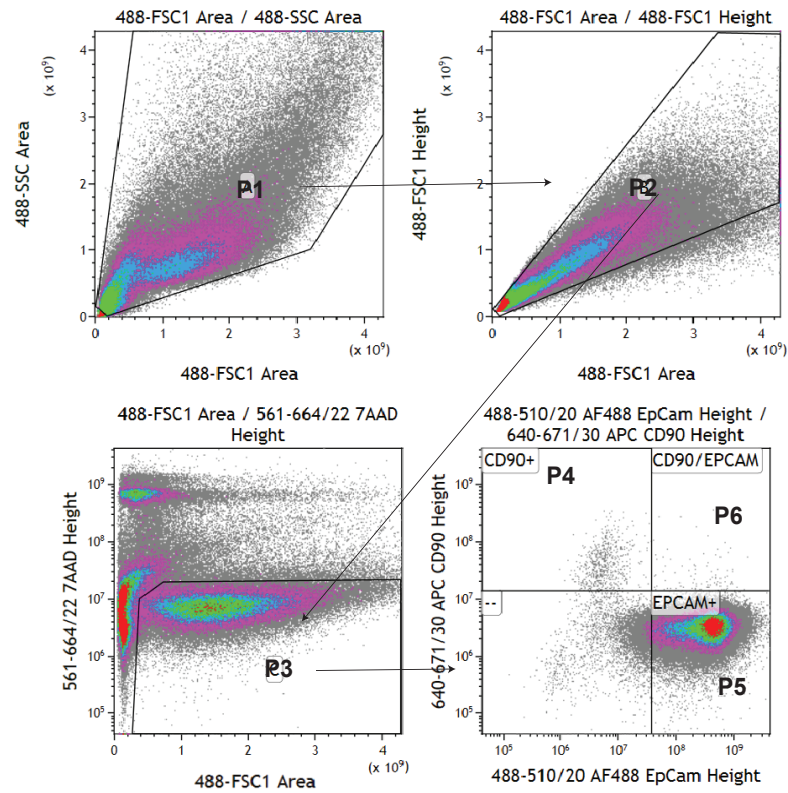
Supplementary Figure 13. Gating strategies. A. Example of gating strategy applied to purify EPCAM negative and positive organoid populations (Supplementary Figure 3C). **B.** Example of gating strategy applied to quantify single (EPCAM or CD90) or double positive (EPCAM/CD90) organoid populations over time (Supplementary Figure 6A). For CD90 and EPCAM gating, we used unlabelled cells of interest, single-color controls (UltraComp beads ThermoFisher, or partially killed cells of interest) followed by automatic compensation matrix calculations (fluorescence-minus-one (FMO) controls for each marker).

Supplementary Table 1. Characteristics of the study participants.

| Line	Gender	Year of birth	Diagnosis	Source	Risk classification	Pre-op treatment	Predominant subtypes
37	F	2013	WT	primary	intermediate	6 weeks VAD	Regressive type
45	M	2014	Metanephric adenoma	primary	n/a	4 weeks AV	n/a
48	F	2014	WT	primary	intermediate	6 weeks AV	Bilateral, material from 1 kidney.
51	F	2013	WT	primary	intermediate	4 weeks AV	Mixed (blastema/stroma/epithelium)
52	F	2010	WT	primary	intermediate	4 weeks AV	Mixed type (blastema/stroma/epithelium)
57	F	2009	WT (Beckwith Wiedemann)	primary	intermediate	4 weeks AV	Mixed type (blastema/epithelium)
58	M	2016	MRTK	primary	n/a	4 weeks AV	n/a
60	F	2015	MRTK	primary	n/a	5 weeks AV	n/a
60	F	2015	MRTK	Met (lymph node)	n/a	5 weeks AV	n/a
64	F	2015	WT	primary	high	4 weeks AV	Mixed (pre-dominant blastemal)
68	M	2011	WT	primary	intermediate	4 weeks AV	Mixed (blastema/stroma/epithelium)
71	F	2011	RCC	primary	n/a	4 weeks AV	n/a
78	M	2016	MRTK	primary	n/a	2 weeks AV	n/a
80	F	2013	WT	primary	intermediate	4 weeks AV	Mixed (minimal blastema/stroma/epithelium)
83	F	2015	WT	primary	intermediate	4 weeks AV + 1 cycle carbo/etoposide	Stromal type
85	F	2013	WT	primary	intermediate	4 weeks AV	Mixed type (blastema/epithelium)
86	M	2016	WT	primary	n/a*	untreated	Epithelial type
88	M	2015	WT	primary	intermediate	4 weeks AV	Stromal type
94	F	2016	WT	primary	intermediate	4 weeks AV	Mixed type (65% blastema)
95	M	2014	WT (Beckwith Wiedemann)	primary	unknown	4 weeks AV	Blastemal predominant
96	M	2014	WT	primary	unknown	4 weeks AV	Blastemal predominant
97	F	2013	WT	primary	intermediate	4 weeks AV	Regressive
98	F	2012	WT (Beckwith Wiedemann)	primary	high	8 weeks AV	Bilateral, material from 1 kidney, Diffuse anaplasia
101	F	2014	WT	primary	intermediate	6 weeks VAD	Stromal subtype

Supplementary Table 1. Characteristics of the study participants. *(Continued)*

Line	Gender	Year of birth	Diagnosis	Source	Risk classification	Pre-op treatment	Predominant subtypes
102	F	2016	Nephrogenic rest (Beckwith Wiedemann)	primary	n/a	4 weeks AV	n/a
103	F	2017	MRTK	primary	n/a	untreated	n/a
107	F	2002	RCC	primary	n/a	untreated	pX11.2 translocation
108	M	2000	RCC	primary	n/a	1 week sunitinib	n/a
109	F	2016	WT	primary	n/a*	untreated	Mixed type (blastema/epithelium/stromal)
119	M	2005	Relapsed Wilms*	Met (liver)	high	untreated	Metastasis with predominantly blastema
PMCMRTK1	F	2015	MRTK	Met (lymph node)	n/a	6 weeks VAD + 1 additional VCR	n/a
CMN010T	M	2018	CMN	primary	n/a	untreated	n/a
CMN012T	F	2018	CMN	primary	n/a	untreated	n/a
WTO03T	M	2016	WT (cystic)	primary	intermediate	untreated	Cysts with predominant stromal component

*Tumor was a second relapse of a WT. Complete remission was reached after chemotherapy treatment of the primary tumor (ACT-D, VCR, DOX, radiotherapy) and of the first relapse (ifosfamide, cyclofosfamide, cycloofosfamide, carboplatin, ETO). Complete remission was again reached by treating the second relapse with VCR and irinotecan and subsequently with ifosfamide, cyclofosfamide, carboplatin, ETO, high dose melphalan, radiotherapy. # According to the SIOP classification, untreated Wilms tumors are classified intermediate risk or higher (unless it is a CMN or CPDN).

3

Chapter 4
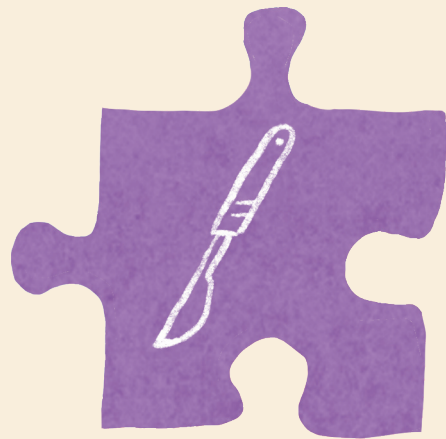
Generation of human kidney tubuloids from tissue and urine

Camilla Calandrini[1,2] and Jarno Drost[1,2]

[1] Princess Máxima Center for Pediatric Oncology, Utrecht, the Netherlands
[2] Oncode Institute, Utrecht, the Netherlands

Abstract

Adult stem cell (ASC)-derived human kidney epithelial organoids, or tubuloids, can be established from healthy and diseased kidney epithelium with high efficiency. Normal kidney tubuloids recapitulate many aspects of their tissue of origin. They represent distinct nephron segments - most notably of the proximal tubule, loop of Henle, distal tubules, and collecting duct - and can be used to study normal kidney physiology. Furthermore, tubuloid technology facilitates disease modeling, e.g., for infectious diseases as well as for cancer. Obtaining kidney epithelial cells for tubuloid generation is, however, dependent on leftover surgical material (e.g., (partial) nephrectomies) or needle biopsies. The ability to grow tubuloids from urine would provide an alternative, less invasive source of healthy kidney epithelial cells. It has been previously shown that tubuloid cultures can be successfully generated from only a few milliliters of freshly collected urine. This article describes the protocols to generate and propagate ASC-derived human kidney tubuloid cultures from tissue and urine samples.

Introduction

Kidneys perform the function of systemically controlling the balance of body fluids. The impairment of their physiological function can be caused by different factors, including diabetes, hypertension, and drug-induced toxicity[1]. For a better understanding of normal kidney physiology as well as the development of renal diseases, the use of representative preclinical models is crucial. In recent years, several *in vitro* kidney models have been generated based on the so-called organoid technology[2]. Organoids are three-dimensional, multicellular structures resembling the morphology and physiology of the tissue (normal or diseased) from which they originate. They can be generated from pluripotent (PSCs) or adult stem cells (ASCs), each with their own characteristics and applications. PSC-derived kidney organoids mimic nephrogenesis[3,4,5]. They can also be established from patient-derived committed cells by forced dedifferentiation (induced pluripotency or iPSC). iPSCs can subsequently be differentiated into the different cell types of the nephron, the functional unit of the kidney, by timely exposure to specific growth factor cocktails. While creating a rather complete mini-organ in a dish, their establishment remains time-consuming, and due to the reprogramming protocol, iPSCs can be susceptible to undesired genetic instability[6]. Furthermore, iPSC organoids are not able to fully mature into adult kidney cells, revealing a transcriptome profile that resembles the fetal kidney at an early development stage[7]. ASC-derived human kidney tubuloids have been shown to recapitulate the renewal of adult kidney epithelium. They primarily represent the proximal tubule, loop of Henle, distal tubules, and collecting duct, as confirmed by the expression of different transporter proteins[8,9,10]. The tubuloid culture protocol allows for the rapid expansion of patient-derived kidney tissue, while retaining a stable genome. Research applications include studying normal kidney physiology, nephrotoxicity, drug testing, as well as disease modelling[8,10,11,12]. A potential limitation of the establishment of patient-derived organoid cultures, including tubuloids, is the availability of fresh tissue. However, several reports have shown that urine can serve as a source for kidney epithelial cells, thereby providing a much simpler, less invasive strategy to obtain patient material for tubuloid cultures[8,13,14]. Indeed, it has been recently shown that tubuloids can be grown from urine[8]. This article describes the establishment and maintenance of tubuloid cultures from kidney tissue and urine.

Protocol

NOTE: The experiments described herein were approved by the medical ethical committee of the Erasmus Medical Center (Rotterdam, the Netherlands) and Princess Máxima Center for Pediatric Oncology (Utrecht, the Netherlands).

1. Generation of human kidney tubuloids from tissue

1. Materials

1. Prewarm multiwell tissue culture plates (6, 12, 24, and 48 wells) overnight at 37 °C.
2. Prepare basal medium (AdDF+++) by adding 1x L-alanine/L-glutamine supplement, 1% w/v 4- (2-hydroxyethyl)-1-piperazine ethanesulfonic acid (HEPES, 10 mM), and 1% penicillin/ streptomycin antibiotics to Advanced DMEM/F12.
3. Prepare culture medium by adding 1.5% B27 supplement, 10% R-spondin-conditioned medium, epidermal growth factor (50 ng/mL), fibroblast growth factor-10 (100 ng/mL), *N*-acetylcysteine (1.25 mM), Rho-kinase inhibitor Y-27632 (10 µM), broad-spectrum antibiotics (0.1 mg/mL), and A83-01 (5 µM) to AdDF+++. Warm to 37 °C before use.
4. Prepare the basement membrane extract (BME) by thawing an aliquot overnight at 4 °C. Keep the BME on ice during the procedure.
5. Prepare collagenase solution by diluting collagenase to a final concentration of 1 mg/mL in AdDF+++, with the addition of 10 µM Y-27632. Warm up to 37 °C.
6. Prepare 10 cm Petri dishes, scalpels, and tweezers. Disinfect the utensils by applying an ultraviolet lamp for 20 min, followed by washings with disinfectant, demi water, and 70% v/v ethanol. Air-dry the utensils.
7. Prewarm a horizontal shaker to 37 °C.

2. Procedure

1. Collect kidney tissue in a 50 mL tube filled with 30-40 mL of AdDF+++ medium. Place the piece of tissue in ~1 mL of medium in a 10 cm Petri dish. Mince the tissue into pieces of ~1 mm³ size using scalpels (**Figure 1A**).
2. Transfer the minced tissue to a 15 mL tube using forceps and scalpels. Add 5 mL of AdDF+++ to the Petri dish, wash, and collect the medium with a 10 mL sterile pipette. Transfer all these contents to the same tube.

3. Centrifuge at 300 × *g* for 5 min at room temperature, and remove the supernatant. Add 3-4 mL of collagenase solution to the 15 mL tube. Move the tube to a horizontal shaker set at 37 °C and a speed of 250 rpm.
4. After the first 15 min of incubation, check the sample and vigorously shake the tube. Repeat until the suspension is homogeneous and most pieces of tissue have disappeared, with a maximum incubation time of 45-60 min. (**Figure 1B**).
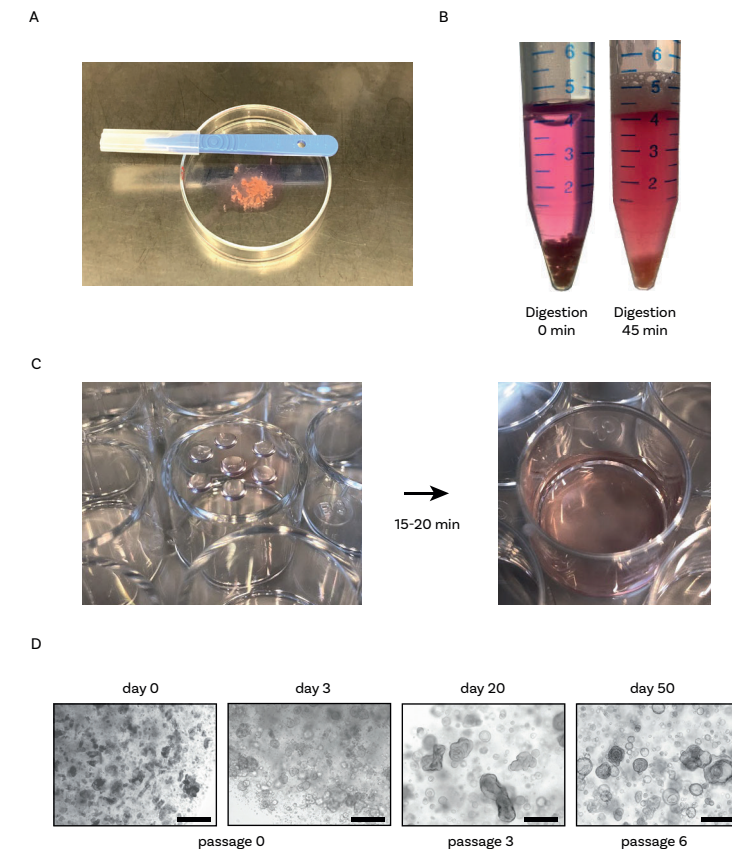
Figure 1. Tissue-derived kidney tubuloid cultures. A. Overview of the procedure to mince kidney tissue. Tissue is minced to a size of ~1 mm³ using scalpels. **B.** Example of correct enzymatic digestion of healthy kidney tissue. Tissue is shown before (left) and after (right) 45 min of enzymatic digestion with collagenase. Few pieces of tissue are still visible at the bottom of the tube, and the solution should become cloudy, indicating the presence of cells in the suspension. **C.** Representative image of cell culture plates after plating of BME droplets containing the processed kidney tissue. After plating the droplets, culture plates are turned upside down (left) and placed in the incubator at 37 °C. After 15-20 min, prewarmed culture

medium is added to the well (right). **D.** Representative brightfield images of tissue-derived tubuloid cultures. The first tubuloid structures become visible 2-3 days after first seeding. With increasing passage numbers, tubuloids typically change morphology to a more cystic phenotype. Scale bars = 300 μm. Abbreviations: BME = basement membrane extract.

5. Fill up the tube with AdDF+++, and mix by inverting the tube 5-10x. Centrifuge at 300 × g for 5 min at 4 °C, and remove the supernatant. If the pellet is red, proceed with step 1.2.6. Otherwise, go to step 1.2.8.

6. Add 1 mL of red blood cell lysis buffer on top of the cell pellet. Gently tap the tube to resuspend the pellet (do not resuspend with pipette tip). Incubate at room temperature for 5 min.

7. Fill up the tube with AdDF+++. Centrifuge at 300 ×g for 5 min at 4 °C, and remove the supernatant. If blood cells are still visible, repeat the procedure once more, starting from step 1.2.6. Otherwise, proceed with step 1.2.8.

8. If chunks of tissue are visible at this point of the protocol, proceed with step 1.2.8. Otherwise, proceed with the measurement of the pellet volume in step 1.2.9. Add 5 mL of AdDF+++ to the tube, and resuspend with a 10 mL sterile pipette. Filter the suspension through a 100 μm nylon cell strainer placed on a 50 mL tube.

9. Transfer the filtered suspension to a new 15 mL tube. Centrifuge at 300 × g for 5 min at 4 °C, and remove the supernatant. Measure the volume of the cell pellet using a p1000 pipette set to a known volume. Carefully pipette up and down to resuspend without creating air bubbles. Transfer the tube to ice for 1 min.

10. Add 70-75% volume of BME to the pellet. Resuspend using a p1000 or p200 pipette, and plate 15 μL droplets in a prewarmed, multiwell cell culture plate (6, 12, or 24 wells, based on total plating volume (<100 μL, 24 wells; 100-200 μL, 12 wells; >200 μL, 6 wells)).

11. Turn the plate upside down, and let the plate rest in the incubator for 15-20 min at 37 °C (**Figure 1C**). Add prewarmed culture medium, and inspect the cultures (**Figure 1C,D**).

2. Generation of human kidney tubuloids from urine

NOTE: Urine is a hostile environment for cells. It is important for a successful execution of this protocol that urine samples are processed as soon as possible, preferably within 4 h from excretion. In the meantime, urine samples should be stored at 4 °C.

1. Materials

1. Prewarm multiwell tissue culture plates (6, 12, 24, and 48 wells) overnight at 37 °C.

2. Prepare washing medium: AdDF+++ supplemented with broad-spectrum antibiotics (0.1 mg/mL) and 10 μM Y-27632.

3. Prepare culture medium as described above. Warm up at 37 °C before use.

4. Prepare BME matrix. Keep on ice during the procedure.
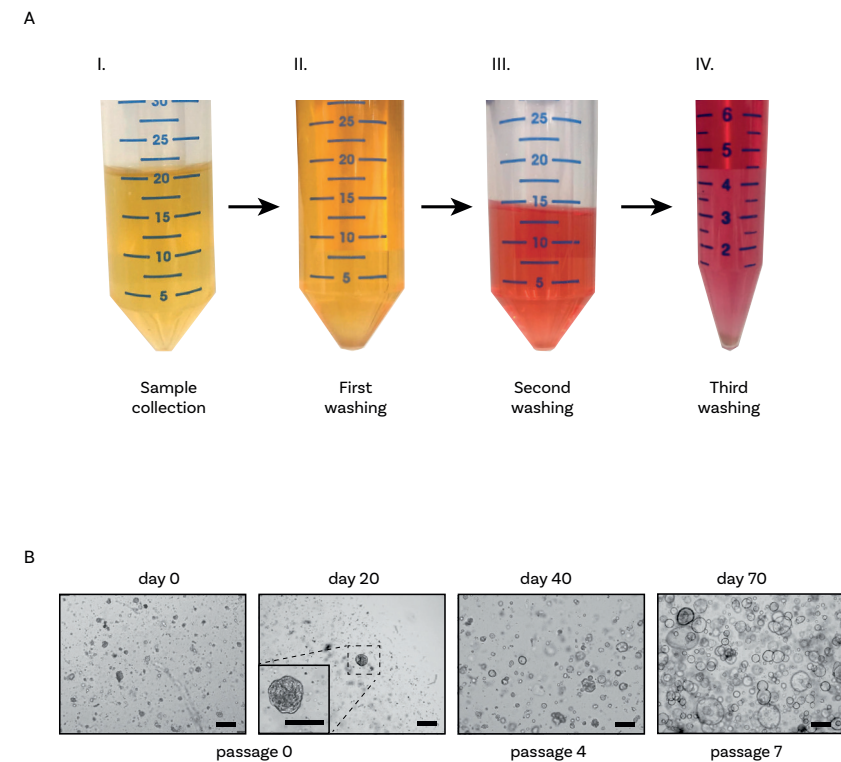
Figure 2. Urine-derived kidney tubuloid cultures. A. Overview of urine sample processing. As soon as possible after collection (I), urine samples are divided into 50 mL tubes and diluted in washing medium (II). After a second washing step (III), the content of the tubes is pooled and a third and final wash step (IV) is performed before plating. **B.** Representative brightfield images of urine-derived tubuloid cultures. The first tubuloid structures and adherent cells should be visible within 21 days after first plating. Scale bars = 300 μm.

2. Procedure

1. Collect a urine sample, and divide it equally into 50 mL tubes (**Figure 2A-I**). Add 10-20 mL of washing medium to each of the tubes. Centrifuge at 300 × g for 5 min at 4 °C (**Figure 2A-II**), and remove the supernatant carefully.
2. Add 10 mL of washing medium to each of the tubes. Carefully resuspend the pellets using a 10 mL sterile pipette. Centrifuge at 300 x g for 5 min at 4 °C (**Figure 2A-III**), and remove the supernatant carefully.
3. Resuspend the pellets, and transfer the contents of all the tubes into one 15 mL tube. Fill the tube with washing medium. Centrifuge at 300 x g for 5 min at 4 °C (**Figure 2A-IV**), and remove the supernatant.
4. Measure the volume of the cell pellet using a p1000 pipette set to a known volume. Carefully pipette up and down to resuspend without creating air bubbles. Transfer the tube to ice for 1 min.
5. Add 70-75% volume of the BME to the pellet. Resuspend using a p1000 or p200 pipette, and plate 15 µL droplets in a prewarmed, multiwell cell culture plate (6, 12, or 24 wells, based on total plating volume (<100 µL, 24 wells; 100-200 µL, 12 wells; >200 µL, 6 wells)).
6. Turn the plates upside down in the incubator for 15-20 min at 37 °C. Add prewarmed culture medium, and inspect the cultures (**Figure 2B**).

3. Expansion of tubuloid cultures

NOTE: Tubuloid cultures can be passaged approximately every 1-2 weeks with a split ratio of 1:2-1:3. They can be typically expanded for a maximum of 15 passages, with line-specific variations.

1. Materials

1. Prewarm multiwell tissue culture plates (6, 12, 24, and 48 wells) overnight at 37 °C.
2. Prepare basal medium (AdDF+++), and keep it on ice during the procedure.
3. Prepare culture medium as previously described. Warm up to 37 °C before use.
4. Prepare BME matrix, and keep on ice during the procedure.
5. Prepare trypsin replacement agent with the addition of Y-27632 to a concentration of 10 µM. Warm up to 37 °C before use.
6. Autoclave non-filtered p10 tips.
7. Cool the centrifuge to 4 °C.

2. Procedure

1. Disrupt the droplets containing the tubuloids by pipetting up and down with a p1000 pipette using the medium present in the well. Use the tip to scrape the bottom of the well, making sure to collect all cells attached to the bottom.
2. Collect the contents in a 15 mL tube. Add 10 mL of AdDF+++. Centrifuge at 300 x g for 5 min at 4 °C, and remove the supernatant.
3. Based on the size of the pellet, add trypsin replacement agent supplemented with 10 µM Y-27632. Use 1 mL of trypsin replacement agent for 200 µL of BME droplets containing tubuloids. Incubate at 37 °C for 5 min.
4. Use a p1000 pipette with tip, and insert a nonfiltered, sterile p10 tip over the 1000 µL tip. Pipette up and down for 20-30x to mechanically disrupt the organoids.
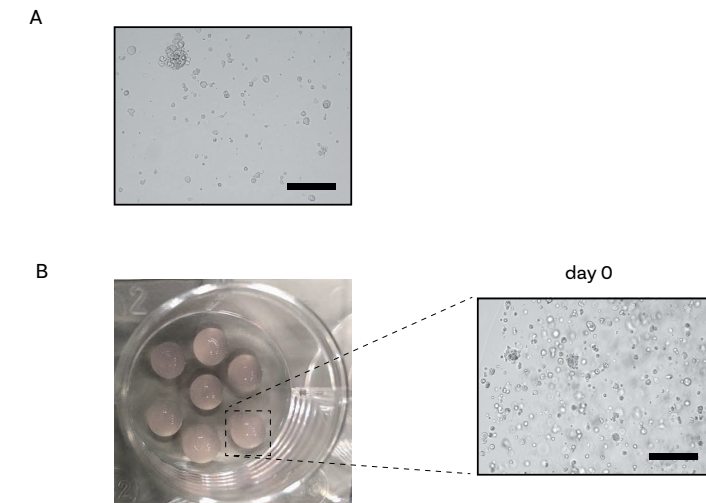
Figure 3. Passaging of kidney tubuloid cultures. A. Representative image of kidney tubuloid cultures after enzymatic digestion. After completing digestion, no more than 10% of intact tubuloid structures should remain. Scale bar = 300µm. **B.** Representative image of kidney tubuloid cultures after plating. Inspection of the cultures confirms that the majority of the tubuloids have been disrupted. Scale bar = 300 µm.

5. Check under the microscope to see if many intact organoids are still present in the tube (**Figure 3A**). If more than 10% of intact organoids are present at this point, repeat from the 5 min incubation in step 3.2.3 to the microscopic observation for intact organoids in step 3.2.5 once more. Otherwise, proceed with step 3.2.6.

6. Fill up the tube with AdDF+++. Centrifuge at 300 × g for 5 min at 4 °C, and remove the supernatant. Measure the volume of the cell pellet using a p1000 pipette set to a known volume. Carefully pipette up and down to resuspend without creating air bubbles. Transfer the tube to ice for 1 min.

7. Add 70-75% volume of BME to the pellet. Resuspend using a p1000 or p200 pipette, and plate 15 µL droplets in a prewarmed, multiwell cell culture plate (6, 12, or 24 wells, based on total plating volume (<100 µL, 24 wells; 100-200 µL, 12 wells; >200 µL, 6 wells)).

8. Turn the plates upside down, and let the plate rest in the incubator for 15-20 min at 37 °C. Add prewarmed culture medium, and inspect the cultures (**Figure 3B**).

Representative results

For kidney tissue, tubuloid structures typically appear within 7 days after establishment (**Figure 1D**). Lack of apparent growth within the first 7 days indicates an unsuccessful outcome of the protocol. Generally, tubuloid cultures need to be passaged within 1-2 weeks after first plating. For urine, cell growth becomes apparent approximately 14-21 days after establishment, with the appearance of compact tubuloid structures and/or adherent cells on the bottom of the plate (**Figure 2B**). Culture establishment most likely has failed if no growth can be detected with a brightfield microscope within 4 weeks after plating. For urine-derived cultures, the first passaging generally occurs between 3 and 4 weeks. While in the first passages, kidney tubuloid cultures consist mainly of compact structures, the presence of cystic epithelial tubuloids increases with the increase of passage number (**Figure 1D** and **Figure 2B**). The successful generation of human kidney tubuloid cultures can be assessed by performing immunohistochemical staining for markers expressed in tubular kidney epithelium, such as paired box gene 8 protein (PAX8) (**Figure 4A,B**).
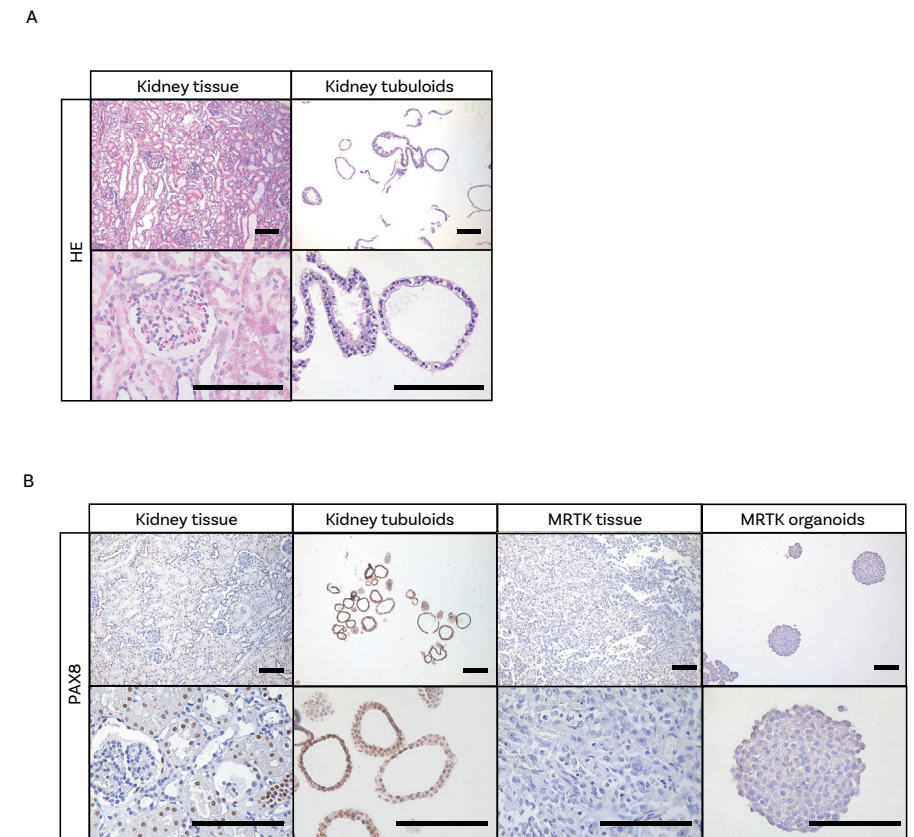
Figure 4. Histological characterization of tubuloid cultures. A. H&E staining of healthy kidney tissue and tubuloids. Scale bars = 100 µm. **B.** Immunohistochemistry of PAX8 in normal kidney tissue, tubuloids, MRTK tissue, and MRTK organoids. PAX8 positivity of the organoid structures confirms their kidney epithelial origin. Healthy kidney tissue shows both positive (tubules) and negative structures (glomeruli). MRTK tissue and organoids were included as negative control. Scale bars = 100 µm. Abbreviations: H&E = hematoxylin and eosin; PAX8 = paired box gene 8; MRTK = malignant rhabdoid tumor of the kidney.

Discussion

Organoids are considered avatars of the tissue from which they are derived. They allow for rapid expansion of patient material while retaining the genotypic and phenotypic characteristics of the tissue of origin[15]. Organoid technology has recently opened the doors for the development of more representative preclin-

ical models, which can be used as important tools to translate findings from the bench to the bedside. Kidney tubuloids are promising *in vitro* models for testing drug-induced nephrotoxicity, a common side effect of many chemotherapeutic drugs[2,8,12]. As such, patient-derived tumor organoid cultures were demonstrated to be predictive for patient response to treatment[16,17,18]. Testing drugs in a high-throughput manner on tubuloids therefore potentially allows better definition of therapeutic windows and decreases the risk of drug-induced nephrotoxicity in patients. Commonly used antibiotics have been described to exert a toxic effect on the kidneys[19]. Although the presence of broad-spectrum antibiotics is necessary for the successful establishment of the cultures by preventing contamination, it is important to consider their potential nephrotoxicity. To date, although no negative effects of antibiotics have been observed on the establishment of tubuloid cultures, further investigation is needed to thoroughly evaluate their effects. Tubuloids can be exploited for studying and modeling diseases[8]. Ciliopathies (pathological dysfunction of cilia) as well as other genetic syndromes affecting the kidney could be studied by either generating tubuloid lines directly from affected subjects, or by using healthy cultures in which disease-specific driver mutations can be introduced via CRISPR/Cas9 genome editing[20]. Although tubuloids are multicellular kidney cultures, they lack several renal cell types, including podocytes and endothelial cells[8]. Moreover, in contrast to some other ASC-derived organoid models, tubuloids have a limited replicative potential as they can be cultured for up to 15 passages. This limited lifespan can, however, be significantly extended by the addition of Wnt to the culture medium[21]. Further optimization of the tubuloid protocol is required to make tubuloids truly representative of the kidney. Although the efficiency of tubuloid establishment from tissue samples is very high (>95%), it can, in rare cases, fail. There can be different causes including: 1) poor quality of the starting material (e.g., necrotic tissue as a consequence of drug treatment), 2) over-digestion of the tissue sample, or 3) contamination of the primary sample. To make sure that the quality of the tissue samples received is sufficient to proceed with the protocol, it is important to maintain close contact with the pathology staff performing the evaluation of the tissue upon surgery. If sufficient material is available, its viability must be confirmed by histological examination (e.g., hematoxylin and eosin staining). Furthermore, to prevent cell lysis during enzymatic digestion, it is important that the incubation procedure is no longer than 1 h. Lastly, to prevent contamination, antibiotics and antifungal agents should be added to the washing and culture media. Urine can contain exfoliated epithelial cells that are not derived from the kidney[22], which can contaminate the tubuloid cultures. These

include, for instance, urothelium cells that are, in contrast to renal tubular cells, positive for tumor protein P63 and negative for PAX8[8]. It is therefore recommended to test the cultures for PAX8 positivity to confirm the purity of established kidney tubuloid lines before proceeding with follow-up experiments (**Figure 4B**). Urine represents a hostile environment for cells due to high osmotic pressure and low pH. It is therefore crucial for the success of the protocol that samples are processed as soon as possible upon urine collection. As such, the collected urine should be diluted and extensively washed with buffered solution as soon as possible to ensure presence of viable cells at the time of seeding. The success rate of tubuloid establishment will significantly decrease if urine is stored for several hours before processing. Lastly, although sterile, urine has a high risk of contamination associated with the collection process. It is therefore important to supplement washing and growth medium with antibiotics and antifungal agents. When taking all the above into account, a success rate of approximately 50% (3/6 samples) can be achieved.

Disclosures

The authors declare no conflicts of interest.

Acknowledgments

References

1. Romagnani, P. et al. Chronic kidney disease. Nature Reviews. Disease Primers. 3, 17088 (2017).

2. Ooms, A. H., Calandrini, C., de Krijger, R. R., Drost, J. Organoid models of childhood kidney tumours. Nature Reviews. Urology. 17 (6), 311-313 (2020).

3. Takasato, M. et al. Kidney organoids from human iPS cells contain multiple lineages and model human nephrogenesis. Nature. 526 (7574), 564-568 (2015).

4. Low, J. H. et al. Generation of human PSC-derived kidney organoids with patterned nephron segments and a de novo vascular network. Cell Stem Cell. 25 (3), 373-387.e9 (2019).

5. Little, M. H., Combes, A. N. Kidney organoids: accurate models or fortunate accidents. Genes & Development. 33 (19-20), 1319-1345 (2019).

6. Papapetrou, E. P. Patient-derived induced pluripotent stem cells in cancer research and precision oncology. Nature Medicine. 22 (12), 1392-1401 (2016).

7. Wu, H. et al. Comparative analysis and refinement of human PSC-derived kidney organoid differentiation with single-cell transcriptomics. Cell Stem Cell. 23 (6), 869-881.e8 (2018).

8. Schutgens, F. et al. Tubuloids derived from human adult kidney and urine for personalized disease modeling. Nature Biotechnology. 37 (3), 303-313 (2019).

9. Jun, D. Y. et al. Tubular organotypic culture model of human kidney. PLoS One. 13 (10), e0206447 (2018).

10. Grassi, L. et al. Organoids as a new model for improving regenerative medicine and cancer personalized therapy in renal diseases. Cell Death & Disease. 10 (3), 1-15 (2019).

11. Yousef Yengej, F. A., Jansen, J., Rookmaaker, M. B., Verhaar, M. C., Clevers, H. Kidney organoids and tubuloids. Cells. 9 (6), 1326 (2020).

12. Calandrini, C. et al. An organoid biobank for childhood kidney cancers that captures disease and tissue heterogeneity. Nature Communications. 11 (1), 1310 (2020).

13. Jansen, J. et al. A morphological and functional comparison of proximal tubule cell lines established from human urine and kidney tissue. Experimental Cell Research. 323 (1), 87-99 (2014).

14. Zhou, T. et al. Generation of human induced pluripotent stem cells from urine samples. Nature Protocols. 7 (12), 2080 (2012).

15. Drost, J., Clevers, H. Organoids in cancer research. Nature Reviews Cancer. 18 (7), 407-418 (2018).

16. Vlachogiannis, G. et al. Patient-derived organoids model treatment response of metastatic gastrointestinal cancers. Science. 359 (6378), 920-926 (2018).

17. Ooft, S. N. et al. Patient-derived organoids can predict response to chemotherapy in metastatic colorectal cancer patients. Science Translational Medicine. 11 (513), eaay2574 (2019).

18. Tiriac, H. et al. Organoid profiling identifies common responders to chemotherapy in pancreatic cancer. Cancer Discovery. 8 (9), 1112-1129 (2018).

19. Morales-Alvarez, M. C. Nephrotoxicity of antimicrobials and antibiotics. Advances in Chronic Kidney Disease. 27 (1), 31-37 (2020).

20. Drost, J. et al. Sequential cancer mutations in cultured human intestinal stem cells. Nature. 521 (7550), 43-47 (2015).

21. Miao, Y. et al. Next-generation surrogate Wnts support organoid growth and deconvolute Frizzled pleiotropy in vivo. Cell Stem Cell. 27 (5), 840-851.e6 (2020).

22. Dörrenhaus, A. et al. Cultures of exfoliated epithelial cells from different locations of the human urinary tract and the renal tubular system. Archives of Toxicology. 74 (10), 618-626 (2000).

Chapter 5

Organoid-based drug screening reveals neddylation as therapeutic target for malignant rhabdoid tumors

Camilla Calandrini[1,2], Sander R. van Hooff[1], Irene Paassen[1,2], Dilara Ayyildiz[1,2], Sepide Derakhshan[1,2], M. Emmy M. Dolman[1], Karin P.S. Langenberg[1], Marieke van de Ven[3], Cecilia de Heus[4], Nalan Liv[4], Marcel Kool[1,5,6], Ronald R. de Krijger[1,7], Godelieve A.M. Tytgat[1], Marry M. van den Heuvel-Eibrink[1], Jan J. Molenaar[1], Jarno Drost[1,2]

[1] Princess Máxima Center for Pediatric Oncology, Heidelberglaan 25, 3584 CS Utrecht, the Netherlands

[2] Oncode Institute, Heidelberglaan 25, 3584 CS Utrecht, the Netherlands

[3] Preclinical Intervention Unit of the Mouse Clinic for Cancer and Ageing (MCCA), NKI, Amsterdam, the Netherlands

[4] Cell Biology, Center for Molecular Medicine, University Medical Center Utrecht, Heidelberglaan 100, 3584 CX Utrecht, the Netherlands

[5] Hopp Children's Cancer Center (KiTZ), 69120 Heidelberg, Germany

[6] Division of Pediatric Neurooncology, German Cancer Research Center DKFZ and German Cancer Consortium DKTK, 69120 Heidelberg, Germany

[7] University Medical Center, Department of Pathology, Heidelberglaan 100, 3584 CX Utrecht, the Netherlands
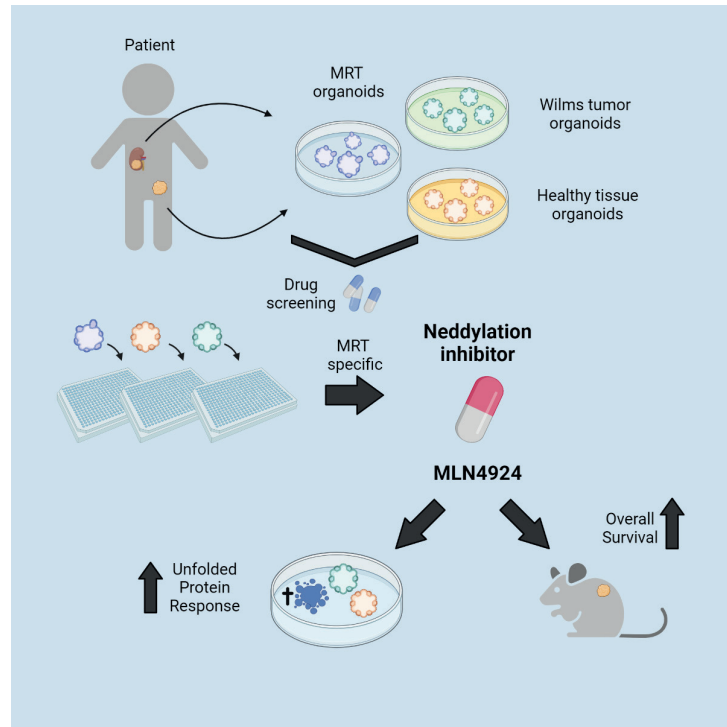
Summary

Malignant rhabdoid tumors (MRTs) represent one of the most aggressive childhood malignancies. No effective treatment options are available, and prognosis is, therefore, dismal. Previous studies have demonstrated that tumor organoids capture the heterogeneity of patient tumors and can be used to predict patient response to therapy. Here, we perform drug screening on patient-derived normal and tumor organoids to identify MRT-specific therapeutic vulnerabilities. We identify neddylation inhibitor MLN4924 as a potential therapeutic agent. Mechanistically, we find increased neddylation in MRT organoids and tissues and show that MLN4924 induces a cytotoxic response via upregulation of the unfolded protein response. Lastly, we demonstrate *in vivo* efficacy in an MRT PDX mouse model, in which single-agent MLN4924 treatment significantly extends survival. Our study demonstrates that organoids can be used to find drugs selectively targeting tumor cells while leaving healthy cells unharmed and proposes neddylation inhibition as a therapeutic strategy in MRT.

Introduction

Malignant rhabdoid tumors (MRTs) are aggressive childhood tumors that occur in infants and young children[1]. They can arise in the brain (atypical teratoid rhabdoid tumor [ATRT]) as well as extracranially (kidney and soft tissues), where they are collectively called MRTs. MRTs are uniquely characterized by one common genetic driver event, bi-allelic loss of *SMARCB1* (95%) or *SMARCA4* (5%), key members of the SWI/SNF chromatin-remodeling complex[2,3]. In addition, MRTs are considered genetically cold tumors with low mutational burden and a lack of chromosomal alterations[4,5]. Therapy is multimodal, consisting of a combination of surgical intervention, radiotherapy, and heavy regimens of chemotherapy[6]. Despite that treatment, the prognosis remains dismal, with an overall survival of only ~25%[7]. Furthermore, survivors suffer from side effects of the intense treatment regimen. MRTs, therefore, remain one of the big challenges in childhood cancer, and the identification of less-toxic therapeutic strategies is urgently needed.

    The lack of physiologically relevant *in vitro* models has hampered therapeutic innovation in the MRT field. Patient-derived organoid models have emerged as robust pre-clinical models for cancer research[8] and to be predictive of patient treatment response[9-13]. We recently succeeded in generating patient-derived organoid models from MRTs of the kidney and demonstrated that these tumor organoids recapitulate the genetic, transcriptional, and DNA methylation profiles of the primary MRT tissue[14,15]. Here, we set out to identify therapeutic agents for patients with MRT by performing drug screens on patient-derived MRT organoid cultures (kidneys and additional established cultures from extrarenal MRTs). By comparing the efficacy of the compounds in MRT to that of organoids derived from Wilms tumor and healthy tissues, we identified the neddylation inhibitor MLN4924 as an MRT-specific vulnerability. MRT organoids demonstrate increased neddylation activity, which we confirmed in patient MRT tissues. Mechanistically, we suggest that this vulnerability is, at least partially, caused by increased endoplasmic reticulum (ER) stress and the activity of the unfolded protein response (UPR) in MRTs. In conclusion, we have identified neddylation inhibition as a promising therapeutic strategy for pediatric MRTs.

Results

Drug screening of MRT organoids reveals tumor- and patient-specific drug sensitivities

To find therapeutic agents for MRTs, we used our previously described patient-derived MRT of the kidney organoid models[14] as a platform for drug screens. In addition, we included an additional established organoid model from an MRT growing in the pelvic area (**Supplementary Table 1**). Extensive analyses revealed that the organoids have retained crucial characteristics of the parental tissue (**Supplementary Figure 1A–E**), as we previously described for our MRTs of the kidney models[14,16]. We screened a total of six MRT organoid lines derived from five patients with MRTs, including three primary tumors, one metastasis, and one case of patient-matching primary and metastatic tissue[14]. We screened an in-house-developed drug library containing approximately 150 targeted compounds (**Figure 1A; Supplementary Table 2**). Screening the library at six different concentrations allowed us to draw dose-response curves. We first selected targeted compounds that appeared most effective in at least five of six screened MRT organoid cultures based on the area under the curve (AUC) values (**Figure 1B, Supplementary Figure 2A,B**), which yielded 21 compounds (**Figure 1C**). Next, we checked for MRT-specific activity of those compounds by comparing the half-maximal inhibitory concentration (IC_{50}) values of the selected drugs with the IC_{50} values of previously screened Wilms tumor organoids[14] (**Supplementary Figure 2C; Supplementary Table 3**). This yielded 14 drugs with more-potent efficacy on MRTs versus Wilms tumor organoids. Among those were drugs previously identified as potential therapies for MRTs, such as histone deacetylase (HDAC) inhibitors, HSP90 inhibitors, and the proteasome inhibitor bortezomib[17-19]. We also identified multiple mTOR inhibitors, which we previously described as having a cytostatic effect in MRTs[20].
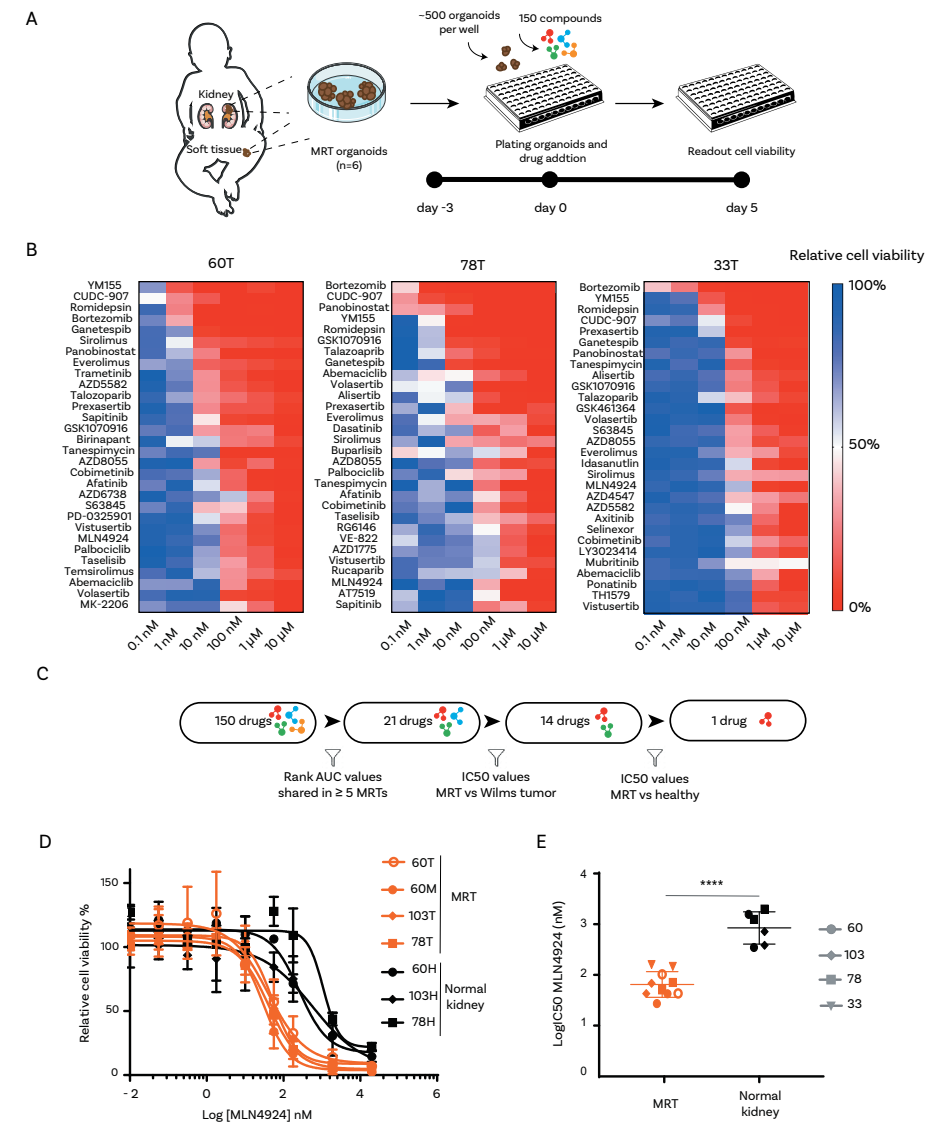
Figure 1. Drug screening of MRT organoids reveals tumor specific drug sensitivities. **A.** Schematic overview of the organoid drug screening workflow. **B.** Compound screening of ~150 targeted drugs were performed on six patient-derived MRT organoid cultures (Supplementary Figure 2A). The top-30 compounds are depicted ranked based on area under the curve (AUC) values for three representative MRT cultures. Color scale blue to red indicates decreasing ATP levels relative to DMSO control as a measure of cell viability. **C.** Schematic of the selection strategy to find MRT-specific drug vulnerabilities. **D.** Dose-response curves of MLN4924 for the indicated MRT and patient-matching healthy kidney-tissue-derived organoid cultures. Error bars represent SD of 2 independent experiments, each consisting of quadruplicate mea-

surements. **E.** Average log(IC_{50}) values of MLN4924 in the indicated MRT- and patient-matching healthy kidney-organoid lines. Each value (two per organoid culture) represents the average of technical quadruplicates of an individual organoid culture. p values were calculated using a two-tailed unpaired Student's t test, two-sided. ****p < 0.0001.

Despite their highly similar genetic-driver landscape, we found that some MRT cultures showed differential sensitivities toward specific drugs. For instance, organoid culture 78T was markedly less sensitive to the inhibitor of apoptosis (IAP) AZD5582 compared with that of other MRT organoid cultures (**Supplementary Figure 2D**). No genetic cause could be identified in whole-genome sequencing (WGS) data of those cultures. Resistance to AZD5582 in pancreatic cancer models was previously linked to decreased expression of TNFR1 and TNFR2[21]. Using bulk RNA sequencing (RNA-seq)[14], we observed significantly reduced expression of both TNFR1 and TNFR2 in 78T compared with that of all other analyzed MRT organoids (**Supplementary Figure 2D**). This may provide an explanation for the decreased sensitivity of 78T to AZD5582 and demonstrates that organoids can be used to find patient-specific drug vulnerabilities. A drug showing efficacy in all tested MRT organoid cultures could be of therapeutic value for treatment of patients with MRTs. We identified MLN4924 as having a consistent IC_{50} value in all screened MRT organoid cultures, which was significantly less than the average IC_{50} value in Wilms tumor organoids (**Supplementary Figure 2C; Supplementary Table 3**). To further confirm the increased vulnerability MRTs to MLN4924 treatment, we tested the effect of the drug on a panel of healthy-tissue-derived organoid lines. We included three patient-matching healthy kidney-tissue-derived organoids, as well as a small intestine and a hepatocyte-derived organoid culture[22-24] to test for potential nephrotoxicity, intestinal toxicity, and hepatotoxicity of MLN4924 treatment, respectively. Furthermore, we expanded the range of concentrations of MLN4924 to determine more-accurately the IC_{50} values for the different organoid lines. MRT organoids were markedly more sensitive to MLN4924 compared with patient-matching healthy kidney organoids and hepatocyte organoids (**Figure 1D, E** and **Supplementary Figure 2E; Supplementary Table 4**). Moreover, we measured an average IC_{50} value for MRT lines of ~75 nM, a concentration well below its reported maximum tolerated plasma dose in adult patients[25]. Small-intestine organoids showed comparable sensitivity to MLN4924 as that of MRT organoids (**Supplementary Figure 2E**). However, so far, no severe side effects related to the intestines have been reported during the first phases of clinical trial for MLN4924[26], which could potentially be explained by the high regenerative capacity of the intestinal lining.

Together, patient-derived MRT organoids can be used for drug testing, allowing us to find patient-specific drug vulnerabilities, as well as MLN4924, as a potentially promising targeted compound for MRT treatment.

Low-dose MLN4924 treatment induces apoptosis in MRT

To further characterize the drug-induced effects, we investigated whether MRT organoids can regrow after MLN4924 washout (**Figure 2A**). Three patient-derived MRT organoid lines with different growth rates were selected to conduct the experiment (**Supplementary Figure 3A**). The mTOR inhibitor sirolimus and doxorubicin were included as controls because these drugs are known to have a cytostatic and cytotoxic effect on MRTs[20], respectively. Indeed, although significant regrowth was observed upon sirolimus withdrawal (**Figure 2B** and **Supplementary Figure 3B**), no regrowth occurred upon removal of doxorubicin (**Figure 2B** and **Supplementary Figure 3B**). Interestingly, no regrowth was observed upon MLN4924 washout in all three tested MRT lines, suggesting that MLN4924 treatment has a cytotoxic effect on MRT (**Figure 2B** and **Supplementary Figure 3B**). To further confirm that, we performed Annexin V/DAPI labeling upon treatment with MLN4924. Compared with the mock control as well as mTOR inhibition, a significant increase of apoptotic (i.e., Annexin V-positive) cells was observed upon MLN4924 treatment (**Figure 2C,D,** and **Supplementary Figure 3C-F**). Of note, no apoptotic response was observed upon MLN4924 treatment of patient-matching normal kidney organoids, again confirming an MRT-specific vulnerability (**Figure 2C, 2D** and **Supplementary Figure 3C,D**). These results were further confirmed by immunofluorescence staining for cleaved caspase 3, demonstrating an increase in positively stained, apoptotic MRT organoids upon MLN4924 treatment compared with normal kidney organoids (**Figure 2E**). Overall, these findings suggest that MLN4924 has a cytotoxic effect in MRT, further substantiating its therapeutic potential.
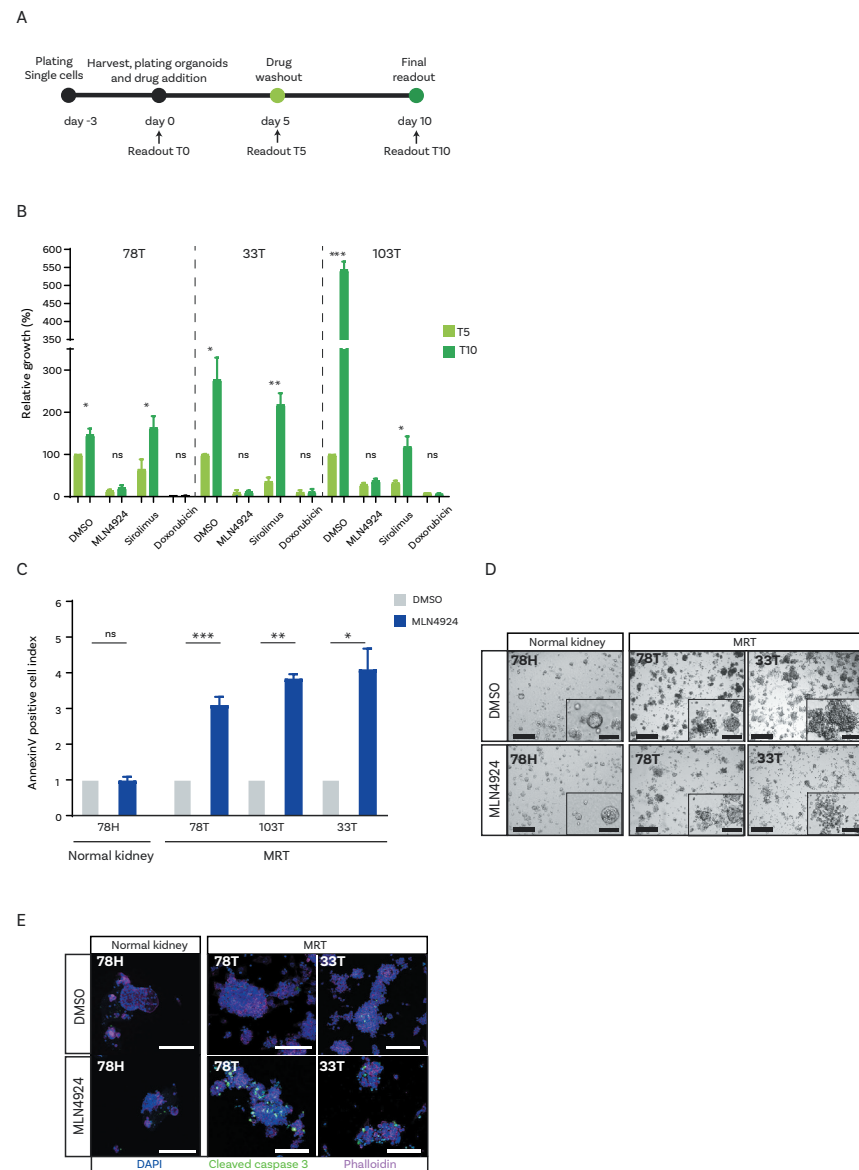
Figure 2. Low-dose MLN4924 treatment induces apoptosis in MRTs. **A.** Experimental overview of the drug-washout experiment. **B.** Bar graph represents cell viability of three MRT organoid lines at day 5 (T5) and day 10 (T10) relative to the DMSO control. 78T, 33T, and 103T MRT organoids were treated with either DMSO (vehicle), MLN4924 (100 nM; = IC$_{70}$), sirolimus (2 nM; = IC$_{70}$), or doxorubicin (100 nM; = IC$_{70}$). Data are represented as means ± SD (n = 3 independent experiments, each consisting of an average of three technical replicates). Regrowth was assessed by comparing T10 to T5 for each drug treatment. p values were calculated using a two-tailed unpaired Student's t test. *p < 0.05, **p < 0.01, ***p < 0.001. Representative

brightfield pictures can be found in Supplementary Figure 3B. **C.** Bar graph representing Annexin-V-positive cell indices of MRTs and normal kidney organoids upon treatment with 50 nM MLN4924 for 120 h. Annexin-V positive cell-index values were calculated by normalizing apoptosis percentages to the respective DMSO vehicles. Data are represented as means ± SEM (n≥3 independent experiments). p values were calculated using a two-tailed unpaired Student's t test. *p < 0.05, **p < 0.01, ***p < 0.001. See also Supplementary Figure 3C,D. **D.** Representative brightfield pictures of MRT and normal kidney organoids treated with DMSO vehicle or 50 nM MLN4924 for 120 h. Related to Figure 2C. Scale bars: 500 μm, zoom in: 150 μm. **E.** Immunofluorescence three-dimensional (3D) imaging of MRT and normal kidney organoids immunolabeled for cleaved caspase 3 (green), phalloidin (magenta), and DAPI (blue) after treatment with DMSO or 50 nM MLN4924 for 120 h. Scale bars: 250 μm.

MRTs demonstrate increased neddylation and a UPR- mediated apoptotic response upon MLN4924 treatment

Neddylation is a post-translational modification that regulates protein turnover via the conjugation of the ubiquitin-like protein NEDD8 to substrates in a three-step enzymatic process[27,28]. MLN4924 is a selective inhibitor of the neddylation-activating enzyme (NAE, enzyme E1), and its action hampers the overall neddylation process, resulting in cell-cycle arrest, apoptosis, or senescence in a cell-type-specific manner[29]. To investigate why MRTs show increased sensitivity toward MLN4924, we first analyzed the level of neddylation activity in MRT. Western blot analyses revealed strongly elevated levels of NEDD8 as well as neddylated proteins in MRT organoids compared with normal kidney and Wilms-tumor-derived organoids (**Figure 3A** and **Supplementary Figure 3G**). As expected, a strong downregulation of neddylated proteins was observed upon MLN4924 treatment in MRT samples (**Figure 3A** and **Supplementary Figure 3G**). Furthermore, and in line with previous reports[30-34], treatment with MLN4924 caused significant upregulation of the pro-apoptotic factor NOXA as well as cell-cycle regulators P21 and WEE1 (**Supplementary Figure 3H,I**). To confirm that the increase in protein neddylation observed in MRT organoids was not induced *in vitro*, we next performed immunohistochemistry for NEDD8 on patient tumor tissues. In line with the expression levels in organoids (**Supplementary Figure 3J**), strong staining for NEDD8 was detected in MRT tissue (**Figure 3B**), whereas low or a complete lack of staining was observed in normal kidney and Wilms tumor tissue, respectively (**Figure 3B**). To find the potential cause of the increased neddylation in MRTs, we assessed mRNA expression levels of several E1 and E2 neddylation enzymes in MRTs, Wilms tumors, and normal kidney tissues and organoids[14,24]. This revealed increased expression of *NAE1* (E1) and *UBE2M* (E2) enzymes in MRTs compared with Wilms tumor and/or normal kidney tissue and organoids (**Figure 3C,D**).
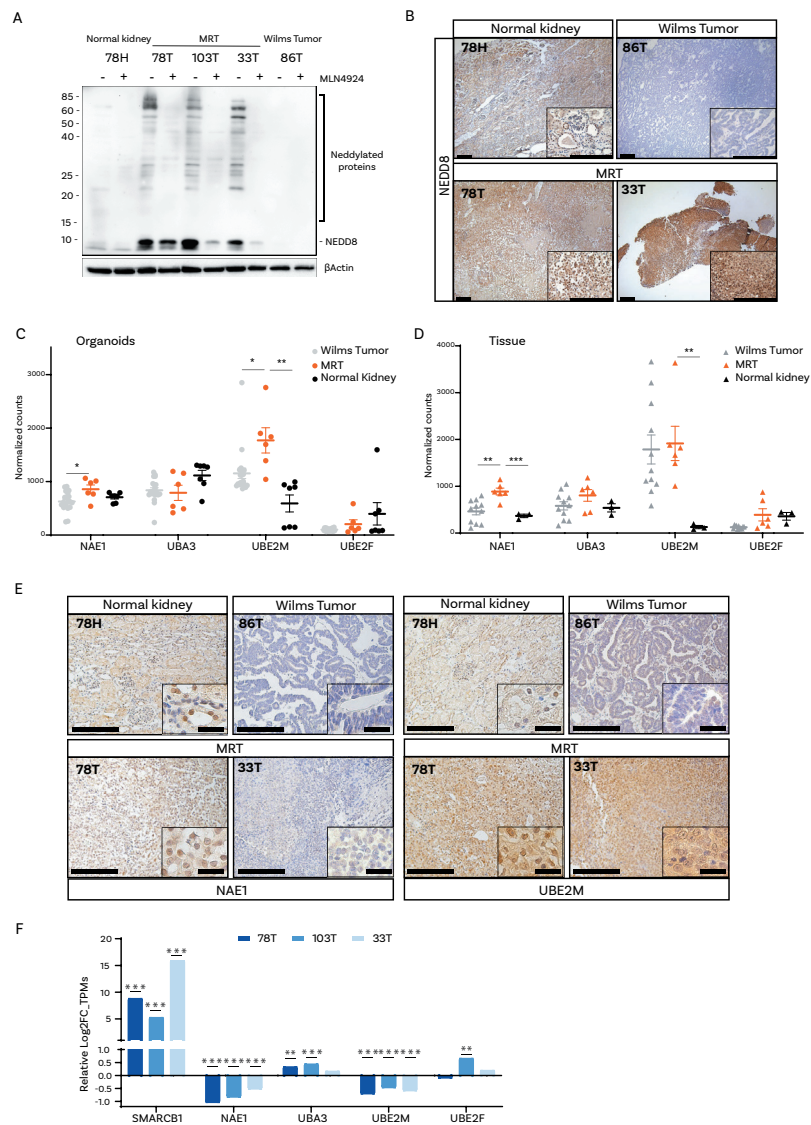
Figure 3. MRT demonstrate increased neddylation activity. A. Western blot analysis of NEDD8 and neddylated protein expression in the indicated organoid cultures treated for 120 h with 50 nM MLN4924 or DMSO. ßactin was included as a loading control. See also Supplementary Figure 3G. **B.** NEDD8 immunostaining on normal kidney (top, left), Wilms tumor (top, right), and MRT tissues (bottom). Scale bars: 200 μm. **C.** Normalized counts of E1 (*NAE1* and *UBA3*) and E2 (*UBE2M* and *UBE2F*) enzymes involved in neddylation pathway. Data are represented as means ± SEM (n≥7). Depicted are values for MRT, Wilms tumor, and normal kidney derived organoids. p values were calculated using a two-tailed unpaired Student's t test. *p < 0.05, **p < 0.01. **D.** Same analysis as in C conducted on tissue samples. Data are represented as

means ± SEM (n≥3). p values were calculated using a two-tailed unpaired Student's t test. *p < 0.05, **p < 0.01, ***p < 0.001. **E.** Immunostaining for enzyme NAE1 (left panel) and UBE2M (right panel) on normal kidney, Wilms tumor, and MRT tissues. Scale bars: 200 μm, zoom in: 25 μm. **F.** Log2-fold change values of enzymes involved in neddylation pathway generated from three *SMARCB1*-reconstituted MRT organoid lines over respective luciferase controls. Log2-fold change values were calculated using the R package DESeq2 starting from transcripts per kilobase million (TPM) values. Experiments were conducted in biological duplicates. Adjusted p values were calculated using the Wald significance test with multiple-testing corrections. **p < 0.01, ***p < 0.001.

We further corroborated these results by western blot (organoids) and immunohistochemistry analyses (tissues) (**Figure 3E** and **Supplementary Figure 3K**). MRTs are typically driven by the inactivation of *SMARCB1*[2,3]. Analyzing gene expression levels of E1 and E2 enzymes in MRT organoids in which *SMARCB1* expression was reconstituted by lentiviral transduction[20] revealed that mRNA levels of *NAE1* and *UBE2M*, the same enzymes we found to be specifically upregulated in MRTs (**Figure 3C,D**), were significantly downregulated upon *SMARCB1* re-expression (**Figure 3F**). Together, our data show that MRTs demonstrate elevated neddylation, which is potentially caused by an increase in E1 and E2 enzyme expression driven by *SMARCB1* loss.

Recent reports have shown that blocking neddylation by treatment with MLN4924 activates UPR[35,36], a cellular mechanism induced by ER stress and the consequent accumulation of misfolded proteins[37,38]. When cells are not able to alleviate severe ER stress, the UPR triggers an apoptotic response via the upregulation of the pro-apoptotic transcription factor CHOP[35]. Interestingly, it has been reported that MRTs display enrichment for UPR gene expression compared with other tumor entities, suggesting that MRTs are characterized by baseline activation of the UPR[17]. By gene set enrichment analysis (GSEA) on bulk RNA-seq data[14], we confirmed that the UPR signature is significantly upregulated in MRT tissues and organoids as compared with Wilms tumors, pediatric renal cell carcinoma and normal kidney (**Figure 4A–D**). To further validate the presence of ER stress and UPR response in MRTs, we performed transmission electron microscopy (TEM) on normal kidney and MRT organoid samples. Although kidney organoid cells showed a healthy-structured ER (**Figure 4E, top left,** and **Supplementary Figure 3L**), MRT cells displayed more, but thinner and fragmented, ER, accompanied by an increased presence of lipid droplets and helical ER filaments; altogether, these are signs of ER stress and UPR activation[40-44] (**Figure 4E, top right,** and **Supplementary Figure 3L**).
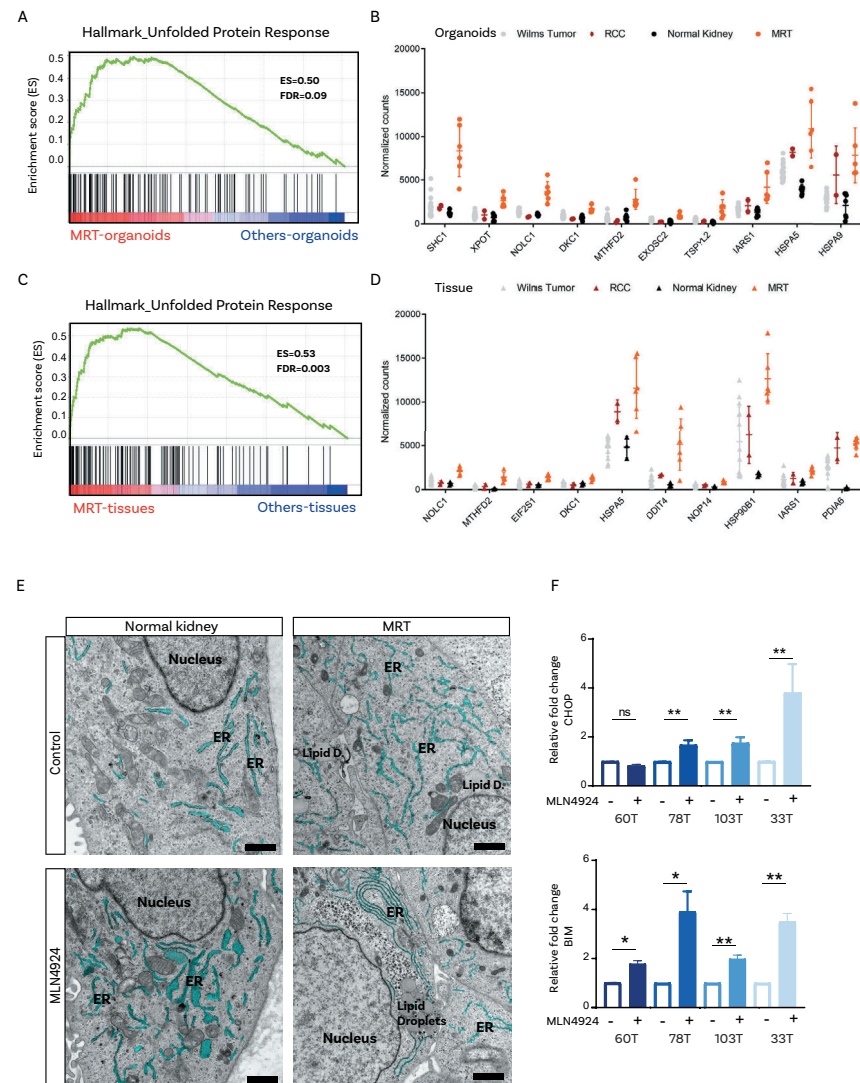
Figure 4. MLN4924 triggers a UPR-mediated apoptotic response. A. GSEA on bulk RNA-seq data, demonstrating enrichment of UPR gene expression in MRT organoids versus Wilms tumor, renal cell carcinoma, and normal kidney organoids (MRT, n = 6; others, n = 30). **B.** Normalized counts of top-10 upregulated genes involved in the UPR as a result of the analysis described in A. Data are represented as means ± SD (n≥2). Depicted are values for MRT, Wilms tumor, renal cell carcinoma, and normal kidney derived organoids. **C.** Same analysis as in A, but in patient MRT tissues versus Wilms tumors, renal cell carcinoma, and normal kidney tissues (biological replicates: MRT, n = 6; others, n = 16) **D.** Normalized count of top-10 upregulated genes involved in the UPR as a result of the analysis described in C. Data are represented as means ± SD (n≥2). Depicted are values for MRT, Wilms tumor, renal cell carcinoma, and normal kidney tissues. **E.** Representative TEM images of normal kidney and MRT

organoids. (Top) Pictures of baseline/control status; (bottom) the effects of treatment with 50 nM MLN4924 for 48 h. Nuclei, ER, and lipid droplets are marked in the figure. The ER has been manually segmented and pseudo-colored for improved visualization (cyan). Scale bars: 500 nm. Additional images can be found in Supplementary Figure 3L. **F.** Relative *CHOP* (top) and *BIM* (bottom) expression in four MRT organoid lines upon treatment with 1 μM MLN4924 for 24 h, normalized to DMSO. Data are represented as means ± SD (n≥3 independent experiments, each consisting of an average of three technical replicates). p values were calculated using a two-tailed unpaired Student's t test. *p < 0.05, **p < 0.01.

Furthermore, we tested the effect of MLN4924 on MRT and normal kidney organoids by TEM. Although normal kidney organoids displayed minor signs of ER stress upon MLN4924 treatment, such as ER dilation, and a minor formation of lipid droplets (**Figure 4E, bottom left,** and **Supplementary Figure 3L**), MRT organoids presented with a dramatic accumulation of lipid droplets and extreme ER phenotypes (fragmented, disorganized, and enlarged; presence of helical fragments or completely missing ER) (**Figure 4E**, **bottom right,** and **Supplementary Figure 3L**).

These MRT-specific phenotypes were also accompanied by the first signs of apoptosis and necrosis (**Supplementary Figure 3L**). To further corroborate the UPR-mediated apoptotic response in MRT upon MLN4924 treatment, we examined the expression of the downstream UPR effector *CHOP* in MRT organoids using qRT-PCR. Compared with the untreated control, significant upregulation of *CHOP* mRNA levels was observed in most of the tested MRT organoid lines upon treatment with MLN4924 (**Figure 4F**). In addition to *CHOP* induction, we observed a significant induction of the apoptotic marker *BIM* (**Figure 4F**), previously described to be activated by *CHOP* in the UPR-mediated apoptotic response[45]. Altogether, these results provide further evidence that MRT organoids experience ER stress and an UPR signature at baseline, which is further induced upon MLN4924 treatment.

MLN4924 inhibits MRT growth and increases survival *in vivo*

After demonstrating the efficacy of MLN4924 *in vitro*, we set out to investigate whether MLN4924 showed activity against MRT *in vivo*. For this purpose, we established an *in vivo* MRT xenograft model by subcutaneous injection of MRT organoids in immunocompromised mice, yielding tumors histologically recapitulating patient MRTs (**Supplementary Figure 4A**). To demonstrate *in vivo* efficacy of MLN4924 in MRT, we subcutaneously injected MRT organoids in immunocompromised mice and administered either vehicle or MLN4924 at 60 mg/kg BID for 5 weeks (five cycles of 5 days on/2 days off) when tumors reached a volume of ~250 mm³ (**Figure 5A**)[29].
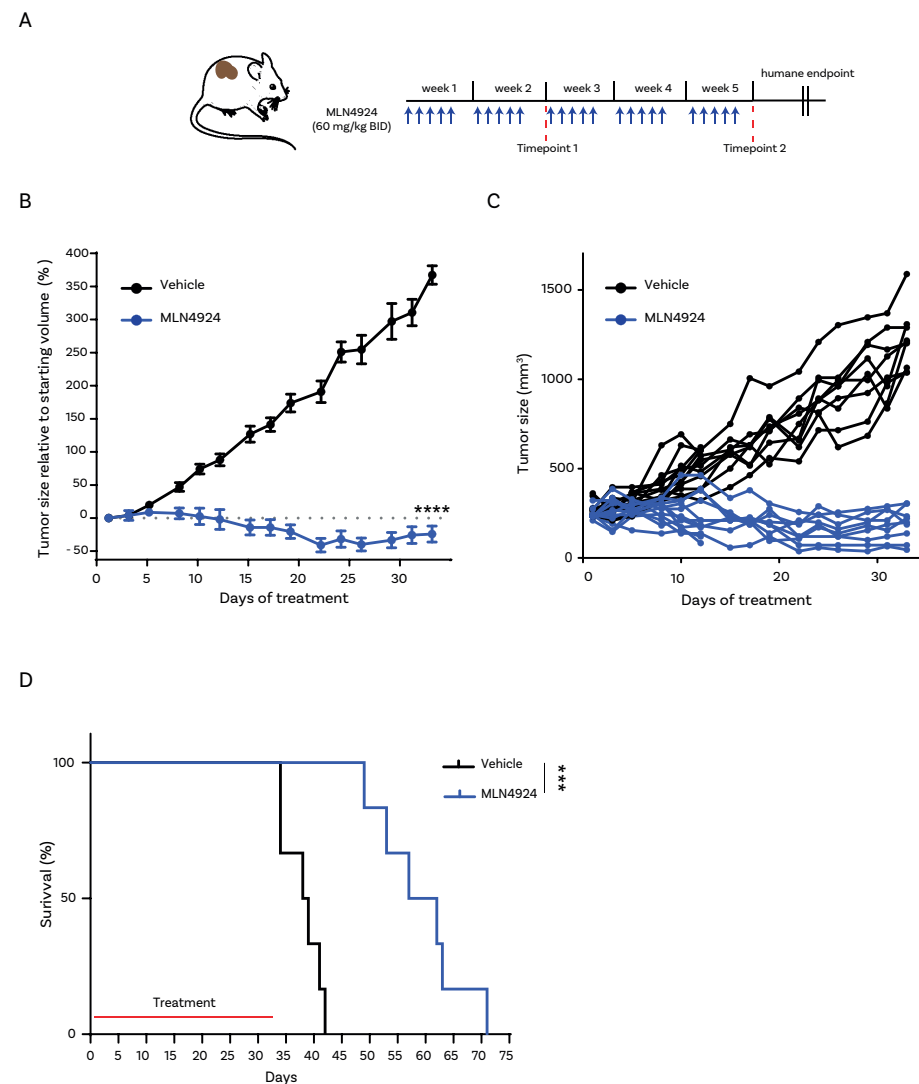
A

B

C

D

Figure 5. MLN4924 demonstrates *in vivo* efficacy in an MRT xenograft model. A. Experimental overview of *in vivo* MLN4924 testing. Twenty-four mice (12 per experimental arm) bearing subcutaneous MRT tumors were injected with either 60 mg/kg BID MLN4924 or vehicle for a total of five cycles (5 days on, 2 days off), as previously described[29]. After completion of two cycles of treatment, as well as at the end of treatment, three mice per arm were sacrificed (time point, 1; time point, 2). The six mice left per arm were used for overall survival studies. **B.** MRT tumor growth in mice treated with either vehicle (black) or 60 mg/kg BID MLN4924 (blue) for up to five cycles. Values depicted are relative to the tumor volume at the start of treatment. Data are represented as means ± SEM (n = 12 until time point 1; n = 9 until time point 2). p value was calculated using a two-tailed unpaired Student's t test. ****p < 0.0001. **C.** MRT tumors volume for single mice in treatment as described in B. **D.** Kaplan-Meier survival

analysis of mice treated as described in A. n = 6 mice per arm. p value was calculated using a two-tailed unpaired Student's t test. ***p < 0.001.

To demonstrate that the *in vitro* observed drug responses recapitulated the *in vivo* response, we also tested the effects of the mTOR inhibitor temsirolimus, showing a cytostatic effect *in vitro* (**Figure 2B, Supplementary Figure 3B, E and F**)[20], in MRT xenografts (5 mg/kg for six cycles of 5 days on/2 days off for 6 weeks). Temsirolimus treatment resulted in a significantly decreased growth rate of the MRT tumors compared with vehicle-treated mice (**Supplementary Figure 4B**). However, tumors still progressed under treatment, indicative of a cytostatic effect. Indeed, histological analysis of the tumors upon treatment termination revealed decreased proliferation and no apparent increase in apoptotic marker expression (**Supplementary Figure 4C**). Instead, we observed significant shrinkage of tumor volume after two to three cycles of MLN4924 treatment, suggesting a cytotoxic effect of MLN4924 on MRT *in vivo* (**Figure 5B,C**). After that, tumor size remained stable during the course of the treatment. In line with that, no dramatic increase in the percentage of cleaved caspase-3-positive cells could be observed, possibly because the tumor size had stabilized at the time of harvesting the tumors (**Supplementary Figure 4D**). Thus, the observed *in vitro* responses of MRT to mTOR and neddylation inhibition were recapitulated *in vivo*, further confirming the predictive value of *in vitro* organoid drug sensitivity for *in vivo* drug response. Furthermore, NEDD8 immunostaining on MRT tissues from vehicle- and MLN4924-treated mice showed a decrease in total NEDD8 levels in MLN4924-treated mice compared with vehicle, indicative of an on-target effect of the treatment (**Supplementary Figure 4E**). Finally, mice treated with MLN4924 showed a significant increase in survival compared with vehicle-treated mice (**Figure 5D**). Histological characterization of kidneys, liver, small intestine, and body weight measurements did not reveal any signs of treatment-related toxicity in MLN4924-treated mice (**Supplementary Figure 5A–D**). In conclusion, using drug screens on patient-derived normal and tumor organoids, we found that the neddylation inhibitor MLN4924 inhibits MRT growth *in vitro* and *in vivo*, supporting future clinical investigation of this compound for the treatment of children with MRT.

Discussion

MRT is an aggressive and often fatal childhood malignancy. Even though patients are treated with intense multimodal therapy, in many cases, tumors become resistant to the treatment. In our study, we found that the neddylation inhibitor MLN4924 has a cytotoxic effect on MRTs specifically. We found an increased neddylation pathway and a UPR signature in MRT organoids and patient tissues, suggesting that neddylation might be an interesting therapeutic target in MRTs, which merits further evaluation. We confirmed our *in vitro* results with an *in vivo* study in an MRT PDX model generated by subcutaneous injection of MRT organoids. To exclude the *in vitro* organoid step from selecting for specific subpopulations of MRT cells, PDX models directly derived from patient tissues could be used. Moreover, tumor growth dynamics are known to be influenced by the microenvironment. Therefore, orthotopic MRT PDX models may provide a more-representative model than the widely used subcutaneous models. Lastly, PDX models of other tumor entities may be used to further test the MRT-specific effects of MLN4924. Patient-derived organoids are a rapidly emerging model for studying cancer biology and identifying therapeutic targets[8,15]. Growing organoids from healthy tissues and exploiting them for drug screening purposes in parallel with tumor organoids, potentially allows for the identification of therapeutic agents targeting tumor cells while leaving healthy cell unharmed[12]. Indeed, recent studies have demonstrated that kidney, hepatocytes, and oral mucosa organoids can be exploited for nephrotoxicity, hepatotoxicity, and oral toxicity testing, respectively[46-48]. Using a similar strategy, we screened kidney, hepatocytes, and small-intestine-derived organoids, which allowed us to find MRT-specific drug vulnerabilities, thereby limiting the possibility of toxic effects of MLN4924 in these healthy tissues. MLN4924, or Pevonedistat, is currently being investigated in phase I–III clinical trials as a single agent (and in combination) for the treatment of different types of adult cancer[49,50]. Promising results from the phase I and II trials recently led to the initiation of the first trial of MLN4924 in pediatric solid and brain tumors, in combination with irinotecan and temozolomide (clinicaltrials.gov: NCT03323034). Our data suggest that monotherapy treatment with MLN4924 induces partial tumor regression but is likely not sufficient to induce complete tumor regression. Therefore, combining MLN4924 with other chemotherapeutic agents could be an interesting therapeutic strategy to explore further. Along the same lines, testing MLN4924 in combination with the current standard-of-care treatment could be of interest. Lastly, given the ability of MLN4924 to cross the blood brain barrier, neddylation inhibition could poten-

tially be applied for the treatment of patients with atypical teratoid rhabdoid tumors (ATRTs) as well[51].

STAR Methods

Data and code availability. Whole genome and RNA sequencing data have been deposited to the European Genome-Phenome Archive (www.ebi.ac.uk/ ega/). Accession number is pending. DNA methylation data has been deposited to GEO (www.ncbi.nlm.nih.gov/geo/) under accession number GSE178737.

Animals. Mouse experiments were conducted in agreement with the Animal Welfare Committee of the Royal Netherlands Academy of Arts and Sciences, and the Netherlands Cancer Institute, The Netherlands. 8-12 weeks old NOD-Scid IL2Rg-null mice, 50% male and 50% females, were used as acceptors for subcutaneous injections of MRT organoids. Mice were stratified into groups without blinding. Sample size were calculated using statistical power analysis.

Patient-derived organoid lines. Experiments with human material were approved by the medical ethical committee of the Erasmus Medical Center (Rotterdam, the Netherlands) and Princess Máxima Center for Pediatric Oncology (Utrecht, the Netherlands). Informed consent was obtained from the parents of all participants (SIOP 2001, UMBRELLA and ITHER studies). Patient-derived organoids cultures have been established with protocols previously described and previously characterized[14]. Briefly, rhabdoid tumor tissues were minced into 1 - mm³ pieces, digested with collagenase (1 mg ml-1,Sigma, C9407) supplemented with Rho-kinase inhibitor Y-27632 (10 μM, Abmole) for 45 minutes at 37 °C. The digested tissue was washed with AdDF+++ and plated in factor-reduced BME (Trevigen, 3533-010-02). MRT and normal kidney organoids were cultured in BME, topped with kidney organoid medium (AdDF+++ supplemented with 1.5% B27 supplement (Gibco), 10% R-spondin-conditioned medium, N-acetylcysteine (1.25 mM, Sigma), Rho-kinase inhibitor Y-27632 (10 μM, Abmole), FGF-10 (100 ng ml-1, Peprotech), A83-01 (5 μM, Tocris Bioscience) and EGF (50 ng ml-1, Peprotech)[24]. Small intestinal and hepatocyte organoids lines have been cultured in conditions previously described[22,23].

Whole genome sequencing and RNA sequencing. Tissue and organoid samples derived from patient 33T have been processed, sequenced and analyzed following the INFORM pipeline[52]. Briefly, whole genome sequencing was performed using 100ng of the Illumina adapter-containing libraries produced with the Agilent Sureselect Version 5 protocol. RNA sequencing libraries were prepared with the TruSeq

RNA Sample Preparation Kit v2 (Illumina) following the manufacturer's instructions. After library preparation all samples were 2x100bp paired-end sequenced on an Illumina HiSeq 4000. Whole genome read pairs were mapped to the 1000 Genomes Phase 2 assembly of the human reference genome (NCBI build 37.1) using the BWA aligner (version 0.6.2). RNA sequencing reads were mapped using the STAR algorithm version 2.3.0e onto the 1000 genomes reference sequence with Gencode version 17 transcript annotations. Whole genome sequencing coverage calculations considered all informative bases of the reference genome, excluding Ns, and were aggregated in 10kbp windows. Bulk RNA sequencing for *SMARCB1* re-expression line 33T has been performed and analyzed as previously described[20]. Bulk RNA sequencing data from different sources[14,24] was merged and normalized counts were generated with the R-package DESeq2 using the vst function[53]. The 2500 most variable genes were used for a principal component analysis of which the 5 first components were used as an input for the tSNE function[22] of the M3C R-package[54].

DNA methylation profiling. Tissue and organoid samples derived from patient 33T have been processed, sequenced and analyzed as previously described[20].

High throughput drug screening and validation. MRT organoids were digested into single cells 3 days prior to the screen. On the day of the screen, MRT organoids were harvested and washed in AdDF+++. Next, organoids were filtered using a 70 μm cell strainer (Falcon) and resuspended in 5% BME in kidney organoid medium. Afterwards, ~500 organoids per well were plated using the Multi-dropTM Combi Reagent Dispenser on repellent black 384-well plates (Corning) to which medium with compounds was added (6 different concentrations, 0.1nM to 10μM) using the Caliper Sciclone – Robotic Liquid Handling robot. Five days after drug addition, ATP levels were measured using CellTiter-Glo 3D (Promega) according to the manufacturer's instructions. Results were normalized to vehicle (100%). For the validation assays, 10 concentrations and 4 technical replicates were included. Drugs were dispensed with Tecan D300e Digital Dispenser. Normal kidney, small intestinal and hepatocytes organoids were prepared following the same protocol as for MRT organoids but plated in respective growth medium. AUC values were calculated with GraphPad Prism v7.04.

Regrowth assay. MRT organoids were dissociated and 5000 single cells were seeded in 70% BME in kidney organoid medium with the addition of different drugs (Sirolimus (MedChem Express), MLN4924 (MedChem Express) and doxorubicin (MedChem Express)) or DMSO (Sigma-Aldrich). Three different plates have been prepared for the experiment. Cell viability was measured for the first plate with CellTiter-Glo 3D reagent (Promega) according to manufacturer's instructions (T0). Five days after, cell viability was assessed for a second plate (T5). At the same time, medium was changed for medium without drugs in the third plate. Five days after drug removal, cell viability was measured again (T10). Results were normalized to the DMSO control of T5 (100%).

Annexin V/DAPI double staining. Organoids were harvested and plated in 5% BME in kidney organoid medium and treated with either DMSO, MLN4924 50nM or Sirolimus 2nM. After 120h, organoids and supernatant were harvested. Organoids were dissociated into single-cell suspensions using TrypLE Express (Thermo Fisher) with the addition of Rho-kinase inhibitor Y-27632. Single-cell suspensions were stained with APC-AnnexinV (BD Biosciences, # 640920) and DAPI (Thermo Fisher, # D9542) in Annexin V binding buffer with the addition of 2.5mM Ca^{2+}. Cells were acquired with Beckman Cytoflex LX flow cytometer. Data was analyzed with software Kaluza analysis v2.1. AnnexinV positive cell index was calculated by normalizing the percentages to DMSO controls.

Western blot. Western blot on organoids was performed as described[22]. NEDD8 (Cell Signaling Technology, #2754), βActin (Abcam, ab-6276), NAE1 (Thermo Fisher, #PA5-59836), UBE2M (Abcam, ab-109507), P21 (Santa Cruz, #SC6246), WEE1 (Santa Cruz, #SC5285) and GAPDH (Abcam, ab-9485) were used as primary antibodies.

Histology and immunohistochemistry. Tissues and organoids were fixed in 4% paraformaldehyde, dehydrated and embedded in paraffin. Immunostaining was performed according to standard protocols on 4 μm sections. The following primary antibodies were used for immunohistochemical staining: NEDD8 (Cell Signaling Technology, #2754), Ki67 (Monosan, MONX10283), cleaved caspase 3 (Cell Signaling Technology, #9661), NAE1 (Thermo Fisher, #PA5-59836) and UBE2M (Abcam, ab-109507). Imaging was performed using Leica DMi8 microscope.

3D immunofluorescence staining. Normal kidney and MRT organoids were disrupted into single cells. Three days later, organoids were harvested and plated in a chambered coverslip (IBIDI, #80826) in a slurry of 5% BME with the addition of DMSO or 50nM MLN4924. After 120h, samples were fixated and 3D imaging on organoids was performed as described[55]. The following antibodies were used: Cleaved caspase 3 (Cell Signaling Technology, #9661), Alexa Fluor 647 phalloidin (Thermo Fisher, # A22287), DAPI (Thermo Fisher, # D9542). Imaging was performed using Leica SP8 microscope.

Resin Electron Microscopy. Organoids - cultured in 5% BME slurry with either DMSO or 50nM MLN4924 - were harvested after 48 hours and fixed in a mixture of 2% formaldehyde and 2.5% glutaraldehyde in 0.1M phosphate buffer pH 7.4 at room temperature for 2 hours. Afterwards, organoids were rinsed and stored

in 1% formaldehyde in 0.1M Phosphate Buffer pH 7.4 at 4°C overnight. Organoids were rinsed again with 0.1M Phosphate Buffer pH 7.4, and post-fixation was performed with 1% OsO4, 1.5% K3Fe(III)(CN)6 in 1M Phosphate Buffer PH 7.4 for 2 hours. Organoids were then dehydrated in a series of acetone (70% overnight, 90% 15 min, 96% 15 min, 100% 3x 30 min), and embedded in Epon (SERVA). Ultrathin sections of 65 nm were cut (Leica Ultracut UCT), collected on formvar and carbon coated TEM grids and stained with uranyl acetate and lead citrate (Leica AC20). Micrographs were collected on a JEM1010 (JEOL) equipped with a Veleta 2k×2k CCD camera (EMSIS, Munster, Germany) or on a Tecnai12 (FEI Thermo Fisher) equipped with a Veleta 2k×2k CCD camera (EMSIS, Munster, Germany) and operating SerialEM software.

RNA isolation, cDNA preparation and qPCR. Organoids were harvested in RLT lysis buffer and RNA was isolated using the Qiagen RNeasy kit (Qiagen) following manufacturer's instruction. The extracted RNA was used for cDNA production using GoScript reverse transcriptase (Promega) following manufacturer's instructions. qPCR was performed using IQ SYBR green mix (Biorad) following manufacturer's instructions. Results were calculated using the ΔΔCt method. Primer sequences: NOXA_FW (GTGTGCTACTCAACTCAG), NOXA_RV (ATTC CTCTCAATTACAATGC)[56], P21_FW (TACCCTTGTGCCTCGCTCAG), P21_RV (GAGAAGATCAGCCGGCGTTT)[22], WEE1_FW (ATTTCTCTGCGTGGGCAGAAG), WEE1_RV (CAAAAGGAGATCCTTCAACTCTGC)[57], BIM_FW (ATGTCTGACTCTGACTCTCG), BIM_RV (CCTTGTGGCTCTGTCTGTAG)[58], CHOP_FW (ACCAAGGGAGAACCAGGAAACG), CHOP_RV (TCACCATTCGGTCAATCAGAGC)[59], GAPDH_FW (TGCACCACCAACTGCTTAGC), GAPDH_RV (GGCA TGGACTGTGGTCA TGAG)[60].

***In vivo* drug study**. 250 000 small size MRT organoids were harvested and implanted subcutaneously in the right flank of NOD-Scid IL2Rgnull mice, in a solution 1:1 with BME. When tumors reached approximately 250mm³, mice were randomized to MLN4924 (n=12 mice), temsirolimus (n=9 mice) or respective vehicles. MLN4924 (60mg/kg) or vehicle (10% cyclodextrin) were injected subcutaneously twice daily for 35 days (5 cycles of 5 days on, 2 days off). Temsirolimus (5mg/kg) or vehicle (saline) were administered via intraperitoneal injection once a day for 42 days (6 cycles of 5 days on, 2 days off). Tumor volume was monitored 3 times a week by caliper measurement. When reaching halfway and the end of the treatment, 3 mice per arm were sacrificed for histological analysis of the tumors and organs. The other 9/6 mice were kept for survival studies. Mice were sacrificed when reaching humane endpoint (tumor >1500 mm³).

Quantification and statistical analysis. For comparison between two sample groups, statistical analysis was conducted using the two-tailed unpaired Student's t tests. All statistical data can be found in the figure legends.

Acknowledgements

Competing interests

Declaration of interests: The authors declare no competing interests.

References

1. Weeks, D.A., Beckwith, J.B., Mierau, G.W., and Luckey, D.W. (1989). Rhabdoid tumor of kidney: a report of 111 cases from the National Wilms' Tumor Study Pathology Center. Am. J. Surg. Pathol. 13, 439–458.

2. Biegel, J.A., Zhou, J.-Y., Rorke, L.B., Stenstrom, C., Wainwright, L.M., and Fogelgren, B. (1999). Germ-line and acquired mutations of INI1 in atypical teratoid and rhabdoid tumors. Cancer Res. 59, 74–79.

3. Versteege, I., Se´venet, N., Lange, J., Rousseau-Merck, M.-F., Ambros, P., Handgretinger, R., Aurias, A., and Delattre, O. (1998). Truncating mutations of hSNF5/INI1 in aggressive paediatric cancer. Nature 394, 203–206.

4. Chun, H.E., Lim, E.L., Heravi-Moussavi, A., Saberi, S., Mungall, K.L., Bilenky, M., Carles, A., Tse, K., Shlafman, I., Zhu, K., et al. (2016). Genome-wide profiles of extra-cranial malignant rhabdoid tumors reveal heterogeneity and dysregulated developmental pathways. Cancer Cell 29, 394–406.

5. Lee, R.S., Stewart, C., Carter, S.L., Ambrogio, L., Cibulskis, K., Sougnez, C., Lawrence, M.S., Auclair, D., Mora, J., Golub, T.R., et al. (2012). A remarkably simple genome underlies highly malignant pediatric rhabdoid cancers. J. Clin. Invest. 122, 2983–2988.

6. Kerl, K., Holsten, T., and Fruhwald, M.C. (2013). Rhabdoid tumors: clinical approaches and molecular targets for innovative therapy. Pediatr. Hematol. Oncol. 30, 587–604.

7. Reinhard, H., Reinert, J., Beier, R., Furtwa¨ngler, R., Alkasser, M., Rutkowski,p S., Fruhwald, M., Koscielniak, E., Leuschner, I., Kaatsch, P., and Graf, N. (2008). Rhabdoid tumors in children: prognostic factors in 70 patients diagnosed in Germany. Oncol. Rep. 19, 819–823.

8. Drost, J., and Clevers, H. (2018). Organoids in cancer research. Nat. Rev. Cancer 18, 407–418.

9. Ganesh, K., Wu, C., O'Rourke, K.P., Szeglin, B.C., Zheng, Y., Sauve´, C.G., Adileh, M., Wasserman, I., Marco, M.R., Kim, A.S., et al. (2019). A rectal cancer organoid platform to study individual responses to chemoradiation. Nat. Med. 25, 1607–1614.

10. Ooft, S.N., Weeber, F., Dijkstra, K.K., McLean, C.M., Kaing, S., van Werkhoven, E., Schipper, L., Hoes, L., Vis, D.J., van de Haar, J., et al. (2019). Patient- derived organoids can predict response to chemotherapy in metastatic colorectal cancer patients. Sci. Transl. Med. 11, eaay2574.

11. Tiriac, H., Belleau, P., Engle, D.D., Plenker, D., Deschˆenes, A., Somerville, T.D.D., Froeling, F.E.M., Burkhart, R.A., Denroche, R.E., Jang, G.-H., et al. (2018). Organoid profiling identifies common responders to chemotherapy in pancreatic cancer. Cancer Discov. 8, 1112–1129.

12. Vlachogiannis, G., Hedayat, S., Vatsiou, A., Jamin, Y., Ferna´ndez-Mateos, J., Khan, K., Lampis, A., Eason, K., Huntingford, I., Burke, R., et al. (2018). Patient-derived organoids model treatment response of metastatic gastrointestinal cancers. Science 359, 920–926.

13. Yao, Y., Xu, X., Yang, L., Zhu, J., Wan, J., Shen, L., Xia, F., Fu, G., Deng, Y., Pan, M., et al. (2020). Patient-derived organoids predict chemoradiation responses of locally advanced rectal cancer. Cell Stem Cell 26, 17–26.e6.

14. Calandrini, C., Schutgens, F., Oka, R., Margaritis, T., Candelli, T., Mathijsen, L., Ammerlaan, C., van Ineveld, R.L., Derakhshan, S., de Haan, S., et al. (2020). An organoid biobank for childhood kidney cancers that captures disease and tissue heterogeneity. Nat. Commun. 11, 1310.

15. Ooms, A.H.A.G., Calandrini, C., de Krijger, R.R., and Drost, J. (2020). Organoid models of childhood kidney tumours. Nat. Rev. Urol. 17, 311–313.

16. Chun, H.-J.E., Johann, P.D., Milne, K., Zapatka, M., Buellesbach, A., Ishaque, N., Iskar, M., Erkek, S., Wei, L., and Tessier-Cloutier, B. (2019). Identification and analyses of extra-cranial and cranial rhabdoid tumor molecular subgroups reveal tumors with cytotoxic T cell infiltration. Cell Rep. 29, 2338–2354.e7.

17. Carugo, A., Minelli, R., Sapio, L., Soeung, M., Carbone, F., Robinson, F.S., Tepper, J., Chen, Z., Lovisa, S., and Svelto, M. (2019). p53 is a master regulator of proteostasis in SMARCB1-deficient malignant rhabdoid tumors. Cancer Cell 35, 204–220.e9.

18. Muscat, A., Popovski, D., Jayasekara, W.S.N., Rossello, F.J., Ferguson, M., Marini, K.D., Alamgeer, M., Algar, E.M., Downie, P., Watkins, D.N., et al. (2016). Low-dose histone deacetylase inhibitor treatment leads to tumor growth arrest and multi-lineage differentiation of malignant rhabdoid tumors. Clin. Cancer Res. 22, 3560–3570.

19. Tran, H.M., Wu, K.-S., Sung, S.-Y., Changou, C.A., Hsieh, T.-H., Liu, Y.-R., Liu, Y.-L., Tsai, M.-L., Lee, H.-L., Hsieh, K.L.-C., et al. (2020). Upregulation of protein synthesis and proteasome degradation confers sensitivity to proteasome inhibitor bortezomib in myc-atypical teratoid/rhabdoid tumors. Cancers (Basel) 12, 752.

20. Custers, L., Khabirova, E., Coorens, T.H.H., Oliver, T.R.W., Calandrini, C., Young, M.D., Vieira Braga, F.A., Ellis, P., Mamanova, L., Segers, H., et al. (2021). Somatic mutations and single-cell transcriptomes reveal the root of malignant rhabdoid tumours. Nat. Commun. 12, 1407.

21. Moon, J.-H., Shin, J.-S., Hong, S.-W., Jung, S.-A., Hwang, I.-Y., Kim, J.H., Choi, E.K., Ha, S.-H., Kim, J.-S., Kim, K.-M., et al. (2015). A novel small-molecule IAP antagonist, AZD5582, draws Mcl-1 down-regulation for induction of apoptosis through targeting of cIAP1 and XIAP in human pancreatic cancer. Oncotarget 6, 26895–26908.

22. Drost, J., van Jaarsveld, R.H., Ponsioen, B., Zimberlin, C., van Boxtel, R., Buijs, A., Sachs, N., Overmeer, R.M., Offerhaus, G.J., Begthel, H., et al. (2015). Sequential cancer mutations in cultured human intestinal stem cells. Nature 521, 43–47.

23. Hu, H., Gehart, H., Artegiani, B., Lo¨pez-Iglesias, C., Dekkers, F., Basak, O., van Es, J., Chuva de Sousa Lopes, S.M., Begthel, H., Korving, J., et al. (2018). Long-term expansion of functional mouse and human hepatocytes as 3D organoids. Cell 175, 1591–1606.e19.

24. Schutgens, F., Rookmaaker, M.B., Margaritis, T., Rios, A., Ammerlaan, C., Jansen, J., Gijzen, L., Vormann, M., Vonk, A., Viveen, M., et al. (2019). Tubuloids derived from human adult kidney and urine for personalized disease modeling. Nat. Biotechnol. 37, 303–313.

25. Swords, R.T., Coutre, S., Maris, M.B., Zeidner, J.F., Foran, J.M., Cruz, J., Erba, H.P., Berdeja, J.G., Tam, W., Vardhanabhuti, S., et al. (2018). Pevonedistat, a first-in-class NEDD8-activating enzyme inhibitor, combined with azacitidine in patients with AML. Blood 131, 1415–1424.

26. Nawrocki, S.T., Griffin, P., Kelly, K.R., and Carew, J.S. (2012). MLN4924: a novel first-in-class inhibitor of NEDD8-activating enzyme for cancer therapy. Expert Opin. Investig. Drugs 21, 1563–1573.

27. Enchev, R.I., Schulman, B.A., and Peter, M. (2015). Protein neddylation: beyond cullin-RING ligases. Nat. Rev. Mol. Cell Biol. 16, 30–44.

28. Kamitani, T., Kito, K., Nguyen, H.P., and Yeh, E.T. (1997). Characterization of NEDD8, a developmentally down-regulated ubiquitin-like protein. J. Biol. Chem. 272, 28557–28562.

29. Soucy, T.A., Smith, P.G., Milhollen, M.A., Berger, A.J., Gavin, J.M., Adhikari, S., Brownell, J.E., Burke, K.E., Cardin, D.P., Critchley, S., et al. (2009). An inhibitor of NEDD8-activating enzyme as a new approach to treat cancer. Nature 458, 732–736.

30. Godbersen, J.C., Humphries, L.A., Danilova, O.V., Kebbekus, P.E., Brown, J.R., Eastman, A., and Danilov, A.V. (2014). The Nedd8-activating enzyme inhibitor MLN4924 thwarts microenvironment-driven NF-kB activation and induces apoptosis in chronic lymphocytic leukemia B cells. Clin. Cancer Res. 20, 1576–1589.

31. Jia, L., Li, H., and Sun, Y. (2011). Induction of p21-dependent senescence by an NAE inhibitor, MLN4924, as a mechanism of growth suppression. Neoplasia 13, 561–569.

32. Knorr, K.L., Schneider, P.A., Meng, X.W., Dai, H., Smith, B.D., Hess, A.D., Karp, J.E., and Kaufmann, S.H. (2015). MLN4924 induces Noxa upregulation in acute myelogenous leukemia and synergizes with Bcl-2 inhibitors. Cell Death Differ. 22, 2133–2142.

33. Liu, X., Jiang, Y., Wu, J., Zhang, W., Liang, Y., Jia, L., Yu, J., Jeong, L.S., and Li, L. (2017). NEDD8-activating enzyme inhibitor, MLN4924 (Pevonedistat) induces NOXA-dependent apoptosis through up-regulation of ATF-4. Biochem. Biophys. Res. Commun. 488, 1–5.

34. Mackintosh, C., García-Domínguez, D.J., Ordonez, J.L., Ginel-Picardo, A., Smith, P.G., Sacristán, M.P., and de Alava, E. (2013). WEE1 accumulation and deregulation of S-phase proteins mediate MLN4924 potent inhibitory effect on Ewing sarcoma cells. Oncogene 32, 1441–1451.

35. Chen, P., Hu, T., Liang, Y., Li, P., Chen, X., Zhang, J., Ma, Y., Hao, Q., Wang, J., Zhang, P., et al. (2016). Neddylation inhibition activates the extrinsic apoptosis pathway through ATF4–CHOP–DR5 axis in human esophageal cancer cells. Clin. Cancer Res. 22, 4145–4157.

36. McGrail, D.J., Garnett, J., Yin, J., Dai, H., Shih, D.J.H., Lam, T.N.A., Li, Y., Sun, C., Li, Y., Schmandt, R., et al. (2020). Proteome instability is a therapeutic vulnerability in mismatch repair-deficient cancer. Cancer Cell 37, 371–386.e12.

37. Cao, S.S., and Kaufman, R.J. (2012). Unfolded protein response. Curr. Biol. 22, R622–R626.

38. Hetz, C. (2012). The unfolded protein response: controlling cell fate decisions under ER stress and beyond. Nat. Rev. Mol. Cell Biol. 13, 89–102.

40. Bernales, S., McDonald, K.L., and Walter, P. (2006). Autophagy counterbalances endoplasmic reticulum expansion during the unfolded protein response. PLoS Biol. 4, e423.

41. Carter, S.D., Tran, N.-H., De Mazière, A., Ashkenazi, A., Klumperman, J., Jensen, G.J., and Walter, P. (2021). The stress-sensing domain of activated IRE1a forms helical filaments in narrow ER membrane tubes. bioRxiv, 2021.2002.2024.432779.

42. Ha, T.W., Jeong, J.H., Shin, H., Kim, H.K., Im, J.S., Song, B.H., Hanna, J., Oh, J.S., Woo, D.-H., Han, J., and Lee, M.R. (2020). Characterization of endoplasmic reticulum (ER) in human pluripotent stem cells revealed increased susceptibility to cell death upon ER stress. Cells 9, 1078.

43. Li, J., Ni, M., Lee, B., Barron, E., Hinton, D.R., and Lee, A.S. (2008). The unfolded protein response regulator GRP78/BiP is required for endoplasmic reticulum integrity and stress-induced autophagy in mammalian cells. Cell Death Differ. 15, 1460–1471.

44. Lu, M., van Tartwijk, F.W., Lin, J.Q., Nijenhuis, W., Parutto, P., Fantham, M., Christensen, C.N., Avezov, E., Holt, C.E., Tunnacliffe, A., et al. (2020). The structure and global distribution of the endoplasmic reticulum network are actively regulated by lysosomes. Sci. Adv. 6, eabc7209.

45. Puthalakath, H., O'Reilly, L.A., Gunn, P., Lee, L., Kelly, P.N., Huntington, N.D., Hughes, P.D., Michalak, E.M., McKimm-Breschkin, J., Motoyama, N., et al. (2007). ER stress triggers apoptosis by activating BH3-only protein Bim. Cell 129, 1337–1349.

46. Driehuis, E., Oosterom, N., Heil, S.G., Muller, I.B., Lin, M., Kolders, S., Jansen, G., de Jonge, R., Pieters, R., Clevers, H., and van den Heuvel-Eibrink, M.M. (2020). Patient-derived oral mucosa organoids as an in vitro model for methotrexate induced toxicity in pediatric acute lymphoblastic leukemia. PLoS ONE 15, e0231588.

47. Meng, Q. (2010). Three-dimensional culture of hepatocytes for prediction of drug-induced hepatotoxicity. Expert Opin. Drug Metab. Toxicol. 6, 733–746.

48. Takasato, M., Er, P.X., Chiu, H.S., Maier, B., Baillie, G.J., Ferguson, C., Parton, R.G., Wolvetang, E.J., Roost, M.S., Chuva de Sousa Lopes, S.M., and Little, M.H. (2015). Kidney organoids from human iPS cells contain multiple lineages and model human nephrogenesis. Nature 526, 564–568.

49. Sekeres, M.A., Fram, R.J., Hua, Z., and Ades, L. (2018). Phase 3 study of first line pevonedistat (PEV) + azacitidine (AZA) versus single-agent AZA in patients with higher-risk myelodysplastic syndromes (HR MDS), chronic myelomonocytic leukemia (CMML) or low-blast acute myelogenous leukemia (AML). J. Clin. Oncol. 36 (suppl), TPS7077.

50. Zhao, Y., Morgan, M.A., and Sun, Y. (2014). Targeting neddylation pathways to inactivate cullin-RING ligases for anticancer therapy. Antioxid. Redox Signal. 21, 2383–2400.

51. Hua, W., Li, C., Yang, Z., Li, L., Jiang, Y., Yu, G., Zhu, W., Liu, Z., Duan, S., Chu, Y., et al. (2015). Suppression of glioblastoma by targeting the overactivated protein neddylation pathway. Neuro-oncol. 17, 1333–1343.

52. Worst, B.C., van Tilburg, C.M., Balasubramanian, G.P., Fiesel, P., Witt, R., Freitag, A., Boudalil, M., Previti, C., Wolf, S., Schmidt, S., et al. (2016). Next generation personalised medicine for high-risk paediatric cancer patients - The INFORM pilot study. Eur. J. Cancer 65, 91–101.

53. Love, M.I., Huber, W., and Anders, S. (2014). Moderated estimation of fold change and dispersion for RNA-seq data with DESeq2. Genome Biol. 15, 550.

54. John, C.R., Watson, D., Russ, D., Goldmann, K., Ehrenstein, M., Pitzalis, C., Lewis, M., and Barnes, M. (2020). M3C: Monte Carlo reference-based consensus clustering. Sci. Rep. 10, 1816.

55. Dekkers, J.F., Alieva, M., Wellens, L.M., Ariese, H.C.R., Jamieson, P.R., Vonk, A.M., Amatngalim, G.D., Hu, H., Oost, K.C., Snippert, H.J.G., et al. (2019). High-resolution 3D imaging of fixed and cleared organoids. Nat. Protoc. 14, 1756–1771.

56. Drost, J., Mantovani, F., Tocco, F., Elkon, R., Comel, A., Holstege, H., Kerkhoven, R., Jonkers, J., Voorhoeve, P.M., Agami, R., and Del Sal, G. (2010). BRD7 is a candidate tumour suppressor gene required for p53 function. Nat. Cell Biol. 12, 380–389.

57. Wang, X., Zhang, W., Yan, Z., Liang, Y., Li, L., Yu, X., Feng, Y., Fu, S., Zhang, Y., Zhao, H., et al. (2016). Radiosensitization by the investigational NEDD8- activating enzyme inhibitor MLN4924 (pevonedistat) in hormone-resistant prostate cancer cells. Oncotarget 7, 38380–38391.

58. Delannoy, A., Wilhelm, E., Eilebrecht, S., Alvarado-Cuevas, E.M., Benecke, A.G., and Bell, B. (2018). BIM and NOXA are mitochondrial effectors of TAF6d-driven apoptosis. Cell Death Dis. 9, 70.

59. Toral, M., Jiménez, R., Romero, M., Robles-Vera, I., Sánchez, M., Salaices, M., Sabio, J.M., and Duarte, J. (2017). Role of endoplasmic reticulum stress in the protective effects of PPARb/d activation on endothelial dysfunction induced by plasma from patients with lupus. Arthritis Res. Ther. 19, 268.

60. Vandesompele, J., De Preter, K., Pattyn, F., Poppe, B., Van Roy, N., De Paepe, A., and Speleman, F. (2002). Accurate normalization of real-time quantitative RT-PCR data by geometric averaging of multiple internal control genes. Genome Biol. 3, H0034.

A

B

C
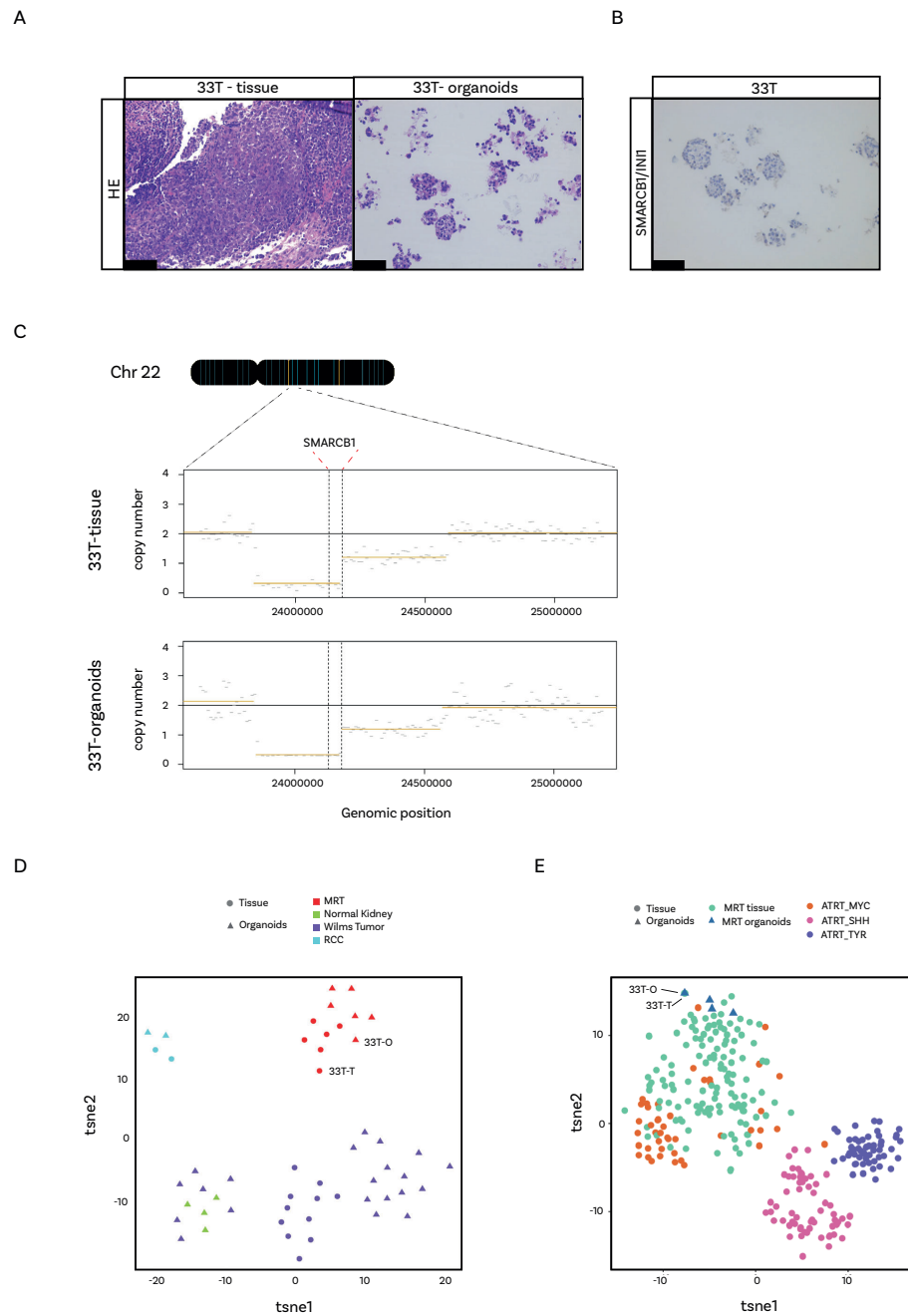
Supplementary Figure 1. 33T organoid line closely represent the tissue of origin. Related to Figure 1. A. Hematoxylin and Eosin staining on tissue (left) and organoids derived thereof (right) of soft tissue MRT 33T. Scale bars: 75 μm. **B**. INI1 (*SMARCB1*) staining of 33T MRT organoids. Scale bar: 75 μm. **C**. Whole Genome Sequencing results for 33T tissue and 33T organoid samples. Depicted are the copy number values for the genomic region harboring *SMARCB1* gene. **D**. tSNE representation of pediatric kidney cancer tissue and organoid gene expression profiles. Samples 33T tissue and organoid localize in the same cluster as other MRT samples. **E**. tSNE representation of cranial and extra-cranial MRT tissue and organoids DNA methylation profiles. Samples 33T tissue and 33T organoid localize together with other extra-cranial MRT, and display an highly similar profile.

D

E
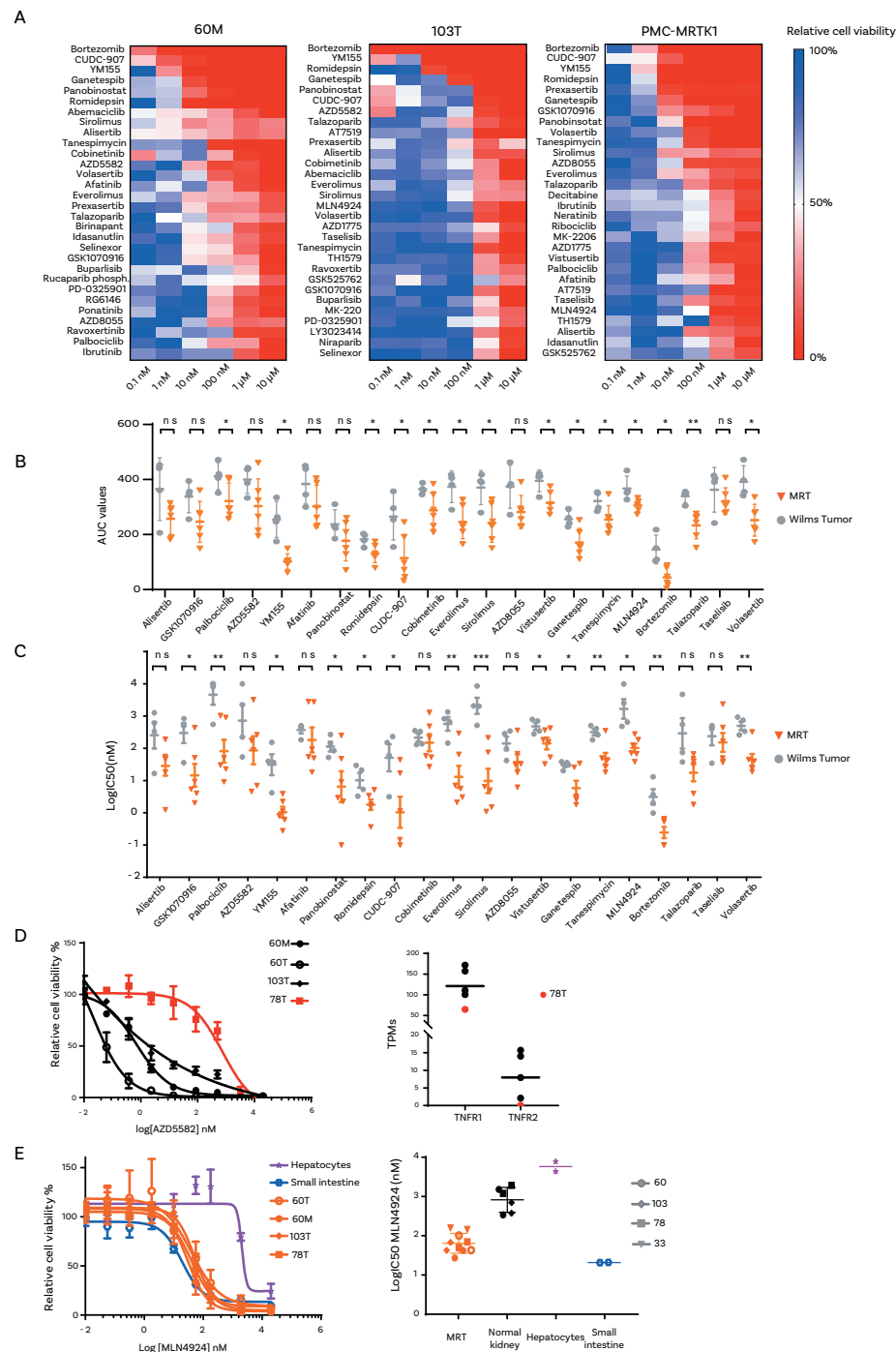
Supplementary Figure 2. Drug screening of MRT organoids reveals tumor and patient-specific drug sensitivities. Related to Figure 1. A. Top 30 compounds ranked based on area under the curve (AUC) values for the indicated 3 MRT organoid cultures. Color scale blue to red indicates decreasing ATP levels relative to DMSO control as measure of cell viability. Compounds present in the top 30 of at least 5 of the 6 screened MRT lines were selected for follow up analysis. **B.** AUC values of 21 compounds in MRT (n=6) and Wilms tumor (n=4) organoid lines. P-values were calculated using a two-tailed unpaired Student's t test, two-sided: * <0.05, ** <0.01. **C.** LogIC$_{50}$ values of 21 compounds in MRT (n=6) and Wilms tumor (n=4) organoid lines. P-values were calculated using a two-tailed unpaired Student's t test, two-sided: * <0.05, ** <0.01, *** <0.001. **D.** Left: Dose response curve of IAP inhibitor AZD5582 in 4 MRT organoid lines. Red curve represents line 78T. Error bars represent SD of 2 independent experiments, each consisting of quadruplicate measurements. Right: Normalized TNFR1 and TNFR2 transcript per million (TPM) values in MRT organoid lines. Red dot represents line 78T. **E.** Left: Dose-response curves of MLN4924 in hepatocytes, small intestine and indicated MRT-derived organoids. Error bars represent SD of 2 independent experiments, each consisting of quadruplicate measurements. Right: Average LogIC$_{50}$ values of MLN4924 in the indicated normal and tumor organoid cultures. Each value (two per organoid culture) represents the average of technical quadruplicates of an individual organoid culture.
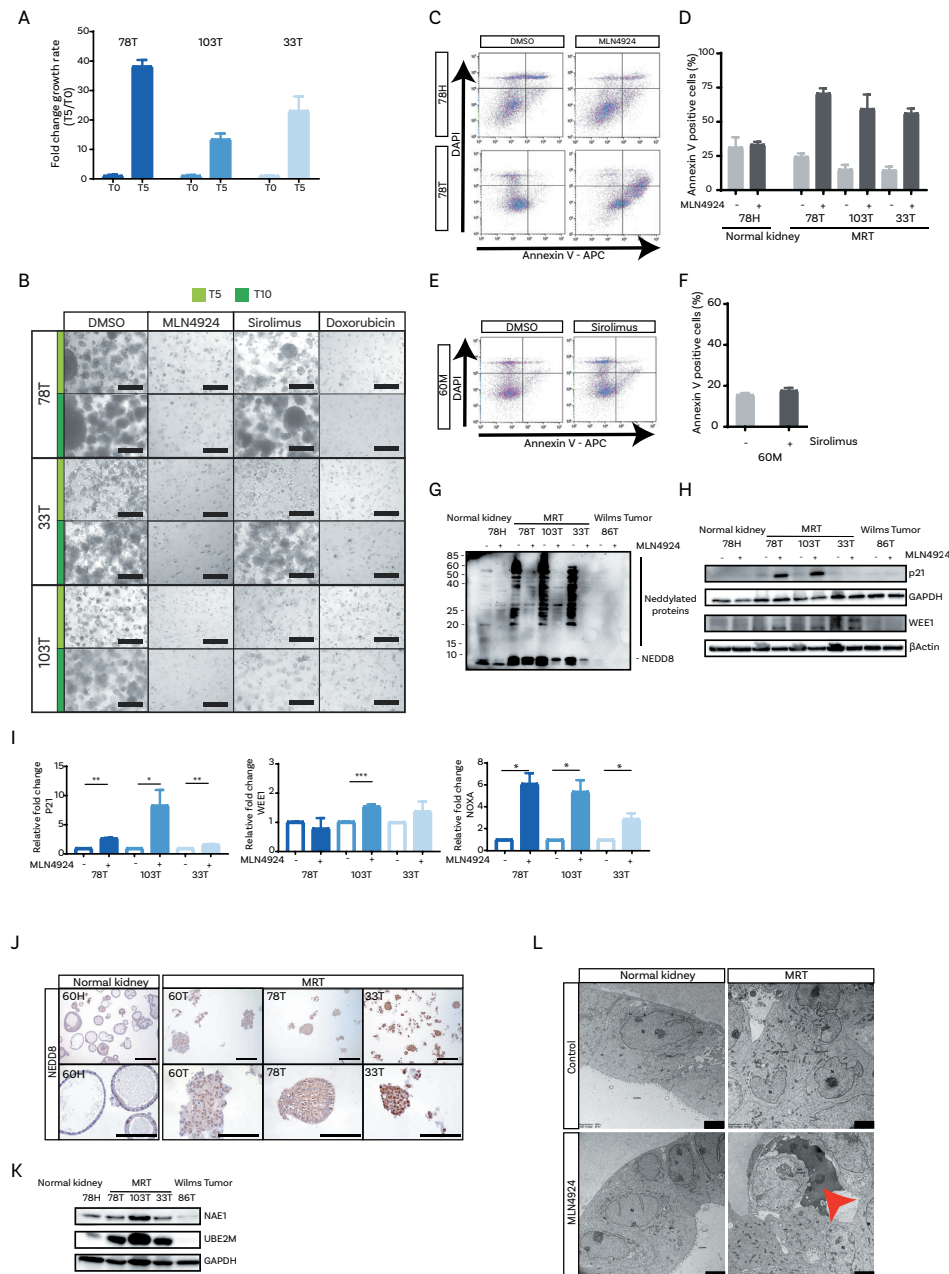
Supplementary Figure 3. MLN4924 treatment induces cytotoxic effects in MRT organoids. Related to Figure 2,3 and 4. A. Fold change growth rate of three MRT organoid lines measured with Cell Titer glo. Growth rates were calculated as ATP levels at day 5 over ATP levels at day 0. **B.** Representative brightfield pictures of 3 MRT organoid lines treated as described in Figure 2A,B. Scale bars: 200μm. **C.** Representative flow cytometry plots for AnnexinV/DAPI stainings of MRT and normal kidney organoid lines treated with either DMSO or 50nM MLN4924 (120h). **D.** Quantification percentage of AnnexinV positive cells of MRT and normal kidney organoids treated as in C. Data are represented as mean ± SEM (n ≥ 3 independent experiments). **E.** Representative flow cytometry plots for AnnexinV/DAPI stainings of MRT organoid line treated with either DMSO or 2nM Sirolimus (120h). **F.** Quantification percentage of AnnexinV positive cells of MRT organoids treated as in E. Data are represented as mean ± SEM (n = 3). **G.** Overexposed image of western blot displayed in Figure 3A revealing low levels of NEDD8 and neddylated protein expression in normal kidney and Wilms tumor organoids. **H.** Western blot analysis of p21 and WEE1 protein expression in the indicated organoid cultures treated for 120 hours with 50nM MLN4924 or DMSO. GAPDH and ßactin were included as loading controls. **I.** Relative *P21* (left), *WEE1* (middle) and *NOXA* (right) expression in three MRT organoid lines upon treatment with 50nM MLN4924 for 120h, normalized to DMSO. Data are represented as mean ± SD (n ≥ 3 independent experiments, each consisting of an average of 3 technical replicates). P-values were calculated using a two-tailed unpaired Student's t test: *<0.05,** <0.01, *** <0.001. **J.** NEDD8 immunostaining on normal kidney and MRT-derived organoids. Scale bars top panel: 200 μm; bottom panel: 100 μm. **K.** Western blot analysis of NAE1 and UBE2M enzymes in the indicated organoid cultures. GAPDH was included as loading control. **L.** Representative TEM images at lower magnification of normal kidney and MRT organoids upon treatment with either DMSO or 50nM MLN4924 for 48h. Red arrow points to necrotic cell. Scale bars: 2μm.
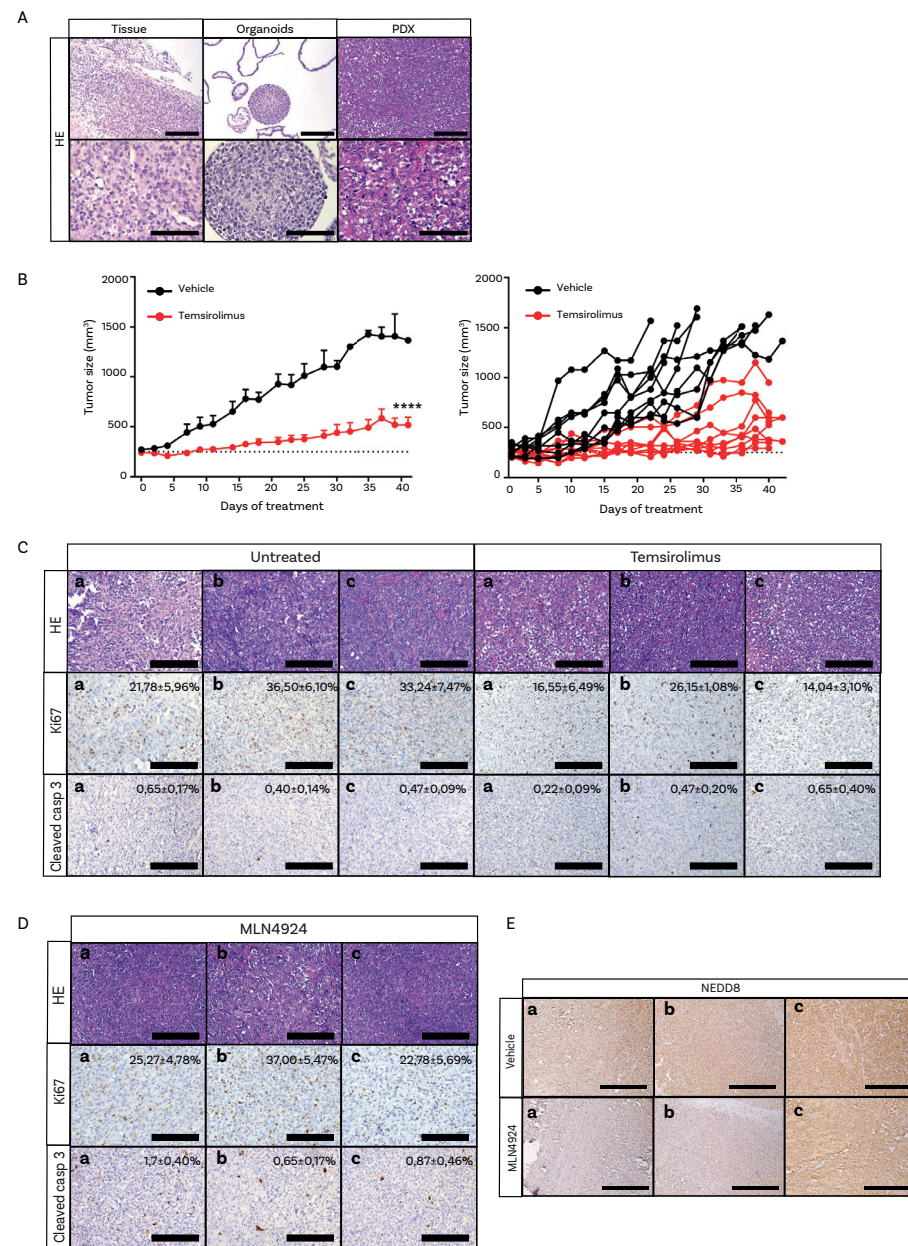
Supplementary Figure 4. Characterization of a novel MRT PDX mouse model. Related to Figure 5. A. Hematoxylin and Eosin staining on 103T primary tissue (left), matching derived organoids (middle) and PDX derived tissue (right). Scale bar top: 200 μm, bottom: 100 μm. **B.** MRT tumor growth in mice (left – grouped; right - single) treated with either vehicle (black) or 5mg/kg temsirolimus (red) for up to 6 cycles (5 days on, 2 days off). P-value was calculated using a two-tailed unpaired Student's t test: **** <0.0001. **C.** Hematoxylin and Eosin, Ki67 and Cleaved caspase 3 staining on untreated (left) and temsirolimus-treated mice (right) tumors. Additionally, percentages of Ki-67 and cleaved caspase 3 positive cells are depicted (average and SDs). Scale bars: 200 μm. **D.** Hematoxylin and Eosin, Ki67 and cleaved caspase 3 staining on MLN4924-treated mice tumors (timepoint2). Additionally, percentages of Ki-67 and cleaved caspase 3 positive cells are depicted (average and SDs). Scale bars: 200 μm. **E.** NEDD8 immunostaining on vehicle (top) and MLN4924-treated mice (bottom) tumors. Scale bars: 500μm.
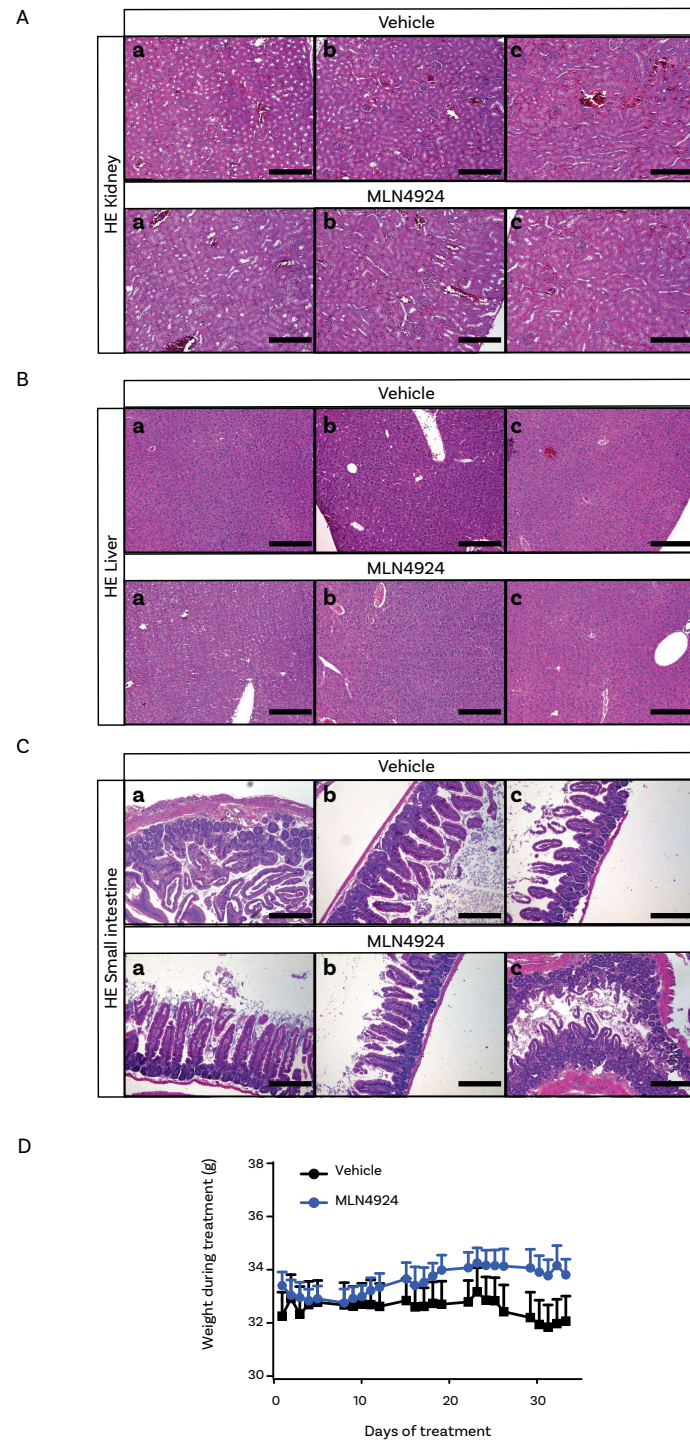
Supplementary Figure 5. No signs of treatment related toxicity in MLN4924 treated mice. Related to Figure 5. A. Hematoxylin and Eosin staining on kidney sections of 5 week-treated mice (timepoint 2). Scale bars: 250 μm. **B.** Hematoxylin and Eosin on liver sections of 5 week-treated mice (timepoint 2). Scale bars: 250 μm. **C.** Hematoxylin and Eosin on small intestine sections of 5 week-treated mice (timepoint 2). Scale bars: 250 μm. **D.** Weight of mice during treatment with either vehicle (black) or 60mg/kg BID MLN4924 (blue).

Supplementary Table 1. Clinical information patient MRT 33T. Related to Figure 1.

Line	Gender	Year of birth	Diagnosis	Source	Location	Pre operative treatment
33T	M	2018	Soft tissue MRT	Primary	Pelvis	Untreated

Supplementary Table 2. List compounds tested in organoid-based drug screening setting. Related to Figure 1.

Compound	Target	Company	Product number
(+)-JQ-1	BRD4	Bioconnect/MedChem Express	HY-13030
Abemaciclib mesylate	CDK4; CDK6	Bioconnect/Selleck Chemicals	S7158
Afatinib	EGFR; HER2	Bioconnect/Selleck Chemicals	S1011
Alectinib	ALK	MTA-2015-0503/Roche/Chugai	N/A
Alisertib	Aurora A kinase	Bioconnect/MedChem Express	HY-10971
AMG 337	c-Met	Bioconnect/MedChem Express	HY-18696
Apatinib mesylate	VEGFR2	Bioconnect/Selleck Chemicals	S2221
AT-406	cIAP1; cIAP2; XIAP	Bioconnect/Selleck Chemicals	S2754
AT7519	pan-CDK	Astex	N/A
Axitinib	VEGFR1; VEGFR2; VEGFR3; PDGFR-β; c-Kit	Bioconnect/Selleck Chemicals	S1005
AZD1775	WEE1	Bioconnect/MedChem Express	HY-10993
AZD4547	FGFR1; FGFR2; FGFR3; FGFR4; KDR	Bioconnect/MedChem Express	HY-13330
AZD5582	cIAP1; cIAP2; XIAP	Bioconnect/MedChem Express	HY-12600
AZD6738	ATR	Bioconnect/Selleck Chemicals	S7693
AZD8055	mTORC1; mTORC2	Bioconnect/Selleck Chemicals	S1555
BCT-100	Arginase	MTA-01211/Bio-Cancer Treatment International Limited	N/A
BIBR 1532	TERT	Bioconnect/Selleck Chemicals	S1186
Binimetinib	MEK1; MEK2	Bioconnect/Selleck Chemicals	S7007
Birinapant	cIAP1; XIAP	Bioconnect/Selleck Chemicals	S7015
Bortezomib	Proteasome	Bioconnect/MedChem Express	HY-10227
Buparlisib	PI3Kα; PI3Kβ; PI3KΔ; PI3Kγ	Bioconnect/Selleck Chemicals	S2247
Cabozantinib S-malate	MET; VEGFR; AXL; RET; KIT	Bioconnect/Selleck Chemicals	S4001
Capmatinib	c-Met	Bioconnect/MedChem Express	HY-13404
CC122	DNA-PK	Bioconnect/MedChem Express	HY-100507
Cediranib	VEGFR(KDR); Flt1; Flt4; c-Kit; PDGFRβ	Bioconnect/Selleck Chemicals	S1017
Ceritinib	ALK	Bioconnect/Selleck Chemicals	S7083
Cobimetinib	MEK1	Bioconnect/MedChem Express	HY-13064
CPI-455	KDM5A; KDM5B; KDM5C	Bioconnect/MedChem Express	HY-100421
Crenolanib	PDGFRα; PDGFRβ; FLT3	Bioconnect/MedChem Express	HY-13223
Crizotinib	c-Met; ALK	Bioconnect/Selleck Chemicals	S1068
CUDC-907	PI3K; HDAC	Bioconnect/MedChem Express	HY-13522
Dabrafenib	BRAFV600E	Bioconnect/MedChem Express	HY-14660
Dasatinib	Abl; Src; c-Kit	Bioconnect/MedChem Express	HY-10181
Decitabine	DNA methyltransferase	Bioconnect/Selleck Chemicals	S1200
Defactinib	FAK	Bioconnect/MedChem Express	HY-12289

Supplementary Table 2. List compounds tested in organoid-based drug screening setting. Related to Figure 1. *(Continued)*

Compound	Target	Company	Product number
Dovitinib	Flt3; c-Kit; FGFR1; FGFR3; VEGFRs	Bioconnect/MedChem Express	HY-50905
EHT 1864 (2HCL)	Rac1; Rac1b; Rac2; Rac3	Bioconnect/MedChem Express	HY-16659
Ensartinib	ALK	Bioconnect/MedChem Express	HY-16590
Entinostat	HDAC1; HDAC3	Bioconnect/Selleck Chemicals	S1053
Entospletinib	SYK	Bioconnect/MedChem Express	HY-15968
Entrectinib	TrkA; TrkB; TrkC; ROS1; ALK	Bioconnect/MedChem Express	HY-12678
Epidaza	HDAC	Bioconnect/MedChem Express	HY-13592
Erlotinib hydrochloride	EGFR	Bioconnect/MedChem Express	HY-12008
Everolimus	mTORC1	Bioconnect/Selleck Chemicals	S1120
EW-7197	ALK4; ALK5	Bioconnect/MedChem Express	HY-19928
FX1	BCL6	Bioconnect/MedChem Express	HY-102027/CS-7688
Galunisertib	ALK5	Bioconnect/Selleck Chemicals	S2230
Ganetespib	HSP90	Bioconnect/Selleck Chemicals	S1159
Glasdegib	SMO	Bioconnect/MedChem Express	HY-16391
GSK J4 hydrochloride	JMJD3; UTX	Bioconnect/Selleck Chemicals	S7070
GSK1070916	Aurora B kinase; Aurora C kinase	Bioconnect/Selleck Chemicals	S2740
GSK2636771	PI3Kβ	Bioconnect/Selleck Chemicals	S8002
GSK269962A	ROCK1; ROCK2	Bioconnect/MedChem Express	HY-15556
GSK461364		Bioconnect/Selleck Chemicals	S2193
I-BET-762	BRD2; BRD3; BRD4	Bioconnect/MedChem Express	HY-13032
I-BRD9	BRD9	Bioconnect/MedChem Express	HY-18975
Ibrutinib	BTK	Bioconnect/Selleck Chemicals	S2680
Icotinib	EGFR	Bioconnect/Selleck Chemicals	S2922
Idasanutlin	p53-MDM2	MTA/Roche	N/A
Imatinib mesylate	v-Abl; c-Kit; PDGFR	Bioconnect/Selleck Chemicals	S1026
Ipatasertib	AKT1; AKT2; AKT3	MTA-OR-214920/Genentech	Barcode: B000823882
IPI549	PI3Kγ	Bioconnect/MedChem Express	HY-100716
KU-55933	ATM	Bioconnect/Selleck Chemicals	S1092
KU-60019	ATM	Bioconnect/Selleck Chemicals	S1570
Lapatinib	EGFR; HER2	Bioconnect/MedChem Express	HY-50898
Larotrectinib sulfate	Trk receptor	Bioconnect/Selleck Chemicals	S7960
Lenvatinib	VEGFR2; VEGFR3; VEGFR1; FGFR1; PDGFRα; PDGFRβ	Bioconnect/MedChem Express	HY-10981
LGK974	PORCN	Bioconnect/MedChem Express	HY-17545
Linsitinib	IGF-1R	Bioconnect/Selleck Chemicals	S1091
LMK-235	HDAC4; HDAC5	Bioconnect/MedChem Express	HY-18998
Lorlatinib	ALK; ROS1	Bioconnect/Selleck Chemicals	S7536

Compound	Target	Company	Product number
LTURM34	DNA-PK	Bioconnect/MedChem Express	HY-101667
LY3023414	PI3Kα; PI3Kβ; PI3KΔ; PI3Kγ; mTORC1; mTORC2; DNA-PK	Bioconnect/MedChem Express	HY-12513
LY3039478	NOTCH	Bioconnect/MedChem Express	HY-12449
Masitinib	c-Kit; PDGFRα; PDGFRβ	Bioconnect/MedChem Express	HY-10209
Merestinib	c-Met	Bioconnect/MedChem Express	HY-15514
Miransertib	AKT1; AKT2; AKT3	Bioconnect/MedChem Express	HY-19719
MK-2206 dihydrochloride	AKT1; AKT2; AKT3	Bioconnect/Selleck Chemicals	S1078
MLN 4924	Nedd8-activating enzyme	Bioconnect/MedChem Express	HY-70062
MM-102	MLL1	Bioconnect/Selleck Chemicals	S7265
Momelotinib	JAK1; JAK2; JAK3	Bioconnect/Selleck Chemicals	S2219
MSC2490484A	DNA-PK	Bioconnect/MedChem Express	HY-101570/CS-0021723
Mubritinib	HER2	Bioconnect/Selleck Chemicals	S2216
MX69	MDM2/XIAP	Bioconnect/MedChem Express	HY-100892
Navitoclax	BCL-2; BCL-XL; BCL-W	Bioconnect/Selleck Chemicals	S1001
Neratinib	HER2; EGFR; weakly KDR; weakly Src	Bioconnect/MedChem Express	HY-32721
Nilotinib	Bcr-Abl	Bioconnect/Selleck Chemicals	S1033
Niraparib	PARP1; PARP2	Bioconnect/MedChem Express	HY-10619
NVP-HDM201	MDM2	Bioconnect/MedChem Express	HY-18658/CS-7654
Olaparib	PARP1; PARP2	Bioconnect/Selleck Chemicals	S1060
OTX-015	BRD2; BRD3; BRD4	Bioconnect/MedChem Express	HY-15743
Palbociclib hydrochloride	CDK4; CDK6	Bioconnect/Selleck Chemicals	S1116
Panobinostat	pan-HDAC	Bioconnect/Selleck Chemicals	S1030
Pazopanib	VEGFR1; VEGFR2; VEGFR3; PDGFRα; PDGFRβ; FGFR1; c-Kit; c-FMS	Bioconnect/MedChem Express	HY-10208
PCI-34051	HDAC8	Bioconnect/Selleck Chemicals	S2012
PD-0325901	MEK1; MEK2	Bioconnect/Selleck Chemicals	S1036
PD-1/PD-L1 inhibitor 1	PD-1; PD-L1	Bioconnect/MedChem Express	HY-19991
Perifosine	AKT1; AKT2; AKT3	Bioconnect/MedChem Express	HY-50909
Pexidartinib	CSF-1R; Kit; Flt3	Bioconnect/MedChem Express	HY-16749
PF-06651600	JAK3	Sigma-Aldrich	PZ0316
Pictilisib	PI3Kα; PI3KΔ	MTA-OR-214920/Genentech	Barcode: B000824090
Pinometostat	DOT1L	Bioconnect/MedChem Express	HY-15593
Plerixafor	CXCR4 and CXCL12	Bioconnect/MedChem Express	HY-10046
Ponatinib	VEGFR2; Bcr-Abl; PDGFRα; FGFR1	Bioconnect/Selleck Chemicals	S1490

5

Supplementary Table 2. List compounds tested in organoid-based drug screening setting. Related to Figure 1. *(Continued)*

Compound	Target	Company	Product number
Prexasertib	CHK1	Bioconnect/MedChem Express	HY-18174
Quizartinib	Flt3	Bioconnect/Selleck Chemicals	S1526
Ravoxertinib	ERK	MTA-OR-214920/Genentech	Barcode: B000847422
Regorafenib	VEGFR1; VEGFR2; VEGFR3; PDGFRβ; Kit; RET; Raf-1	Bioconnect/MedChem Express	HY-10331
RG6146	BRD2; BRD3; BRD4; BRDT	Bioconnect/MedChem Express	HY-15846
Ribociclib	CDK4; CDK6	Bioconnect/MedChem Express	HY-15777
Romidepsin	HDAC1; HDAC2	Bioconnect/MedChem Express	HY-15149
Rucaparib phosphate	PARP1; PARP2	Bioconnect/Selleck Chemicals	S1098
Ruxolitinib	JAK1; JAK2	Bioconnect/MedChem Express	HY-50856
S63845	MCL-1	Active Biochem	A-6044
Sapitinib	EGFR; HER2; HER3	Bioconnect/Selleck Chemicals	S2192
SAR405	VPS34	Bioconnect/MedChem Express	HY-12481
Saracatinib	Src; c-YES; FYN; LYN; BLK; FGR; LCK; Abl; EGFR	Bioconnect/Selleck Chemicals	S1006
Savolitinib	c-Met	Bioconnect/MedChem Express	HY-15959
Selinexor	CRM1	Bioconnect/Selleck Chemicals	S7252
Selumetinib	MEK1	Bioconnect/Selleck Chemicals	S1008
SHP099 hydrochloride	SHP2	Bioconnect/MedChem Express	HY-100388A
Sirolimus	mTORC1	Bioconnect/MedChem Express	HY-10219
Sonidegib	SMO	Bioconnect/Selleck Chemicals	S2151
Sorafenib	Raf-1; B-Raf; VEGFR-2	Bioconnect/MedChem Express	HY-10201
Sunitinib	VEGFR2; PDGFRβ; c-Kit	Bioconnect/MedChem Express	HY-10255A
Talazoparib	PARP1; PARP2	Bioconnect/Selleck Chemicals	S7048
Tanespimycin	HSP90	Bioconnect/Selleck Chemicals	S1141
Taselisib	PI3Kα mutant	MTA-OR-214920/Genentech	Barcode: B000824007
Tazemetostat	EZH2	Bioconnect/MedChem Express	HY-13803
Temsirolimus	mTORC1	Bioconnect/MedChem Express	HY-50910
TH1579	MTH1	MTA-01180/Karolinska Institute	N/A
Tivantinib	c-Met	Bioconnect/MedChem Express	HY-50686
Tofacitinib citrate	JAK1; JAK2; JAK3	Bioconnect/MedChem Express	HY-40354A
Trametinib	MEK1; MEK2	Bioconnect/Selleck Chemicals	S2673
Vandetanib	VEGFR2; VEGFR3; EGFR	Bioconnect/MedChem Express	HY-10260
Varlitinib	EGFR; HER2	Bioconnect/MedChem Express	HY-10530
VE-822	ATR	Bioconnect/MedChem Express	HY-13902
Vemurafenib	BRAFV600E	MTA-OR-214920/Genentech	Barcode: B000847423
Venetoclax	BCL-2	Bioconnect/Selleck Chemicals	S8048

Supplementary Table 2. List compounds tested in organoid-based drug screening setting. Related to Figure 1. *(Continued)*

Compound	Target	Company	Product number
Vismodegib	SMO	Bioconnect/Selleck Chemicals	S1082
Vistusertib	mTORC1; mTORC2	Bioconnect/MedChem Express	HY-15247
Volasertib	PLK1	Bioconnect/Selleck Chemicals	S2235
Vorinostat	pan-HDAC	Bioconnect/MedChem Express	HY-10221
XAV-939	TNKS1; TNKS2	Bioconnect/Selleck Chemicals	S1180
YM155	Survivin	Bioconnect/Selleck Chemicals	S1130
YO-01027	γ-secretase	Bioconnect/MedChem Express	HY-13526

Supplementary Table 3. IC$_{50}$ values calculated for 21 compounds selected to be effective in MRT organoids with high throughput screen. Related to Figure 1. Depicted are IC$_{50}$ values in nM for MRT and Wilms tumor organoids.

Compounds	Wilms tumor organoids				MRT organoids					
	86T	51T	80T	68T	60T	60M	78T	103T	PMC-MRTK1	33T
Alisertib	1269,379	607,4217	16,61207	331,404	46,31986	1,238347	18,38024	190,5361	55,89496	47,98525
GSK1070916	499,5766	832,5003	35,92697	535,2651	5,3937	9,329102	2,027387	437,9809	4,045574	50,83938
Palbociclib	10000	8052,064	551,5255	10000	9,144548	30,394	22,66428	1035,969	50,48414	904,5606
AZD5582	54,13936	223,5501	2239,331	10000	4,578087	6,975636	3207,248	174,4084	88,36696	261,8739
YM155	39,6615	152,7631	4,184901	36,46169	0,277726	0,613708	1,118448	2,232815	0,799041	3,879848
Afatinib	183,5831	498,027	414,9593	489,2636	18,2762	49,57753	93,75108	2796,192	54,47462	2741,336
Panobinostat	83,7606	51,93498	140,6347	267,5866	2,928997	2,280389	0,1	249,9013	9,144877	47,68784
Romidepsin	21,19222	3,270906	5,346637	29,41557	0,363137	1,817592	1,814912	3,41598	1,525695	5,17299
CUDC-907	150,579	60,83263	3,15493	231,8376	0,147146	0,1	0,1	44,16935	1,126086	16,93876
Cobimetinib	332,6365	130,1085	354,2446	138,1705	26,94572	53,27852	58,2981	216,3687	1294,217	484,107
Everolimus	671,9404	1342,291	144,2083	826,4782	3,067224	5,634001	2,113336	292,0015	7,097215	64,74051
Sirolimus	8595,837	2074,949	2028,878	516,4556	1,511844	1,091644	6,451272	212,0099	5,010256	75,26935
AZD8055	344,0332	285,1171	41,84209	98,5609	6,189407	30,97314	32,70687	359,1061	17,95727	67,85764
Vistusertib	346,4543	700,432	280,0334	785,8492	32,75877	158,989	184,7839	424,2348	53,11749	368,563
Ganetespib	36,14703	38,09812	20,0987	30,57044	2,548778	1,786219	3,231008	25,82117	2,949879	34,12586
Tanespimycin	412,0466	261,3945	183,9005	507,9346	28,07002	27,03526	50,06838	352,4386	18,1977	43,41458
MLN 4924	479,1447	649,0021	2521,53	9963,622	38,29661	71,71244	67,4289	277,0183	125,9323	185,3542
Bortezomib	13,06318	3,650067	2,013179	0,981955	0,533068	0,1	0,1	0,1	0,657145	0,604935
Talazoparib	4706,78	73,78713	37,59124	547,6214	3,954517	32,02215	1,80892	47,93841	39,67495	66,80501
Taselisib	504,2772	398,4241	34,75765	452,1677	40,41938	165,0988	49,93929	441,5304	36,44308	2351,47
Volasertib	743,7863	337,8724	260,0842	931,5568	40,14909	18,81806	25,31325	322,3383	25,0982	45,07073

Supplementary Table 4. IC$_{50}$ values calculated for MLN4924 in MRT, normal kidney, hepatocytes and small intestine derived organoids. Related to Figure 1. Each value represents the average of n=2 independent experiments, each consisting of 4 technical replicates.

	Organoid line	Average IC$_{50}$ MLN4924 (nM)
MRT	60T	85
	60M	35
	78T	54
	103T	63
	33T	154
Normal Kidney	60H	617
	78H	1481
	103H	861
Hepatocytes	KK2	6830
Small intestine	STE076	23

Chapter 6

Normal and tumor-derived organoids as a drug screening platform for tumor-specific drug vulnerabilities
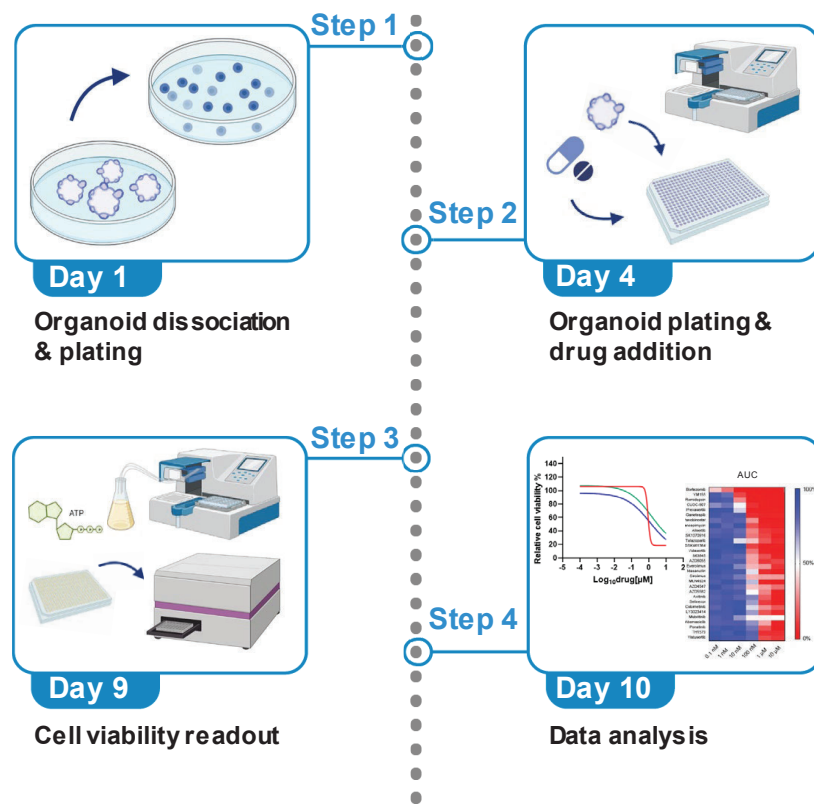
Camilla Calandrini[1,2,3] and Jarno Drost[1,2,4]

[1] Princess Máxima Center for Pediatric Oncology, Utrecht, the Netherlands
[2] Oncode Institute, Utrecht, the Netherlands
[3] Technical contact
[4] Lead contact

Step 1

Day 1
Organoid dissociation & plating

Step 2

Day 4
Organoid plating & drug addition

Step 3

Day 9
Cell viability readout

Step 4

Day 10
Data analysis

Summary

Patient-derived tumor organoids can be predictive of patient's treatment responses, and normal tissue-derived organoids allow for drug toxicity testing. Combining both types of organoids therefore enables screening for tumor-specific drug vulnerabilities. Here, we provide a detailed protocol for organoid drug screening using, as proof-of-principle, patient-derived malignant rhabdoid tumor organoids. The protocol can be adapted for drug testing on any tumor and/or normal tissue-derived organoid culture. For complete details on the use and execution of this protocol, please refer to Calandrini et al. 2021.

Before you begin

The protocol below describes in detail how to perform drug screens on organoid cultures (**Figure 1**). For example, we use patient-derived malignant rhabdoid tumor (MRT) organoid cultures[1-3]. Yet, the protocol can be easily adapted to any type of tumor and/or normal tissue-derived organoid culture model.

Genetic characterization of tumor organoids before drug screening

Timing: 1–4 weeks

1. Verification tumor organoid cultures: It is crucial to verify the cancerous nature of the established organoid cultures before performing any drug screening experiments. This can be done in different ways, including:
   a. Targeted PCR amplification and subsequent Sanger sequencing of any known tumor-specific somatic mutations identified in the parental tissue;
   b. SNP array to confirm the presence of the same copy number alterations in organoid and parental tissue;
   c. Whole exome/genome sequencing of the organoid culture and subsequent comparison to the genetic profiles of parental tissue.

Note: In case no genetic information is available for the tumor tissue, immunohistochemistry analysis of known tumor markers could be performed on tissue and organoid samples. For instance, in case of MRT, INI1 staining should be performed to confirm lack of expression in tumor cells[4].

Preparation screening: Layout screening plate, expansion organoid cultures, preparation reagents and equipment

Timing: 1–4 months

2. Preparation plate layout: Prepare a plating layout, specifying how many compounds and concentrations will be tested. This is crucial to assess the number of organoids required for the drug screen experiment (see step 3). In this protocol, we describe how to perform a drug screen in a 384-well plate layout, with an optimal plating volume of 40 μL per well.
   a. We recommend to test a broad range of concentrations for each compound in order to capture a full dose response curve.

Note: this can be achieved by using dilutions ranging from 10 pM up to 10–100 M. For compounds in clinical development, a literature search can be done to find the most optimal concentration ranges.

   b. The inclusion of a positive and a negative/vehicle control is highly recommended.

Note: The vehicle control is required to set the 100% viability threshold at the day of the read-out and to calculate the effect of increasing concentrations of the drug on organoid viability. As vehicle control, the solvent used to dissolve the drug should be used (e.g. dimethylsulfoxide (DMSO)).

CRITICAL: it is important to test the maximum volume of vehicle that can be added to the organoids without affecting cell viability. For instance, we recommend keeping DMSO volumes below 0.5% vol/vol.

   c. When designing the plating layout, ensure that the same final vehicle volume is present in all the wells included in the experiment.
   d. When designing a drug screening experiment, test every concentration with a minimum of three technical replicates.
   e. Randomize the position of the triplicates to ensure that no bias is induced due to location in which the cells are plated within the 384-well plate.
   f. To prevent edge effects, do not plate cells in the outer wells of the screening plate. Instead, plate PBS.

CRITICAL: evaporation of the medium during the drug screening procedure can interfere with the accuracy of the cell viability readout. To prevent evaporation, fill all empty wells with PBS or adDMEM/F12 +++. Dispense 40 µL volume per well. If evaporation is considerable, higher volumes of PBS (up to 80 µL) should be considered.

   g. Include wells with medium only (e.g., adDMEM/F12 +++) in the plate layout to be able to determine the background signal on the day of the readout.

3. Expansion of tumor organoid cultures: To proceed with the drug screening, a sufficient number of organoids is required. The number of organoids required depends on:
   a. The growth characteristics of the organoid culture, such as proliferation rate and organoid appearance (i.e., number of cells per organoid);
   b. The number of drugs to be tested;
   c. The number of different concentrations to be tested per drug.

4. Organoid growth curve: Before performing the drug screen, an organoid growth curve should be performed to identify the number of organoids needed to achieve the optimal viability at the endpoint of the experiment (maximum viability value before reaching growth curve plateau phase). As indication, seed between 250 to 1000 organoids per well.

Note: This protocol describes the procedure for drug testing in organoids. As such, we plate intact organoid structures and not single cells. In the specific case of MRT cultures, we plate 500 organoids with an approximate size of 3–6 cells per organoid per well.

5. Calibration tubing: When using an automated system for organoid dispensing, it is crucial to calibrate the equipment before every drug screen to achieve an accurate plating. We refer to the manufacturer's instructions for further details about calibration.
6. Preparation Milli Q, Ethanol 70%, and PBS: Aliquot Milli Q water, Ethanol 70% (vol/vol) and PBS into 50 mL tubes. For each line that will be plated, prepare a total of ~500 mL Milli Q, 250 mL Ethanol 70% vol/vol and 50 mL PBS. Store the aliquots at 4°C for a minimum of 12 h.

Materials and methods

AdDMEM/F12 +++ medium

Reagent	Final concentration	Amount
Hepes	10 mM	5 mL
Glutamax	1X	5 mL
Penicillin/Streptomycin	100 U/mL	5 mL
Advanced DMEM/F12		500 mL
Total		**515 mL**

Store AdDMEM/F12 +++ medium at 4°C for up to 4 weeks.

Organoid medium for MRT growth

The organoid medium for MRT growth was established by Schutgens et al. (2019), adapted from the medium originally developed for normal kidney tubuloids growth[5].

Reagent	Final concentration	Amount
A83-01	5 µM	50 µL
B27 supplement	1.5%	750 µL
Human EGF	50 ng/mL	5 µL
Human FGF10	100 ng/mL	50 µL
N-acetylcysteine	1.25 mM	125 µL
Primocin	0.1 mg/mL	50 µL
RhoKinase inhibitor Y-27632	10 µM	50 µL
R-spondin conditioned medium	10%	5 mL
AdDMEM/F12 +++		43.92 mL
Total		**50 mL**

Store organoid medium at 4°C for up to 3 weeks.

Step-by-step method details

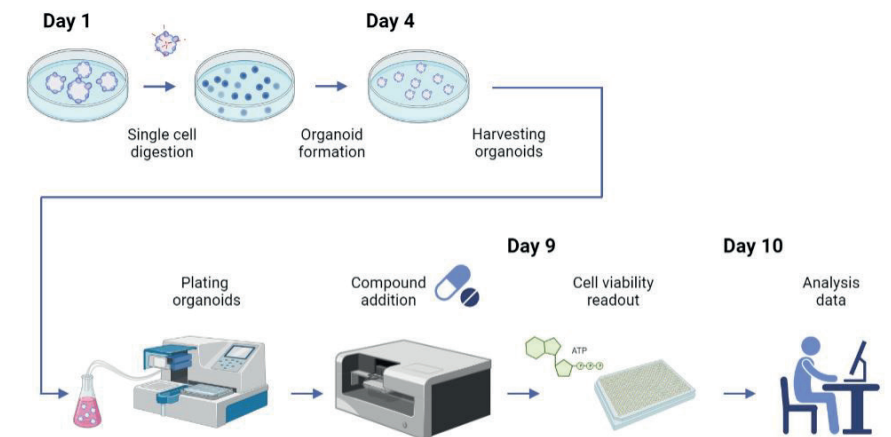### Single cell dissociation and plating of organoids

Figure 1. Schematic overview of the protocol

Day 1

Timing: 1h (per organoid line)

This section describes the experimental steps to expand and plate organoids for drug screening. We use MRT organoids as example, but in principle the same steps can be applied to any type of organoid model.

1. Collect the organoids embedded in a BME droplet with a p1000 pipette using the culture medium in the well and transfer to a 15 mL tube.
2. Pipette up and down to disrupt the BME droplets.
3. Fill up the tube with ice-cold adDMEM/F12 +++.
4. Centrifuge at 300 x g for 5 min at 4°C.
5. Remove supernatant.
6. Add pre-warmed (37°C) TrypLE with addition of 10 µM Y-27632 to the pellet. Use 1 mL solution per 200 µL of harvested BME.
7. Incubate for 3–4 min at 37°C.
8. To mechanically dissociate the organoids, pipette up and down for 10–15 times using a fire polished glass pipette.
9. Visually inspect the organoid mixture under a brightfield microscope. At this point, most of the suspension should composed out of single cells.

Optional: if this is not the case, repeat steps 7–9 once more. **Troubleshooting 1**

10. Fill up the tube with ice-cold adDMEM/F12 +++.

11. Centrifuge at 300 x g for 5 min at 4°C.

12. Remove supernatant.

13. Measure the pellet size using a p100/p1000 pipette set to a known volume, or make use of falcon tubes filled with standard volumes to infer the volume of the pellet. Add 70% volume of ice-cold BME to the pellet.
    Optional: if organoids tend to stick to the plastic surface of the tip when pipetting, precoat the tip by pipetting up and down with adDMEM/F12 +++.

14. Carefully resuspend the pellet in the leftover supernatant without creating air bubbles and plate the mixture with droplets of 15–20 µL volume into pre-warmed 12 well or 6 well plates.

15. Place the plate in the 37°C incubator upside down for 20–25 min, to prevent adherence of the cells to the plate bottom.

16. Add pre-warmed (37°C) organoid culture medium to the wells and inspect the culture under a brightfield microscope (**Figure 2A**).

Preparation of organoids for dispensing into multi-well drug screening plates

Day 4

Timing: 1-2h (per organoid line)

This section describes the harvesting, counting and preparation of the organoid solutions for dispensing into multi-well drug screening plates. We use MRT organoids as example, but the basic principles can be generally applied to any type of organoid model.

17. Visually inspect the organoid cultures using a brightfield microscope to assess their viability and size. As example, MRT organoids should be at the 3–6 cells stage. (**Figure 2A**) **Troubleshooting 2**

18. Collect the organoids embedded in a BME droplet with a p1000 pipette using the culture medium in the well and transfer to a 15 mL tube.

19. Fill up the tube with ice-cold adDMEM/F12 +++.

20. Centrifuge at 300 x g for 5 min at 4°C.

21. Remove supernatant.

22. Repeat washing step by adding 10 mL of ice-cold adDMEM/F12 +++ and re-suspend the pellet. **Troubleshooting 3**

23. Centrifuge at 300 x g for 5 min at 4°C.

24. Remove supernatant; add 5 mL of adDMEM/F12 +++ and resuspend the pellet.

25. Filter the organoid solution through a 70 µm strainer placed on top of a 50 mL tube. (**Figure 2A**) **Troubleshooting 4**

26. Transfer the filtered solution to a 15 mL tube.

27. Centrifuge at 300 x g for 5 min at 4°C.

28. Remove supernatant and resuspend pellet in a total volume of 1 mL, making use of ice-cold adDMEM/F12 +++ to achieve the correct volume.

CRITICAL: The organoid suspension must be thoroughly mixed to obtain a homogeneous solution that is devoid of cell clumps. This step is critical for an as accurate as possible estimation of the number of organoids in solution.

29. Take 1–5 µL of the organoid mix and count the number of organoids using a hemocytometer.
    Note: each organoid is count as a single unit.

30. Calculate how many organoids are present in 1 mL. If the number of organoids is sufficient, transfer the required volume to a new tube and proceed with protocol. Otherwise, re-plate the organoids as described in steps 10–16 to further expand the culture.
    Note: The total number of organoids needed depends on the number of wells required for the experiment. In the case of a 384-well plate set-up, plate 500 organoids per well (in total ~ 160,000 organoids per 384-well plate).

31. Prepare the organoid solution by mixing organoids, organoid culture medium and 5% vol/vol BME matrix in a 50 mL tube or a sterile flask. Mix by inversion - preventing air bubbles - and put on ice.
    Note: The total volume required depends on the number of wells that are used for the experiment. In a 384-well plate set-up, dispense a total volume of 40 µL per well, for a total of ~13 mL volume per screening plate. Calculate extra volume to compensate for plating inaccuracy/ dead volume needed for dispensing. We recommend calculating at least 10% extra volume/ organoids per screen.
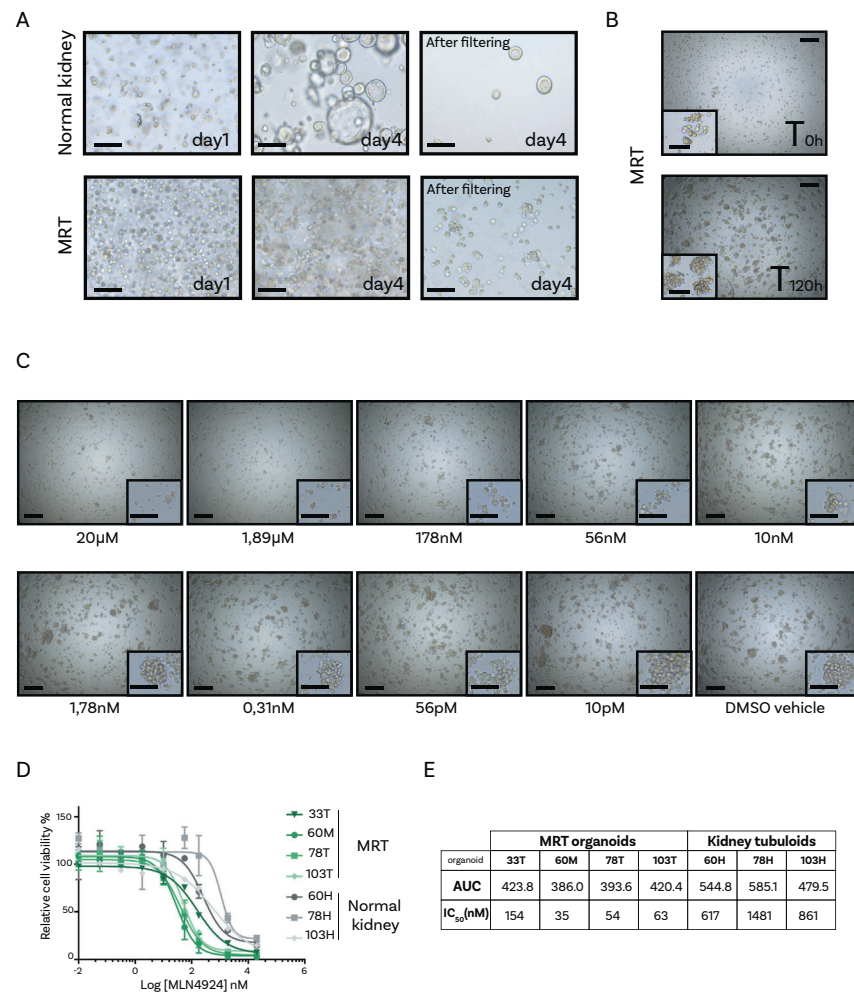
6

Figure 2. Patient-derived organoids as drug screening platform. A. Representative brightfield images of normal kidney tubuloids (top) and MRT organoids (bottom) at different stages of preparation for drug screening. Sample at single cell state (step 16, left), sample prior to harvesting (step 17, middle) and sample after filtering (step 25, right). Scale bars 200 μm. **B**. Representative brightfield images of MRT organoids upon plating in 384-well drug screening plates at timepoint T_{0h} (top) and timepoint T_{120h} (bottom). Scale bars 500 μm, zoom in 200 μm. **C**. Brightfield images of MRT organoids plated in 384-well drug screening plates and treated with a range of different MLN4924 concentrations (20 μM–10 pM) for a 5-day period. Scale bars 500 μm, zoom in 200 μm. **D**. Example of dose-response curves of MLN4924 for the indicated MRT and normal kidney tubuloid organoid cultures. Error bars represent SD of 2 independent experiment, each consisting of 4 technical replicates. **E**. Example of area under the curve (AUC) and inhibitory half concentration (IC_{50}) values calculated from the drug screening data presented in D. Adapted from Calandrini et al. 2021.

Dispensing organoid mixture into 384-well drug screening plates
Day 4
Timing: 30 min (per organoid line)
The following steps describe the plating of the organoid solution into 384-well screening plates. In order to plate the organoids in the most accurate manner make use of a reagent dispenser machine (e.g., Multidrop Combi Reagent dispenser (ThermoFisher)). The reagent dispenser should be placed on a cleaned bench or in a flow hood to ensure a sterile environment. Note that all solutions should be ice-cold to prevent polymerization and solidification of the BME in the tubing.

32. Clean, disinfect and cool down the tubing of the reagent dispenser by flushing with 100 mL (2 x 50 mL tube) of Milli Q water, followed by flushing with 100 mL of 70% vol/vol Ethanol, and finally once more with 100 mL of Milli Q water.
33. Wash the tubing with 25 mL PBS. To avoid medium evaporation during the experiment, dispense 40 μL of PBS solution to the wells of the 1st and 24th column (outer wells of the multi-well plate).
34. Prepare the tubing for organoid solution dispensation by flushing with 25 mL of ice-cold adDMEM/F12 +++. Subsequently, plate 40 μL of adDMEM/F12 +++ solution to the wells of the 2nd and 23rd column, as well as to the top and bottom rows on the multi-well plate.
35. Before dispensing, gently invert the organoid-containing solution to ensure that the mixture is as homogenous as possible.
36. Empty the tubing and prime the organoid mixture until the solution has filled every capillary of the tubing.

CRITICAL: Make sure that the tubing is ice-cold before priming the organoid mixture. Proceed promptly to avoid the tubing from reaching 15°C–18°C and the BME to solidify.

37. Proceed with the plating of the organoid mixture to the drug screening plate by dispensing 40 μL of organoid mixture to the selected columns/wells.

CRITICAL: To ensure a homogeneous distribution of the organoids during dispensing, gently swirl the solution while plating. Make sure not to generate air bubbles by swirling too vigorously.

38. In a separate screening plate, dispense the organoid mixture in several (at least 3) wells to measure cell viability at timepoint 0 (T0). (**Figure 2B**) This is described in more detail in steps 47–53.

39. Directly after finishing with dispensing the organoid mixture, empty the tubing and prime Milli Q water to start the cleaning procedure.

CRITICAL: do not leave the tubing primed with organoid mixture to avoid clogging due to BME polymerization and/or precipitation of reagents.

40. Continue with the cleaning procedure by flushing the tubing with 100 mL (2 x 50 mL tubes) Milli Q water, followed by 100 mL of 70% vol/vol Ethanol and again 100 mL of Milli Q water.

41. Visually inspect all plates to confirm that the organoids are plated homogeneously throughout the different wells and plates.

42. Place the screening plates in an incubator at 37°C. Wait at least 4 h before proceeding with the addition of the drugs.
   Optional: Use leftover organoids for genomic DNA extraction and subsequent genotyping applications.

Compound addition - Low throughput
Day 4
Timing: 30 min
This section describes the addition of the compounds to the screening plates. Based on the number of compounds and concentrations to test, different automated systems for drug dispensing can be used. Here, we describe the addition of compounds for a low throughput screening using the Tecan D300e Digital Dispenser (HP). The machine should be used in a clean bench set up, preferably positioned in a chemical fume hood.

43. Thaw the drug aliquots. Prepare intermediate drug dilutions, if required.

44. In the Tecan D300e software, open the plating layout previously prepared (see section "*before you begin*", step 2).

45. Add the compounds and vehicle fluids to the wells following the Tecan D300e software instructions.

46. Place plates back into the incubator at 37°C.

Readout cell viability with Cell Titer Glo 3D
Day 9
Timing: 45 min (per multi-well plate)
Here, we describe the procedure for cell viability measurements using Cell Titer Glo 3D (Promega). In this protocol, the readout is performed at 2 timepoints, T_0 (day of plating) and T_{120h} (5 days, endpoint experiment).

47. Make sure the Cell Titer Glo 3D (Promega) and the multi-well screening plates are at 21°C before starting.

48. Visually inspect plates to ensure that the organoids in the wells containing the vehicle control have grown as expected. (**Figure 2B,C**) **Troubleshooting 5**

49. Prepare and clean the tubing of the multidrop Combi as illustrated in step 32.

CRITICAL: Use solutions stored at 16°C–24°C since temperature fluctuations can interfere with Cell Titer Glo 3D luminescence readout.

50. Use the multidrop combi system to dispense 40 µL of Cell Titer Glo 3D (1:1) in each well.

CRITICAL: During dispensing, protect the tubing from light exposure by covering with aluminum foil.

51. Use a horizontal shaker to agitate the multi-well plate(s) for 5 min at 600 rpm.

CRITICAL: Prior to shaking, wipe the lid of the plate from any condensed water, as this may cause bubble formation and interference with the accuracy of the readout.

52. Incubate the multi-well plate(s) covered with aluminum foil for 25 min at 16°C–24°C.

53. Measure the luminescence signal per well using a suitable reader (e.g., FLUO-star Omega, BMG Labtech).

6

Expected outcomes

This protocol allows for drug testing of any patient-derived organoid culture in a low- to medium throughput manner. If effective, a visible reduction in cell growth compared to vehicle control should be detectable after 120 h incubation with the compounds of interest (**Figure 2C**). After the readout, dose response curve can be generated and parameters such as Area Under the dose response Curve (AUC) and inhibitory half concentration (IC_{50}) values can be calculated (**Figure 2D,E**). This set-up can be used to identify tumor-specific and/or patient-specific therapeutic vulnerabilities, as described[1-3,6,7].

Quantification and statistical analysis

In order to convert raw luminescence data to dose-response curves, one can make use of Microsoft Excel and/or GraphPad Prism software.

1. Open the raw data in Microsoft Excel.
2. Retrieve the information of the plating layout to determine which value corresponds to which sample.
3. Calculate the average background luminescence value using the values of the wells containing only medium (no cells (i.e., 0% viability value)). Subtract the average background value from the values of the other wells.
4. Calculate the average luminescence value of the vehicle control wells. This value will be set as 100% viability. **Troubleshooting 6**
5. Calculate relative cell viability percentage of the other wells using the following equation:

*Viability well = (luminescence value well / luminescence vehicle control)
* 100%*

6. Transfer the relative cell viability values calculated and corresponding drug concentration – converted in logarithm values - to GraphPad Prism, under the XY table option.
7. Draw dose response fitting curves by selecting New analysis/Nonlinear regression curve/ log(inhibitor) vs response – variable slope. **Troubleshooting 7**
8. In the resulting table, you will find the calculated IC_{50} value.

9. Calculate AUC values making use of the option Area under curve under the tab Analyze.
10. To evaluate growth ratios of the organoid lines, compare luminescence values measured at timepoint T_0 with those measured at T_{120h}, using the following equation:

*Growth ratio = (luminescence value untreated well T_{120} /
luminescence value untreated well T_0)*

Limitations

In order to perform drug screening in a low to medium-throughput fashion, a significant number of organoids are required. Depending on the type of organoid model, this expansion step can range from several weeks to sometimes even months after establishment of the culture from primary material. As a consequence, drug screening in some cases is only possible several months after culture establishment[8,9]. Although it remains unclear whether prolonged organoid culturing results in the enrichment of specific tumor subclones, we recommend performing any type of drug testing assay on early passage cultures.

Cultures conditions used for growing tumor organoids were often optimized for the growth of normal tissues[8]. As a consequence, the presence of normal cells in the tumor resection specimen can result in overgrowth by normal organoids[10]. This can be prevented by using culture conditions that selectively support tumor cells growth. For instance, in the case of *TP53*-mutated tumors, the P53 stabilizing agent Nutlin-3a can be added to the culture medium[1,11]. When considering the case of MRT of the kidney – P53 wild type tumors of mesenchymal origin, characterized by a lack of epithelial differentiation[12,13] - MRT organoids can be separated from contaminating normal kidney epithelial cells based on the negativity for epithelial markers, such as EPCAM[1]. When these strategies are not possible, it is important to ensure that the tissue specimen is not contaminated with normal tissue. For instance, part of the obtained specimen can be used for histological examination. In any case, it should be verified that the organoid culture is still representative of the parental (tumor) tissue prior to drug screening (see characterization of tumor organoid cultures). Furthermore, although organoids have been shown to be valid models that recapitulate features of the tissue they were derived from, the lack of vasculature, tumor microenvironment and immune cells

are still important limitations to be considered[8,9,14], which currently still limits the use of organoids for immunotherapy testing.

Here, we describe the use of patient-derived organoids to test drug efficacy in a 120 h (5 day) time window. The here-described timelines and operations can be adjusted based on (1) the growth speed of the cultures and, as a consequence, the potential need for medium refreshing and (2) the stability of the tested compounds. If longer treatment periods are required, adjustments to the protocol – such as medium refreshing, organoid passaging, and compound re-addition – have to be considered.

The Cell Titer Glo 3D assay is used in this protocol to infer the relative cell viability from the metabolic activity of cells via the quantification of ATP molecules. This readout cannot therefore distinguish between a cytostatic (reduction in growth) and a cytotoxic (cell death) effect of the tested compounds, since both would cause a reduction in ATP production compared to an untreated control. Therefore, to further characterize the drug-induced effects, additional validation experiments such as apoptosis and cell proliferation assays should be performed[2].

Troubleshooting

Problem 1

Intact organoids or pieces of organoids remain after the digestion procedure (step 9).

Potential solution

Carefully increase the incubation time with TrypLE, followed by mechanical disruption (up and down pipetting). Repeat the process for a maximum of 3 times. Stop the procedure as soon as substantial cell lysis (>30%) is detected in the solution. Cell death quantification should be performed via staining with markers/dyes discriminating live and dead cells (e.g., Trypan blue). Note that it is not always possible to fully digest organoids into a single cell suspension without causing significant cell death in the cultures. In such a case, aim for obtaining a suspension that is as homogeneous as possible, performing mechanical and enzymatic disruption until organoids are dissociated into fragments of equal size (< 70 μm). At this point, big organoid fragments still present in solution can be filtered out using a 70 μm strainer. Notably, take the size of the disrupted organoids into consideration when determining the correct timing for organoid harvesting for drug screening (step 17).

Problem 2

Organoids did not reach optimal size for drug screening plating (step 17) because (1) the culture is still composed out of single cells or (2) the structures are too big (diameter > 70 μm).

Potential solution

Wait (>3 days) until the culture has recovered and organoids have reached a sufficient size before harvesting. A longer period of recovery upon single cell digestion could be a sign of a too harsh/ not careful handling of the organoids. Optimize the timing of and method for organoid dissociation. Reschedule the harvesting of the organoids. It is critical to follow the optimized digestion protocol of the organoid lines strictly and consistently, as it will ensure a predictable growth rate of the cultures and make the results reproducible.

Problem 3

Large amount of BME is present after washing steps (step 22).

Potential solution

When dealing with large amounts of BME (> 800 μL), at the moment of harvesting divide the content in to several falcon tubes, so that a maximum of 400 μL BME is present in each tube. If the issue persists, before proceeding with the filtering step, it is recommended to perform a short enzymatic digestion with TrypLE or Cell Recovery Solution.

Problem 4

Insufficient organoids remain after filtering (step 25).

Potential solution

Loss of organoids during the filtering step can be caused by (1) insufficient digestion of the culture when plating (see problem 2); (2) high content of BME remaining in the organoid solution. When a considerable amount of BME is still visible at step 24 (recognizable as a thick white ring on top of the organoid pellet), wash the organoid pellet once more with ice-cold adDMEM/F12 +++. If after filtering a layer of BME is still present on top of the filter, add 5/10 mL of ice-cold adDMEM/F12 +++ to the strainer and use the tip of a 10 mL pipette to scrape the surface of the strainer. At this point, if part of the solution cannot pass through the filter, use a new strainer.

Problem 5

Insufficient growth in untreated control wells at T_{120h} (step 48).

Potential solution

Possible causes include: (1) inadequate growth factor activity in the culture medium which can be solved by making a new batch of medium; (2) limited viability of the organoids at the moment of plating, which can be solved by using less harsh conditions during digestion and plating of the cultures; (3) the growth of the organoids was reduced due to the different plating set-up (5% BME slurry instead of 70% BME), which can be solved by performing a growth curve replicating the screening conditions prior to the screen, to verify changes in growth rate.

Problem 6

Large variation in cell viability values between technical replicates (step 4).

Potential solution

This can be caused by an insufficient number of plated organoids per well and/or by a non-homogeneous dispensing of the organoids. Repeat the screen and dispense more organoids per well. If the organoid cultures show a change in growth speed during the expansion phase, we recommend to replicate the growth curve experiment to assess the best organoid seeding density. To avoid a heterogeneous dispensing of the organoids upon plating, ensure that a homogeneous population of organoids is present at the moment of harvesting. Furthermore, be mindful that the organoid solution should be regularly inverted/mixed prior and during dispensing to avoid sinking of the organoids to the bottom of the tube.

Problem 7

Drug screening results are not reproducible (step 7).

Potential solution

This could be caused by (1) overgrowth of normal cells/ cross-contamination with other lines; (2) low quality/deterioration of drug aliquots. To verify that no cross-contamination has taken place in the organoid cultures, harvest genomic DNA and verify via genotyping/SNP array that the genomic profile is matching those of the early passage cultures and parental tumor tissue. Check the storing conditions and the lifetime/stability of the used compounds; make use of fresh aliquots when repeating the screen.

Acknowledgements

Declarations of interests

The authors declare no competing interests.

References

1.   Calandrini, C., Schutgens, F., Oka, R.,Margaritis, T., Candelli, T., Mathijsen, L., Ammerlaan, C., van Ineveld, R.L., Derakhshan, S., and de Haan, S. (2020). An organoid biobank for childhood kidney cancers that captures disease and tissue heterogeneity. Nat. Commun. 11, 1–14.

2.   Calandrini, C., van Hooff, S.R., Paassen, I., Ayyildiz, D., Derakhshan, S., Dolman, M.E.M., Langenberg, K.P., van de Ven, M., de Heus, C., and Liv, N. (2021). Organoid-based drug screening reveals neddylation as therapeutic target for malignant rhabdoid tumors. Cell Rep. 36, 109568.

3.   Custers, L., Khabirova, E., Coorens, T.H., Oliver,T.R., Calandrini, C., Young, M.D., Braga, F.A.V., Ellis, P., Mamanova, L., and Segers, H. (2021). Somatic mutations and single-cell transcriptomes reveal the root of malignant rhabdoid tumours. Nat. Commun. 12, 1–11.

4.   Sigauke, E., Rakheja, D., Maddox, D.L., Hladik, C.L., White, C.L., Timmons, C.F., and Raisanen, J. (2006). Absence of expression of SMARCB1/INI1 in malignant rhabdoid tumors of the central nervous system, kidneys and soft tissue: an immunohistochemical study with implications for diagnosis. Mod. Pathol. 19, 717–725.

5.   Schutgens, F., Rookmaaker, M.B., Margaritis, T., Rios, A., Ammerlaan, C., Jansen, J., Gijzen, L., Vormann, M., Vonk, A., and Viveen, M. (2019). Tubuloids derived from human adult kidney and urine for personalized disease modeling. Nat. Biotechnol. 37, 303–313.

6.   Driehuis, E., van Hoeck, A., Moore, K., Kolders, S., Francies, H.E., Gulersonmez, M.C., Stigter, E.C., Burgering, B., Geurts, V., and Gracanin, A. (2019). Pancreatic cancer organoids recapitulate disease and allow personalized drug screening. Proc. Natl. Acad. Sci. 116, 26580–26590.

7.   Kim, M., Mun, H., Sung, C.O., Cho, E.J., Jeon, H.-J., Chun, S.-M., Shin, T.H., Jeong, G.S., Kim, D.K., and Choi, E.K. (2019). Patient-derived lung cancer organoids as in vitro cancer models for therapeutic screening. Nat. Commun. 10, 1–15.

8.   Drost, J., and Clevers, H. (2018). Organoids in cancer research. Nat. Rev. Cancer 18, 407–418.

9.   Veninga, V., and Voest, E.E. (2021). Tumor organoids: opportunities and challenges to guide precision medicine. Cancer Cell 39, 1190–1201.

10. Dijkstra, K.K., Monkhorst, K., Schipper, L.J., Hartemink, K.J., Smit, E.F., Kaing, S., de Groot, R., Wolkers, M.C., Clevers, H., and Cuppen, E. (2020). Challenges in establishing pure lung cancer organoids limit their utility for personalized medicine. Cell Rep. 31, 107588.

11. Drost, J., van Jaarsveld, R.H., Ponsioen, B., Zimberlin, C., van Boxtel, R., Buijs, A., Sachs, N., Overmeer, R.M., Offerhaus, G.J., and Begthel, H. (2015). Sequential cancer mutations in cultured human intestinal stem cells. Nature 521, 43–47.

12. Young, M.D., Mitchell, T.J., Custers, L., Margaritis, T., Morales-Rodriguez, F., Kwakwa, K., Khabirova, E., Kildisiute, G., Oliver, T.R., and de Krijger, R.R. (2021). Single cell derived mRNA signals across human kidney tumors. Nat. Commun. 12, 1–19.

13. Judkins, A.R., Mauger, J., HT, A., Rorke, L.B., and Biegel, J.A. (2004). Immunohistochemical analysis of hSNF5/INI1 in pediatric CNS neoplasms. Am. J. Surg. Pathol. 28, 644–650.

14. Ooms, A.H., Calandrini, C., de Krijger, R.R., and Drost, J. (2020). Organoid models of childhood kidney tumours. Nat. Rev. Urol. 17, 1–3.

Chapter 7
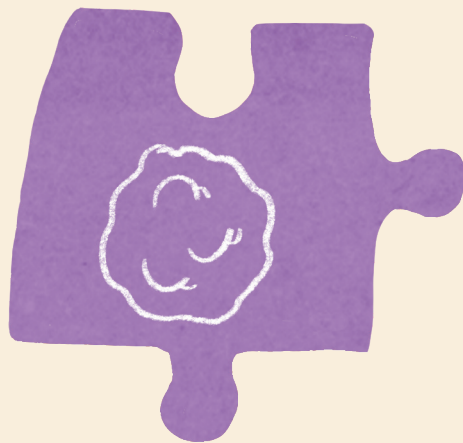
Patient-derived tumor organoids to find therapeutic interventions for relapsed Wilms tumors

Camilla Calandrini[1,2], Alissa Groenendijk[1], Sofia Doulkeridou[1,2], Dilara Ayyildiz[1,2], Jesper Brok[3,4], Reem Al-Saadi[5], Daniela Perotti[6], Filippo Spreafico[7], Marry van de Heuvel-Eibrink[1], Annelies Mavinkurve-Groothuis[1] and Jarno Drost[1,2]

[1] Princess Máxima Center for Pediatric Oncology, Heidelberglaan 25, 3584 CS Utrecht, the Netherlands

[2] Oncode Institute, Heidelberglaan 25, 3584 CS Utrecht, the Netherlands

[3] Developmental Biology and Cancer Research and Teaching Department, UCL Great Ormond Street Institute of Child Health, University College London, UK

[4] Department of Paediatric Haematology and Oncology, Rigshospitalet, Copenhagen University Hospital, Denmark Division of Pediatric Oncology, Denmark

[5] University College London, UCL Great Ormond Street Institute of Child Health, 30 Guilford Street, London WC1N 1EH, UK

[6] Molecular Bases of Genetic Risk and Genetic Testing Unit, Department of Research, Fondazione IRCCS Istituto Nazionale Dei Tumori, Milan, Italy

[7] Department of Medical Oncology and Hematology, Pediatric Oncology Unit, Fondazione IRCCS Istituto Nazionale Dei Tumori, Milan, Italy

Abstract

Wilms tumor is the most common pediatric renal malignancy, accounting for ~ 6% of all childhood cancers. While overall survival rates exceed 90%, patients experiencing disease relapse face a worse outcome. Among these, patients diagnosed with high-risk and refractory relapsed Wilms tumor carry dismal survival chances, between 40-10%. The development of novel therapeutic strategies able to treat these children is imperative. In recent years little improvement has been achieved in the treatment of relapsed Wilms tumor patients mostly due to the lack of representative preclinical models available to study the disease and to perform drug testing. Tumor organoids are emerging as relevant *in vitro* preclinical models, able to capture key characteristics of the parental tumor tissues. Furthermore, several studies have demonstrated their ability to recapitulate patients response to therapy. In this study, we describe the generation of patient-derived organoid models from relapsed Wilms tumor cases collected from all across Europe, with an overall efficiency of 50%. After performing genetic and phenotypic characterization, we utilized the established models to perform explorative drug screening and identify therapeutic vulnerabilities in a clinically relevant timeframe. As result, we uncover both patient-specific hits, as well as general relapsed Wilms tumor vulnerability towards EGFR/HER2 inhibitors. Our results pave the way for the implementation of patient-derived organoids for future clinical applications.

Introduction

Wilms tumor (WT) is the most common pediatric renal tumor, accounting for about 90% of all kidney cancer diagnosis[1]. In Europe, children are treated following the SIOP protocol, consisting of preoperative chemotherapy, followed by surgical removal of the affected kidney and postoperative chemotherapy (and/or radiotherapy), adjusted to tumor histology and stage[2, 3]. The distribution of the three cellular phases characteristic of WT histology - epithelial, stromal, and blastemal cells - contributes to the stratification of patients into risk groups. Specifically, a predominant blastemal content and/or presence of diffuse anaplasia (enlarged, hyperchromatic nuclei and presence of aberrant mitotic figures) are characteristics associated with high-risk, and therefore worse outcome. Although nowadays overall survival rates have reached 90%[2, 4, 5], about 15% of patients experience (recurrent) disease relapse[6, 7].

Wilms tumor relapses (RWT) mostly occur within 2 years from the first diagnosis, and it often manifests in lungs, abdomen, liver and more rarely in bones and brain[6, 8]. RWT cases are rare, with 4 to 5 patients diagnosed per year in the Netherlands[9]. Based on histology, stage and therapeutic interventions administered as treatment of the primary tumor, RWT patients can be classified into three risk groups, namely AA, BB and CC[2, 6, 7]. The assignment to these groups determines which therapeutic regimen is given to the patient. While AA patients display a relatively good prognosis (70-80% overall survival (OS)), BB and CC patients show a dismal outcome, with OS of 40-50% and 10%, respectively[10-13]. The poor survival rates measured for these patients reflect the ineffectiveness of the therapeutic interventions currently in use. The identification of novel, more effective therapeutic options is therefore imperative.

In vitro models to study RWT are scarce and often do not represent the genotypic and phenotypic landscape of the original tumors[3, 14]. This, together with the rarity of the RWT cases, has hampered the discovery of novel therapies. Recently, we described the generation of the first pediatric renal cancer organoid biobank, containing ~40 WT organoid models established with high efficiency mostly from primary WT cases[15]. These patient-derived organoid models demonstrated to be representative of the original tumor tissues at the genetic, transcriptomic, and phenotypic level. Given the several studies reporting the ability of patient-derived tumor organoids to predict patient response to therapy[16-19], we exploited WT organoids for pilot drug screening[15]. In this study, we aimed to generate and characterize RWT patient-derived organoid models and to utilize them to per-

form explorative drug screening for the identification of novel (patient-specific) therapeutic interventions.

Results

Establishment of RWT cultures

Within the existing SIOP-RTSG framework, we collected tumor tissue samples of 23 RWT patients from 10 different European countries (**Figure 1A**). We received resection material (n = 13) or needle biopsies (n = 10) of RWT mostly localized in lungs, abdomen, and liver, from patients belonging to all 3 risk group categories (**Figure 1B-D**). Of the 23 samples received, 3 were lost due to suboptimal sample handling (**Figure 1E**), such as an incorrect freezing procedure of the tissue. Of the 20 residual samples, 2 were discarded due the lack of viable tumor cells in the specimen as determined by Hematoxylin and Eosin (H&E) staining.

   Overall, a total of 18 RWT samples with viable tumor content were processed to generate patient-derived tumor organoids (**Table 1**), following a previously established protocol[15]. After the first 4 attempts, we observed that not all RWT samples were able to adapt and expand in 3D culture conditions, but rather preferred to adhere to the bottom of the culture plates and expand as a monolayer. In another case, the culture performed better (i.e. higher proliferation rate) in suspension, in the absence of basement membrane extract (BME).

   Given the different preferences for *in vitro* expansion, starting from sample RWT_70, all samples received were processed and plated in three different conditions: 70% BME (3D), 2D and suspension (3D, no BME). Following these adaptations, we were able to successfully generate 9 organoid cultures from 18 obtained RWT specimens (50% success rate). When examining different criteria such as tumor location, quantity of tissue received and patient risk group stratification, no significant association between any of this criteria and establishment efficiency was observed (**Figure 1F-H**). Overall, 4 RWT lines were successfully established in 70% BME, 4 in a 2D-growing monolayer and 1 in suspension (**Figure 2**). Thus, we were able to establish 9 unique patient-derived RWT cultures with an efficiency of establishment of 50%.

Table 1. Characteristics of RWT samples included in the study. Grey color indicates data that could not be retrieved. N/A, not available.

Patient	Gender	YoB	Histology	Anaplasia reported	Source	Biopsy/Resection	Risk group	Outcome	Line successfully established
RWT_42	Female	2004	N/A	N	Liver	Biopsy	CC	Alive with evidence of disease	N
RWT_60	Female	2015	Predominant blastemal	N	Abdomen	Resection	AA	Alive without evidence of disease	N
RWT_62	Male	2014	N/A	Y	Lung	Resection	CC	Deceased	Y
RWT_66	Female	2009	N/A	N	Abdomen	Resection	CC	Deceased	N
RWT_70	Male	2011	Predominant epithelial	N	Lung	Resection	BB	Alive without evidence of disease	N
RWT_77	Female	2015	N/A	N	Abdomen	Biopsy	BB	Alive without evidence of disease	Y
RWT_104	Female	2019	Predominant stromal	N/A	Lung	Biopsy	AA	Alive with evidence of disease#	Y
RWT_107		2012	Predominant blastemal	N/A	Liver	Resection			N
RWT_110					Lung	Biopsy			N
RWT_111	Male	2008	Predominant blastemal	N	Psoas muscle	Resection	BB	Alive with evidence of disease	N
RWT_112					Lung	Biopsy			N
RWT_117	Female	2013	Predominant stromal	N	Brain	Resection	BB	Alive with evidence of disease	Y
RWT_118					Lung	Biopsy			N
RWT_119*	Male	2005	Predominant blastemal	N	Liver	Resection	BB	Alive without evidence of disease	Y
RWT_123	Male	2003	Blastemal, epithelial	N	Lung	Resection	BB	Alive without evidence of disease	Y
RWT_125	Male	2017	N/A	Y	Lung	Resection	CC	Deceased	Y
RWT_126	Female	2014	Blastemal, epithelial	N	Abdomen	Resection	CC	Alive with evidence of disease#	Y
RWT_136	Male	2017	Predominant blastemal	N	Lung	Biopsy	AA	Alive with evidence of disease	Y

* Reported as 119T in Calandrini et al, 2020
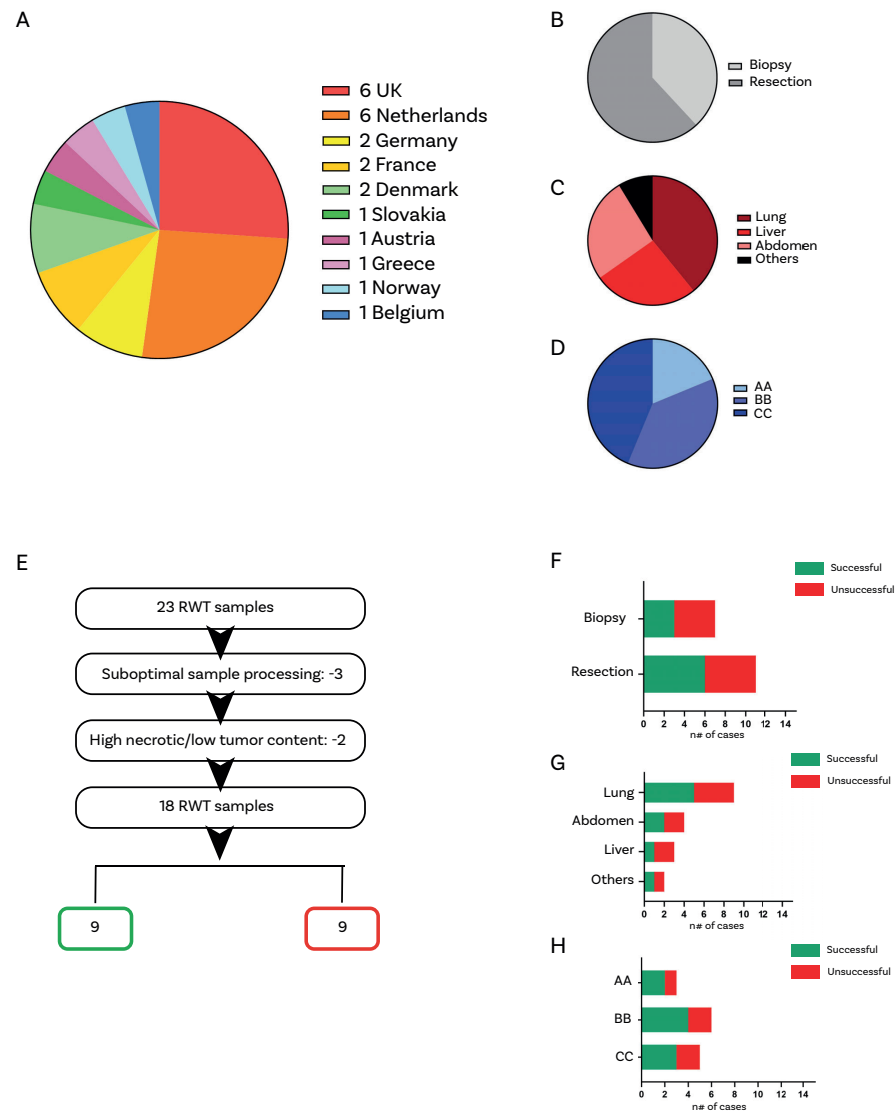# Second relapse reported to occur during treatment

7

Figure 1. Establishment of patient-derived RWT organoid cultures. A. Pie chart depicting the number of RWT samples collected per country. B-D. Pie charts representing the source of tissue material (needle biopsy or resection) (B), anatomical location (C) and patient risk group (D). E. Flow chart summarizing the selection of RWT samples included in the study. F-H. Bar graphs representing number of successful and unsuccessful RWT cultures divided by tissue source (F), tumor location (G) and risk group category (H).
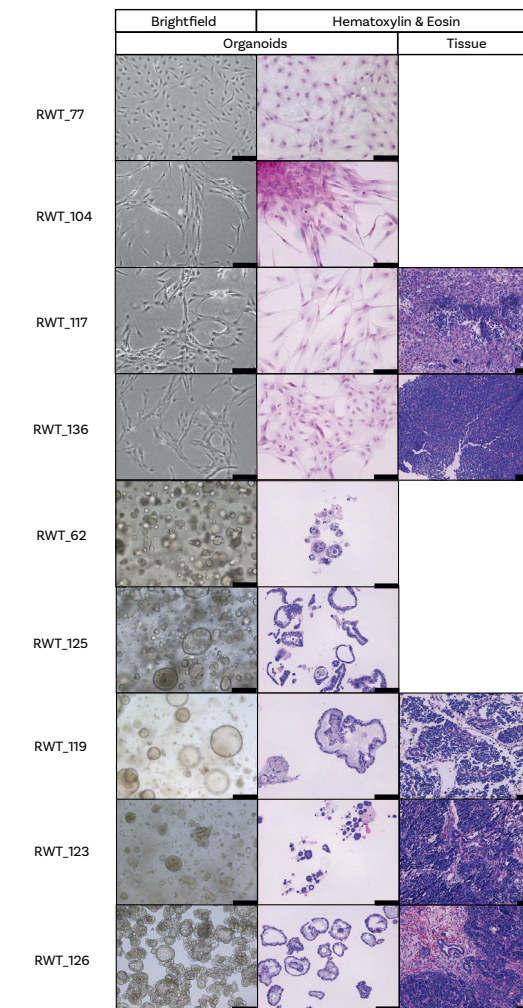

Figure 2. Histological characterization of RWT organoids. Brightfield pictures of established RWT cultures (first column), followed by H&E staining of the same cultures (second column) and, if available, of matching tumor tissue (third column). Scale bars: 100μm.

Phenotypic characterization of RWT cultures

To phenotypically characterize the established RWT cultures, we first performed histological characterization using H&E staining. As previously observed for primary WT organoids[15], RWT cultures retain features typical of epithelium, stroma and/or blastemal cells. While epithelial tubular-like structures were mostly observed in 3D cultures (both 70% BME and suspension), stromal cells were primarily observed in the 2D cultures (Figure 2). For 5/9 RWT lines, we were able to obtain

patient-matching tumor tissue to perform H&E characterization. Comparison of the organoids with matching tissues showed that the appearance of the RWT cultures grown in 3D showed similarities to the histology of the parental tumor tissues (**Figure 2**).To characterize the cellular composition of the RWT organoid cultures, we performed flow cytometry to assess EPCAM, CD90(THY1) and NCAM1 expression, markers previously identified to be representative of epithelial, stromal, and blastemal cells, respectively, in primary WT organoid cultures[15]. In the monolayer cultures, we could detect populations of cells that stained positive for CD90 and NCAM1, while the cultures were devoid of EPCAM-positive epithelial cells (**Figure 3A, Supplementary Figure 1A**).
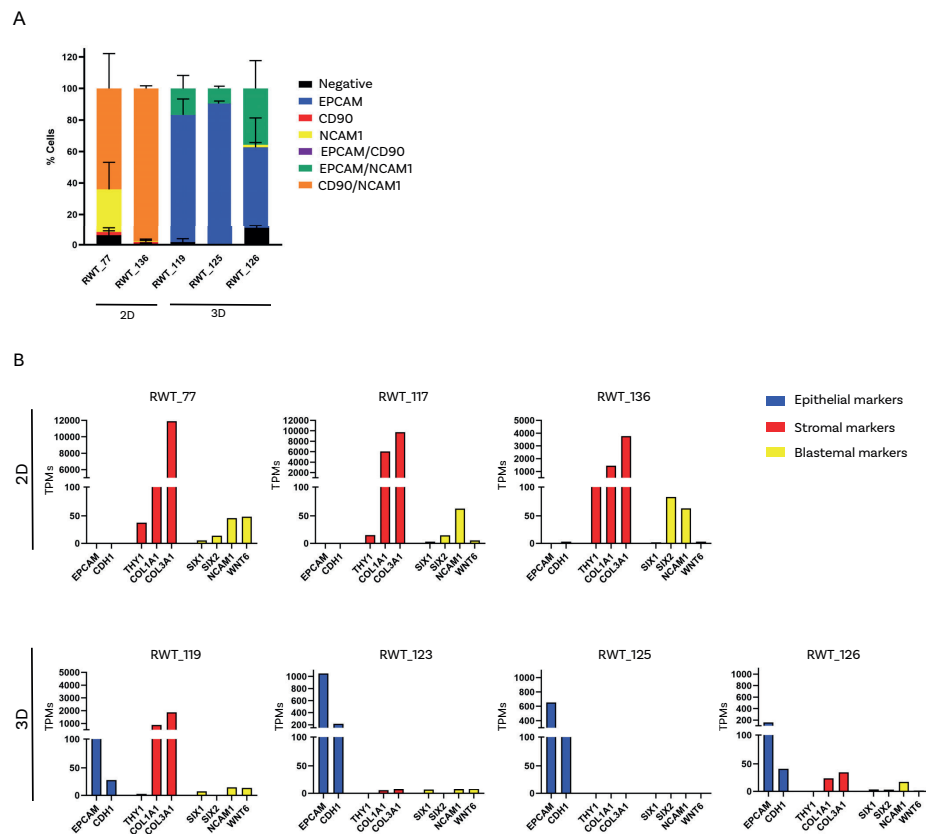

Figure 3. Heterogeneous expression of epithelial, stromal, and blastemal markers in RWT cultures. A. Quantification of EPCAM, CD90 and NCAM1 protein expression using flow cytometry analyses. Bar graphs represent mean ± SD of 3 independent experiments. **B.** Normalized gene expression levels (TPM) from RNA-seq data for the depicted RWT cultures. Displayed are characteristic markers of epithelial, stromal and blastemal cells.

In contrast, the 3D cultures were primarily composed of EPCAM-positive epithelial cells as well as NCAM1/EPCAM double positive cells. Interestingly, we could observe patient-specific differences in the expression of these markers. As example, culture RWT_77 displayed a greater population of blastemal marker NCAM1-only positive cells compared to RWT_136, suggesting the presence of a larger blastemal cell population in this culture.

To further confirm these observations, we performed bulk RNA sequencing (RNA-seq) on a subset of RWT cultures. We included 2D- (n=3) and 3D-growing (n=4) RWT lines. Indeed, epithelial marker expression (*EPCAM*, *CDH1)* was detected in all 3D lines, but not in the monolayer cultures, confirming that 2D cultures are devoid of epithelial cells. On the contrary, expression of stromal markers such as *COL3A1* and *COL1A1* was generally higher in 2D compared to 3D cultures (**Figure 3B, Supplementary Figure 1B**). Interestingly, we observed expression of putative blastemal markers (*SIX1, SIX2, NCAM1*) in 6/7 lines independent of culture conditions, further confirming that both 3D and 2D culturing allows for blastemal cells expansion.

Thus, RWT organoid cultures are composed of blastemal, epithelial, and stromal cells. While 3D culturing seems to primarily facilitate expansion of epithelial and epithelial-like blastemal cells, monolayer culturing promotes expansion of stromal and stromal-like blastemal cells.

Genetic characterization of RWT cultures

Next, we set out to define the genetic landscape of RWT organoid cultures using whole genome sequencing (WGS). All 9 RWT lines displayed several copy number alterations (CNAs) that are typically found in WT, such as gains of chromosome 1q, 6, 7 and/or 12, or loss of chromosome 4, 16q or 17p (**Figure 4**)[20-24]. Furthermore, we identified single nucleotide variants (SNVs) in genes described to be frequently mutated in WT, such as *WT1, CTNNB1, WTX, SIX1, BCORL1, DROSHA* and *MYCN*[20, 22, 24-26].

RWT_62 and RWT_125, both originated from tumors with diffuse anaplasia, harbored *TP53* mutations and 17p LOH, consistent with complete loss of P53 function[27]. RWT_126T displayed a combination of *SIX1* (p.Q177R) and *DROSHA* (p.E1147K) mutations, previously described to be associated with poor prognosis[20, 21, 28]. Furthermore, RWT_104 was characterized by the presence of mutations in both *WT1* and *CTNNB1* genes[29], whereas RWT_123T harbored a *MYCN* p.P44L gain of function mutation, previously associated with high-risk WT[21, 26, 30, 31].
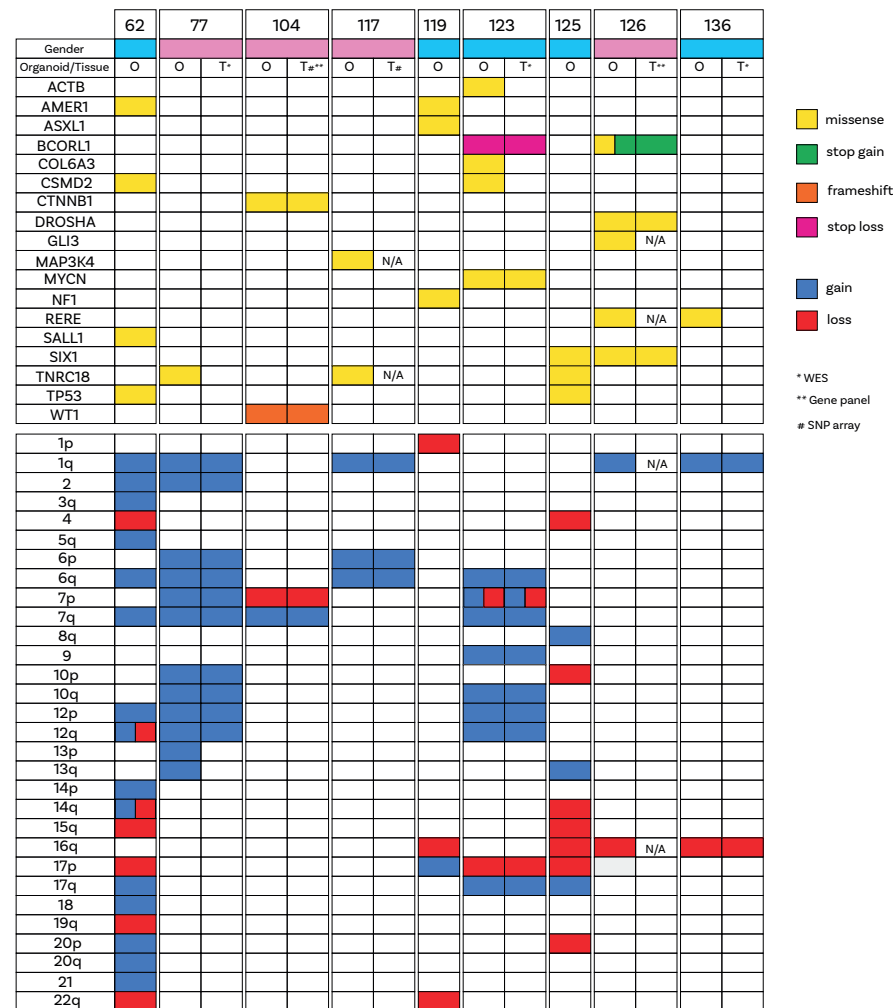
Figure 4. Genetic characterization of RWT cultures reveals known driver mutations and copy number alterations. Overview of single nucleotide variants and copy number alterations found in RWT organoids (O). Comparison with available tissue data (T) from WES, gene panel sequencing and SNP array sources revealed genetic resemblance of the RWT cultures to the original tumor tissues. N/A : not available.

To evaluate the resemblance of RWT organoids to the original tumor tissues at the genetic level, we compared WGS data of RWT organoids with available genetic data (WES/Oncogene panel/SNP array) of patient-matching tissues[32]. This revealed that RWT cultures displayed a genetic landscape alike the tumor tissues of origin (**Figure 4**).

In conclusion, RWT cultures closely recapitulate the genetic driver landscape of patients with WTs, representing therefore a relevant model for RWT.

Drug screening on RWT cultures reveals patient-specific drug sensitivities

Next, we set out to utilize the successfully established and characterized RWT organoid cultures for drug testing to identify patient-specific or RWT-specific drug sensitivities. To evaluate the feasibility of obtaining drug screening results within a clinically relevant time frame for RWT patients, we aimed to perform drug screening as soon as possible after obtaining the patient material. The time needed to obtain sufficient number of cells to perform drug screening varied considerably among the RWT cases, from a minimum of 3 up to 9 months (median: 3 months; average: 4,5 months) (**Supplementary Figure 2A**). As expected, RWT cultures derived from larger resection specimens were typically screened faster than RWT cultures derived from needle biopsies (**Supplementary Figure 2B**).

We tested a library of approximately 100 compounds, composed of chemotherapeutic agents and targeted compounds currently in clinical use or in an advanced stage clinical trial[15, 33]. Testing multiple concentrations per drug allowed us to draw dose-response curves and calculate area under the curve (AUC) and inhibitory half concentration (IC_{50}) values. Unsupervised hierarchical clustering of AUC data revealed similarities in drug responses between RWT lines regardless of their culture method, risk group or growth speed (**Figure 5A, Supplementary Figure 2C,D**), suggesting that drug screening results reflect RWT biological differences and not culture-induced artifacts.

RWT patients are treated with chemotherapy regimens, based on the assigned risk groups[6, 7]. Among the commonly used chemotherapeutics are Doxorubicin, Etoposide, Vincristine, and Irinotecan. We observed that Doxorubicin treatment caused a similar effect in reducing cell viability in the majority of the RWT lines, while response to Vincristine varied considerably among the different cultures (**Figure 5B**). When grouping the RWT lines based on risk category, we observed no significant difference in drug sensitivities (**Figure 5C**). Notably, we did not measure a significant response of any RWT line to Etoposide, a compound routinely administered for RWT treatment (**Figure 5B,C**). Overall, we measured significant effect of Vincristine, Doxorubicin and Irinotecan, while the lack of sensitivity observed for Etoposide questions the added value of this compound in the treatment of RWT patients.
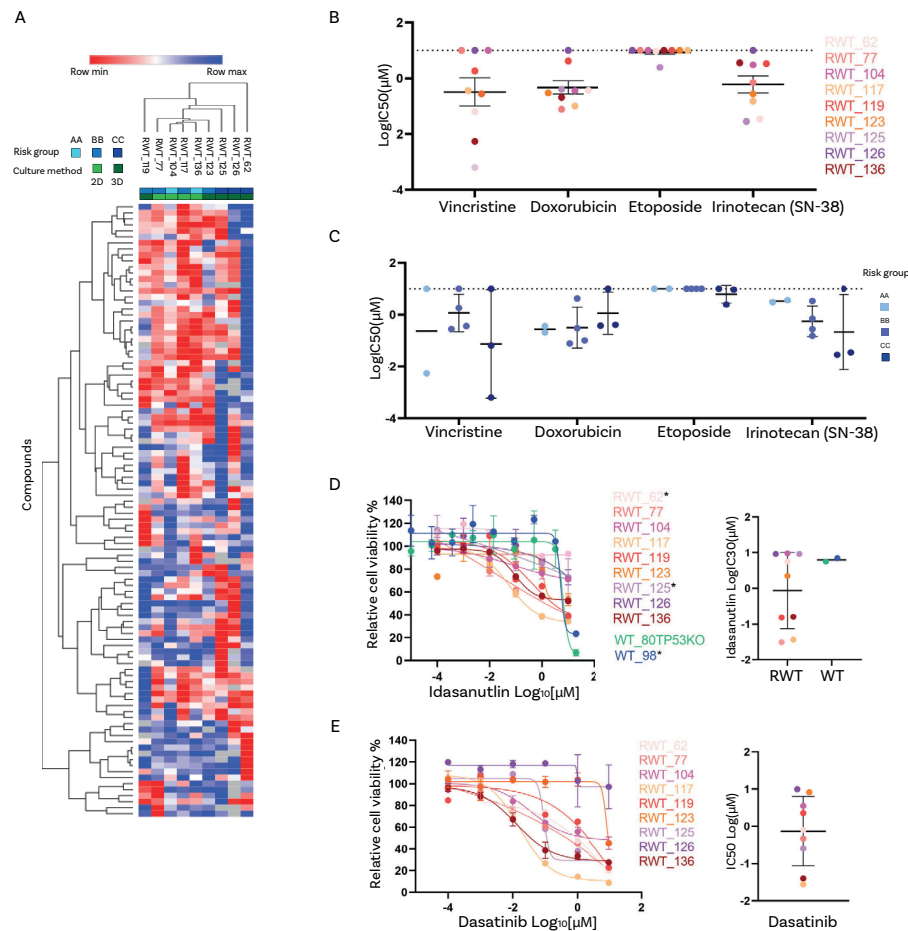
Figure 5. Drug screening on RWT organoids reveals patient-specific drug sensitivities. A. Unsupervised hierarchical clustering of AUC drug screening data, showing that clustering is independent of culture conditions and risk group. Color scale blue to red indicates decreasing AUC values. Color scale is relative to each compound (row). Grey color indicates AUC values not available. **B**. LogIC$_{50}$ values calculated of Vincristine, Doxorubicin, Etoposide and Irinotecan (SN-38) on the indicated RWT cultures. Represented are mean ± SD values. In case IC$_{50}$ value was not reached, the highest tested concentration (10µM) was used for the calculations. **C**. LogIC$_{50}$ values calculated of Vincristine, Doxorubicin, Etoposide and Irinotecan (SN-38) grouped by risk category. Represented are mean (AA) and mean ± SD values (BB,CC). In case IC$_{50}$ value was not reached, the highest tested concentration (10µM) was used for the calculations. **D**. Left: Dose response curve of Idasanutlin on the indicated RWT and primary WT cultures. * indicates lines with reported anaplastic features. Line WT_80T-*TP53*KO was included as negative control for P53 function. Right: LogIC$_{30}$ values of Idasanutlin on the indicated RWT and primary WT organoid cultures. In case IC$_{30}$ value was not reached,

the highest tested concentration (10µM) was used for the calculations. **E**. Dose response curve (left) and LogIC$_{50}$ (right) of Dasatinib on the indicated RWT cultures. Lines RWT_117 and RWT_136 display high sensitivity, while RWT_123 and RWT_126 show a more resistant phenotype. In case IC$_{50}$ value was not reached, the highest tested concentration (10µM) was used for the calculations.

While investigating tumor-specific drug vulnerabilities, we observed differential sensitivity to Idasanutlin, a p53 stabilizer agent. We found that RWT_62 and RWT_125 were markedly less sensitive compared to lines RWT_77, 117, 119 and 136 (**Figure 5D**). Indeed, WGS had confirmed the complete loss of TP53 in RWT_62 and RWT_125, explaining therefore the insensitivity of these cultures to the treatment (**Figure 4**). Interestingly, RWT_104, RWT_123 and RWT_126 also showed insensitivity to Idasanutlin treatment, but no *TP53* mutations were identified using WGS. Insensitivity to Idasanutlin however suggests that these lines have acquired an aberrant p53 function, likely via alternative mechanisms.

Comparing the top 10 ranked compounds based on AUC values of each of the RWT lines (**Supplementary Table 1**), we found that RWT_117 showed high sensitivity to the Abl/Src inhibitor Dasatinib. Drawing dose-response curve for Dasatinib in all RWT lines confirmed the increased sensitivity of line RWT_117 and additionally identified RWT_136 as sensitive line (AUC rank for Dasatinib: 12), while RWT_123 and RWT_126 were significantly more resistant (AUC rank for Dasatinib: > 60) (**Figure 5E**). Next to a higher expression of *ABL1*, direct target of Dasatinib, we found that several markers, previously associated with sensitivity to Dasatinib treatment[34], were also highly expressed in sensitive cultures (**Supplementary Figure 2E**). Among these markers, we find members and substrates of the Src family kinases, such as *LYN* and *CAV1*. The overexpression of these markers in RWT_117 and RWT_136 suggest a possible role of Src family kinases in the development of these tumors, which should be further investigated.

EGFR/HER2 inhibition impedes RWT organoid growth

Next, to identify drugs that were effective in all – or the majority of - RWT organoid cultures, we compared AUC values of our RWT cultures with those available for organoid cultures derived from other pediatric tumor entities. We calculated Z-score values and compared sensitivities among the different tumor types. When inspecting the top 5 most sensitive drugs for RWT (negative Z-score values), we identified two EGFR inhibitors: Erlotinib and Afatinib (**Figure 6A**). Analysis of LogIC$_{50}$ values confirmed that RWT organoid cultures were significantly more sensitive to both Afatinib and Erlotinib treatment when compared to organoids derived from other pediatric tumor entities (**Figure 6B,C**). Notably, within the RWT

cultures, CC group samples showed a significant higher sensitivity to Erlotinib, but not to Afatinib, when compared to AA group cultures (**Supplementary Figure 3A,B**).

Given the sensitivity of RWT cultures to EGFR (Erlotinib) and EGFR/HER2 (Afatinib) inhibition, we set out to investigate the expression of EGFR and HER2 in RWT organoids and tissues. RNA-seq analysis revealed presence of *EGFR* and *ERBB2* mRNA expression in RWT organoids (**Figure 6D**). To confirm this on the protein level, we performed immunohistochemistry staining on organoids and available matching tissues. EGFR and HER2 protein expression was indeed confirmed in RWT organoids, as well as in tissue specimens, where we observed EGFR positivity in 4/4 and HER2 positivity in 3/4 tested samples (**Figure 6E, Supplementary Figure 3C**). The levels of EGFR and HER2 expression however did not correlate with the sensitivity of the RWT lines to Erlotinib or Afatinib (**Supplementary Figure 3D-F**). Lastly, we tested whether sensitivity to EGFR/HER2 inhibition was specific for RWT or a general WT vulnerability. Comparison of LogIC$_{50}$ values revealed similar sensitivities of primary WT to Erlotinib and Afatinib treatment compared to RWTs (**Supplementary Figure 3G**). Overall, we identified EGFR/HER2 inhibition as potential therapeutic vulnerability of RWTs, as well as of primary WTs.

EGF is necessary for RWT organoid establishment and growth

The medium used for RWT organoid growth contains, amongst others, the growth factors EGF and FGF10[15, 35]. To determine whether the use of this culture medium is responsible for the sensitivity to EGFR/HER2 inhibition, we cultured RWT_77 (sensitive to Erlotinib and Afatinib) and MRT_1 (insensitive to both inhibitors) in complete medium, medium without EGF and medium without EGF/FGF10, and tested the effect of EGFR/HER2 inhibition. As a result, we first observed a significant reduction in cell growth for RWT_77, but not for MRT_1, in the conditions lacking EGF and EGF/FGF10, suggesting indeed a growth dependency of RWT on EGF (**Figure 6F, Supplementary Figure 3H**). In the absence of EGF and EGF/FGF10 we observed a decrease in sensitivity to Erlotinib and Afatinib treatment for RWT_77, but not for MRT_1 (**Supplementary Figure 3I**). To further test if the dependency on EGF was induced by the culturing methods, we set to re-generate RWT cultures from tissue samples, in complete culture medium or medium lacking EGF. Whereas MRT1 organoids could be efficiently established in the presence or absence of EGF, RWT organoids could not be established in the absence of EGF (**Figure 6G**), indicating that EGF dependency is a tumor-intrinsic characteristic of RWT, that is not induced by culture conditions.
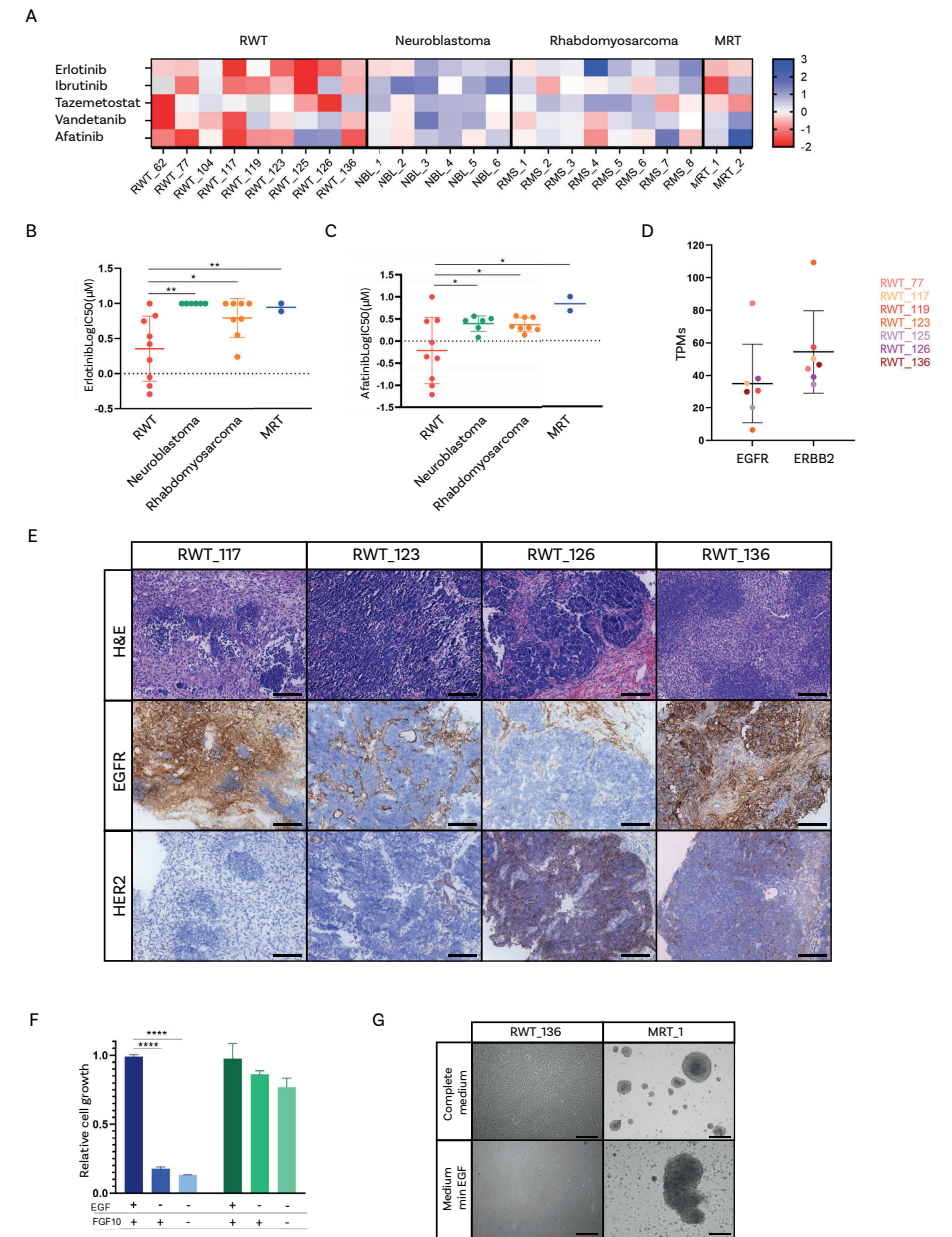
Figure 6. EGFR/HER2 inhibition as therapeutic intervention for RWTs. A. Heatmap depicting top 5 rank AUC z-score values calculated between RWT and other pediatric tumor cultures (neuroblastoma, rhabdomyosarcoma and malignant rhabdoid tumors (MRT)). **B.** LogIC$_{50}$ values for EGFR inhibitor Erlotinib in RWT, neuroblastoma, rhabdomyosarcomas and malignant rhabdoid tumors (MRT) cultures. In case IC$_{50}$ value was not reached, the highest tested

concentration (10µM) was used for the calculations. Represented are mean (MRT) and mean ± SD values (n≥6). P-value were calculated using a two-tailed Student's t test, two-sided: * < 0.05, ** <0.01. **C**. LogIC$_{50}$ values for EGFR/HER2 inhibitor Afatinib in RWT, neuroblastoma, rhabdomyosarcomas and MRT cultures. In case IC$_{50}$ value was not reached, the highest tested concentration (10µM) was used for the calculations. Represented are mean (MRT) and mean ± SD values (n≥6). P-value were calculated using a two-tailed Student's t test, two-sided: * < 0.05. **D**. Transcript per million values (TPMs) for *EGFR* and *ERBB2* (gene encoding HER2) in the depicted RWT cultures. **E**. H&E (top), EGFR (middle) and HER2 (bottom) staining on RWT tissues. Scale bars: 100µm. **F**. Cell viability measured in lines RWT_77 and MRT_1 cultured in medium lacking EGF or both EGF and FGF10, relative to complete culture medium. Cell viability was measured with CellTiter-Glo. Represented are mean ± SD values. P-value were calculated using a two-tailed Student's t test, two-sided: **** < 0.0001. **G**. Representative brightfield pictures of cultures generated from RWT_136 and MRT_1 tissues in complete culture medium (top) and medium lacking EGF (bottom). MRT_1 was taken along as negative control (cultures not dependent on EGF). Scale bars: 100µm.

In conclusion, we have generated 9 unique patient-derived RWT cultures that closely recapitulate the characteristics of the original tissues. We have exploited these models for drug screening purposes and identified patient-specific drug vulnerabilities, as well as EGFR/HER2 inhibitors as promising compounds for the treatment of RWT patients.

Discussion

The identification of novel therapeutic avenues for high-risk RWT patients is dependent on the availability of preclinical models representative of the original tumor tissues. Until recently, only an handful of *in vitro* cultures was available to study RWT, monophasic 2D-growing cell lines, mostly of stromal origin, failing to represent the cellular heterogeneity and genetic landscape of RWT tumors[3]. Using the organoid technology, we established patient-derived RWT models able to recapitulate genetic - and partial phenotypic - features of the original RWT tissues. While markers identifying epithelial, stromal and blastemal cells have been found expressed in RWT lines, single cell sequencing approaches are needed to further evaluate cellular and genetic heterogeneity within the RWT cultures.

In this study, we have collected RWT samples to generate patient-derived organoid models and perform drug screening to identify patient-specific treatment in a clinically relevant time window. To be able to address the feasibility of this strategy, parameters such as efficiency of establishment and turnaround time need to be evaluated.

The adaptation of the protocols previously applied to culture primary WTs – including expansion in 2D and suspension - allowed to achieve a success rate of establishment of 50% for RWT cultures. This is considerably lower than for primary WT organoids (~75%)[15]. While for few samples the failed establishment was caused by outgrowth of healthy lung or liver cells in culture,[36, 37] for other samples the reasons are still unknown. The lack of proliferation observed for some starting RWT cultures suggests that growth factors are missing in the culture medium. To increase efficiency of establishment, methodical testing should be performed to identify such media components. The discrepancy in success rate of establishment and culture methods between primary and relapsed WT organoids is an interesting observation, likely the result of fundamental biological differences characterizing primary and relapsed disease.

For 6/8 patients we were able to obtain drug screening results in a relevant time window (i.e., patients were still alive; 2/2 AA patients; 3/3 BB patients; 1/3 CC patients), while 2 patients passed away before the drug screening was performed (2/3 CC patients) (**Table 1**). Although promising, these results stress the need to further shorten the time for RWT cultures establishment and drug screening. This is crucial especially when considering very-high risk CC patients, which are the ones most in need for alternative therapeutic interventions. Data collected until now suggests that starting with a larger quantity of tumor material (resection rather than biopsy) can result in a faster expansion of the cultures and therefore should be preferred, when possible. Furthermore, testing the effect of additional growth factors in the culture media on RWT growth could further shorten drug screening turnaround time.

In this study we identified EGFR/HER2 inhibition as potential common therapeutic intervention for RWT patients. Reports on EGFR and HER2 expression on WT are scarce and for RWT even absent. EGFR positive staining was registered in 13-38% of primary WT tissues[38, 39], while HER2 staining has been previously associated with epithelial differentiation [40, 41], or it has been found absent[39]. In our cohort of RWT samples we registered expression of both EGFR and HER2 in the majority of the samples, suggesting an important role for these receptors in RWT development. To further investigate the potential therapeutic value of this approach in RWTs, Erlotinib and Afatinib treatment should be tested in a *in vivo* setting, e.g. on RWT xenograft models[42].

Overall, this pilot study shows the feasibility of generating representative RWT models and perform middle-throughput drug screening to identify novel (patient-specific) therapeutic vulnerabilities. To achieve the goal of a personalized

medicine approach, future efforts should be focusing on increasing efficiency of RWT cultures establishment and shortening turnaround time.

Material and Methods

RWT tissue collection and processing. RWT tissues from outside the Netherlands were shipped at -20°C or 4°C and promptly processed upon arrival, typically within 72 hours from surgery. Local RWT samples were processed within few hours from surgery. RWT samples were minced with scalpels into 1 mm^3 pieces and further digested with collagenase-D supplemented with 10μM Rho-Kinase inhibitor Y-27632 for up to 1 hour at 37 °C in a horizontal shaker. After a washing step in AdDF +++ (Advanced DMEM/F12 with addition of 5% Glutamax, 5%Hepes and 5% Pen/Strep) if blood cells were present in the specimen, the digested tissue was treated with red blood cell lysis buffer for 5 minutes at room temperature. The resulting digested tissue was divided in 3 parts: 1/3 was plated in 70% BME droplets; 1/3 was plated in standard culture plates to form adherent cultures; 1/3 was plated in suspension or repellent plates, to promote growth in suspension. Inform consent was obtained from the parents of all participants (UMBRELLA, ITHER studies).

RWT organoids culturing. RWT organoids were cultured and expanded in kidney organoid medium (KOM): AdDF+++ supplemented with 1.5% B27 supplement (GIBCO), 10% Rspondin-conditioned medium, N-acetylcysteine (1.25 mM, Sigma), Rho-kinase inhibitor Y-27632 (10 mM, Abmole), A83-01 (5 mM, Tocris Bioscience), FGF10 (100 ng ml-1, Peprotech), and EGF (50 ng ml-1, Peprotech)[35]. RWT cultures were passaged by mechanical disruption and/or enzymatic digestion (TrypLE + 10μM Rho-Kinase inhibitor) based on morphology.

Histology and immunohistochemistry. Organoids and tissues were fixed in 4% paraformaldehyde, dehydrated, and embedded in paraffin. Immunohistochemistry staining was performed on 4μm sections using standard protocols. Hematoxylin and Eosin staining was conducted following standard protocols. 2D growing RWT cultures were fixed in 4% paraformaldehyde on IBIDI chambers prior to staining. The following primary antibodies have been used: EGFR (Cell Signaling Technology, #4267); EGFR (Invitrogen, #280005); HER2 (ThermoFisher, MA5-14509); HER2 (Roche, # 790-4493). Images were acquired with Leica DM6 microscope.

Assessment marker expression via flow cytometry. RWT cultures were dissociated into single-cell suspension using TrypLE Express (ThermoFisher) with the addition of 10μM Rho-Kinase inhibitor Y-27632. Single-cells suspensions were stained with the following primary conjugated antibodies and dyes: APC-CD90/THY1 (Biolegend, 328113), AF488-EPCAM (Biolegend, 324210), BV421-NCAM/CD56 (Biosciences, 562752), 7AAD (Biolegend, 420403). Cells were acquired using Beckman Cytoflex XL flow cytometer. A minimum of 10 000 events was recorded per experiment. Gating was determined based on unstained populations. Compensation was performed following FMO strategies.

Whole genome sequencing. DNA isolation from RWT cultures was performed using the ReliaPrep gDNA Tissue Miniprep System (Promega) following manufacturers instructions. Samples were sequenced on Illumina NovaSeq6000 sequencer by Hartwig Medical Foundation to 30x coverage. Sequence reads were mapped against human reference genome GRCh38 by using Burrows-Wheeler Aligner v0.7.17 mapping tool with the settings 'bwa mem -M -c 100'. Sequence reads were marked for duplicates by using Sambamba v0.6.8. Raw variants were multisample-called by using the GATK HaplotypeCaller v4.1-3.0. The variants who did not meet the quality requirements (i.e., Quality Depth (QD)<2, mapping quality (MQ)<40, Fisher strand (FS)>60) were filtered out. Non-synonymous mutations (missense mutation, start loss, stop gain, inframe insertion/deletion and frame shift) above VAF>0.1 were identified in known driver genes due to lacking matching normal for the organoid samples. Variants were further filtered based on pathogenicity report from PolyPhen and ClinVar. Copy number variations (CNVs) were calculated based on the estimated copy number by Control-Freec v11.5 using a 1000 bp window.

RNA sequencing. RNA from RWT cultures was extracted using Trizol reagent (Invitrogen), according to manufacturers instructions. Quality was checked with Bioanlayzer2100 RNA Nano 6000 chips (Agilent). Paired-end sequencing was performed with Illumina HiSeq by Novogene (Cambridge). Reads were mapped to human reference genome GRCh38 by STAR aligner using standard settings. Raw read counts were obtained via featureCounts function of the subread package v1.6.5 using gene annotation of gencode (release 37) for human reference genome GRCh38.

Medium and low put drug screening. Drug screening was performed as previously described[33]. Briefly, RWT 3D cultures were harvested and washed with AdDF+++. After a filtering passage using a 70μm strainer, cells were resuspended in KOM medium with the addition of 5% BME (only for RWT lines expanded in BME). RWT 2D cultures were harvested using enzymatic treatment (10μM TrypLE + Rho-Kinase inhibitor), washed, and resuspended in KOM medium. Between 250-500 organoids and 1000-2000 single cells were plated per well of a 384 well plate

using the Multidrop Combi Reagent Dispenser. 18-24 hours later, compounds were added using robotic liquid handling system Biomek i7 or the Tecan D300e Digital Dispenser. After 120 hours, readout was performed using Cell Titer-Glo 3D, following manufacturer's instructions. Results were normalized to DMSO vehicle (100% viability). Data was analyzed with software GraphPad Prism. Unsupervised hierarchical clustering was performed using online tool Morpheus (software.broadinstitute.org /morpheus/).

References

1. Breslow N, Olshan A, Beckwith JB, Green DM. Epidemiology of Wilms tumor. Medical and pediatric oncology. 1993;21(3):172-81.

2. Van Den Heuvel-eibrink MM, Hol JA, Pritchard-Jones K, Van Tinteren H, Furtwängler R, Verschuur AC, et al. Rationale for the treatment of Wilms tumour in the UMBRELLA SIOP–RTSG 2016 protocol. Nature Reviews Urology. 2017;14(12):743-52.

3. Brok J, Treger TD, Gooskens SL, van den Heuvel-Eibrink MM, Pritchard-Jones K. Biology and treatment of renal tumours in childhood. European Journal of Cancer. 2016;68:179-95.

4. Pritchard-Jones K, Moroz V, Vujanić G, Powis M, Walker J, Messahel B, et al. Treatment and outcome of Wilms' tumour patients: an analysis of all cases registered in the UKW3 trial. Annals of oncology. 2012;23(9):2457-63.

5. Schulpen M, Visser O, Reedijk AM, Kremer LC, Zwaan CM, Eggermont AM, et al. Significant improvement in survival of advanced stage childhood and young adolescent cancer in the Netherlands since the 1990s. European Journal of Cancer. 2021;157:81-93.

6. Spreafico F, Pritchard Jones K, Malogolowkin MH, Bergeron C, Hale J, De Kraker J, et al. Treatment of relapsed Wilms tumors: lessons learned. Expert review of anticancer therapy. 2009;9(12):1807-15.

7. Brok J, Mavinkurve-Groothuis AMC, Drost J, Perotti D, Geller JI, Walz AL, et al. Unmet needs for relapsed or refractory Wilms tumour: Mapping the molecular features, exploring organoids and designing early phase trials - A collaborative SIOP-RTSG, COG and ITCC session at the first SIOPE meeting. Eur J Cancer. 2021;144:113-22.

8. Grundy P, Breslow N, Green DM, Sharples K, Evans A, D'Angio GJ. Prognostic factors for children with recurrent Wilms' tumor: results from the Second and Third National Wilms' Tumor Study. Journal of Clinical Oncology. 1989;7(5):638-47.

9. Brok J, Lopez-Yurda M, Tinteren HV, Treger TD, Furtwängler R, Graf N, et al. Relapse of Wilms' tumour and detection methods: a retrospective analysis of the 2001 Renal Tumour Study Group–International Society of Paediatric Oncology Wilms' tumour protocol database. The Lancet Oncology. 2018;19(8):1072-81.

10. Dome JS, Graf N, Geller JI, Fernandez CV, Mullen EA, Spreafico F, et al. Advances in Wilms tumor treatment and biology: progress through international collaboration. Journal of Clinical Oncology. 2015;33(27):2999.

11. Malogolowkin M, Cotton CA, Green DM, Breslow NE, Perlman E, Miser J, et al. Treatment of Wilms tumor relapsing after initial treatment with vincristine, actinomycin D, and doxorubicin. A report from the National Wilms Tumor Study Group. Pediatric blood & cancer. 2008;50(2):236-41.

12. Reinhard H, Reinert J, Beier R, Furtwängler R, Alkasser M, Rutkowski S, et al. Rhabdoid tumors in children: prognostic factors in 70 patients diagnosed in Germany. Oncology reports. 2008;19(3):819-23.

13. Dome JS, Cotton CA, Perlman EJ, Breslow NE, Kalapurakal JA, Ritchey ML, et al. Treatment of anaplastic histology Wilms' tumor: results from the fifth National Wilms' Tumor Study. J Clin Oncol. 2006;24(15):2352-8.

14. Alami J, Williams BR, Yeger H. Derivation and characterization of a Wilms' tumour cell line, WiT 49. International journal of cancer. 2003;107(3):365-74.

15. Calandrini C, Schutgens F, Oka R, Margaritis T, Candelli T, Mathijsen L, et al. An organoid biobank for childhood kidney cancers that captures disease and tissue heterogeneity. Nature communications. 2020;11(1):1-14.

16. Vlachogiannis G, Hedayat S, Vatsiou A, Jamin Y, Fernández-Mateos J, Khan K, et al. Patient-derived organoids model treatment response of metastatic gastrointestinal cancers. Science. 2018;359(6378):920-6.

17. Tiriac H, Belleau P, Engle DD, Plenker D, Deschênes A, Somerville TD, et al. Organoid profiling identifies common responders to chemotherapy in pancreatic cancer. Cancer discovery. 2018;8(9):1112-29.

18. Ooft SN, Weeber F, Dijkstra KK, McLean CM, Kaing S, van Werkhoven E, et al. Patient-derived organoids can predict response to chemotherapy in metastatic colorectal cancer patients. Science translational medicine. 2019;11(513).

19. Ganesh K, Wu C, O'Rourke KP, Szeglin BC, Zheng Y, Sauvé C-EG, et al. A rectal cancer organoid platform to study individual responses to chemoradiation. Nature medicine. 2019;25(10):1607-14.

20. Walz AL, Ooms A, Gadd S, Gerhard DS, Smith MA, Auvil JMG, et al. Recurrent DGCR8, DROSHA, and SIX homeodomain mutations in favorable histology Wilms tumors. Cancer cell. 2015;27(2):286-97.

21. Wegert J, Ishaque N, Vardapour R, Geörg C, Gu Z, Bieg M, et al. Mutations in the SIX1/2 pathway and the DROSHA/DGCR8 miRNA microprocessor complex underlie high-risk blastemal type Wilms tumors. Cancer cell. 2015;27(2):298-311.

22. Gadd S, Huff V, Walz AL, Ooms AH, Armstrong AE, Gerhard DS, et al. A Children's Oncology Group and TARGET initiative exploring the genetic landscape of Wilms tumor. Nature genetics. 2017;49(10):1487-94.

23. Natrajan R, Williams R, Hing S, Mackay A, Reis-Filho J, Fenwick K, et al. Array CGH profiling of favourable histology Wilms tumours reveals novel gains and losses associated with relapse. The Journal of Pathology: A Journal of the Pathological Society of Great Britain and Ireland. 2006;210(1):49-58.

24. Ooms AH, Gadd S, Gerhard DS, Smith MA, Auvil JMG, Meerzaman D, et al. Significance of TP53 mutation in Wilms tumors with diffuse anaplasia: A report from the children's oncology group. Clinical Cancer Research. 2016;22(22):5582-91.

25. Ruteshouser EC, Robinson SM, Huff V. Wilms tumor genetics: mutations in WT1, WTX, and CTNNB1 account for only about one-third of tumors. Genes, Chromosomes and Cancer. 2008;47(6):461-70.

26. Williams RD, Al-Saadi R, Natrajan R, Mackay A, Chagtai T, Little S, et al. Molecular profiling reveals frequent gain of MYCN and anaplasia-specific loss of 4q and 14q in Wilms tumor. Genes, Chromosomes and Cancer. 2011;50(12):982-95.

27. Bardeesy N, Falkoff D, Petruzzi M-J, Nowak N, Zabel B, Adam M, et al. Anaplastic Wilms' tumour, a subtype displaying poor prognosis, harbours p53 gene mutations. Nature genetics. 1994;7(1):91-7.

28. Spreafico F, Ciceri S, Gamba B, Torri F, Terenziani M, Collini P, et al. Chromosomal anomalies at 1q, 3, 16q, and mutations of SIX1 and DROSHA genes underlie Wilms tumor recurrences. Oncotarget. 2016;7(8):8908.

29. Maiti S, Alam R, Amos CI, Huff V. Frequent association of β-catenin and WT1 mutations in Wilms tumors. Cancer research. 2000;60(22):6288-92.

30. Williams RD, Al-Saadi R, Chagtai T, Popov S, Messahel B, Sebire N, et al. Subtype-specific FBXW7 mutation and MYCN copy number gain in Wilms' tumor. Clinical Cancer Research. 2010;16(7):2036-45.

31. Williams RD, Chagtai T, Alcaide-German M, Apps J, Wegert J, Popov S, et al. Multiple mechanisms of MYCN dysregulation in Wilms tumour. Oncotarget. 2015;6(9):7232.

32. Worst BC, van Tilburg CM, Balasubramanian GP, Fiesel P, Witt R, Freitag A, et al. Next-generation personalised medicine for high-risk paediatric cancer patients–The INFORM pilot study. European journal of cancer. 2016;65:91-101.

33. Calandrini C, Drost J. Normal and tumor-derived organoids as a drug screening platform for tumor-specific drug vulnerabilities. STAR Protocols. 2022;3(1):101079.

34. Huang F, Reeves K, Han X, Fairchild C, Platero S, Wong TW, et al. Identification of candidate molecular markers predicting sensitivity in solid tumors to dasatinib: rationale for patient selection. Cancer research. 2007;67(5):2226-38.

35. Schutgens F, Rookmaaker MB, Margaritis T, Rios A, Ammerlaan C, Jansen J, et al. Tubuloids derived from human adult kidney and urine for personalized disease modeling. Nature biotechnology. 2019;37(3):303-13.

36. Dijkstra KK, Monkhorst K, Schipper LJ, Hartemink KJ, Smit EF, Kaing S, et al. Challenges in establishing pure lung cancer organoids limit their utility for personalized medicine. Cell reports. 2020;31(5):107588.

37. Weeber F, Ooft SN, Dijkstra KK, Voest EE. Tumor organoids as a pre-clinical cancer model for drug discovery. Cell chemical biology. 2017;24(9):1092-100.

38. Little SE, Bax DA, Rodriguez-Pinilla M, Natrajan R, Messahel B, Pritchard-Jones K, et al. Multifaceted dysregulation of the epidermal growth factor receptor pathway in clear cell sarcoma of the kidney. Clinical cancer research. 2007;13(15):4360-4.

39. Vasei M, Modjtahedi H, Ale-Booyeh O, Mosallaei A, Kajbafzadeh AM, Shahriari M, et al. Amplification and expression of EGFR and ERBB2 in Wilms tumor. Cancer genetics and cytogenetics. 2009;194(2):88-95.

40. Ragab SM, Samaka RM, Shams TM. HER2/neu expression: a predictor for differentiation and survival in children with Wilms tumor. Pathology & Oncology Research. 2010;16(1):61-7.

41. Salem M, Kinoshita Y, Tajiri T, Souzaki R, Tatsuta K, Higashi M, et al. Association between the HER2 expression and histological differentiation in Wilms tumor. Pediatric surgery international. 2006;22(11):891-6.

42. Murphy AJ, Chen X, Pinto EM, Williams JS, Clay MR, Pounds SB, et al. Forty-five patient-derived xenografts capture the clinical and biological heterogeneity of Wilms tumor. Nature communications. 2019;10(1):1-13.
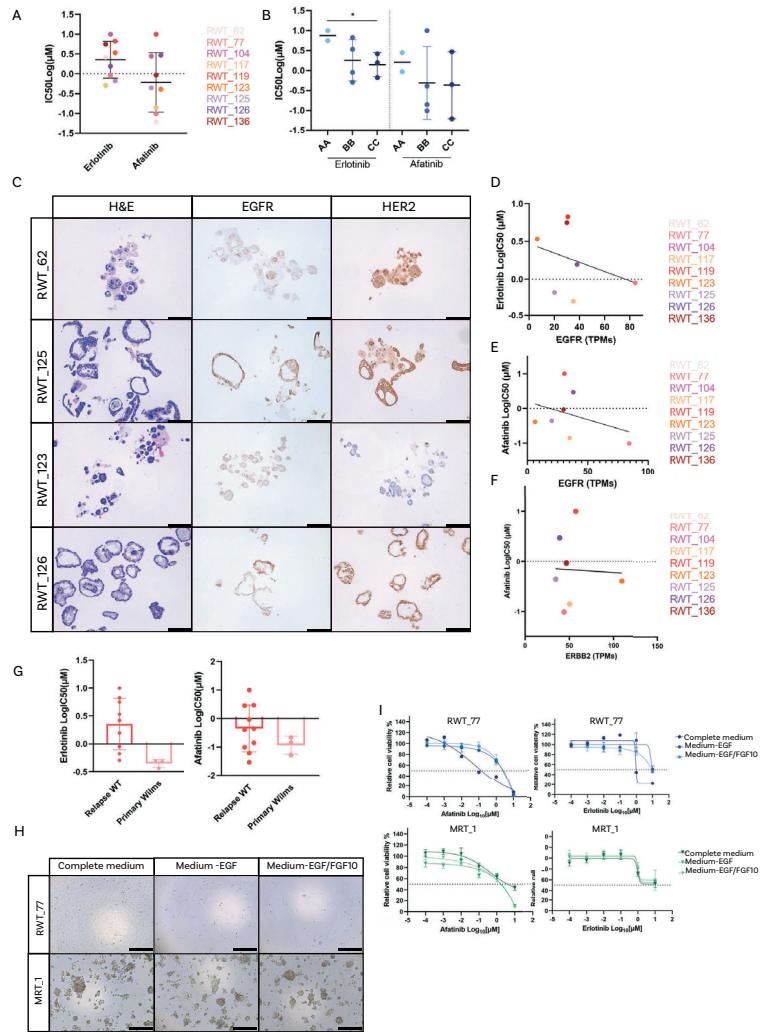
Supplementary Figures

A

B
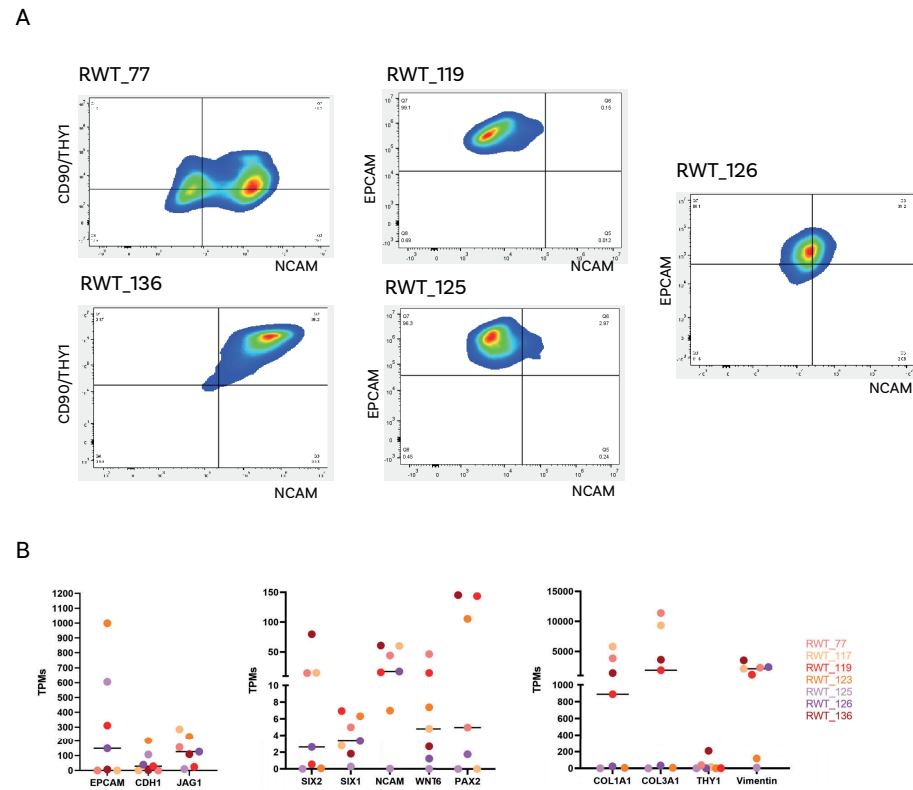
Supplementary Figure 1. A. Scatterplot of flow cytometry analysis of 5 RWT lines for the quantification of markers EPCAM, CD90/THY1 and NCAM1. **B**. Transcript per million values (TPMs) of markers for epithelial (left), blastemal (center) and stromal (right) cell populations across different RWT cultures using RNA-seq.
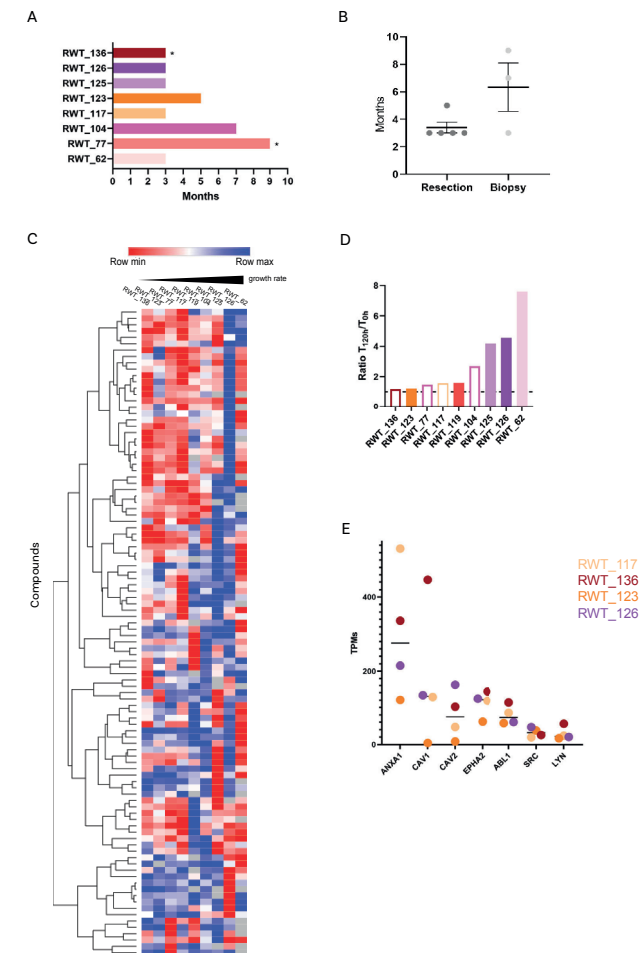
Supplementary Figure 2. A. Bar graph quantifying time needed to perform medium-through-put screening on the depicted RWT lines, starting from the moment tissue samples have been processed into culture. Symbol * identifies lines for which a larger compound library (~200 compounds) was tested. **B**. Dot plot representation of time needed to perform medium-throughput drug screening, grouped by quantity of starting material (resection, biopsy). **C**. Unsupervised hierarchical clustering of AUC drug screening data, demonstrating that patterns of drug sensitivity do not correlate with growth rate. Color scale blue to red indicates decreasing AUC values. Color scale is relative to each compound (row). Grey color indicates AUC values not available. **D**. Growth ratios calculated for the depicted RWT cultures, measured with Cell titer-Glo. Ratios were calculated by dividing Cell titer-Glo values measured 120h after seeding (T_{120h}) to values measured at the moment of seeding (T_{0h}). White colored bars depict 2D growing RWT lines. **E**. TPM values of genes related to Dasatinib sensitivity measured in sensitive (RWT_117, RWT_136) and insensitive lines (RWT_123, RWT_126)[34]. High expression of these markers has been correlated to high sensitivity to Dasatinib in several human cancer cell lines.

Supplementary Figure 3. **A**. LogIC$_{50}$ values for EGFR inhibitor Erlotinib and EGFR/HER2 inhibitor Afatinib in RWT cultures. Represented are mean ± SD values (n=9). **B**. LogIC$_{50}$ values for EGFR inhibitor Erlotinib and EGFR/HER2 inhibitor Afatinib in RWT cultures, clustered by risk group. Represented are mean (AA) and mean ± SD values (BB, CC) of LogIC$_{50}$ (n ≥3). P-value were calculated using a two-tailed Student's t test, two-sided: * < 0.05. **C**. H&E (left), EGFR (center) and HER2 (right) immunostaining on RWT organoids. Scale bars: 100μm. **D-F**. Linear regression analysis between expression of EGFR/HER2 and LogIC$_{50}$ values of Erlotinib and Afatinib in RWT cultures. r^2 values: 0.10 (D); 0.12 (E); 0.001 (F). **G**. LogIC$_{50}$ values of Erlotinib and Afatinib in RWT and primary WT. **H**. Representative brightfield pictures of lines RWT_77 and MRT_1 cultured in complete medium (left), medium minus EGF (center) and medium minus EGF/FGF10 (right). Scale bars: 100μm. **I**. Dose response curves for Afatinib (left) and Erlotinib (right) in lines RWT_77 and MRT_1 cultured in the described different media conditions.

Supplementary Table 1 Top 10 compound rank based on AUC values for each screened RWT line.

	RWT_62		RWT_77		RWT_104		RWT_117		RWT_119	
1	Fimepinostat	166.0	YM-155	146.3	Romidepsin	170.9	YM-155	27.45	YM-155	101.2
2	Bortezomib	201.0	Actinomycin D	162.2	Actinomycin D	200.4	Romidepsin	107.6	Actinomycin D	203.1
3	Vandetanib	210.0	Bortezomib	186.4	Bortezomib	225.6	Actinomycin D	112.1	Bortezomib	210.4
4	Palbociclib	274.6	Romidepsin	209.9	Fimepinostat	288.8	Bortezomib	180.2	Camptothecin	245.3
5	Daunorubicin	285.4	Carfilzomib	229.6	Ganetespib	315.3	Fimepinostat	240.5	Carfilzomib	272.7
6	MK-2206	295.1	THZ1	257.3	Panobinostat	319.3	Panobinostat	241.9	Cobimetinib	278.3
7	Vincristine	297.2	Fimepinostat	259.2	Everolimus	323.6	Dasatinib	267.8	Ixazomib	280.2
8	Tazemetostat	306	Ganetespib	283.4	Ixazomib	334.5	Ganetespib	270.9	Ganetespib	286.3
9	YM-155	311.0	Trametinib	301.4	Daunorubicin	339.8	Ixazomib	280.0	Neratinib	304.4
10	Doxorubicin	311.9	Panobinostat	308.3	Mitoxantrone	358.2	Docetaxel	282.3	Osimertinib	313.0

	RWT_123		RWT_125		RWT_126		RWT_136	
1	Bortezomib	151.3	Actinomycin D	172.9	Ganetespib	124.6	Romidepsin	262.2
2	Romidepsin	166.4	Vincristine	180.0	SN-38 (Irinotecan)	159.9	Actinomycin D	309.5
3	Actinomycin D	194.8	Romidepsin	181.7	Bortezomib	198.6	Bortezomib	319.8
4	Panobinostat	254.6	Bortezomib	200.3	Ixazomib	216.7	Carfilzomib	332.2
5	Fimepinostat	256.5	Docetaxel	235.7	Actinomycin D	227.2	Fimepinostat	350.0
6	Ixazomib	283.2	Fimepinostat	250.6	Fimepinostat	231.0	Vinblastine	353.1
7	Trametinib	306.0	SN-38 (Irinotecan)	252.6	Gemcitabine	236.7	Docetaxel	358.5
8	Vinblastine	307.9	Panobinostat	263.5	Venetoclax	239.2	Panobinostat	375.7
9	Mitoxantrone	314.4	AZD5582	268.2	XAV-939	241.9	THZ1	388.2
10	Vincristine	319.4	CYC065	275.5	Panobinostat	244.0	Vincristine	390.3

Chapter 8

Discussion

Camilla Calandrini[1]

[1] Princess Máxima Center for Pediatric Oncology, Oncode Institute, Heidelberglaan 25, 3584 CS
Utrecht, the Netherlands

Pediatric renal and rhabdoid tumors: the challenges

Pediatric kidney tumors are among the most common childhood malignancies. They comprise a wide spectrum of distinct subtypes, which differ in incidence, histology and prognosis. Among these we encounter Wilms tumor, the most common renal malignancy, followed by rarer presentations, such as clear cell sarcoma of the kidney (CCSK), renal cell carcinomas (RCCs) and malignant rhabdoid tumors of the kidney (MRTKs). The 90% survival rate of children with Wilms tumor is considered one of the big successes of modern pediatric oncology[1]. However, this result was achieved at the expense of short and long-term toxicity, caused by the harsh chemotherapy and/or radiotherapy treatments[2]. Furthermore, about 10% of pediatric renal tumor patients does not respond to the standard of care treatments[3]. Among these, we encounter refractory relapsed Wilms tumors and MRTK patients. Not only affecting the kidney, malignant rhabdoid tumors (MRT) can occur in several location of the body. Overall, ~70% of these patients does not survive the disease.

Given that current therapies are at the verge of toxicity tolerability, to further increase survival rates and improve quality of life for these patients, innovative therapeutic interventions need to be developed. To forge therapeutic innovation, the scientific community strives to increase understanding of how pediatric renal and rhabdoid tumors arise and progress. To achieve this goal, the development of novel preclinical models that faithfully mirror characteristics of patient tumors, is pivotal.

Organoid models of pediatric renal and rhabdoid tumors

In this thesis, we described the successful development of patient-derived organoid models from pediatric renal and rhabdoid tumors. The established protocols allowed for the generation of the very first pediatric tumor organoid biobank, comprising more than 50 patient-derived organoid models, originated from a wide spectrum of pediatric renal tumors, including Wilms tumors, MRTKs and RCCs (**Chapter 3**[4]). Their extensive characterization has revealed that histological, (epi)genetic and transcriptomic features of the parental tissues are captured to a large extend in these models[4,5]. This collection of patient-derived tumor organoids has greatly increased the number of preclinical *in vitro* models available to the scientific community to study these rare malignancies. Furthermore, to our knowledge, MRTK organoid cultures represent the first tumor organoid model of non-epithelial origin that can be expanded in the long term. Our protocols there-

8

fore pave the way for the establishment of additional pediatric tumor organoid models, also of non-epithelial origin.

Pediatric renal and rhabdoid tumor organoid models display a unique combination of features lacking in other conventional preclinical models. One of the advantages of their use is the high efficiency of establishment from primary patient material, which greatly surpasses that reported for cancer cell lines[6, 7]. This characteristic is of utmost importance, especially for rare tumor presentations such as MRTs and relapsed Wilms tumors. Wilms tumor organoids represent the first *in vitro* model described to allow the expansion of the three histological phases of Wilms tumor – epithelial, blastemal, and stromal – in one culture system. This consists of a great improvement compared to monophasic 2D and spheroid cultures, able to expand primarily stromal and blastemal cells, respectively[6, 8, 9]. Furthermore, Wilms tumor organoids can maintain these cell populations throughout passaging, with only slight enrichments observed for epithelial and blastemal cell populations. In comparison, PDTX models generated from Wilms tumor tissues seem to significantly amplify the growth of the blastemal component as soon as after the first passage *in vivo*[10]. This suggests that patient-derived organoids can better represent the intratumor cellular heterogeneity typical of Wilms tumors, compared to other *in vitro* and *in vivo* models.

In **Chapter 3**, we demonstrated that MRTK and Wilms tumor organoids are able to maintain a stable genetic makeup over time, faithfully representing the genetics of the tumor tissues they were derived from[4]. This represents a significant improvement compared to other preclinical models. MRT cancer cell lines generally do not recapitulate the low mutation burden and stable karyotype typical of these tumors, often acquiring additional mutations and chromosomal gain and losses not reported to generally occur in MRT tumors[11]. Likewise, cancer cell lines derived from Wilms tumors often fail to represent the genetics of the parental tumors[12-14]. Furthermore, PDTX models have been reported to acquire mouse-specific genetic changes, which transform the genetic landscape of the original tumor[10, 15].

2D-growing and (epithelial) spheroid cultures can be mainly established from *TP53* mutant Wilms tumor samples, representative of about 7% of all Wilms tumor cases[8, 9, 16]. Similarly, genetically engineered mouse models are able to recapitulate the genetic profile of a small subgroup of patients[16], namely those carrying *WT1* mutations and *IGF2* upregulation[17], or even rarer *LIN28* overexpression[18]. The protocols we developed allow for the establishment and expansion of organoid cultures from Wilms tumor samples characterized by diverse genetic backgrounds, including high-risk blastemal and anaplastic Wilms tumor, as well as low and intermediate risk samples[4]. Moreover, our protocols allow for the establishment of organoid cultures from both primary and relapsed tumors (**Chapter 3**[4],**Chapter 7**). Patient-derived organoids offer therefore the opportunity to investigate the molecular features characterizing and discriminating these tumor samples. Furthermore, these organoid models can be applied to investigate relevant clinical issues such as acquired resistance to chemotherapy treatment, frequently observed in high-risk cases and in a subgroup of - yet non identified – intermediate-risk patients[1].

The possibility of generating normal tissue-derived organoid counterparts, such as kidney tubuloid cultures (**Chapter 4**[19]), is another advantage of the use of the organoid technology. As described in **Chapter 5**[5] and **Chapter 6**[20], normal tissue-derived organoid cultures, derived not only from kidney tissue but from several other normal tissues, can be exploited to identify compounds with cancer-specific, and therefore potentially less toxic, therapeutic effects. This approach can be even applied in a patient-matching fashion, since kidney tubuloid cultures can be generated from adjacent normal kidney tissue accessible upon nephrectomy, or even from urine samples (**Chapter 4**)[19].

Pediatric renal and rhabdoid tumor organoids combine the ease of use and expansion of classical *in vitro* models with the ability of capturing the genetic and phenotypic complexity of native tumor tissues[4], representing therefore a one-of-a-kind model with the potential of filling the gap between bench and bedside.

Limitations and future perspectives of pediatric renal and rhabdoid tumor organoid models

Like any other model system, organoid technology has its limitations too. In general, organoids are likely not able to capture the overall intra-tumoral heterogeneity of the original tumors since they are established either from needle biopsies or from pieces of larger tumor resections. Previous studies have shown that establishment of organoid cultures from different regions of the same tumor can indeed result in lines with different genetic and phenotypic characteristics[21, 22]. Especially when considering Wilms tumors, known for their high genotypic and phenotypic heterogeneity[23, 24], this can represent a limitation in the use of organoids for translational studies, since drug screening results would mimic the response of just a fraction of the original tumor. To achieve a better representa-

tion *in vitro* of the intratumor heterogeneity present *in vivo*, when possible, patient-derived organoid cultures should be generated from multiple tumor regions.

Albeit we demonstrated that Wilms tumor organoids display the cellular heterogeneity present in the parental tumors - retaining blastema, epithelium and stroma - and that they can maintain this cellular heterogeneity through serial passaging, further studies are needed to evaluate to what extend phenotypic and genetic heterogeneity can be represented in these cultures in the long term. Insights on this matter could be obtained via the application of single cell sequencing approaches in organoid cultures harvested after differential time periods in culture. This approach would also offer clues regarding the presence of clonal dynamics in these organoid cultures.

Presence of normal cells in the tumor specimen can be detrimental for the establishment of pure tumor organoid cultures, since it can result in rapid overgrowth of normal cells and complete loss of tumor cells overtime[25-27]. In **Chapter 3** and **Chapter 7** we describe this phenomenon, which has negatively impacted the success rates of establishment of pediatric renal organoid cultures as well. The growth advantage of normal cells over tumor cells *in vitro* may seem counterintuitive. However, an explanation for this can be found in the composition of the growth media. Since these have been initially developed to sustain growth of normal tissue-derived organoids, and only later adapted for tumor organoid growth, the efficient expansion of healthy cells is to be expected. This is also the case for kidney tuboloid cultures, for which minor adaptations in the culture medium has allowed us to establish pediatric renal tumor organoid cultures, which, however, did not prevent healthy cells from growing out[28]. In our experience, several precautions must be taken to limit the risk of overgrowth of normal cells. Starting from a pure tumor specimen represents the easiest solution. Histological analysis of part of the obtained specimen should therefore always be performed. To ensure that healthy cells are not overtaking the culture, routine checks of the organoid morphology via brightfield microscopy and careful recording of splitting ratios and timelines are useful strategies to apply. Any change in morphology and/or splitting ratios in the first weeks are useful indicators of potential contamination with normal tissue organoids. In some cases, however, the tumor growth patterns are not so distinct from those of healthy cells. SNP arrays and/or sanger sequencing of tumor-specific mutations can be performed to confirm this hypothesis. However, this approach is only possible when genetic data from the patient tumor is available. When healthy organoids are contaminating the cultures, several options are available to purify the tumor cells. For instance, tumor-specific mutations that confer resistance to specific culture conditions

can be exploited. As example, addition of P53 stabilizer Nutlin-3 can be applied to purify *TP53* mutant organoid cultures from surrounding wild type *TP53* cells[29]. Another strategy employs cell surface proteins exclusively expressed on tumor or on healthy cells to separate them via flow cytometry. Following such strategy, we successfully purified MRTK cultures from kidney tuboloid contamination via sorting for epithelial marker EPCAM, found only expressed in tuboloid cultures (**Chapter 3**[4]). Even though we have described successful methods to purify tumor cells from healthy cells contamination, for many cases neither of these strategies can be applied, resulting in the loss of the cultures and, consequentially, in a drop in establishment efficiency.

Patient-derived organoids can be used for modeling tumor initiation and progression[29, 30]. In **Chapter 3** we set out to artificially model anaplasia via the introduction of *TP53* mutations in intermediate-risk Wilms tumor organoids[4, 31]. Interestingly, histological analysis on *TP53* mutant organoids revealed absence of anaplastic features. While we have not been able to model an anaplastic phenotype, these results may suggest that *TP53* mutations are not sufficient to initiate anaplasia, and that additional events are required. These findings support the results of Wegert et al., which described *TP53* mutant Wilms tumors devoid of anaplastic features[32]. The *TP53* mutant Wilms tumor organoid line we generated could be exploited to understand how this stepwise evolution of Wilms tumors, from the acquisition of a *TP53* mutation to the manifestation of an anaplastic phenotype, takes place. Measuring chromosomal instability[29] and performing genetic characterization at different timepoints, could give further insights into this mechanism of tumor evolution and aid the identification of new therapeutic interventions for these high-risk patients.

Another interesting approach to study pediatric renal tumor development consists of modeling tumorigenesis via the introduction of known driver mutations in normal kidney cultures, as previously described for colorectal cancer[29, 30]. However, disease modeling in adult stem cells derived tuboloid cultures comes with important limitations. For instance, the embryonal origin of Wilms tumors suggests that its cell-of-origin is to be found in early nephrogenic progenitor cells[33]. Given that these are not retained in tuboloid cultures, it is likely that the introduction of driver mutations will not result in a cancerous phenotype[28, 34]. For modeling tumorigenesis, pluripotent stem cells derived kidney organoids represent a more suitable alternative, as discussed in **Chapter 2** [34, 35].

The use of patient-derived organoids has many advantages, including the efficiency of establishment and faithful representation of the tumor tissue of origin. However, organoid cultures are not able to fully recapitulate an *in vivo*

system, as key components of the tumor microenvironment are lacking[36, 37]. Among others, organoid cultures miss vasculature, cancer associated fibroblasts and immune cells, all elements known to significantly influence drug response *in vivo*[38]. The implementation of such features could represent new opportunities for improved modelling *in vitro* of the drug response measured *in vivo,* and could allow for testing of innovative therapeutic approaches. Following this line, the development of co-culture methods where the interaction between pediatric renal tumor organoids and immune cells are mimicked, could represent the set up for *in vitro* testing of immunotherapy approaches, one of the new frontiers in cancer treatment. MRTs have been reported to show relatively high levels of tumor infiltrating T-cells and immune cytolytic activity, comparable to those measured for highly immunogenic adult melanoma and lung adenocarcinomas, suggesting that immunotherapy approaches could be applied as treatment strategy for these high-risk patients[39]. Furthermore, recent studies have reported high expression of the checkpoint surface molecule B7-H3 in ATRT patients, and the first *in vivo* tests conducted on ATRT PDXT models treated with B7-H3 CAR-T cells resulted in an outstanding complete tumor remission[40]. Examples of successful tumor organoid/ immune T cells co-culture methods have been described for several adult cancer organoid models, demonstrating feasibility[41-45].

Overall, several limitations are present in the establishment and use of pediatric renal and rhabdoid tumor organoid models. The implementation of the described new features in these culture systems has the potential to upgrade them to even more accurate avatars of the original tumors.

Exploiting patient-derived organoids for drug screening purposes

Given the close resemblance to the parental tissues, pediatric renal and rhabdoid tumor organoids represent an intriguing model for *in vitro* drug testing. The use of organoids as platform for drug screening has already been explored in studies conducted on several adult malignancies[25, 46-52]. The conclusions, although promising, highlighted important caveats. In this thesis, we successfully made use of (relapsed) Wilms tumor and MRT organoids for drug screening purposes (**Chapter 3**[4],**Chapter 5**[5] and **Chapter 7**). We pursued both a personalized medicine approach and a more universal therapeutic vulnerability discovery approach.

A personalized medicine approach aims to identify patient-specific vulnerabilities (e.g., via whole exome sequencing and drug screening) and to exploit such findings to assign the most suitable treatment per individual. As example of

the use of this strategy, in **Chapter 7** we identified Src/Abl inhibitor Dasatinib as relapsed Wilms tumor patient-specific drug vulnerability. To assess the feasibility of the use of pediatric renal tumor organoids as clinical tool for personalized medicine purposes, parameters such as efficiency and time of establishment need to be closely evaluated.

In **Chapter 3** and **Chapter 7**, we describe the generation of patient-derived organoid cultures with efficiencies that varied from 50% (relapsed Wilms tumor) to close to 100% (MRTKs)[4, 5]. To achieve the goal of a patient-specific approach to therapy, we face the challenge of reaching 100% establishment efficiency for all tumor types. Albeit the great results achieved for MRTKs, further studies should be carried out to improve success rates for other pediatric renal tumors. This is especially the case for relapsed Wilms tumors and for clear cell sarcoma of the kidney, for which up to date no *in vitro* models have been generated[3].

In addition to a high establishment efficiency, a rapid expansion rate of the organoids cultures is of crucial importance to be able to feed results back to the patients as soon as possible. This is of utmost relevance for high-risk patients, for which the standard of care treatment is destined to fail, and alternative therapies are urgently needed. Refractory relapsed Wilms tumor patients belong to this category. In **Chapter 7**, we describe a feasibility study with the aim to establish relapsed Wilms tumor organoid cultures and subject them to drug screening, in order to identify possible patient-specific alternative therapeutic interventions. We successfully established 9 relapsed Wilms tumor models and performed drug screening within an average time of 4.5 months after culture establishment. For 6 patients, we could obtain drug screening results in a clinically relevant timeframe, as we were able to couple these results back to treating physicians while patients were alive and/or still receiving treatment according to standard protocols. However, for 2 patients, although screened within 3 months, we were not able to obtain results on time, as they had already passed away. Of notice, these patients belonged to the very-high risk group, carrying the worst prognosis. Lastly, for a few RWT patients drug screening results were obtained more than 6 months after receiving the specimen, a considerably long timeframe. This could be explained by the little amount of tumor material received to initiate the cultures (needle biopsies).

Altogether, these observations stress that further optimizations in efficiency of organoid culture establishment and in timing for drug screening are needed to ensure the implementation of pediatric renal tumor organoids for personalized medicine purposes. To achieve this, efforts should be focusing on improving culture conditions, via the identification of additional growth factors that can

boost growth and efficiency of establishment. Furthermore, additional efforts could focus on reducing the number of cells needed for drug screening. This could be achieved by reducing the number of concentrations tested per compound, or via the assembly of smaller, more tumor-specific compound libraries, where only compounds for which patients could actively enter a clinical trial are included for screening.

Next to a patient-tailored treatment approach, patient-derived organoids can be exploited for tumor-specific therapy discovery. This approach aims to identify tumor type-specific vulnerabilities with minimal toxic off-target effects. Rather than patient-specific, this strategy pinpoints therapeutic susceptibilities common to patients diagnosed with the same tumor entity. In comparison with a personalized medicine approach, this strategy can be applied only when a cohort of patient-derived organoids from the same tumor type has been established and characterized. We described the use of this approach in **Chapter 5**, allowing us to identify neddylation inhibitor MLN4924 as compound specifically hampering MRT growth[5].

The use of normal tissue-derived organoids to predict treatment-related side effects is an intriguing application that could be adopted to identify less-toxic therapeutic interventions. Previously explored in the context of oral mucosa[53] and liver[54], we took this approach in **Chapter 5**, where we tested toxic effects of MLN4924 treatment in kidney, small intestine and liver organoids, to asses nephrotoxicity, intestinal toxicity and hepatotoxicity, respectively[5]. Although our approach aided the identification of an effective compound with little toxic side effects, this experimental set up allowed to assess toxicity only in a limited selection of healthy tissues. To facilitate the identification of compounds with higher efficacy in tumor organoids compared to normal tissue-derived organoids, datasets of drug sensitivities values, collected from a wide range of normal tissue-derived tissue organoids, should be generated. The gathering of such data could aid the identification of toxic effects before *in vivo* studies are performed. As example, liver[55], lung[56] and cardiac[57] organoids could be of great interest in the context of pediatric cancer patient treatment, given the high rates of toxicity routinely measured in these organs upon treatment. For pediatric renal tumor patients, nephrotoxicity management is of great interest since renal disfunction and consequent renal failure are among the most frequent treatment-related side effects[2]. Kidney tubuloid cultures can be exploited for this purpose, as we demonstrated in **Chapter 5**[5, 19, 28]. However, these cultures mainly recapitulate proximal and distal tubules, and are devoid of other kidney structures, such as

glomeruli (podocytes and endothelial cells)[28]. Consequentially, only tubular toxicity can be assessed. Further improvement of the protocols for kidney tubuloid generation, as well as of the culture conditions, are needed to enrich this model with other kidney cell types. Alternatively, pluripotent stem cell-derived kidney organoids, able to better capture a more complete kidney architecture, could be implemented to model both tubular and glomeruli toxicity[58] (**Chapter 2**[34]).

For both personalized medicine and a more universal therapy discovery approaches, patient-derived organoids should display a predictive value for patient response to therapy. Previous studies conducted on adult cancers have shown encouraging results, demonstrating that tumor organoids can mirror patient response to chemotherapy, targeted therapy, and radiotherapy[46-51, 59]. However, the same reports have also shown that such predictive values are not universal. As example, for the treatment with 5FU and oxaliplatin in gastrointestinal cancer, no correlation with patient response to treatment was observed in patient-matching tumor organoids[48]. This observation stresses the importance of validating findings in multiple independent preclinical models before proceeding with testing in a clinical setting. Most importantly, future clinical trials are necessary to assess the predictive value of the pediatric renal and rhabdoid tumor organoid models we have established. To assess predictability, patient-derived organoids should be treated with the same drugs as the patients, and their response to treatment should be evaluated and compared to the patient's response [60]. Albeit feasible for primary Wilms tumor patients, the rarity of non-Wilms tumor and refractory Wilms tumor malignancies represents an obstacle to the set up of a clinical trial of this nature. International collaborations are essential to achieve this goal.

Future perspectives in the treatment of pediatric renal and rhabdoid tumor patients

Treatment regimens currently available for pediatric renal and rhabdoid tumors are at verge of therapeutic tolerance, with no room for inclusion of additional chemotherapies. To improve survival rates without increasing toxicity, alternative treatment approaches need to be pursued.

Targeted therapies, in contrast to the systemic effects of chemotherapy, interfere with cell-specific molecular mechanisms, in principle resulting in a detrimental effect in a more targeted fashion. In this thesis, we were able to identify putative targeted therapeutic interventions for relapsed Wilms tumors (EGFR/HER2 inhibitors) and MRTs (neddylation inhibitor)[5]. However, many studies have

shown that monotherapy approaches ultimately lead to the development of treatment resistance mechanisms, which culminate in disease relapse and patient demise[61, 62]. To prevent this, a strategy where targeted agents, identified using patient-derived organoids, are administered in combination with standard chemotherapy regimens could be applied. To bring this combination strategy to the clinic, several steps need to be taken. Firstly, efficacy of the selected therapies needs to be confirmed in (several) independent *in vivo* tumor models, to validate the robustness of the *in vitro* results. If sufficient prove that a significant effect is registered *in vivo*, with no signs of severe toxicity, early phase clinical trials can be initiated, to assess safety profiles and efficacy. Patients showing signs of resistance to standard of care treatment could be treated with these targeted compounds in a regimen that intercalates their use with the standard of care cycles of chemotherapy. If a significant survival benefit is measured, the use of targeted compounds could even translate in a reduction of the number of chemotherapy cycles needed, which could consequentially reduce the burden of side effects. Clinical testing of novel therapeutic interventions is a long process, which also requires enough patients to be enrolled. This is a major challenge for pediatric tumor patients, especially for the rare relapsed Wilms tumor and MRT patients[63]. To achieve enough enrolled patients, international collaborations are, again, essential.

As example of first steps towards the implementation of targeted therapy for MRT treatment, following up on the research presented in **Chapter 5** of this thesis, we are currently investigating the additive effect of MLN4924 in the treatment of MRTs in addition to commonly used chemotherapeutics doxorubicin/vincristine in MRT PDTX models. Preliminary results show tumor regression in the combination treatment strategy, while standard of care and MLN4924 as single agents seem not to induce an objective response in an independent model (*collaboration with St. Jude Children's Research Hospital (Memphis, USA), personal correspondence*). The results of this study could serve as ground for the initiation of a clinical trial in MRT patients.

Next to the use of patient-derived organoids for middle throughput drug screening, as described in **Chapter 6**[20], other more unbiased strategies can be applied to identify pediatric renal and rhabdoid tumor therapeutic vulnerabilities. Recent studies have shown the feasibility of conducting genome-wide CRISPR-Cas9 screens on organoids, from both murine and human origin, to identify genes essential for tumor cell survival, whose function can be impaired by small molecule inhibitors[64-66]. Applying this strategy could overcome some of the limitations of drug screening approaches. Among others, genome-wide screens sig-

nificantly expand the number of targets that can be tested in one experimental set up. Furthermore, while compounds can exhibit off-target effects, especially when administered at high concentrations, knockout or knockdown screens should - in principle - identify the consequences of hampering the function of one single target gene.

Studying the molecular mechanisms underlying renal and rhabdoid tumor oncogenesis can also reveal possible therapeutic strategies. As described in Custers et al., RNA sequencing performed on MRT organoids after re-expression of *SMARCB1* uncovered combination of HDAC and mTOR inhibitors as possible differentiation therapy strategy[67]. In this study, this combination treatment was able to mimic the differentiated phenotype observed upon *SMARCB1* re-expression in MRT organoids. The application of this strategy has already been proven effective in other tumor types, such as acute promyelocytic leukemia and high-risk neuroblastoma[68, 69]. Enforcing differentiation and consequential terminal cell cycle arrest via pharmacological intervention could therefore represent another promising avenue for the treatment of pediatric renal and rhabdoid tumor patients.

Concluding remarks

In this thesis, we describe for the first time the application of organoid technology to pediatric cancer research. We successfully established more than 50 unique patient-derived organoid models, generated from a wide spectrum of pediatric renal and rhabdoid tumors for which preclinical models were scarce. This organoid collection, available to the scientific community, provides the opportunity to study these rare malignancies with the advantages of an *in vitro* setting, while the molecular and cellular complexity of the original tumor tissues are largely recapitulated. We demonstrated the feasibility of exploiting these models for the identification of personalized medicine approaches, as well as for the discovery of novel tumor-specific drug vulnerabilities. Furthermore, we exemplified the use of normal tissue-derived organoids to identify less toxic therapeutic interventions. The work presented in this thesis sets the first steps towards the implementation of the organoid technology as tool for improving the treatment of children with cancer.

References

1. Van Den Heuvel-eibrink MM, Hol JA, Pritchard-Jones K, Van Tinteren H, Furtwängler R, Verschuur AC, et al. Rationale for the treatment of Wilms tumour in the UMBRELLA SIOP–RTSG 2016 protocol. Nature Reviews Urology. 2017;14(12):743-52.

2. Termuhlen AM, Tersak JM, Liu Q, Yasui Y, Stovall M, Weathers R, et al. Twenty-five year follow-up of childhood Wilms tumor: a report from the Childhood Cancer Survivor Study. Pediatric blood & cancer. 2011;57(7):1210-6.

3. Brok J, Treger TD, Gooskens SL, van den Heuvel-Eibrink MM, Pritchard-Jones K. Biology and treatment of renal tumours in childhood. European Journal of Cancer. 2016;68:179-95.

4. Calandrini C, Schutgens F, Oka R, Margaritis T, Candelli T, Mathijsen L, et al. An organoid biobank for childhood kidney cancers that captures disease and tissue heterogeneity. Nature communications. 2020;11(1):1-14.

5. Calandrini C, van Hooff SR, Paassen I, Ayyildiz D, Derakhshan S, Dolman MEM, et al. Organoid-based drug screening reveals neddylation as therapeutic target for malignant rhabdoid tumors. Cell reports. 2021;36(8):109568.

6. Wegert J, Bausenwein S, Roth S, Graf N, Geissinger E, Gessler M. Characterization of primary Wilms tumor cultures as an in vitro model. Genes, Chromosomes and Cancer. 2012;51(1):92-104.

7. Kodack DP, Farago AF, Dastur A, Held MA, Dardaei L, Friboulet L, et al. Primary patient-derived cancer cells and their potential for personalized cancer patient care. Cell reports. 2017;21(11):3298-309.

8. Wegert J, Zauter L, Appenzeller S, Otto C, Bausenwein S, Vokuhl C, et al. High-risk blastemal Wilms tumor can be modeled by 3D spheroid cultures in vitro. Oncogene. 2020;39(4):849-61.

9. Alami J, Williams BR, Yeger H. Derivation and characterization of a Wilms' tumour cell line, WiT 49. International journal of cancer. 2003;107(3):365-74.

10. Murphy AJ, Chen X, Pinto EM, Williams JS, Clay MR, Pounds SB, et al. Forty-five patient-derived xenografts capture the clinical and biological heterogeneity of Wilms tumor. Nature communications. 2019;10(1):1-13.

11. Fasler-Kan E, Aliu N, Haecker F-M, Maltsev N, Ruggiero S, Cholewa D, et al. Chromosomal heterogeneity of the G-401 rhabdoid tumor cell line: unusual partial 7p trisomy. Frontiers in medicine. 2019;6:187.

12. Brandt A, Löhers K, Beier M, Leube B, de Torres C, Mora J, et al. Establishment of a conditionally immortalized wilms tumor cell line with a homozygous WT1 deletion within a heterozygous 11p13 deletion and UPD limited to 11p15. PloS one. 2016;11(5):e0155561.

13. Royer-Pokora B, Busch M, Beier M, Duhme C, de Torres C, Mora J, et al. Wilms tumor cells with WT1 mutations have characteristic features of mesenchymal stem cells and express molecular markers of paraxial mesoderm. Human molecular genetics. 2010;19(9):1651-68.

14. Faussillon M, Murakami I, Bichat M, Telvi L, Jeanpierre C, Nezelof C, et al. Molecular cytogenetic anomalies and phenotype alterations in a newly established cell line from Wilms tumor with diffuse anaplasia. Cancer genetics and cytogenetics. 2008;184(1):22-30.

15. Ben-David U, Ha G, Tseng Y-Y, Greenwald NF, Oh C, Shih J, et al. Patient-derived xenografts undergo mouse-specific tumor evolution. Nature genetics. 2017;49(11):1567-75.

16. Gadd S, Huff V, Walz AL, Ooms AH, Armstrong AE, Gerhard DS, et al. A Children's Oncology Group and TARGET initiative exploring the genetic landscape of Wilms tumor. Nature genetics. 2017;49(10):1487-94.

17. Hu Q, Gao F, Tian W, Ruteshouser EC, Wang Y, Lazar A, et al. Wt1 ablation and Igf2 upregulation in mice result in Wilms tumors with elevated ERK1/2 phosphorylation. The Journal of clinical investigation. 2011;121(1):174-83.

18. Urbach A, Yermalovich A, Zhang J, Spina CS, Zhu H, Perez-Atayde AR, et al. Lin28 sustains early renal progenitors and induces Wilms tumor. Genes & development. 2014;28(9):971-82.

19. Calandrini C, Drost J. Generation of Human Kidney Tubuloids from Tissue and Urine. JOVE-JOURNAL OF VISUALIZED EXPERIMENTS. 2021(170).

20. Calandrini C, Drost J. Normal and tumor-derived organoids as a drug screening platform for tumor-specific drug vulnerabilities. STAR Protocols. 2022;3(1):101079.

21. Bolhaqueiro AC, Ponsioen B, Bakker B, Klaasen SJ, Kucukkose E, van Jaarsveld RH, et al. Ongoing chromosomal instability and karyotype evolution in human colorectal cancer organoids. Nature genetics. 2019;51(5):824-34.

22. Roerink SF, Sasaki N, Lee-Six H, Young MD, Alexandrov LB, Behjati S, et al. Intra-tumour diversification in colorectal cancer at the single-cell level. Nature. 2018;556(7702):457-62.

23. Popov SD, Sebire NJ, Vujanic GM. Wilms' Tumour–Histology and Differential Diagnosis. 2016.

24. Cresswell GD, Apps JR, Chagtai T, Mifsud B, Bentley CC, Maschietto M, et al. Intra-tumor genetic heterogeneity in Wilms tumor: clonal evolution and clinical implications. EBioMedicine. 2016;9:120-9.

25. van de Wetering M, Francies HE, Francis JM, Bounova G, Iorio F, Pronk A, et al. Prospective derivation of a living organoid biobank of colorectal cancer patients. Cell. 2015;161(4):933-45.

26. Dijkstra KK, Monkhorst K, Schipper LJ, Hartemink KJ, Smit EF, Kaing S, et al. Challenges in establishing pure lung cancer organoids limit their utility for personalized medicine. Cell reports. 2020;31(5):107588.

27. Karthaus WR, Iaquinta PJ, Drost J, Gracanin A, Van Boxtel R, Wongvipat J, et al. Identification of multipotent luminal progenitor cells in human prostate organoid cultures. Cell. 2014;159(1):163-75.

28. Schutgens F, Rookmaaker MB, Margaritis T, Rios A, Ammerlaan C, Jansen J, et al. Tubuloids derived from human adult kidney and urine for personalized disease modeling. Nature biotechnology. 2019;37(3):303-13.

29. Drost J, Van Jaarsveld RH, Ponsioen B, Zimberlin C, Van Boxtel R, Buijs A, et al. Sequential cancer mutations in cultured human intestinal stem cells. Nature. 2015;521(7550):43-7.

30. Matano M, Date S, Shimokawa M, Takano A, Fujii M, Ohta Y, et al. Modeling colorectal cancer using CRISPR-Cas9–mediated engineering of human intestinal organoids. Nature medicine. 2015;21(3):256-62.

31. Ran F, Hsu PD, Wright J, Agarwala V, Scott DA, Zhang F. Genome engineering using the CRISPR-Cas9 system. Nature protocols. 2013;8(11):2281-308.

32. Wegert J, Vokuhl C, Ziegler B, Ernestus K, Leuschner I, Furtwängler R, et al. TP53 alterations in Wilms tumour represent progression events with strong intratumour heterogeneity that are closely linked but not limited to anaplasia. The Journal of Pathology: Clinical Research. 2017;3(4):234-48.

33. Young MD, Mitchell TJ, Vieira Braga FA, Tran MG, Stewart BJ, Ferdinand JR, et al. Single-cell transcriptomes from human kidneys reveal the cellular identity of renal tumors. science. 2018;361(6402):594-9.

34. Ooms AH, Calandrini C, de Krijger RR, Drost J. Organoid models of childhood kidney tumours. Nature Reviews Urology. 2020;17(6):311-3.

35. Waehle V, Ungricht R, Hoppe PS, Betschinger J. The tumor suppressor WT1 drives progenitor cell progression and epithelialization to prevent Wilms tumorigenesis in human kidney organoids. Stem cell reports. 2021;16(9):2107-17.

36. Drost J, Clevers H. Organoids in cancer research. Nature Reviews Cancer. 2018;18(7):407-18.

37. Clevers H. Modeling development and disease with organoids. Cell. 2016;165(7):1586-97.

38. Senthebane DA, Rowe A, Thomford NE, Shipanga H, Munro D, Al Mazeedi MA, et al. The role of tumor microenvironment in chemoresistance: to survive, keep your enemies closer. International journal of molecular sciences. 2017;18(7):1586.

39. Leruste A, Tosello J, Ramos RN, Tauziède-Espariat A, Brohard S, Han Z-Y, et al. Clonally expanded T cells reveal immunogenicity of rhabdoid tumors. Cancer cell. 2019;36(6):597-612. e8.

40. Theruvath J, Sotillo E, Mount CW, Graef CM, Delaidelli A, Heitzeneder S, et al. Locoregionally administered B7-H3-targeted CAR T cells for treatment of atypical teratoid/rhabdoid tumors. Nature medicine. 2020;26(5):712-9.

41. Yuki K, Cheng N, Nakano M, Kuo CJ. Organoid models of tumor immunology. Trends in immunology. 2020.

42. Bar-Ephraim YE, Kretzschmar K, Clevers H. Organoids in immunological research. Nature Reviews Immunology. 2020;20(5):279-93.

43. Schnalzger TE, de Groot MH, Zhang C, Mosa MH, Michels BE, Röder J, et al. 3D model for CAR-mediated cytotoxicity using patient-derived colorectal cancer organoids. The EMBO journal. 2019;38(12):e100928.

44. Dijkstra KK, Cattaneo CM, Weeber F, Chalabi M, van de Haar J, Fanchi LF, et al. Generation of tumor-reactive T cells by co-culture of peripheral blood lymphocytes and tumor organoids. Cell. 2018;174(6):1586-98. e12.

45. Tsai S, McOlash L, Palen K, Johnson B, Duris C, Yang Q, et al. Development of primary human pancreatic cancer organoids, matched stromal and immune cells and 3D tumor microenvironment models. BMC cancer. 2018;18(1):1-13.

46. Vlachogiannis G, Hedayat S, Vatsiou A, Jamin Y, Fernández-Mateos J, Khan K, et al. Patient-derived organoids model treatment response of metastatic gastrointestinal cancers. Science. 2018;359(6378):920-6.

47. Ganesh K, Wu C, O'Rourke KP, Szeglin BC, Zheng Y, Sauvé C-EG, et al. A rectal cancer organoid platform to study individual responses to chemoradiation. Nature medicine. 2019;25(10):1607-14.

48. Ooft SN, Weeber F, Dijkstra KK, McLean CM, Kaing S, van Werkhoven E, et al. Patient-derived organoids can predict response to chemotherapy in metastatic colorectal cancer patients. Science translational medicine. 2019;11(513).

49. Yao Y, Xu X, Yang L, Zhu J, Wan J, Shen L, et al. Patient-derived organoids predict chemoradiation responses of locally advanced rectal cancer. Cell stem cell. 2020;26(1):17-26. e6.

50. Tiriac H, Belleau P, Engle DD, Plenker D, Deschênes A, Somerville TD, et al. Organoid profiling identifies common responders to chemotherapy in pancreatic cancer. Cancer discovery. 2018;8(9):1112-29.

51. Kopper O, De Witte CJ, Lõhmussaar K, Valle-Inclan JE, Hami N, Kester L, et al. An organoid platform for ovarian cancer captures intra-and interpatient heterogeneity. Nature medicine. 2019;25(5):838-49.

52. Sachs N, de Ligt J, Kopper O, Gogola E, Bounova G, Weeber F, et al. A living biobank of breast cancer organoids captures disease heterogeneity. Cell. 2018;172(1-2):373-86. e10.

53. Driehuis E, Oosterom N, Heil S, Muller I, Lin M, Kolders S, et al. Patient-derived oral mucosa organoids as an in vitro model for methotrexate induced toxicity in pediatric acute lymphoblastic leukemia. PloS one. 2020;15(5):e0231588.

54. Meng Q. Three-dimensional culture of hepatocytes for prediction of drug-induced hepatotoxicity. Expert opinion on drug metabolism & toxicology. 2010;6(6):733-46.

55. Hu H, Gehart H, Artegiani B, Löpez-Iglesias C, Dekkers F, Basak O, et al. Long-term expansion of functional mouse and human hepatocytes as 3D organoids. Cell. 2018;175(6):1591-606. e19.

56. Rock JR, Onaitis MW, Rawlins EL, Lu Y, Clark CP, Xue Y, et al. Basal cells as stem cells of the mouse trachea and human airway epithelium. Proceedings of the National Academy of Sciences. 2009;106(31):12771-5.

57. Mills RJ, Parker BL, Quaife-Ryan GA, Voges HK, Needham EJ, Bornot A, et al. Drug screening in human PSC-cardiac organoids identifies pro-proliferative compounds acting via the mevalonate pathway. Cell stem cell. 2019;24(6):895-907. e6.

58. Takasato M, Pei XE, Chiu HS, Maier B, Baillie GJ, Ferguson C, et al. Kidney organoids from human iPS cells contain multiple lineages and model human nephrogenesis. Nature. 2015;526(7574):564-8.

59. Pasch CA, Favreau PF, Yueh AE, Babiarz CP, Gillette AA, Sharick JT, et al. Patient-derived cancer organoid cultures to predict sensitivity to chemotherapy and radiation. Clinical Cancer Research. 2019;25(17):5376-87.

60. Weeber F, Ooft SN, Dijkstra KK, Voest EE. Tumor organoids as a pre-clinical cancer model for drug discovery. Cell chemical biology. 2017;24(9):1092-100.

61. Housman G, Byler S, Heerboth S, Lapinska K, Longacre M, Snyder N, et al. Drug resistance in cancer: an overview. Cancers. 2014;6(3):1769-92.

62. Lim Z-F, Ma PC. Emerging insights of tumor heterogeneity and drug resistance mechanisms in lung cancer targeted therapy. Journal of hematology & oncology. 2019;12(1):1-18.

63. Bond MC, Pritchard S. Understanding clinical trials in childhood cancer. Paediatrics & child health. 2006;11(3):148-50.

64. Ringel T, Frey N, Ringnalda F, Janjuha S, Cherkaoui S, Butz S, et al. Genome-scale CRISPR screening in human intestinal organoids identifies drivers of TGF-β resistance. Cell Stem Cell. 2020;26(3):431-40. e8.

65. Murakami K, Terakado Y, Saito K, Jomen Y, Takeda H, Oshima M, et al. A genome-scale CRISPR screen reveals factors regulating Wnt-dependent renewal of mouse gastric epithelial cells. Proceedings of the National Academy of Sciences. 2021;118(4).

66. Joung J, Konermann S, Gootenberg JS, Abudayyeh OO, Platt RJ, Brigham MD, et al. Genome-scale CRISPR-Cas9 knockout and transcriptional activation screening. Nature protocols. 2017;12(4):828-63.

67. Custers L, Khabirova E, Coorens TH, Oliver TR, Calandrini C, Young MD, et al. Somatic mutations and single-cell transcriptomes reveal the root of malignant rhabdoid tumours. Nature communications. 2021;12(1):1-11.

68. Huang M, Ye Y-c, Chen S, Chai J-R, Lu J-X, Gu L-J, et al. Use of all-trans retinoic acid in the treatment of acute promyelocytic leukemia. 1988.

69. Matthay KK, Villablanca JG, Seeger RC, Stram DO, Harris RE, Ramsay NK, et al. Treatment of high-risk neuroblastoma with intensive chemotherapy, radiotherapy, autologous bone marrow transplantation, and 13-cis-retinoic acid. New England Journal of Medicine. 1999;341(16):1165-73.

8

Appendices

Nederlandse samenvatting

Nierkanker is een van de meest frequente vormen van kinderkanker, waarvan Wilms tumoren het meest voorkomende subtype is. De overlevingskans bij dit tumortype is 90%, maar de nasleep van de ingrijpende behandeling legt een langdurige en zware last op patiënten. Bij meer zeldzame vormen van nierkanker bij kinderen, zoals maligne rhabdoïde tumoren van de nier (MRTK) en herhaald terugkerende Wilms tumoren (RWT), is de prognose slechter. Om de overlevings-kansen en kwaliteit van leven voor patiënten te verbeteren zijn daarom nieuwe therapieën nodig. Verschillende factoren, waaronder het gebrek aan pre-klinische modellen die een adequate representatie geven van de verschillende karakte-ristieken van de niertumoren, hebben de ontwikkeling van nieuwe therapieën echter belemmerd.

Recente ontwikkelingen maken het mogelijk om multicellulaire, zelforgani-zerende 3D structuren vanuit een enkele stamcel buiten het lichaam te laten groeien. Deze zogenaamde 'organoïden' zijn mini-organen die de architectuur en functie van het oorspronkelijke weefsel (deels) behouden en kunnen vanuit zowel gezond als kwaadaardig weefsel gekweekt worden. Tumororganoïden kunnen met hoge efficiëntie uit primair materiaal gewonnen worden en behouden de histologische en genetische opmaak van de tumor. Meerdere studies hebben daarnaast aangetoond dat tumororganoïden op dezelfde manier reageren op the-rapeutische interventie als de oorspronkelijke tumor. Dit maakt deze organoïden aantrekkelijke preklinische modellen voor het screenen van nieuwe medicijnen.

De in deze thesis beschreven onderzoeken hebben als doel de totstandbren-ging van tumororganoïden van (nier)kanker bij kinderen, welke zullen dienen als preklinisch modelsysteem voor de screening van medicijnen. Deze screening moet leiden tot de identificatie van nieuwe, minder toxische, medicatie.

In **hoofdstuk 2** worden huidig beschikbare modelsystemen voor de studie van nierkanker bij kinderen met elkaar vergeleken. Wij beschouwen hierbij tevens or-ganoïden modellen van de gezonde nier, welke uit zowel adulte stamcellen (ASC) als geïnduceerde pluripotente stamcellen (iPSCs) verkregen kunnen worden. De voor- en nadelen van beide benaderingen worden in dit hoofdstuk behandeld.

In **hoofdstuk 3** rapporteren wij de eerste biobank bestaande uit tumororgano-iden verkregen uit materiaal van patiënten van de kinderleeftijd. Deze collectie organoïden omvat een breed spectrum van meer dan 50 tumorsoorten, inclusief Wilms Tumoren, MRTK en RCC. We beschrijven eveneens het eerste *in vitro* model welke de drie-fasen structuur (epitheel, stroma en blastema) van Wilms tumoren behoudt. Daarnaast presenteren wij MRTK organoïden als het eerste organoïden

model van niet-epitheliale oorsprong. De organoïden in de biobank zijn histolo-gisch, (epi)genetisch en op transcriptoom niveau gekarakteriseerd en vertonen belangrijke overeenkomsten met de originele tumoren. Deze biobank is zodoende een collectie van nieuwe pre-klinische modellen voor de studie van kinderkanker.

De biobank beschreven in **hoofdstuk 3** bevat naast tumororganoïden ook or-ganoïden van gezond nierweefsel afkomstig van dezelfde patiënten. In **hoofdstuk 4** beschrijven en illustreren wij in detail hoe deze gezonde organoïden, tevens bekend als tuboloiden, verkregen en gekweekt kunnen worden uit zowel weefsel als urine.

Maligne rhabdoïde tumoren (MRTs) komen naast de nier ook voor in andere delen van het lichaam. MRTs, waaronder MRTKs, zijn zeer agressieve tumoren: 70% van de patiënten overleeft de ziekte niet. In **hoofdstuk 5** identificeren wij nieuwe therapeutische interventies middels screening van medicijnen op MRT organoïden. We identificeren de neddylatie remmer MLN4924 als een speci-fieke remmer van MRT groei. MRTs hebben toegenomen neddylatie niveaus en MLN4924 heeft cytotoxische effecten middels stimulatie van de 'unfolded pro-tein response'. Ten slotte laten wij zien dat MLN4924 tumorgroei belemmerd en overleving bevorderd in een muismodel.

Voor de selectie van medicatie die MRT specifiek en minder toxisch is, hebben wij tevens gebruik gemaakt van organoïden welke verkregen zijn uit gezond weef-sel. Door screening resultaten op organoïden van zowel tumor als gezond weef-sel te vergelijken, hebben wij medicijnen geselecteerd welke alleen effectief zijn tegen MRTs. Deze screening strategie wordt in **hoofdstuk 6** beschreven in een protocol en heeft geleid tot het excluderen van medicatie welke toxische effecten heeft op de lever, dunne darm en nieren.

In **hoofdstuk 7** rapporteren wij de resultaten van een haalbaarheidsstudie uitgevoerd op RWTs, met als doel om medicatie te screenen binnen een klinisch relevante tijdsduur. We beschrijven het verzamelen van RWT-samples vanuit heel Europa. De organoïden verkregen uit deze samples dienen als bron voor de scree-ning van medicatie ter identificatie van kwetsbaarheden in RWTs. Wij verkrijgen in totaal 9 RWT organoïdenlijnen, resulterend in een effectiviteit van 50% om een succesvol organoïde model te maken. Dit resulteert in een aanzienlijke toename in beschikbare pre-klinische modellen voor RWTs. Voor het merendeel van de patiënten waren wij in staat om screening resultaten te verkrijgen terwijl de pa-tiënten nog onder behandeling en/of in leven waren. Wij identificeren medicatie voor specifieke patiënten, zoals EGFR/HER2 remming als generieke behandeling voor RWTs.

Concluderend beschrijft dit proefschrift als eerste de toepassing van organoï-dentechnologie bij kinderkanker. Wij hebben meer dan 50 unieke organoïdenlijnen opgezet, verkregen uit tumoren waarvoor preklinische modellen voorheen schaars waren. Deze verzameling organoïden maken het nu mogelijk om deze zeldzame maligniteiten te bestuderen met de voordelen van een *in vitro* systeem, terwijl de karakteristieken van de tumor veelal behouden blijven. Wij demonstreren de mogelijkheid om deze modellen in te zetten bij screenend onderzoek naar nieuwe medicatie en identificeren zodoende nieuwe therapeutische mogelijkheden voor hoog-risico patiënten. Dit werk betekend een eerste stap richting de implemen-tatie van organoïdentechnologie ter verbetering van de behandeling van kinder-kanker.

English Summary

Pediatric renal tumors are among the most frequent malignancies in children. The majority of patients is diagnosed with Wilms tumors. While survival rates have reached 90%, patients still suffer from severe long-term side effects, caused by the harsh therapy regiments. Furthermore, patients affected by rarer renal tumor subtypes, such as malignant rhabdoid tumor of the kidney (MRTK) and recurrent relapsed Wilms tumor (RWT), carry a dismal prognosis. To improve survival rates and quality of life for pediatric renal tumor patients, alternative therapies need to be sought.

In recent years therapeutic innovation has been impaired by different factors, including the lack of preclinical models able to closely represent characteristics of pediatric kidney tumors. New frontiers in cell culture techniques allow for the establishment and expansion of multicellular structures, derived from stem cells, that self organize to grow in a 3D fashion. These "mini organs", able to mimic the architecture – and partial function - of the original tissues, are named organoids. Organoids can be generated from healthy tissues as well as from tumors. Tumor organoids can be established with high efficiency from patient tumor material, while maintaining characteristics of the original tissue, such as histology and genetic makeup. Furthermore, several studies have shown that tumor organoids are able to mirror the response to therapy registered in patients, making them appealing models for drug screening purposes.

In this thesis we aimed to apply the organoid technology to establish pediatric kidney cancer organoid models and to utilize them for the identification of novel – less toxic - therapeutic strategies.

In **Chapter 2**, we compare the different organoid models available to study and model pediatric kidney tumors, including organoid models of healthy kidney. Kidney organoids can be generated from stem cells present in adult tissues (Adult Stem Cells, ASC) or from committed cells that are forced into dedifferentiation (Induced Pluripotent Stem Cells, iPSC). In this chapter we discuss the advantages and disadvantages of the use of ASC- and iPSC- derived kidney organoid cultures.

In **Chapter 3** we present the first organoid biobank generated from pediatric patient material. This collection of organoids accounts for more than 50 different models, generated from a wide spectrum of different tumor types, including Wilms tumor, MRTK and RCCs. We describe the first *in vitro* model for Wilms tumor able to capture all three cellular phases typical of these tumors: epithelial, stromal and blastemal components. Furthermore, we present MRTK organoids as the

first organoid model developed from cells of non-epithelial origin. In this chapter we performed histological, (epi)genetic and transcriptomic characterization of the organoid culture and conclude that they resemble the original tumors to a great extent. Overall, we successfully established novel representative preclinical models of pediatric renal tumors.

Next to the tumor organoids, in **Chapter 3** we describe the generation of patient-matching kidney organoids, also referred to as tubuloid cultures. In **Chapter 4** we illustrate a detailed protocol for the establishment and expansion of such cultures originated from both tissue and urine samples.

Besides affecting the kidneys, malignant rhabdoid tumors (MRTs) can arise in several other locations of the body. MRTs - including MRTKs - are extremely aggressive, causing for 70% of the patients to not survive the disease. In **Chapter 5** we make use of MRT organoid models to perform drug screening and identify novel therapeutic interventions for these high-risk patients. We identified neddylation inhibitor MLN4924 to be specifically hampering MRT growth. Mechanistically, we found increased neddylation levels in MRTs and that treatment with MLN4924 induced a cytotoxic effect via the upregulation of the unfolded protein response. Lastly, we also demonstrate that MLN4924 significantly impaired MRT growth and extended survival in a *in vivo* mouse model.

In order to narrow down the selection and identify MRT-specific, less toxic compounds, we made use of normal-tissue derived organoids. Comparing drug screening results obtained from MRTs to those of healthy organoids allowed us to identify compounds effective in MRTs yet with neglectable effects on healthy cultures. This drug screening strategy, illustrated as protocol in **Chapter 6**, allowed us to exclude drugs that could induce toxic effects in liver, small intestine and kidneys.

In **Chapter 7**, we report the results of a feasibility study conducted on RWTs. We describe the collection of RWT samples from all over Europe to generate organoid cultures and perform drug screening to identify RWT drug vulnerabilities in a clinically relevant timeframe. As result, we established 9 RWT cultures, with an overall efficiency of 50%, greatly increasing the number of preclinical models available to study RWTs. For the majority of the patients we obtained drug screening results while patients were still alive and/or under treatment, therefore in a relevant timeframe. Furthermore, we identified both patient-specific drugs as well as EGFR/HER2 inhibition as general sensitivity of RWT patients.

In conclusion, in this thesis we present for the first time the application of the organoid technology to pediatric cancer research. We successfully generated more than 50 unique patient-derived organoid cultures for which preclinical models were scarce. This collection of organoids provides with the opportunity to study these rare malignancies with the advantages of an *in vitro* model, while the characteristics of the original tumors are still recapitulated to a large extend. We demonstrate that it is feasible to use these models to perform drug screening and identify novel therapy for high-risk pediatric patients. The work presented in this thesis sets the first steps towards the implementation of the organoid technology as tool for improving treatment of children with cancer.

Riassunto in italiano

I tumori renali pediatrici sono tra i piú frequenti tumori che colpiscono infanti e adolescenti. La maggior parte delle diagnosi sono di tumore di Wilms, mentre una piccola percentuale prevede casi di tumori maligni rabdoidi (MRT) o altre forme piú rare. Sebbene si tratti di tumori aggressivi, la maggior parte dei bambini e adolescenti raggiunge completa guarigione grazie a una combinazione di protocolli chemoterapeutici, radioterapia e rimozione chirurgica del tumore. Tuttavia, una parte di questi pazienti non sopravvive, segno che le terapie farmacologiche oggigiorno in uso non sono efficaci per tutti i pazienti. Per raggiungree l'obiettivo di una guarigione completa per tutti i pazienti è necessario perció ricercare approcci terapeutici alternativi.

Per identificare nuovi medicinali, efficaci anche in pazienti con prognosi infausta, i ricercatori si avvalgono di modelli preclinici. Questi modelli sono capaci di riprodurre caratteristiche dei tumori d'origine, sebbene in una forma piú semplificata perchè studiati all'esterno del corpo umano. In questo contesto, i modelli preclinici sono cellule tumorali - isolate durante operazioni chirurgiche - che vengono stimolate a riprodursi e a crescere nell'ambiente di laboratorio. Questi modelli sono utilizzati per misurare la risposta di cellule tumorali a diversi farmaci prima che essi vengano somministrati ad un paziente. In questo modo, piú farmaci possono essere testati allo stesso tempo e solo quelli che dimostrano un effetto evidente verranno poi presi in considerazione per trial clinici su pazienti. Ad oggi, i modelli preclinici di tumori renali pediatrici sono scarsi o, per alcuni sottotipi, del tutto inesistenti. Questo è dovuto a due motivi principali: alla raritá di questi tumori e all'inefficacia dei protocolli fino ad ora in uso per lo stabilimento di linee cellulari tumorali. Pertanto, per poter fare progressi nel trattamento di bambini con tumori renali ad alto rischio, lo sviluppo di modelli preclinici è un primo passo di vitale importanza.

Lo scopo di questo progetto di dottorato è quello di generare nuovi modelli preclinici per tumori renali infantili e di dimostrare la fattibilitá del loro utilizzo per l'identificazione di nuove terapie farmacologiche per pazienti ad alto rischio.

Per sviluppare nuovi modelli, vista l'inefficacia dei protocolli classici, ci siamo avvalsi di una nuova tecnologia, quella dell'organoide. Gli organoidi, come esemplificato dallo stesso nome, sono modelli preclinici che mimicano la struttura di un organo. Gli organoidi crescono in tre dimensioni e assomigliano maggiormente a un organo o a un tumore in miniatura, se presi a confronto con le classiche linee cellulari tumorali a crescita bi-dimensionale.

Nel **Capitolo 1** di questa tesi introduciamo i tumori renali infantili, facendo particolare attenzione ai casi ad alto rischio, e introduciamo la nascita della tecnologia dell'organoide applicata alla ricerca oncologica.

Nel **Capitolo 2** descriviamo i modelli ad oggi disponibili per ricercare e modellare tumori renali pediatrici. In particolare, descriviamo i vari modelli di organoidi, da quelli che mimicano il rene, a quelli che derivano direttamente da tumor renali infantili.

Nel **Capitolo 3** presentiamo la generazione e caratterizzazione di più di 50 diversi modelli di organoidi derivati da pazienti con tumori renali infantili, dai più frequenti tumori di Wilms, ai più rari e aggressivi MRT. In questo capitolo dimostriamo il valore aggiunto di questi modelli nella ricerca oncologica pediatrica.

Nel **Capitolo 4** descriviamo in dettaglio i protocolli da noi messi a punto per la generazione di organoidi del rene derivati direttamente da campioni di tessuto, o da campioni di urina.

Nel **Capitolo 5** dimostriamo l'utilizzo di organoidi derivati da pazienti affetti da MRT per l'identificazione di medicinali efficaci contro questi tumori molto aggressivi.

Nel **Capitolo 6** presentiamo in dettaglio i protocolli utilizzati per condurre screen farmacologici su linee di organoidi derivati da tumori e da tessuti sani.

Nel **Capitolo 7** descriviamo la generazione e caratterizzazione di 9 modelli di organoidi derivati da pazienti affetti da rarissimi tumori di Wilms recidivi.

Infine, nel **Capitolo 8** discutiamo come i risultati ottenuti da questo studio possono contribuire al miglioramento della ricerca oncologica pediatrica.

Resumo em português

Os tumores renais pediátricos estão entre os cancros mais frequentes que ocorrem em crianças e adolescentes. A maioria dos diagnósticos é de tumor de Wilms, enquanto uma pequena porcentagem prevê casos de malignidade rabdóide (MRT) ou outras formas mais raras. Apesar de serem tumores agressivos, a maioria das crianças e adolescentes recuperam-se completamente graças a uma combinação de protocolos quimioterápicos, de radioterapia e remoção cirúrgica do tumor. No entanto, atualmente alguns destes pacientes não sobrevivem, sinal de que as terapias em uso não são eficazes para todos os pacientes. Para atingir o objetivo de recuperação completa de todos os pacientes, é necessário, portanto, investigar abordagens terapêuticas alternativas.

Para identificar novos medicamentos, que também sejam eficazes em pacientes com prognóstico desfavorável, pesquisadores usam modelos pré-clínicos. Esses modelos são capazes de reproduzir características dos tumores originais de forma mais simplificada para serem estudados fora do corpo humano. Neste contexto, os modelos pré-clínicos são células tumorais - isoladas durante operações cirúrgicas - que são estimuladas a se reproduzir e crescer em ambiente laboratorial. Esses modelos são usados para avaliar a resposta das células de cancro a diferentes fármacos antes de serem administradas a um paciente. Dessa forma, vários medicamentos podem ser testados e apenas aqueles que demonstram um efeito claro serão considerados para ensaios clínicos em pacientes. Até ao momento, os modelos pré-clínicos de tumores renais pediátricos são escassos ou, para alguns subtipos, inexistentes. Isso deve-se a dois motivos principais: a raridade desses tumores e a ineficácia dos protocolos utilizados para o estabelecimento de linhagens tumorais. Portanto, para avançar no tratamento de crianças com cancro renal de alto risco, o desenvolvimento de modelos pré-clínicos é um passo importante.

O objetivo deste projeto de doutoramento é gerar novos modelos pré-clínicos para tumores renais infantis e demonstrar a viabilidade do seu uso para a identificação de novas terapias medicamentosas para pacientes de alto risco.

Dada a ineficácia dos protocolos clássicos, fizemos uso de uma nova tecnologia para desenvolver novos modelos, chamados organoides. Os organoides são modelos pré-clínicos que replicam a estrutura de um órgão, são capazes de crescer em três dimensões e são mais semelhantes a um órgão ou tumor em miniatura quando comparados às linhas de células cancerígenas clássicas.

No **Capítulo 1** desta tese apresentamos os tumores renais infantis, com atenção especial aos casos de alto risco, e apresentamos o desenvolvimento da tecnologia organoide aplicada à pesquisa do cancro.

No **Capítulo 2** descrevemos os modelos disponíveis até ao momento para pesquisa e modelagem de tumores renais pediátricos. Em particular, descrevemos os vários modelos de organoides, desde os que mimetizam o rim, até aqueles que derivam diretamente de tumores renais infantis.

No **Capítulo 3** apresentamos a geração e caracterização de mais de 50 modelos organoides diferentes derivados de pacientes com tumores renais infantis, desde os tumores de Wilms mais frequentes até os MRTs mais raros e agressivos. Neste capítulo, demonstramos o valor agregado desses modelos na pesquisa do cancro pediátrico.

No **Capítulo 4** detalhamos os protocolos que estabelecemos para o desenvolvimento de organoides renais derivados diretamente de amostras de tecido ou de amostras de urina.

No **Capítulo 5** demonstramos o uso de organoides derivados de pacientes de MRT para a identificação de fármacos eficazes contra esses tumores.

No **Capítulo 6** apresentamos em detalhe os protocolos usados para realizar testes farmacológicos em linhas de organoides derivados de tumores e tecidos saudáveis.

No **Capítulo 7** descrevemos a geração e caracterização de 9 modelos organoides derivados de pacientes com tumores de Wilms recorrentes muito raros.

Para concluir, no **Capítulo 8** discutimos como os resultados obtidos neste estudo podem contribuir para o aprimoramento da pesquisa do cancro pediátrico.

Curriculum Vitae

Camilla Calandrini was born on January 9th 1993 in Ravenna (Italy) from Italian father and Portuguese mother. In 2012, she obtained her high school degree at Liceo Scientifico "A. Oriani" in Ravenna, Italy. In the same year, she started the Bachelor Biotechnology at the University of Bologna. During this study, she performed an internship at the department of human genetics, studying the role of *CHRFAM7A* gene variants in autism onset. She was also one of the founding members of "Minerva", a non-profit organization with the aim of promoting science communication to the general public. In 2015, she obtained her Bachelor degree *cum laude*.

In the fall of 2015, Camilla moved to Utrecht, the Netherlands, to start the Master program Cancer, Stem Cells and Developmental Biology at Utrecht University. During this study, she performed her first internship in the lab of Dr. Wigard Kloosterman at UMC Utrecht, under the supervision of Dr. Alessio Marcozzi. Here, she made used of the CRISPR/Cas9 technology to study the impact of structural genomic variations in congenital diseases. Her second internship was performed at the Hubrecht Institute in the lab of Prof. dr. Geert Kops, where she studied the molecular mechanisms underlying anaphase bridges formation in colorectal cancer using patient-derived organoids.

In the summer of 2017 she obtained her Master degree, after which she started her PhD trajectory at the Princess Máxima Center for Pediatric Oncology, Utrecht. During her PhD, she joined the lab of Dr. Jarno Drost to establish patient-derived organoid models of different pediatric kidney cancers subtypes and to investigate their use for the identification of novel therapies. The results of these studies are presented in this thesis. During her time as PhD student, Camilla joined the PriMá PhD group, organizing events to support other PhD students, and sang in the in-house band "To The Max!". In June 2022 she started to work as Scientist at Sanquin Diagnostic Services.

List of publications

This thesis

Camilla Calandrini and Jarno Drost. *Normal and tumor-derived organoids as a drug screening platform for tumor-specific drug vulnerabilities.* STAR Protocols. 2022;3(1):101079.

Camilla Calandrini, Sander R. van Hooff, Irene Paassen, Dilara Ayyildiz, Sepide Derakhshan, M. Emmy M. Dolman, Karin P.S. Langenberg, Marieke van de Ven, Cecilia de Heus, Nalan Liv, Marcel Kool, Ronald R. de Krijger, Godelieve A.M. Tytgat, Marry M. van den Heuvel-Eibrink, Jan J. Molenaar, Jarno Drost. *Organoid-based drug screening reveals neddylation as therapeutic target for malignant rhabdoid tumors.* Cell reports. 2021;36(8):109568.

Camilla Calandrini and Jarno Drost. *Generation of Human Kidney Tubuloids from Tissue and Urine.* JOVE-JOURNAL OF VISUALIZED EXPERIMENTS. 2021(170).

Ariadne H.A.G. Ooms#, **Camilla Calandrini**#, Ronald R. de Krijger and Jarno Drost. *Organoid models of childhood kidney tumours.* Nature Reviews Urology. 2020;17(6):311-3.

Camilla Calandrini#, Frans Schutgens#, Rurika Oka, Thanasis Margaritis, Tito Candelli, Luka Mathijsen, Carola Ammerlaan, Ravian L. van Ineveld, Sepide Derakhshan, Sanne de Haan, Emmy Dolman, Philip Lijnzaad, Lars Custers, Harry Begthel, Hindrik H.D. Kerstens, Lindy L. Visser, Maarten Rookmaaker, Marianne Verhaar, Godelieve A.M. Tytgat, Patrick Kemmeren, Ronald R. de Krijger, Reem Al-Saadi, Kathy Pritchard-Jones, Marcel Kool, Anne C. Rios, Marry M. van den Heuvel-Eibrink, Jan J. Molenaar, Ruben van Boxtel, Frank C. P. Holstege, Hans Clevers, Jarno Drost. *An organoid biobank for childhood kidney cancers that captures disease and tissue heterogeneity.* Nature communications. 2020;11(1):1-14.

Other publications

Lars Custers#, Eleonora Khabirova#, Tim H. H. Coorens#, Thomas R. W. Oliver, **Camilla Calandrini**, Matthew D. Young, Felipe A. Vieira Braga, Peter Ellis, Lira Mamanova, Heidi Segers, Arie Maat, Marcel Kool, Eelco W. Hoving, Marry M. van den Heuvel-Eibrink, James Nicholson, Karin Straathof, Liz Hook, Ronald R. de Krijger, Claire Trayers, Kieren Allinson, Sam Behjati and Jarno Drost. *Somatic mutations and*

single-cell transcriptomes reveal the root of malignant rhabdoid tumours. Nature communications. 2021;12(1):1-11.

Michael T. Meister, Marian J. A. Groot Koerkamp, Terezinha de Souza, Willemijn B. Breunis, Ewa Frazer-Mendelewska, Mariël Brok, Jeff DeMartino, Freek Manders, **Camilla Calandrini**, Hinri H. D. Kerstens, Alex Janse, M. Emmy M. Dolman, Selma Eising, Karin P. S. Langenberg, Marc van Tuil, Rutger R. G. Knops, Sheila Terwisscha van Scheltinga, Laura S. Hiemcke-Jiwa, Uta Flucke, Johannes H. M. Merks, Max M. van Noesel, Bastiaan B. J. Tops, Jayne Y. Hehir-Kwa, Patrick Kemmeren, Jan J. Molenaar, Marc van de Wetering, Ruben van Boxtel, Jarno Drost and Frank C. P. Holstege. *Mesenchymal tumor organoid models recapitulate rhabdomyosarcoma subtypes.* bioRxiv. 2022:2022.01.03.474504.

# These authors contributed equally to this work

Author contribution per chapter

Chapter 1
C.C. wrote the chapter, supervised by J.D.

Chapter 2
C.C. and A.H.G.O. wrote the manuscript, supervised by J.D. R.R.d.K reviewed the manuscript.

Chapter 3
C.C., F.S. and J.D. designed and performed experiments. R.O., H.K., P.K. and R.v.B. analyzed WGS data. T.M., T.C., L.C., L.V., P.L. and F.H. analyzed (single-cell) RNA-seq data. C.C., F.S., C.A., S.D., S.d.H., E.D., J.M. and J.D. established and maintained organoid cultures and performed drug screens. L.M. performed CRISPR targeting of organoids. R.v.I. and A.C.R. performed 3D imaging. H.B. and R.d.K. performed immunohistochemical staining. M.R. and M.V. were involved in study design. R.A.-S. and K.P.-J. supported sample curation. R.d.K. staged the tumor organoids. M.K. performed DNA methylation array analyses. G.A.M.T. and M.H.E. established logistics of obtaining clinical samples of tumor tissue and obtained informed consent for the study. H.C. and J.D. conceived of the study and wrote the paper.

Chapter 4
C.C. developed and optimized the protocol. J.D supervised the research. C.C. and J.D. wrote the manuscript.

Chapter 5
C.C. and J.D. designed and performed experiments. C.C. and S.D. maintained organoid cultures and performed drug screens. E.D., K.P.S.L and J.J.M. set up the drug screening library. S.v.H. performed analysis of whole genome sequencing and RNA sequencing data; I.P. performed and analyzed *SMARCB1* re-expression experiment; D.A. and M.K. analyzed DNA methylation data; M.v.d.V performed and coordinated *in vivo* experiments; N.L. and C.d.H. performed TEM experiment and analyzed electron microscopy images; R.d.K. performed histological evaluation of tumor organoids and tissues. G.A.M.T. and M.v.d.E obtained informed consent from patients and established pipeline to obtain tumor tissues. J.D. conceived the study and J.D and C.C wrote the paper.

Chapter 6

C.C. developed and optimized the protocol. J.D supervised the research. C.C. and J.D. wrote the manuscript.

Chapter 7

C.C. and J.D. designed and performed experiments. C.C. and S.D. maintained organoid cultures and performed drug screens. A.G. retrieved patient clinical data. D.A. processed WGS and RNAseq data and analyzed WGS data. R.A-S. supported sample curation. J.B., D.P., F.S., M.v.d.E., A.M. and J.D. conceived the study. J.D. and C.C. wrote the paper.

Chapter 8

C.C. wrote the chapter, supervised by J.D.

all the nice talks and for all the rides to Woerden. You got this girl! **Jiayou** and **Marjolein**: it is always nice to see how vibrant and hopeful are PhD students of the first year. Thank you both for bringing back this feeling in the lab and good luck with your journey! **Arianna**, grazie per tutti i consigli e per tutto l'aiuto che mi hai dato in questi anni. Sei davvero una forza della natura! **Juliane**, thank you for your kindness, sweetness and contagious Xmas spirit! I wish you all the best, also with your new adventure as Joren's mommy! **Dilara**, è stato un piacere lavorare con te e parlare di libri e serie tv. Anche se non ti perdoneró mai il fatto che ti sia piaciuto Squid game ☺! **Frans**, it has been a pleasure to work together on the biobank paper, I wish you all the good luck with your training! **Sofia**, it has been so nice to have you around. Working with you always felt natural. Looking forward to organize the next fancy dinner together with Bas and of course little Nora! **Yvonne**, your happiness and joy is contagious. Never loose your smile and laugh, it is so precious! **Jolanda**, I am so happy you join the Drost group, we couldn't wish for a better match! Good luck with everything. **Kim**, I wish you all the good luck with the start of your PhD. And good luck also to **Puck**, the new Kim ☺

Thank you to all the students that joined our lab in the years: **Thomas**, **Marloes**, **Chloe**, **Chiara**, **Josephine**, **Carla** and **Laura**. Wish you all good luck with your scientific careers. Special thanks goes to **Luka**, for all your hard work! I wish you all the best.

At the beginning of 2022, an important fusion has taken place. Now the Drost group has acquired fantastic new members. But first of all, a special thank goes to **Frank**. Thank you for caring so much about your people. And thank you for listening to me when "the phone accident" happened. I wish you all the best. **Thanasis**, thank you for all your scientific insight, you are a wizard! **Tito**, quando ci sei tu è impossibile non sorridere. Grazie per le risate e per il tuo humor. **Philip**, I will never thank you enough for asking me to join the house band back in 2018. Thank you for making To The Max! possible. **Eduard**, thank you for being an awesome guitar player, can't wait for the day we will play Paramore together ☺ Terezinha, *obrigada* for helping out with the translation to Portuguese of the thesis summary, my grandparents will be very grateful! **Jeff** and **Michael**, thank you for the nice chats at lunch, and good luck with finishing up! **Ewa**, continua ad allenarti con l'italiano, sei proprio brava! **Marian**, it has been a real pleasure working together. **Mariel**, thank you for the times we sang and listen to music in the histology lab. **Tomasz**, having you around was so much fun! I will miss listening to your crazy stories during FACS. I wish you all the best. Thank you also to **Lindy** and **Aleksandra**.

Thank you to the external people that joined work discussion: **Alissa**, good luck with your PhD track. **Ronald**, grazie per il tuo aiuto in questi anni, è stato un vero piacere lavorare con te. **Lieve**, thank you for giving me the opportunity to work on this Kika project.

To our Retreat buddies, the van Boxtel group. **Ruben**, thank you for the nice talks and for your inspiring enthusiasm. **Axel** and **Karlijn**, I wish you the best for the next steps in your careers! **Diego** and **Flavia**, good luck with the next shows of To the Max! **Eline**, thank you for all the good times in the PriMa PhD group. And thank you to all of you guys: **Arianne**, **Rurika**, **Niels**, **Mark**, **Freek** and **Jurrian**.

To our office neighbors: **Evelyn**, you made these years special. The Máxima wouldn't have been the same without you. Your joy, happiness and kindness are precious. Never loose your sparkle. **Femke**, thank you for all the nice times in MLI. I admire your strength and determination. I miss our afternoon chats during culturing very much! **Margit**, good luck with your new life adventures. **Karin**, it has been very nice to have you around. **Marc**, thank you for the nice conversations about music and wine. Hopefully we will share another nice bottle in the future ☺ Thank you also to **Laurens**, **Seok Young** and **Lin**.

Jules, thank you for helping me out surviving the "phone accident". Without you, I would have probably loose it! **Valentina**, iniziare insieme questo percorso di dottorato è stato fantastico. Siamo state l'una la valvola di sfogo dell'altra, e ci siamo aiutate a vicenda per ricordarci di non mollare mai. Grazie di cuore per tutte le chiacchiere e per aver ascoltato i miei drammi. Il mondo scientifico è davvero fortunato ad avere una mente brillante come la tua! Thank you also to **Vera**, **Rico**, **Kirsten**, **Jordy** and **Jessica** for the nice times together!

Thank you to all the (old) members of the Molenaar group: **Emmy**, thank you for your guidance at the beginning of my PhD, you are amazing! Thank you to all the people of the HTS facility: **Bianca**, **Anke**, **Kim**, **Vicky** and **Selma**. **Sander** and **Karin**, working together for the ITHER project has been a pleasure! Thank you also to **Michael**, **Kaylee**, **Lindy A.**, **Lindy V.**, **Marlinde, Elisa, Michelle** and **Josephine**.

Thank you to the Rios group, with special mention to **Ravian, Hannah** and **Rijndert**.

My Máxima experience wouldn't have been the same without **To the Max!** Therefore, a very special thanks goes to all the members of the band, past and present.

Furthermore, a big thank you goes to all the members of the **PriMa PhD** committee. I am very proud of the work we have done. Keep going!

Alle amicizie fatte durante il periodo di universitá a Bologna: **Erica**, o per meglio dire Dottoressa Erica ☺, grazie per essermi sempre stata accanto per tutti questi anni, anche da lontano, e grazie per la tua costante amicizia. Ti voglio un mondo di bene. **Tilly**, il mio Tillone. Sei una boccata d'aria fresca. Grazie per tutte le risate, le serate alla Quieta Magione (a bussare sui muri di casa, e a dormire mentre Erica e Bea andavano a ballare!) e per tutti i bei ricordi che abbiamo creato insieme. **Bea**, grazie per essere stata una splendida coinquilina e compagna di avventure! **Luca**, grazie per il sostegno che mi hai dato, soprattutto nei momenti difficili. Grazie per essere venuto a trovarmi nella piccola cameretta di Utrecht, e per avermi aiutato con il trasloco! Sei uno su mille. **Elisa**, grazie per essere mia amica da cosí tanto tempo, e per avermi raggiunta qua a Utrecht! Con te non ci si annoia mai. Sono giá in trepida attesa del nostro prossimo duetto!

To my Dutch friends: **Olga**, thank you for being my friend. Thank you for helping me through the rough times, when I was alone in a country that wasn't mine. I watched you getting engaged, married, changing career path and now having a beautiful baby boy. I am so proud of you. Having you on my side as paranymph will be an honor. **Anne**, I will never forget how much you did for me when I just moved to the Netherlands. You are a special person. Wish you all the good luck with your PhD journey!

Jelmer and **Gerdine**, thank you for all the Rook games, the frikandellen and Turkish pizzas together. **Vasco** and **Loes**, thank you for the nice times together. Can't wait to meet baby Jim ☺

To all the members of the **Klooster popchoir**, it is true: "*If you get too worried, what you ought to do is sing!*". Making music together is really something magical. Carlien, I imagine you walking in fields of gold. Special thanks goes to **Agnes**, for being an awesome vocal coach and for designing a perfect cover for this book – couldn't be more happy!

Aan mijn Nederlandse familie: Thank you for all your support. I feel honored to be part of this beautiful family. **Corrie, Hennie, Judith, Jos, Lars, Ivar, Karin, Nando, Joris** en **Friso**, bedankt! Dank ook aan **Irene**, **Wim** en **Ineke**, **Tom** en **Wil**.

I feel extremely lucky to have all my four grandparents still with me: **nonna Liliana** e **nonno Lorenzo**, grazie per tutto l'amore che mi avete dato in questi anni, soprattutto sottoforma di cibo! Vi voglio un mondo di bene. **Avó Francisca** e **avô Fernando**, obrigada pelo amor e carinho. As viagens a Portugal são sempre as melhores. Gosto muito de vocês.

Obrigada também a **Fernando**, **Sandra**, **Afonso** e **Manuel**.

A mia sorella e ai miei fratelli, **Awa**, **Mirko** e **Thomas**. Vi guardo crescere da lontano, ed è difficile. Vi penso ogni giorno e sono tanto orgogliosa di quello che state diventando. Vi auguro di avere una vita felice, piena di gioia e amore. Grazie per tutti i bei momenti passati insieme. Vi voglio bene.

Grazie ai miei zii d'adozione, **Ketty** e **Matteo**. Non vedo l'ora di pianificare un nuovo viaggio verso la prossima capitale europea. Questa volta insieme al Piccolo Gigi ☺

A **Marco**, grazie per tutto quello che hai fatto per me. E grazie per essere sempre accanto alla mamma.

Mamma e **papá**, grazie per tutti i sacrifici che avete fatto per me. So bene che non sono stati pochi. Grazie per tutto l'amore che mi avete dato e continuate a dare. Grazie per avermi lasciato andare e avermi dato la possibilitá di rincorrere i miei sogni. Grazie per aver creduto in me e nelle mie scelte. Anche se lontani, vi porto nel cuore con me ogni giorno, ovunque vada. Vi voglio un mondo di bene.

And finally, to **Richard**. Thank you for all your love and support. Every time I have doubted myself throughout these years, you were there to put me back on track. Every time I was too stressed (sometimes way too stressed!), you were there to cheer me up. Thank you for all the times we cooked fancy dinners, made plans, watched tv, finished a puzzle, discussed science and made music together. You make me feel home. I can't wait to see what the future holds for us. I know for sure that, as long as we stick together, it will be just fine. Alles komt goed. Ti amo fino alla luna e ritorno... e un pochettino di piú.

Birds flying high, you know how I feel
Sun in the sky, you know how I feel
Breeze driftin' on by, you know how I feel
It's a new dawn
It's a new day
It's a new life for me ...

And I'm feeling good

Nina Simone (1965)